ISSN 1949-8470 (online)

World Journal of *Radiology*

World J Radiol 2014 September 28; 6(9): 636-740

Published by Baishideng Publishing Group Inc

WJR World Journal of Radiology

A peer-reviewed, online, open-access journal of Radiology

Editorial Board

2014-2017

The *World Journal of Radiology* Editorial Board consists of 365 members, representing a team of worldwide experts in radiology. They are from 36 countries, including Afghanistan (1), Argentina (2), Australia (5), Austria (7), Belgium (2), Brazil (8), Canada (6), Chile (1), China (43), Croatia (1), Denmark (4), Egypt (6), France (5), Germany (22), Greece (10), India (12), Iran (6), Ireland (2), Israel (3), Italy (47), Japan (13), Netherlands (1), New Zealand (1), Pakistan (1), Poland (2), Portugal (1), Serbia (1), Singapore (3), Slovakia (1), South Korea (18), Spain (4), Sweden (2), Switzerland (4), Thailand (1), Turkey (26), United Kingdom (11), and United States (82).

Yue-Qi Zhu, *Shanghai*

Croatia

Goran Kusec, Osijek

Denmark

Poul E Andersen, *Odense*
Lars J Petersen, *Aalborg*
Thomas Z Ramsoy, *Frederiksberg*
Morten Ziebell, *Copenhagen*

Egypt

Mohamed F Bazeed, *Mansoura*
Mohamed Abou El-Ghar, *Mansoura*
Reem HA Mohamed, *Cairo*
Mohamed R Nouh, *Alexandria*
Ahmed AKA Razek, *Mansoura*
Ashraf A Zytoon, *Shebin El-Koom*

France

Sabine F Bensamoun, *Compiègne*
Romaric Loffroy, *Dijon*
Stephanie Nougaret, *Montpellier*
Hassane Oudadesse, *Rennes*
Vincent Vinh-Hung, *Fort-de-France*

Germany

Henryk Barthel, *Leipzig*
Peter Bannas, *Hamburg*
Martin Beeres, *Frankfurt*
Ilja F Ciernik, *Dessau*
A Dimitrakopoulou-Strauss, *Heidelberg*
Peter A Fasching, *Erlanegn*
Andreas G Schreyer, *Regensburg*
Philipp Heusch, *Duesseldorf*
Sonja M Kirchhoff, *Munich*
Sebastian Ley, *Munich*
Adel Maataoui, *Frankfurt am Main*
Stephan M Meckel, *Freiburg*
Hans W Muller, *Duesseldorf*
Kay Raum, *Berlin*
Dirk Rades, *Luebeck*
Marc-Ulrich Regier, *Hamburg*
Alexey Surov, *Halle*
Martin Walter, *Magdeburg*
Axel Wetter, *Essen*
Christoph Zilkens, *Düsseldorf*

Greece

Panagiotis Antoniou, *Thessaloniki*
Nikos Efthimiou, *Athens*
Dimitris Karnabatidis, *Patras*
George Latsios, *Athens*
Stylianos Megremis, *Iraklion*
Alexander D Rapidis, *Athens*
Kiki Theodorou, *Larissa*
Ioannis A Tsalafoutas, *Athens*
Evanthia E Tripoliti, *Ioannina*
Athina C Tsili, *Ioannina*

India

Ritesh Agarwal, *Chandigarh*
Chandan J Das, *New Delhi*
Prathamesh V Joshi, *Mumbai*
Naveen Kalra, *Chandigarh*
Chandrasekharan Kesavadas, *Trivandrum*
Jyoti Kumar, *New Delhi*
Atin Kumar, *New Delhi*
Kaushala P Mishra, *Allahabad*
Daya N Sharma, *New Delhi*
Binit Sureka, *New Delhi*
Sanjay Sharma, *New Delhi*
Raja R Yadav, *Allahabad*

Iran

Majid Assadi, *Bushehr*
SeyedReza Najafizadeh, *Tehran*
Mohammad Ali Oghabian, *Tehran*
Amir Reza Radmard, *Tehran*
Ramin Sadeghi, *Mashhad*
Hadi Rokni Yazdi, *Tehran*

Ireland

Tadhg Gleeson, *Wexford*
Frederik JAI Vernimmen, *Cork*

Israel

Dafna Ben Bashat, *Tel Aviv*
Amit Gefen, *Tel Aviv*
Tamar Sella, *Jerusalem*

Italy

Adriano Alippi, *Rome*
Dante Amelio, *Trento*
Michele Anzidei, *Rome*
Filippo F Angileri, *Messinas*
Stefano Arcangeli, *Rome*
Roberto Azzoni, *San Donato milanese*
Tommaso V Bartolotta, *Palermo*
Tommaso Bartalena, *Imola*
Livia Bernardin, *San Bonifacio*
Federico Boschi, *Verona*
Sergio Casciaro, *Lecce*
Emanuele Casciani, *Rome*
Musa M Can, *Napoli*
Alberto Cuocolo, *Napoli*
Michele Ferrara, *Coppito*
Mauro Feola, *Fossano*
Giampiero Francica, *Castel Volturno*
Luigi De Gennaro, *Rome*
Giulio Giovannetti, *Pisa*
Francesca Iacobellis, *Napoli*
Formato Invernizzi, *Monza Brianza*
Francesco Lassandro, *Naples*
Lorenzo Livi, *Florence*
Pier P Mainenti, *Napoli*
Laura Marzetti, *Chieti*
Giuseppe Malinverni, *Crescentino*
Enrica Milanesi, *Turin*
Giovanni Morana, *Treviso*
Lorenzo Monti, *Milan*
Silvia D Morbelli, *Genoa*
Barbara Palumbo, *Perugia*
Cecilia Parazzini, *Milan*
Stefano Pergolizzi, *Messina*
Antonio Pinto, *Naples*
Camillo Porcaro, *Rome*
Carlo C Quattrocchi, *Rome*
Alberto Rebonato, *Perugia*
Giuseppe Rizzo, *Rome*
Roberto De Rosa, *Naples*
Domenico Rubello, *Rovigo*
Andrea Salvati, *Bari*
Sergio Sartori, *Ferrara*
Luca M Sconfienza, *Milano*
Giovanni Storto, *Rionero*
Nicola Sverzellati, *Parma*
Alberto S Tagliafico, *Genova*
Nicola Troisi, *Florence*

Japan

Yasuhiko Hori, *Chiba*
Hidetoshi Ikeda, *Koriyama*
Masahito Kawabori, *Sapporo*
Tamotsu Kamishima, *Sapporo*
Hiro Kiyosue, *Yufu*
Yasunori Minami, *Osaka-sayama*
Yasuhiro Morimoto, *Kitakyushu*
Satoru Murata, *Tokyo*
Shigeki Nagamachi, *Miyazaki*
Hiroshi Onishi, *Yamanashi*
Morio Sato, *Wakayama Shi*
Yoshito Tsushima, *Maebashi*
Masahiro Yanagawa, *Suita*

Netherlands

Willem Jan van Rooij, *Tilburg*

New Zealand

W Howell Round, *Hamilton*

Pakistan

Wazir Muhammad, *Abbottabad*

Poland

Maciej S Baglaj, *Wroclaw*

Piotr Czauderna, *Gdansk*

Portugal

Joao Manuel RS Tavares, *Porto*

Serbia

Olivera Ciraj-Bjelac, *Belgrade*

Singapore

Gopinathan Anil, *Singapore*
Terence KB Teo, *Singapore*
Cher Heng Tan, *Singapore*

Slovakia

Stefan Sivak, *Martin*

South Korea

Ki Seok Choo, *Busan*
Seung Hong Choi, *Seoul*
Dae-Seob Choi, *Jinju*
Hong-Seok Jang, *Seoul*
Yong Jeong, *Daejeon*
Chan Kyo Kim, *Seoul*
Se Hyung Kim, *Seoul*
Joong-Seok Kim, *Seoul*
Sang Eun Kim, *Seongnam*
Sung Joon Kwon, *Seoul*
Jeong Min Lee, *Seoul*
In Sook Lee, *Busan*
Noh Park, *Goyang*
Chang Min Park, *Seoul*
Sung Bin Park, *Seoul*
Deuk Jae Sung, *Seoul*
Choongsoo Shin, *Seoul*
Kwon-Ha Yoon, *Iksan*

Spain

Miguel A De Gregorio, *Zaragoza*
Antonio Luna, *Jaén*
Enrique Marco de Lucas, *Santander*
Fernando Ruiz Santiago, *Granada*

Sweden

Dmitry Grishenkov, *Stockholm*
Tie-Qiang Li, *Stockholm*

Switzerland

Nicolau Beckmann, *Basel*
Christian Boy, *Bern*
Giorgio Treglia, *Bellinzona*

Stephan Ulmer, *Kiel*

Thailand

Sirianong Namwongprom, *Chiang Mai*

Turkey

Kubilay Aydin, *Istanbul*
Ramazan Akdemir, *Sakarya*
Serhat Avcu, *Ankara*
Ayse Aralasmak, *Istanbul*
Oktay Algin, *Ankara*
Nevbahar Akcar, *Meselik*
Bilal Battal, *Ankara*
Zulkif Bozgeyik, *Elazig*
Nazan Ciledag, Aakara
Fuldem Y Donmez, *Ankara*
Gulgun Engin, *Istanbul*
Ahmet Y Goktay, *Izmir*
Oguzhan G Gumustas, *Bursa*
Kaan Gunduz, *Ankara*
Pelin Ozcan Kara, *Mersin*
Kivanc Kamburoglu, *Ankara*
Ozgur Kilickesmez, *Istanbul*
Furuzan Numan, *Istanbul*
Cem Onal, *Adana*
Ozgur Oztekin, *Izmir*
Seda Ozbek (Boruban), *Konya*
Selda Sarikaya, *Zonguldak*
Figen Taser, *Kutahya*
Baran Tokar, *Eskisehir*
Ender Uysal, *Istanbul*
Ensar Yekeler, *Istanbul*

United Kingdom

Indran Davagnanam, *London*
M DC Valdés Hernández, *Edinburgh*
Alan Jackson, *Manchester*
Suneil Jain, *Belfast*
Long R Jiao, *London*
Miltiadis Krokidis, *Cambridge*
Pradesh Kumar, *Liverpool*
Peter D Kuzmich, *Derby*
Georgios Plataniotis, *Brighton*
Vanessa Sluming, *Liverpool*

United States

Garima Agrawal, *Saint Louis*
James R Brasic, *Baltimore*
Rajendra D Badgaiyan, *Buffalo*
Ulas Bagci, *Bethesda*
Anat Biegon, *Stony Brook*
Ramon Casanova, *Winston Salem*
Wenli Cai, *Boston*
Zheng Chang, *Durham*
Corey J Chakarun, *Long Beach*
Kai Chen, *Los Angeles*
Hyun-Soon Chong, *Chicago*
Marco Cura, *Dallas*
Ravi R Desai, *Bensalem*
Delia DeBuc, *Miami*
Carlo N De Cecco, *Charleston*
Timm-Michael L Dickfeld, *Baltimore*
Subba R Digumarthy, *Boston*
Huy M Do, *Stanford*
Todd A Faasse, *Grand Rapids*
Salomao Faintuch, *Boston*
Girish M Fatterpekar, *New York*
Dhakshinamoorthy Ganeshan, *Houston*
Robert J Griffin, *Little Rock*
Andrew J Gunn, *Boston*
Sandeep S Hedgire, *Boston*
Timothy J Hoffman, *Columbia*
Mai-Lan Ho, *San Francisco*
Juebin Huang, *Jackson*
Abid Irshad, *Charleston*
Matilde Inglese, *New York*
El-Sayed H Ibrahim, *Jacksonville*
Paul R Julsrud, *Rochester*
Pamela T Johnson, *Baltimore*
Ming-Hung Kao, *Tempe*
Sunil Krishnan, *Houston*
Richard A Komoroski, *Cincinnati*
Sandi A Kwee, *Honolulu*
King Kim, *Ft. Lauderdale*
Guozheng Liu, *Worcester*
Yiyan Liu, *Newark*
Venkatesh Mani, *New York*
Lian-Sheng Ma, *Pleasanton*
Rachna Madan, *Boston*
Zeyad A Metwalli, *Houston*
Yilong Ma, *Manhasset*
Hui Mao, *Atlanta*
Feroze B Mohamed, *Philadelphia*
Gul Moonis, *Boston*
John L Nosher, *New Brunswick*
Rahmi Oklu, *Boston*
Aytekin Oto, *Chicago*
Bishnuhari Paudyal, *Philadelphia*
Rajul Pandya, *Youngstown*
Chong-Xian Pan, *Sacramento*
Jay J Pillai, *Baltimore*
Neal Prakash, *Duarte*
Reza Rahbar, *Boston*
Ali S Raja, *Boston*
Gustavo J Rodriguez, *El Paso*
David J Sahn, *Portlsand*
Steven Schild, *Scottsdale*
Ali R Sepahdari, *Los Angeles*
Li Shen, *Indianapolis*
JP Sheehan, *Charlottesville*
Atul B Shinagare, *Boston*
Sarabjeet Singh, *Boston*
Charles J Smith, *Columbia*
Kenji Suzuki, *Chicago*
Monvadi Srichai-Parsia, *Washington*
Sree H Tirumani, *Boston*
Hebert A Vargas, *New York*
Sachit Verma, *Philadelphia*
Yoichi Watanabe, *Minneapolis*
Li Wang, *Chapel Hill*
Carol C Wu, *Boston*
Shoujun Xu, *Houston*
Min Yao, *Cleveland*
Xiaofeng Yang, *Atlanta*
Qingbao Yu, *Albuquerque*
Aifeng Zhang, *Chicago*
Chao Zhou, *Bethlehem*
Hongming Zhuang, *Philadelphia*

WJR World Journal of Radiology

Contents

Monthly Volume 6 Number 9 September 28, 2014

World Journal of Radiology
Volume 6 Number 9 September 28, 2014

Contents

AIM AND SCOPE

World Journal of Radiology (*World J Radiol*, *WJR*, online ISSN 1949-8470, DOI: 10.4329) is a peer-reviewed open access academic journal that aims to guide clinical practice and improve diagnostic and therapeutic skills of clinicians.

WJR covers topics concerning diagnostic radiology, radiation oncology, radiologic physics, neuroradiology, nuclear radiology, pediatric radiology, vascular/interventional radiology, medical imaging achieved by various modalities and related methods analysis. The current columns of *WJR* include editorial, frontier, diagnostic advances, therapeutics advances, field of vision, mini-reviews, review, topic highlight, medical ethics, original articles, case report, clinical case conference (clinicopathological conference), and autobiography.

We encourage authors to submit their manuscripts to *WJR*. We will give priority to manuscripts that are supported by major national and international foundations and those that are of great basic and clinical significance.

INDEXING/ABSTRACTING

World Journal of Radiology is now indexed in PubMed Central, PubMed, Digital Object Identifier, and Directory of Open Access Journals.

NAME OF JOURNAL
World Journal of Radiology

ISSN
ISSN 1949-8470 (online)

LAUNCH DATE
December 31, 2009

FREQUENCY
Monthly

EDITORIAL OFFICE
Jin-Lei Wang, Director
Xiu-Xia Song, Vice Director
World Journal of Radiology
Room 903, Building D, Ocean International Center,
No. 62 Dongsihuan Zhonglu, Chaoyang District,
Beijing 100025, China
Telephone: +86-10-59080039
Fax: +86-10-85381893
E-mail: editorialoffice@wjgnet.com
Help Desk: http://www.wjgnet.com/esps/helpdesk.aspx
http://www.wjgnet.com

PUBLISHER
Baishideng Publishing Group Inc
8226 Regency Drive,
Pleasanton, CA 94588, USA
Telephone: +1-925-223-8242
Fax: +1-925-223-8243
E-mail: bpgoffice@wjgnet.com
Help Desk: http://www.wjgnet.com/esps/helpdesk.aspx
http://www.wjgnet.com

PUBLICATION DATE
September 28, 2014

INSTRUCTIONS TO AUTHORS
Full instructions are available online at http://www.wjgnet.com/1949-8470/g_info_20100316162358.htm.

ONLINE SUBMISSION
http://www.wjgnet.com/esps/

World Journal of Radiology

Submit a Manuscript: http://www.wjgnet.com/esps/
Help Desk: http://www.wjgnet.com/esps/helpdesk.aspx
DOI: 10.4329/wjr.v6.i9.636

World J Radiol 2014 September 28; 6(9): 636-642
ISSN 1949-8470 (online)

TOPIC HIGHLIGHT

WJR 6th Anniversary Special Issues (6): CT

Echography in brain imaging in intensive care unit: State of the art

Anselmo Caricato, Sara Pitoni, Luca Montini, Maria Grazia Bocci, Pina Annetta, Massimo Antonelli

Anselmo Caricato, Sara Pitoni, Luca Montini, Maria Grazia Bocci, Pina Annetta, Massimo Antonelli, Department of Anesthesiology and Intensive Care Medicine, Catholic University of the Sacred Heart, "A. Gemelli" Teaching Hospital, Intensive Care Unit, 00168 Roma, Italy

Author contributions: Caricato A, Pitoni S and Antonelli M designed the paper; Montini L produced images; Bocci MG and Annetta P critically revised the paper; Caricato A wrote the paper.

Correspondence to: Anselmo Caricato, Assistant Professor, Department of Anesthesiology and Intensive Care Medicine, Catholic University of the Sacred Heart, Largo A. Gemelli 8, 00168 Roma, Italy. anselmo.caricato@fastwebnet.it
Telephone: +39-339-3974355 Fax: +39-6-97252605
Received: January 10, 2014 Revised: March 18, 2014
Accepted: July 15, 2014
Published online: September 28, 2014

Abstract

Transcranial sonography (TCS) is an ultrasound-based imaging technique, which allows the identification of several structures within the brain parenchyma. In the past it has been applied for bedside assessment of different intracranial pathologies in children. Presently, TCS is also used on adult patients to diagnose intracranial space occupying lesions of various origins, intracranial hemorrhage, hydrocephalus, midline shift and neurodegenerative movement disorders, in both acute and chronic clinical settings. In comparison with conventional neuroimaging methods (such as computed tomography or magnetic resonance), TCS has the advantages of low costs, short investigation times, repeatability, and bedside availability. These noninvasive characteristics, together with the possibility of offering a continuous patient neuro-monitoring system, determine its applicability in the monitoring of multiple emergency and non-emergency settings. Currently, TCS is a still underestimated imaging modality that requires a wider diffusion and a qualified training process. In this review we focused on the main indications of TCS for the assessment of acute neurologic disorders in intensive care unit.

Key words: Brain sonography; Transcranial sonography; Ultrasounds; Cerebral sonography; Brain imaging; Hydrocephalus; Cerebral hemorrhage

Core tip: Transcranial sonography (TCS) is an ultrasound-based imaging technique, which allows the identification of several structures within the brain parenchyma, not only in neonates, but also in adult patients. It can be used to diagnose intracranial space occupying lesions of various origins, intracranial hemorrhage, hydrocephalus and midline shift. In comparison with computed tomography scan, TCS has the advantages of low costs, short investigation times, repeatability, and bedside availability. These noninvasive characteristics, together with the possibility of offering a continuous patient neuro-monitoring system, determine its applicability in multiple emergency settings.

Caricato A, Pitoni S, Montini L, Bocci MG, Annetta P, Antonelli M. Echography in brain imaging in intensive care unit: State of the art. *World J Radiol* 2014; 6(9): 636-642 Available from: URL: http://www.wjgnet.com/1949-8470/full/v6/i9/636.htm DOI: http://dx.doi.org/10.4329/wjr.v6.i9.636

INTRODUCTION

Definitions

In the last years, due to new ultrasounds technology, echographic imaging of the brain parenchyma has been obtained not only in children, but also in adults. Several authors have found a good visualization of cerebral structures using transcranial B-mode ultrasounds through a

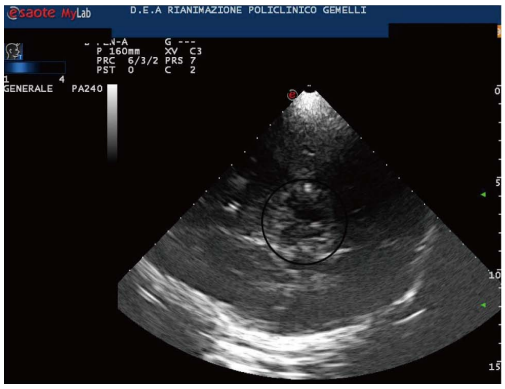

Figure 1 Midbrain transverse scan. The butterfly-shaped mesencephalic brainstem surrounded by the echogenic basal cisterns is shown in the circle.

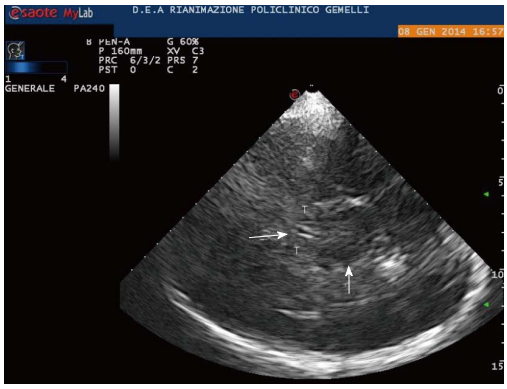

Figure 2 Diencephalic transverse scan. The third ventricle can be visualized as a highly echogenic double-line image (arrow head on the left). Mesencephalon is indicated by the arrow head on the right. T: Thalamus.

transtemporal approach [transcranial sonography (TCS)].

In the past, the skull was considered unsuitable for sonographic examination because of its thick structure. Aaslid *et al*[1] described a "temporal window", the thinner part of the temporal bone located just above the zygomatic arch, and observed that low-frequency ultrasounds may well penetrate inside the skull in this zone. Since then, TCS has been proposed for bedside identification of many different intracranial pathologies, in both acute and chronic settings, such as intracranial space occupying lesions of various origins (intracranial hemorrhage), hydrocephalus, midline shift and neurodegenerative movement disorders. In comparison with conventional neuroimaging methods such as computed tomography (CT) and Magnetic Resonance, TCS has the advantages of low costs, short investigation times, repeatability, and bedside availability. These noninvasive characteristics, together with the possibility of offering a continuous patient neuro-monitoring system, determine its wide applicability in the monitoring of multiple emergency settings including Intensive Care Units, trauma centers and the context of emergency transportations (*i.e.*, aeromedical flights, helicopter transfers, *etc.*)[2,3].

The main limitation of TCS is its dependence to an adequate temporal acoustic window. In fact, between 5%-18% of patients the exam is not feasible due to a particularly thick structure of the temporal bone[4]. Higher percentage of failure rate was described in people of Asian ethnic origin[5].

In this context, patients with skull defects, such as those who underwent decompressive craniectomy, allow a very accurate assessment of brain parenchyma by TCS[2].

In this review, we summarize the usefulness of this technique for the assessment of acute neurological disorders in the intensive care unit, describing proposed indications, technical considerations, main advantages and limitations.

TCS technique

The patient lies in a supine position, and the examiner usually sits at the head of the examination table, firmly positioning the ultrasound probe on the temporal zone. The location of the acoustic window may be variable. In fact, it can be either located in the anterior part of the temporal bone, close to the vertical portion of the zygomatic bone, or, more frequently, posteriorly and close to the pinna of the ear. A low-frequency probe with a 2.0-2.5 MHz phased array transducers is appropriate to insonate the brain through the intact skull. In case of decompressive craniectomy, a standard abdominal convex phased-array probe with a mean central frequency of 4 MHz and an abdominal setting can be used.

Usually, the examination starts with the identification of the mesencephalic brainstem in the axial plane parallel to the "orbitomeatal line", so to obtain CT-like images (Midbrain transverse scan; Figures 1 and 2). The butterfly-shaped mesencephalic brainstem surrounded by the echogenic basal cisterns is the "landmark" of this scan, and can be observed in 90%-95% of the patients.

Tilting the probe about 10° upwards, a diencephalic transverse scan may be obtained. In this section, the third ventricle can be visualized as a highly echogenic double-line image, due to ipsilateral and controlateral inner layer of the hyperechogenic ependima (Figures 2-4).

Just posteriorly, *thalami* are depicted as hypoecogen/hysoecogen structures surrounding the third ventricle (Figure 2). Anteriorly, the frontal horn of the contralateral *lateral ventricle* is visualized as hypoechogenic structure, well visible between two parallel lines corresponding to the medial and lateral layer of the ependima (Figure 4). At this plane, the largest transverse diameters of the third ventricle and of the frontal horns of the contralateral lateral ventricle may be measured[6,7]. It may be useful to pay attention that image is generated by a sectorial probe, and the proportions are different in the central and in the lateral part of the image. Thus, lateral ventricle ipsilateral to the probe is often depicted at the same depth of the third ventricle.

The insonation planes are usually the midbrain and diencephalic transverse ones, even though the coronal orientation has been described. A free hand multiplanar approach has been observed, especially on surgically decompressed patients[2], and attempts of standardized

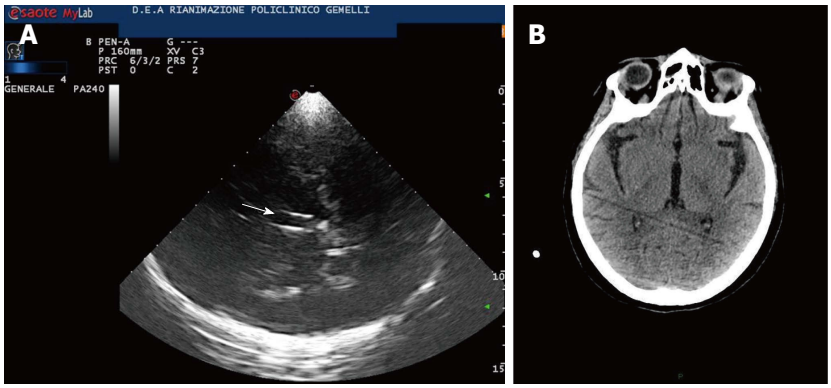

Figure 3 Third ventricle. A: Diencephalic transverse scan. A small enlargement (12 mm) of third ventricle is shown (arrow); B: Third ventricle in computed tomography (CT). CT scan correspondent of Figure 3A is shown.

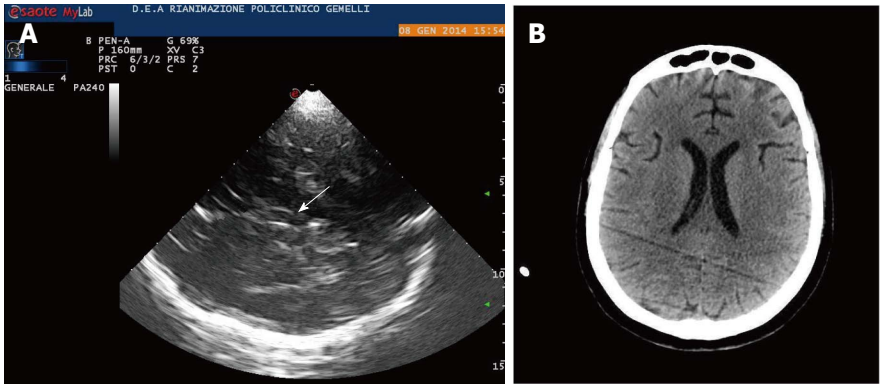

Figure 4 Lateral ventricles. A: Lateral ventricles in echography. Frontal horns of lateral ventricles are visualized as hypoechogenic structure, well visible between two parallel lines corresponding to the medial and lateral layer of the ependima. The three parallel lines correspond to lateral layers of ependima and septum pellucidum. The image is generated by a sectorial probe, and lateral ventricle ipsilateral to the probe is depicted at the same depth of the third ventricle. Arrow shows third ventricle, Small arrow heads on the left show frontal horns of lateral ventricles; B: Lateral ventricles in computed tomography (CT). CT scan of lateral ventricles correspondent of Figure 4A is shown.

approaches have been reported[8]. A standardization of insonation planes would be very useful for comparison and follow-up of sonographic findings.

With the blind technique, landmarks regularly visualized, even in moderate sonographic conditions (identification rates of > 75%) are mesencephalon, pons, third ventricle, lateral ventricles, falx, thalamus, basal ganglia, pineal gland and temporal lobe[7]. Moreover, ultrasound (US) perfusion imaging can be enhanced by the application of echo-contrast harmonic imaging modalities[9,10].

CLINICAL APPLICATION

Intracranial hemorrhage

In spontaneous or traumatic cerebral hemorrhage (ICH), hematoma enlargement is the most important modifiable prognostic factor; thus, monitoring of the volume of the hemorrhage is the first priority in the acute phase[11,12].

CT's widespread acute availability makes it the primary diagnostic modality for ICH. However, in the first hours after the diagnosis, TCS may be very useful to monitor an early ICH enlargement. In fact, TCS allows the visualization of acute ICH, as an hyperechoic sharply demarcated mass within the brain parenchyma. The accuracy is limited to the first 4-6 d after the onset of the ICH, when the hematoma remains more echogenic than the surrounding brain tissue.

Several authors studied the correlation between CT and TCS in cerebral hemorrhage. Seidel confirmed CT diagnosis by TCS in 18/23 cases (78%)[9]. Mäurer *et al*[13] published a study on TCS in 151 stroke patients correctly differentiating between ischemia and hemorrhage in 95%. 12% had an insufficient temporal bone window for transcranial insonation.

Perez *et al*[14] prospectively studied 46 patients with supratentorial ICH evaluated within 3 h of onset. In 8 cases ICH was not observed by TCS: 5 patients showed a small-sized ICH on CT, and in 3 cases hematoma was located in brainstem or in cerebellum. In the remaining patients a very good correlation was observed for each diameter of the mass and for total hematoma volume ($r = 0.82$, $P < 0.001$).

TCS was also evaluated to detect hemorrhagic transformation in the early phase of ischemic stroke. Seidel *et al*[15] found an excellent correlation between TCS and CT on 20 patients with hemorrhagic transformation; in 2 cases small cortical hematoma was not diagnosed.

From these data, TCS seems an interesting option for ICH monitoring; actually, its accuracy appears insufficient to support therapeutic decisions in the acute setting.

Recent studies evaluated the impact of echo contrast agents on visualization of ICH by TCS. By using ultra-

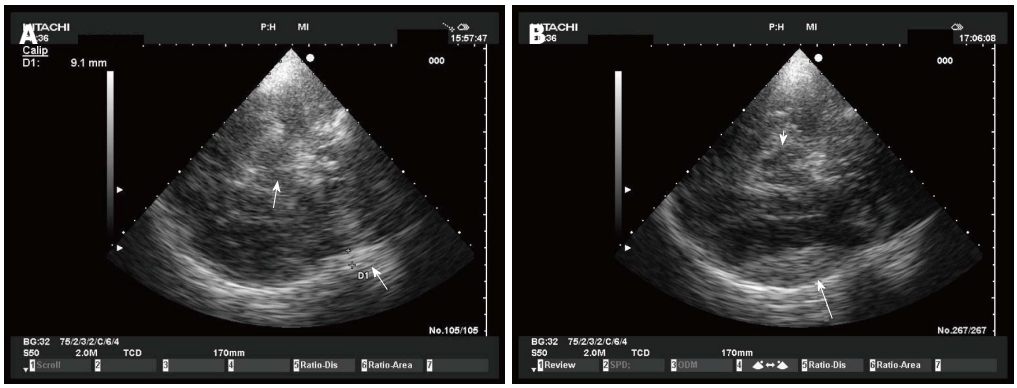

Figure 5 Epidural hematoma in echography. A: Epidural hematoma. A small epidural hematoma (arrow on the right) is shown as an hyperechogenic image just inside the skull. Arrow on the left indicates mesencephalon; B: Epidural hematoma. The same epidural hematoma of Figure A (arrow) 1 h later. White arrow indicates mesencephalon.

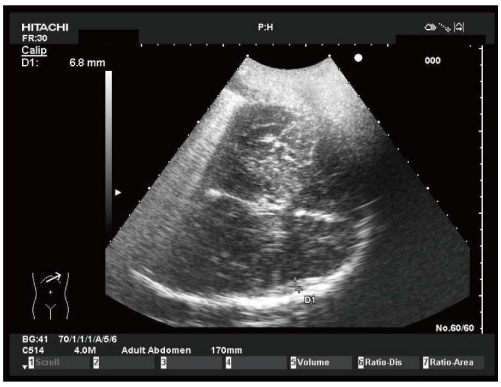

Figure 6 Epidural hematoma in decompressive craniectomy. A small acute epidural hematoma is shown as a hyperechogenic mass lesion controlateral to decompressive craniectomy.

sound perfusion imaging, Kern *et al*[16] observed a reduction in contrast agent arrival in the ICH core, which led to better delineation of the lesion borders from adjacent tissue. Correlation with CT was very good (r = 0.94, 95%CI: 0.81-0.98, $P < 0.001$). Similar results were reported by Vicenzini[17] and Kern[18].

US perfusion imaging has a wide diffusion in myocardial, renal and musculoskeletal tissue, and might be an option even for brain under difficult insonation conditions; actually, the real advantage of this technique on TCS is still unknown.

Epidural and Subdural hemorrhage

Epidural and subdural hematoma (EDH, SDH) are potentially life-threatening complications after severe, moderate and mild traumatic brain injury. If undetected and untreated, they may lead to progressive transtentorial herniation with loss of consciousness, pupillary dilation, and further neurologic deficits. In EDH-patients, the CT scan remains the diagnostic gold standard, but early bedside detection of acute EDH by TCS has been described[19]. By using a midbrain transverse scan, contralateral skull became well visible even in absence of decompressive craniectomy, and an epidural hematoma can be observed as an hyperechogenic image just inside the skull (Figures 5-7). Prospective data on usefulness of this technique for EDH detection are lacking and should be encouraged.

The extent of SDH has also been diagnosed and monitored by TCS [20]. In particular, SDH has been quantified by measuring the distance between the skull and the dural border of the arachnoid, described as a highly echogenic membrane. In this context, Niesen *et al*[20] reliably detected SDH in 22 of the 25 patients with confirmed SDH (88%). In the remaining 3 patients, the temporal bone window was insufficient for TGS investigation. Extent of SDH measured by CT and TCS correlated linearly (r = 0.849)[20].

In conclusion, TCS, when performed by a trained sonographer, may represent a possible method for noninvasively monitoring early hematoma growth at the bedside of patients with or without skull defects, with the role of complementing the CT scan diagnostic technique.

Midline shift

In the diencephalic transverse scan, midline dislocation (MLD) and hydrocephalus can be diagnosed through TCS scanning. The MLD can be observed and measured through two different methods.

According to the method described by Seidel *et al*[7], the third ventricle should be considered as a marker of the midline. The distance between third ventricle and external side of the temporal bone (A), needs to be measured. The same calculation can be repeated for the contralateral side (B). A MLD of the third ventricle is then estimated according to the formula MLD = (A - B)/2.

In that study, a reproducibility of sonographic MLD measurements corresponding to 0.3 ± 0.2 mm was reached in 10 healthy volunteers. This technique has been widely investigated by several studies in patients with acute cerebrovascular disease and after traumatic brain injury, and a very good correlation between sonographic and CT measurement of MLD are reported[21-23].

After decompressive craniectomy this method may be difficult. Bone defects, temporal cephalhematomas, or changes in intracranial anatomy secondary to trauma

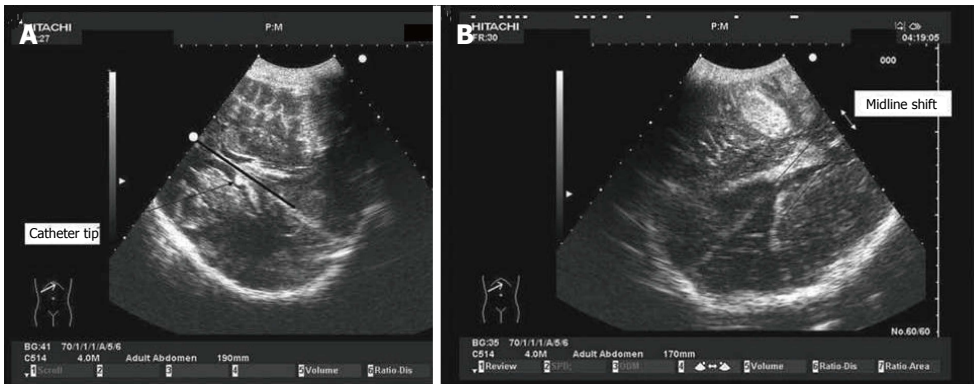

Figure 7 Midline shift in decompressive craniectomy. Images obtained through decompressive craniectomy. Midline was identified with the interventricular line. The distance between the extension of falx and the interventricular line was measured as midline shift (MLS). In the case on the left (A), the extension of the falx exactly overlaps with the interventricular line (dark line). On the right (B), MLS caused by a temporal hematoma is shown.

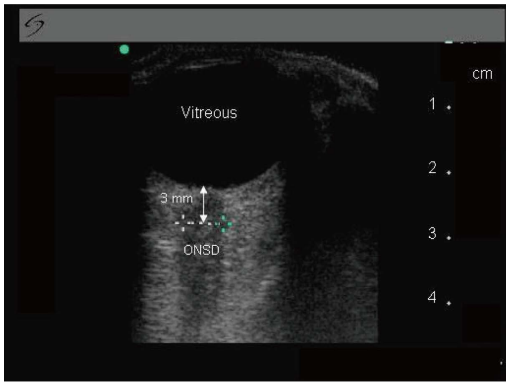

Figure 8 Optic nerve sheath diameter. Using a 7.5-MHz linear probe on the closed upper eyelid, the optic nerve was visualized as a linear hypoechoic structure with clearly defined margins posterior to the globe. Sheath diameter was measured 3 mm behind the globe. ONSD: Optic nerve sheath diameter.

may all induce bias in the measure. In such a condition, Caricato *et al*[2] described a further method to visualize the MLD. This technique has shown an excellent agreement with CT scan measurements. In an axial plane, the midline, defined as the line between the two lateral ventricles, is measured by a convex probe with an abdominal preset. After localizing the falx cerebri, both on frontal and occipital sides, the distance between the extension of falx and the interventricular line is assessed; the present measurement is the MLD (Figure 8). The last method, which is still to be externally validated, seems rather simple and accurate because measurements are obtained on direct observation of the images and not by indirect mathematical calculations.

Hydrocephalus

Posthemorrhagic hydrocephalus is a frequent complication after subarachnoid hemorrhage or parenchymal hemorrhage; furthermore external ventricular drainage may be necessary after severe traumatic injury to control intracranial hypertension. In these conditions, direct visualization of cerebral ventricles may be required, and critical patients have to be moved to radiology for CT scan.

In this context, TCS may be an useful option. In fact, previous studies compared sonographic and CT measurements of ventricular diameters, founding a good agreement. This was observed in particular for the measurement of third ventricle, that is depicted in a plane orthogonal to the probe, and doesn't need angle correction. As we reported above, direct measurement of lateral ventricles is more difficult since its angle with the probe, and a generally moderate correlation with CT scan is reported. Actually, Kiphuth *et al*[21] observed that TCS was a reliable technique to predict the need of cerebrospinal fluid drainage. In patients with external ventricular drainage (EVD), they estimated that a cut-off value of an increase of 5.5 mm in ventricle width after clamping had an high sensitivity (100%) and negative predictive value (100%). They suggested that an increase in ventricular width lower than the cut-off was an indication for a safe removal of EVD.

In conclusion, even if the technique still requires a wide validation, it seems to be an interesting option when repetitive CT measurement have to be performed to monitor obstructive hydrocephalus in intensive care Unit.

Evaluation of intracranial hypertension

Optic nerve sheath diameter: Measurement of optic nerve sheath diameter has been proposed as a measure of increased intracranial pressure in a variety of settings[24-26]. In fact, the sheath around the optic nerve is a continuation of the dura; thus, a rise in ICP is transmitted to the optic nerve, eventually resulting in swelling of the optic disc and in a sheath diameter grater than the normal. The technique is easy and a quick learning curve is described. According with Cennamo *et al*[27], patients were examined in the supine position. Using a 7.5-MHz linear probe on the closed upper eyelid, the optic nerve was visualized as a linear hypoechoic structure with clearly defined margins posterior to the globe. Sheath diameter was measured 3.00 mm behind the globe, and a value greater than 5.00 mm was considered abnormal.

The technique has been described more than 20 years ago; even if some criticism should be considered[28], it is

proposed as screening test to rule out intracranial hypertension noninvasively at the bedside.

CONCLUSION

In neurointensive care transcranial Doppler is often used for the evaluation of the cerebral blood flow, diagnosis and monitoring of vasospasm, and autoregulation in patients with different types of brain injury. Beyond the classic indications of transcranial doppler, B-mode ultrasounds can be used as imaging technique to monitor patients in ICU, and may often reduce the indication to CT scan. In this review we summarized the main indications for TCS in intensive care unit. In our opinion, it is a still underestimated imaging modality that requires a wider diffusion. As for any other sonographic assessment, TCS is a highly user-dependent technique, and requires expertise to perform accurate evaluation. In this context, physicians working in neurologic intensive care medicine should be trained not only to apply Doppler methods for investigation of cerebral vessels but also in transcranial B-mode sonography; further studies should be encouraged for a better comprehension of usefulness and limits of this technique as option to brain CT.

REFERENCES

1 **Aaslid R**, Markwalder TM, Nornes H. Noninvasive transcranial Doppler ultrasound recording of flow velocity in basal cerebral arteries. *J Neurosurg* 1982; **57**: 769-774 [PMID: 7143059]

2 **Caricato A**, Mignani V, Bocci MG, Pennisi MA, Sandroni C, Tersali A, Antonaci A, de Waure C, Antonelli M. Usefulness of transcranial echography in patients with decompressive craniectomy: a comparison with computed tomography scan. *Crit Care Med* 2012; **40**: 1745-1752 [PMID: 22610180 DOI: 10.1097/CCM.0b013e318246b6ea]

3 **Libert N**, Boutonnet M, Giraud N, Tourtier JP, de Rudnicki S. Transcranial echography: an interesting tool for aeromedical evacuations. *Crit Care Med* 2012; **40**: 3331-3332; author reply 3332 [PMID: 23164789 DOI: 10.1097/CCM.0b013e3182675c60]

4 **Wijnhoud AD**, Franckena M, van der Lugt A, Koudstaal PJ, Dippel ED. Inadequate acoustical temporal bone window in patients with a transient ischemic attack or minor stroke: role of skull thickness and bone density. *Ultrasound Med Biol* 2008; **34**: 923-929 [PMID: 18243493 DOI: 10.1016/j.ultrasmedbio.2007.11.022]

5 **Yoshimura S**, Koga M, Toyoda K, Mukai T, Hyun BH, Naganuma M, Nagatsuka K, Minematsu K. Frontal bone window improves the ability of transcranial color-coded sonography to visualize the anterior cerebral artery of Asian patients with stroke. *AJNR Am J Neuroradiol* 2009; **30**: 1268-1269 [PMID: 19213827]

6 **Seidel G**, Kaps M, Gerriets T. Potential and limitations of transcranial color-coded sonography in stroke patients. *Stroke* 1995; **26**: 2061-2066 [PMID: 7482650 DOI: 10.1161/01.STR.26.11.2061]

7 **Seidel G**, Kaps M, Gerriets T, Hutzelmann A. Evaluation of the ventricular system in adults by transcranial duplex sonography. *J Neuroimaging* 1995; **5**: 105-108 [PMID: 7718936]

8 **Kern R**, Perren F, Kreisel S, Szabo K, Hennerici M, Meairs S. Multiplanar transcranial ultrasound imaging: standards, landmarks and correlation with magnetic resonance imaging. *Ultrasound Med Biol* 2005; **31**: 311-315 [PMID: 15749552 DOI: 10.1016/j.ultrasmedbio.2004.12.006]

9 **Seidel G**, Meyer-Wiethe K, Berdien G, Hollstein D, Toth D, Aach T. Ultrasound perfusion imaging in acute middle cerebral artery infarction predicts outcome. *Stroke* 2004; **35**: 1107-1111 [PMID: 15031454 DOI: 10.1161/01.STR.0000124125.19773.40]

10 **Bartels E**, Bittermann HJ. Transcranial contrast imaging of cerebral perfusion in patients with space-occupying intracranial lesions. *J Ultrasound Med* 2006; **25**: 499-507 [PMID: 16567439]

11 **Brouwers HB**, Greenberg SM. Hematoma expansion following acute intracerebral hemorrhage. *Cerebrovasc Dis* 2013; **35**: 195-201 [PMID: 23466430 DOI: 10.1159/000346599]

12 **Dowlatshahi D**, Demchuk AM, Flaherty ML, Ali M, Lyden PL, Smith EE. Defining hematoma expansion in intracerebral hemorrhage: relationship with patient outcomes. *Neurology* 2011; **76**: 1238-1244 [PMID: 21346218 DOI: 10.1212/WNL.0b013e3182143317]

13 **Mäurer M**, Shambal S, Berg D, Woydt M, Hofmann E, Georgiadis D, Lindner A, Becker G. Differentiation between intracerebral hemorrhage and ischemic stroke by transcranial color-coded duplex-sonography. *Stroke* 1998; **29**: 2563-2567 [PMID: 9836768 DOI: 10.1161/01.STR.29.12.2563]

14 **Pérez ES**, Delgado-Mederos R, Rubiera M, Delgado P, Ribó M, Maisterra O, Ortega G, Alvarez-Sabin J, Molina CA. Transcranial duplex sonography for monitoring hyperacute intracerebral hemorrhage. *Stroke* 2009; **40**: 987-990 [PMID: 19164795 DOI: 10.1161/STROKEAHA.108.524249]

15 **Seidel G**, Cangür H, Albers T, Burgemeister A, Meyer-Wiethe K. Sonographic evaluation of hemorrhagic transformation and arterial recanalization in acute hemispheric ischemic stroke. *Stroke* 2009; **40**: 119-123 [PMID: 18988915 DOI: 10.1161/STROKEAHA.108.516799]

16 **Kern R**, Kablau M, Sallustio F, Fatar M, Stroick M, Hennerici MG, Meairs S. Improved detection of intracerebral hemorrhage with transcranial ultrasound perfusion imaging. *Cerebrovasc Dis* 2008; **26**: 277-283 [PMID: 18648201 DOI: 10.1159/000147456]

17 **Vicenzini E**, Delfini R, Magri F, Puccinelli F, Altieri M, Santoro A, Giannoni MF, Bozzao L, Di Piero V, Lenzi GL. Semiquantitative human cerebral perfusion assessment with ultrasound in brain space-occupying lesions: preliminary data. *J Ultrasound Med* 2008; **27**: 685-692 [PMID: 18424642]

18 **Kern R**, Krogias C, Meyer-Wiethe K, Renault G, Kablau M, Sallustio F, Eyding J, Meves S, Seidel G, Meairs S: Diagnosis of acute ischemic vs. hemorrhagic stroke with transcranial ultrasound imaging – a prospective multi-center study. *Cerebrovasc Dis* 2006; **21** (suppl 4): 34

19 **Caricato A**, Mignani V, Sandroni C, Pietrini D. Bedside detection of acute epidural hematoma by transcranial sonography in a head-injured patient. *Intensive Care Med* 2010; **36**: 1091-1092 [PMID: 20213067 DOI: 10.1007/s00134-010-1801-0]

20 **Niesen WD**, Burkhardt D, Hoeltje J, Rosenkranz M, Weiller C, Sliwka U. Transcranial grey-scale sonography of subdural haematoma in adults. *Ultraschall Med* 2006; **27**: 251-255 [PMID: 16596509 DOI: 10.1055/s-2006-926544]

21 **Kiphuth IC**, Huttner HB, Struffert T, Schwab S, Köhrmann M. Sonographic monitoring of ventricle enlargement in posthemorrhagic hydrocephalus. *Neurology* 2011; **76**: 858-862 [PMID: 21288979 DOI: 10.1212/WNL.0b013e31820f2e0f]

22 **Stolz E**, Gerriets T, Fiss I, Babacan SS, Seidel G, Kaps M. Comparison of transcranial color-coded duplex sonography and cranial CT measurements for determining third ventricle midline shift in space-occupying stroke. *AJNR Am J Neuroradiol* 1999; **20**: 1567-1571 [PMID: 10512247]

23 **Llompart Pou JA**, Abadal Centellas JM, Palmer Sans M, Pérez Bárcena J, Casares Vivas M, Homar Ramírez J, Ibáñez Juvé J. Monitoring midline shift by transcranial color-coded sonography in traumatic brain injury. A comparison with cranial computerized tomography. *Intensive Care Med* 2004; **30**: 1672-1675 [PMID: 15197433 DOI: 10.1007/s00134-004-2348-8]

24 **Newman WD**, Hollman AS, Dutton GN, Carachi R. Measurement of optic nerve sheath diameter by ultrasound: a means of detecting acute raised intracranial pressure in hydrocephalus. *Br J Ophthalmol* 2002; **86**: 1109-1113 [PMID: 12234888 DOI: 10.1136/bjo.86.10.1109]
25 **Moretti R**, Pizzi B, Cassini F, Vivaldi N. Reliability of optic nerve ultrasound for the evaluation of patients with spontaneous intracranial hemorrhage. *Neurocrit Care* 2009; **11**: 406-410 [PMID: 19636971]
26 **Dubost C**, Le Gouez A, Jouffroy V, Roger-Christoph S, Benhamou D, Mercier FJ, Geeraerts T. Optic nerve sheath diameter used as ultrasonographic assessment of the incidence of raised intracranial pressure in preeclampsia: a pilot study. *Anesthesiology* 2012; **116**: 1066-1071 [PMID: 22258019 DOI: 10.1097/ALN.0b013e318246ea1a]
27 **Cennamo G**, Gangemi M, Stella L: The comparison between endocranial pressure and optic nerve diameter: an ultrasonographic study. *Doc Ophthalmol Proc Ser* 1987; **48**: 603-606 [DOI: 10.1007/978-94-009-3315-6_99]
28 **Copetti R**, Cattarossi L. Optic nerve ultrasound: artifacts and real images. *Intensive Care Med* 2009; **35**: 1488-1489; author reply 1488-1489 [PMID: 19367390 DOI: 10.1007/s00134-009-1494-4]

P- Reviewer: Brigo F, Llompart-Pou J, Zanini MA
S- Editor: Ji FF **L- Editor**: A **E- Editor**: Lu YJ

World Journal of Radiology

Submit a Manuscript: http://www.wjgnet.com/esps/
Help Desk: http://www.wjgnet.com/esps/helpdesk.aspx
DOI: 10.4329/wjr.v6.i9.643

World J Radiol 2014 September 28; 6(9): 643-656
ISSN 1949-8470 (online)

TOPIC HIGHLIGHT

WJR 6th Anniversary Special Issues (6): CT

From histology to micro-CT: Measuring and modeling resorption cavities and their relation to bone competence

Jef Vanderoost, G Harry van Lenthe

Jef Vanderoost, G Harry van Lenthe, Biomechanics Section, Department of Mechanical Engineering, KU Leuven, 3001 Leuven, Belgium
Author contributions: Vanderoost J and van Lenthe GH solely contributed to this paper.
Correspondence to: G Harry van Lenthe, PhD, Biomechanics Section, Department of Mechanical Engineering, KU Leuven, Celestijnenlaan 300c b2419, 3001 Leuven, Belgium. vanlenthe@.kuleuven.be
Telephone: +32-16-322595 Fax: +32-16-322595
Received: December 22, 2013 Revised: April 22, 2014
Accepted: July 25, 2014
Published online: September 28, 2014

Abstract

The process of bone remodelling plays an essential role in the emergence and maintenance of bone geometry and its internal structure. Osteoclasts are one of the three main bone cell types that play a crucial role in the bone remodelling cycle. At the microstructural level, osteoclasts create bone deficits by eroding resorption cavities. Understanding how these cavities impair the mechanical quality of the bone is not only relevant in quantifying the impact of resorption cavities in healthy bone and normal aging, but maybe even more so in quantifying their role in metabolic bone diseases. Metabolic bone diseases and their treatment are both known to affect the bone remodelling cycle; hence, the bone mechanical competence can and will be affected. However, the current knowledge of the precise dimensions of these cavities and their effect on bone competence is rather limited. This is not surprising considering the difficulties in deriving three-dimensional (3D) properties from two-dimensional (2D) histological sections. The measurement difficulties are reflected in the evaluation of how resorption cavities affect bone competence. Although detailed 3D models are generally being used to quantify the mechanical impact of the cavities, the representation of the cavities themselves has basically been limited to simplified shapes and averaged cavity properties. Qualitatively, these models indicate that cavity size and location are important, and that the effect of cavities is larger than can be expected from simple bone loss. In summary, the dimensions of osteoclast resorption cavities were until recently estimated from 2D measures; hence, a careful interpretation of resorption cavity dimensions is necessary. More effort needs to go into correctly quantifying resorption cavities using modern 3D imaging techniques like micro-computed tomography (micro-CT) and synchrotron radiation CT. Osteoclast resorption cavities affect bone competence. The structure-function relationships have been analysed using computational models that, on one hand, provide rather detailed information on trabecular bone structure, but on the other incorporate rather crude assumptions on cavity dimensions. The use of high-resolution representations and parametric descriptions could be potential routes to improve the quantitative fidelity of these models.

Key words: Resorption cavities; Histology; Micro-computed tomography

Core tip: Osteoclasts create bone deficits by eroding resorption cavities. Understanding how these cavities impair the mechanical quality of the bone is relevant in both in healthy bone and in metabolic bone diseases. However, the current knowledge of their dimensions and effect on bone competence remains limited. Until recently cavity dimensions were estimated from two-dimensional measures (histology), hence, careful interpretation was necessary. With new imaging techniques quantifying resorption cavities in three-dimensional becomes feasible. Computational models have shown that resorption cavities affect bone competence. The use of high-resolution representations and parametric descriptions could improve the quantitative fidelity of these models.

Vanderoost J, van Lenthe GH. From histology to micro-CT: Measuring and modeling resorption cavities and their relation to bone competence. *World J Radiol* 2014; 6(9): 643-656 Available from: URL: http://www.wjgnet.com/1949-8470/full/v6/i9/643.htm DOI: http://dx.doi.org/10.4329/wjr.v6.i9.643

INTRODUCTION

The process of bone remodelling plays an essential role in emergence and maintenance of bone geometry and its internal structure. This system has been extensively investigated from different angles, including its biology, chemistry and (bio) mechanical consequences. From a structural and mechanical point of view the most essential part of the process is the resorption and formation of bone performed by the basic multicellular units (BMU). This group of cells is responsible for bone loss and bone gain and determines the mechanical properties of the bone both in structure and material properties. In case of metabolic bone diseases, the functioning of these cells is altered. Structurally, and consequently mechanically, resorption cavities formed during resorption, determine the bone deficit. These cavities are an essential element in modelling and predicting the effect of bone disease and treatment. Despite this fact, the effort going into specifically quantifying these cavities and their effect on bone strength is relatively limited. Besides that, measuring methods are numerous and their results require careful interpretation when used for modelling purposes. This review aims at bundling the knowledge on these cavities and their biomechanical role. More specifically, its goal is: (1) to provide an overview of methods that can quantify the geometric properties of resorption; and (2) to apply this information to critically review biomechanical models that incorporate these geometric properties. Our premise is a mechanical point of view; hence, for the purpose of this review we will focus on direct impact of the presence of cavities on bone competence rather than investigating the dynamic parameters of the remodelling process. Our focus lies on bone remodelling in trabecular bone. Since trabecular bone has a much higher specific bone surface than cortical bone, it is more vulnerable to these surface-based processes[1,2].

METHODOLOGY

PubMed was searched in the first half of 2012 to identify relevant literature. The search terms used were "resorption cavities", "Howship's lacunae", "resorption", "erosion", "remodelling" separately and in combination with "bone", "trabecular bone" or "cancellous bone". For the modelling section combinations with "remodelling", "model" and "finite elements" were also used. Subsequently numerous cross-references were followed through. This review does not claim to cover all publications related to the subject. Specifically in section 5 (Characteristics of resorption cavities) only a selection of publications was included, given the vast amount of studies analysing transiliac bone biopsies.

RESORPTION CAVITIES AND THE BONE REMODELLING CYCLE

Frost first introduced the concept of the BMU[3]. These units are a group of cells which, in a coordinated way, control the bone remodelling process. A team of osteoclasts perform the bone resorption. These irregularly shaped cells remove old bone and form the resorption cavities or Howship's lacunae, which are later refilled by the osteoblasts. The osteoblasts perform the bone formation by excreting the building blocks of the bone matrix (unmineralised bone or osteoid) and have a role in the mineralisation of this soft bone[4,5]. Some osteoblasts get entombed in the bone matrix and differentiate to osteocytes. The cytoplasmic processes of these osteocytes extend trough a network of canaliculi. It is assumed that this network monitors the local strain environment and thus has a role in the signalling process of bone remodelling[2,5,6]. Other osteoblasts die or become bone lining cells. These cells digest unmineralised osteoid and might be involved in the localization and initiation of remodelling[5]. The result of BMU action, the packet of new bone, is called a bone structural unit (BSU)[7]. Bone structural units are the Haversian systems or osteons in cortical bone, and semi lunar structures separated by cement lines in trabecular bone[8]. The BMU exists and moves in three dimensions, excavating and refilling a tunnel through cortical bone or a trench across the surface of cancellous bone[9].

After resorption, an intermediary phase, called "reversal phase" as introduced by Baron[10], exists in which mononuclear cells occupy the lacunae and no resorption takes place[11]. It is in this phase that the cement line is formed.

Formation and resorption are coupled, both in space and in time. It has been observed that osteoclasts occupy the more superior parts of resorption lacunae, while mononuclear cells and preosteoblast-like cells are situated in the deeper parts. This supports the hypothesis that these cell types precede each other in the remodelling process[11]. It is likely that formation is preceded by resorption and they may even occur simultaneously in the same remodelling unit[4,6,12-15], yet interruptions in the process, both in formation and resorption, have been hypothesized[14]. It has been suggested that mononuclear cells are also active in the resorption process, by digesting the organic matrix constituents[11].

QUANTIFICATION OF RESORPTION CAVITIES

Almost all knowledge concerning resorption cavities is derived from transilliac bone biopsies. The main focus in this review is therefore on the measurement and in-

terpretation of resorption cavity properties obtained from biopsies following the nomenclature conventions proposed by Parfitt *et al*[16]. Biomarker data is increasingly used to analyse bone remodelling. However despite the problems cited below, the transilliac bone biopsies remain the golden standard for measuring bone turnover[17].

Transillac bone biopsies

The three-dimensional (3D) characteristics of resorption cavities are generally extrapolated from two-dimensional (2D) features measured on histological sections using stereological formulas. However this extrapolation is not without flaws since it assumes unbiased and random sampling and isotropy, which are not fulfilled in bone[18]. 2D widths are transformed to 3D thicknesses by using the parallel plate model[19] and the distribution is corrected for missing measurements[20]. There are also intraobserver, interobserver, intermethod and sample variations that have to be taken into account[11,13,18,21].

During histomorphometric analysis different staining methods can be used which highlight certain features. Toluidine blue is used to identify cavities under polarized light by looking at the presence of cut off collagen fibers (disruption of the lamellar system) at the edge of the cavity[13,18,22]. The polarized light allows visualisation of the orientation of collagen lamellae along the mineralized bone surface. The identification of scalloped surfaces can however be subjective[23]. Tartrate-resistand acid phospahtase can be used to mark active osteoclasts and thus "active" cavities[24]. Von Kossa/van Gieson staining allows to discriminate osteoid from mineralized bone[18].

Besides the general problems with histomorphometry, cavity related measurements are also influenced by choosing which cavities to include. Measurement of cavities always presents a snap shot, where not only active sites are visible but also aborted sites, where resorption "prematurely" stopped, interrupted sites, where resorption is temporarily halted, and reversals sites[25]. Distinguishing between these sites is not straightforward and assuming cavities are first completely eroded before osteoblasts start refilling is also an oversimplification[25]. Some authors[11] perform the technically difficult task of identifying specific cell types (osteoclasts, mononuclear cells, pre-osteoblast-like cells) in the cavities to distinguish between different stages in resorption and thus identify "completed" cavities with the largest depth obtained in the cycle[22,18]. But the presence of these cells might be heterogeneous and might be dependent on the specific histological section[13]. Therefore, most cavities might not represent effective "active" resorption and cautious interpretation of resorption related parameters is necessary. Moreover, small erosions may be difficult to distinguish from minor surface irregularities and whether these erosions are seen depends on the magnification[25]. Specifically, cavities with depth below 3 μm are often omitted[14,26]. When all cavities are included, the resulting average size is smaller than the size of the completed ones, but including all cavities leads to valuable information concerning the distribution of cavities and the eroded surface at a certain time point. It has to be realized that the deep cavities that cause perforation cannot be identified or included in the measurements[13,18,23,27]. When investigating treatment effects it is useful to label surfaces using calcein in order to be sure that they were actively forming during the period of treatment[28].

The administration of two time-spaced doses of tetracycline prior to bone biopsy enables assessment of dynamic indices of bone formation[18]. However, resorption can't be assessed dynamically (with the exception of biological markers), since removed bone is invisible; hence only indirect measurements are available. As a consequence it is not possible to tell from these static measures how much resorption is actually going on[4,13].

Quantification of erosion depth in transilliac bone biopsies

The depth of a cavity is generally indicated by erosion depth (E.De). Indirect measurements are more common, in which the depth is calculated from other parameters or assumed to be similar to formation parameters. Wall thickness (W.Th) is the most widely used (Figure 1). It is the distance between cement lines of "resting" cancellous surfaces without osteoid or lacunae, reflecting the amount of bone created during a remodelling event[4,5,11,13]. Eriksen[11] did not find a significant difference between the distribution of completed wall thickness and pre-osteoblast-like cell, or deepest, resorption depths in healthy subjects. Another measure is osteoid thickness[13]. A third measure is mean interstitial bone thickness, calculated from measurement of W.Th on both sides of a trabecula and the mean trabecular plate thickness, but this is not as reliable[13,29]. However, when the bone balance, calculated as the difference between W.Th and E.De[8], is not zero, these parameters do not correctly represent the resorption depth.

Two direct methods have been developed to quantify the depth of a cavity (E.De) (Figure 1). Eriksen *et al*[11] introduced the method of lamellar counting. The average lamellar width is measured and the number of lamellae cut at the cavity edges is counted (Figure 1). The method relies heavily on accurate identification of cells to classify cavities: when this identification is not possible, cavities are excluded (about 24%)[13]. A disadvantage of this method is that it is impossible to count the lamellae correctly when different BSU with different orientations overlap. Besides that, the lamellar thickness inside an osteon can vary and not all lamellae are parallel to the surface which is an assumption in this method[30].

In the other direct method, the pre-resorption surface is reconstructed and used to measure cavity dimensions[31]. This method is generally computerized and applies an interactive curve fitting method to the cavity edge. All identifiable cavities are included regardless of their stage of completion[27]. Large differences between the results of both methods have been observed[13,32]. They are partly explained by the number of cavities in-

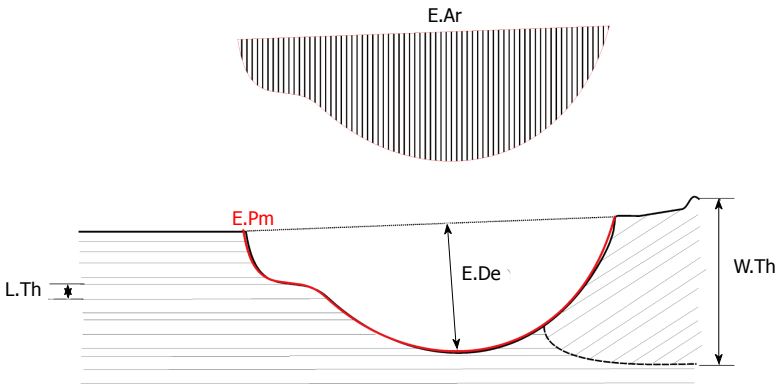

Figure 1 Schematic representation of different resorption cavity related measurements on 2D histological sections: Eroded area, erosion perimeter, wall thickness and lamellar thickness. E.Ar: Eroded area; E.Pm: Erosion perimeter; W.Th: Wall thickness; L.Th: Lamellar thickness.

cluded and the choice of maximum or mean depth: Eriksen method measures are systematically larger because the cavities are "completed" (with pre-osteoblast like cells), unidentified cavities were omitted and a constant lamellar width is assumed[27,32]. Cohen-Solal *et al*[32] used the Garrahan method on completed cavities only (covered with osteoid), but still found values significantly lower than Eriksen. Roux *et al*[30] developed a method similar to Garrahan's, and performed a direct comparison with the lamellar counting method. A rather high correlation was found ($R^2 = 0.76$, $P = 0.0001$) but with significantly lower values for the computerized method. Due to line reconstruction problems, cavities at the end of a trabecula could not be measured, while a higher number of lacunae were omitted during lamellar counting due to poor visibility of eroded lamellae. Again, the lacunae included seemed to determine the E.De outcome.

The measurement difficulties including the large variability and lack of consensus on the measurement technique have led to the publication of a recommendation not to directly evaluate resorption cavity depth in transiliac biopsies[33]. However, E.De has a large mechanical impact (see below) and thus remains an important parameter in the assessment of the impact of resorption cavities on bone competence.

Quantification of erosion surface and volume in transilliac bone biopsies

The shape of a cavity can very; hence cavity width and area can differ even for constant E.De[28]. Consequently, taking parameters into account that go beyond erosion depth can be important when investigating the effect of disease and treatment on bone resorption. On histological sections, the total eroded perimeter (E.Pm) is the basic measure for the extend of cavities (Figure 1). The widely used erosion surface/bone surface (ES/BS) is calculated using this E.Pm. Just like all cavity measurement on biopsies, ES/BS is a snapshot of resorption and not a dynamic parameter[33]. ES/BS is also a relative measure: adding a resorption cavity to the surface not only increases the eroded surface (ES) but also increases the total bone surface (BS) in the histological section, since the crenate surface of a cavity is larger than undamaged surface before resorption (Figure 1). Similar to E.De, some authors[11] further specify this surface depending on the cells and activity present in the lacunae. Osteoclast surface, Oc.S/BS, is often interpreted as "active" erosion surface in contrast to reversal surface. The relative amount of both types is case-dependent and interpretation of ES/BS can therefore be misleading, *i.e.*, an increased ES/BS can be caused by an increased reversal phase and not necessarily by increased osteoclast activity[33]. Other formation parameters like osteoid surface (OS/BS) and osteoblast surface (Ob.S/BS) might be good indicators for related resorption parameters in healthy subjects with a stable bone balance. In general OS/BS seems to be larger than ES/BS. Several possible explanations exist: formation is slower, formation is initiated before the completion of resorption and/or the presence of arrested resorption cavities[34].

The erosion volume or remodelling space, calculated from eroded area (Figure 1), is rarely determined on biopsies although it is highly correlated to bone resorption rate as indicated by urinary excretion of total deoxypyridioline[30]. Some authors measure the E.Pm for each individual cavity (cavity length or eroded length) as an indication for shape changes of individual cavities[31,35].

Quantification of number of cavities in transilliac bone biopsies

The number of cavities per bone surface (Nc/BS) is rarely measured, although it is a simple measure. Activation frequency (Ac.f) is more widely used. In theory, Ac.f is the number of new remodelling units activated anywhere on the surface in a given time and thus a good measure for the number of cavities present at a certain time. In practice the Ac.f is calculated as the inverse of the total period (remodelling period + quiescent period). This doesn't correspond exactly with the conceptual definition[13] and doesn't take into account the 3D organisation of a BMU and the distance it travels[9]. Being a highly derived variable the issues in calculation, assumptions and interpretation are numerous[33] and interpretation is often complicated. Ac.f is thus especially interesting in a qualitative sense as to compare whether, in a certain situation, new cavities are introduced. Since cavities exist in different stages of resorption and cavities with interrupted resorption exist, the quantitative values cannot be readily used to assess the total numbers of cavities present at a certain time point.

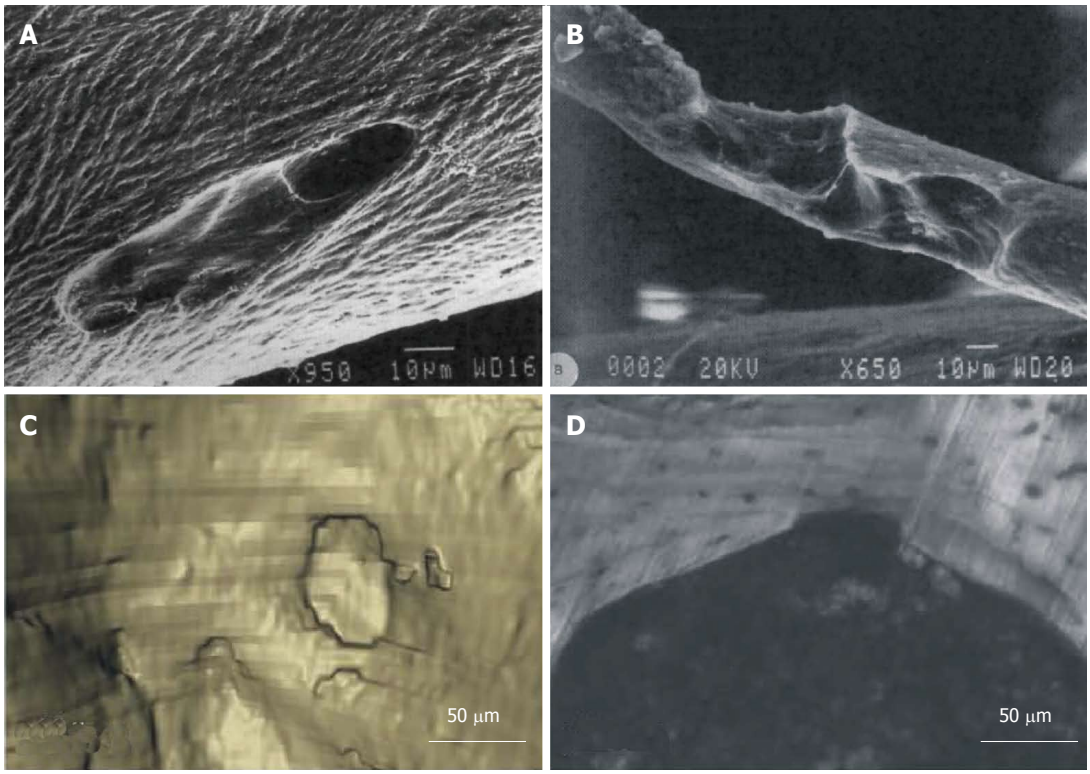

Figure 2 Three-dimensional visualizations of resorption cavities. Using scanning electron microscope (A, B) reprinted from[37] and serial milling (C: Three-dimensional reconstruction; D: Corresponding cross section image) reprinted from[38].

New imaging techniques

The use of 2D histomorphometry has limitations. Neither can it discriminate an increase in the number of remodelling events from an increase in the size of each individual event[9] nor can the full volumetric extend of a cavity be measured[36]. The development of 3D methods to asses BMU's are essential to advance our ability to study how alterations in its morphology occur with disease and treatment[28]. Scanning Electron Microscope (SEM) images give a good indication of the 3D nature of resorption cavities as can be seen in Figure 2A and B[37]. But currently, no clinical imaging devices are able to detect resorption cavities because of their small size compared to image resolution. It has been shown that high-resolution images (at least 1.4 µm or better) are required to consistently identify and measure individual resorption cavities[38].

Recent developments in imaging techniques show great potential to quantify cavities in 3D and detect them automatically. Specifically, individual resorption cavities were measured in 3D on animal vertebrae using serial milling[38] (Figure 2C and D). This technique was able to reveal that cavity size and location are related to the local trabecular microarchitecture. Goff *et al*[39] found that, on the human vertebral trabecular bone samples they investigated, half of the cavities were located on the intersections of trabeculae and most others were on plate like-trabeculae oriented in the main loading direction (cranial-caudal). Next to that confocal laser microscopy and vertical scanning profilometry have recently been used to measure bone resorbing activity, extending *in vitro* measurements from ES/BS under microscope to full 3D measurements of volume and depth[40,41].

Synchrotron-radiation based computer tomography (SR-CT) and high-resolution micro computer tomography (µCT) are technically able to obtain the necessary detail, but might not be able to capture enough cavities per specimen to characterize a population. The most promising development probably lies in high-resolution *in-vivo* µCT. Schulte *et al*[42] recently presented a new time-lapsed imaging method which allows quantification of dynamic resorption parameters at a resolution of 10.5 µm. They were able to effectively measure 3D ES and BS by comparing subsequent 3D reconstructions of the same bone separated by 4 wk. The non-invasive nature of this technology allows longer periods of investigation and might enable researchers to reveal time-dependent evolutions in resorption; yet improvements in image resolution are needed to be able to dynamically track individual resorption cavities.

CHARACTERISTICS OF RESORPTION CAVITIES

The following section will provide a limited overview of measured cavity properties in health and specific disease. It does not cover the full range of studies analysing transiliac bone biopsies, but aims at providing a general indication of resorption cavity properties found in literature and showing the wide range of values that have been reported.

This is relevant in relation to biomechanical modelling since, as discussed in section 6, several biomechanical models neither incorporate the most relevant nor most accurate properties. Based on measurement issues described before, we will focus on E.De and W.Th as measures for cavity depth. For the extend of cavities we will provide data on ES.BS and when available on EV/BV. All reported data in this section are related to transiliac bone biopsies, except when indicated differently.

Healthy bone

Cavities are often elongated, have varying depths and can lie close together. Sizes varied from 50 μm × 20 μm to 1000 μm × 1000 μm, most were 200 μm × 500 μm in size[37]. In a single cavity about 0.05 mm³ of bone tissue is removed[5]. The frequency distribution of cavity sizes in a trabecular bone sample is skewed: there are few very deep cavities and a large amount of shallow ones[13]. This is the case for all measurement methods, although, as explained above, the method and choice of included cavities does make a difference[8,11,14,43].

It seems reasonable to accept that there is no difference in the biology of the bone remodelling process at different skeletal sites. Hence, if there would be a link between microdamage and resorption activity, this would impact local erosion measurements, since some bones are more heavily and frequently strained leading to more microdamage[2]. Since the local loading environment is site-dependent and leading to differences in local trabecular microstructure, it is expected that different erosion patterns occur as well. Indeed, bone structure and turnover appeared different between the distal radius and the iliac crest. Specifically, W.Th, ES/BS and Ac.f were significantly lower in the distal radius[44]. Given the fact that most cavity-related studies are based on bone biopsies from the iliac crest, these results should be critically reviewed before extrapolating the results to other skeletal sites.

There is little information regarding the location of the cavities on the trabecular surface itself. Analysis of trabecular thinning and connectedness of trabecular bone revealed that the site of activation of new BMU's may be preferentially located were trabeculae are either thinner or thicker, such as trabecular intersections[27,45,46]. This would be consistent with the microdamage-theory since these locations are highly strained. Most remodelling is likely targeted at replacing fatigue-microdamaged bone or at removing hyper mineralized bone[9].

Age-related changes in resorption cavity properties have been observed (Table 1). For children, growth to peak bone mass is realised by high formation, with Ac.f and W.Th decreasing with age, while bone resorption parameters (ES/BS) don't vary significantly[23]. In adults, there is continued reduction in bone formation taking place with age as shown by a reduced W.Th[8,29,47,48], while resorption continues with an unchanged or even increased amount of resorbed surface[24,27,43,49]. No or only a small decrease in E.De has been reported[22,24,27]. A small decrease in (average) E.De would be a logical consequence of reduced W.Th because more shallow cavities, which were incompletely refilled, remain on the bone surface. But it also possible that resorption has increased and has caused deep perforation cavities, which are not measured: their absence in the cavity depth distribution would also shift the average depth to lower values.

Neither sex nor ethnic differences seem to exist when it comes to resorption parameters like E.De, W.Th and ES/BS, at least before menopause[14,24,27,43,48,50,51]. But with menopause, there are significant differences between the sexes. In menopause, the age-related reduction in W.Th is accelerated and more BMU's are born (increased Ac.f), while resorption itself is hardly affected. As a consequence bone turnover is accelerated and females are subjected to an accelerated trabecular bone loss[5,6,15,51-53]. Three to five years after menopause, the W.Th seems to recover to the premenopausal values and a more or less steady state emerges, in which the remodelling rate is still higher than premenopausal due to a higher Ac.f, but lower than during menopause[6,53]. In men, this "temporarily" acceleration does not happen and the "normal" decrease in W.Th with age accompanied by with unchanged resorption, continues[51,54,55].

Effect of osteoporosis

Metabolic bone diseases alter the bone remodelling cycle and can thus change the resorption cavity properties (Table 2). As we demonstrate below for osteoporosis, the limitations of the measurement methods hinder clear interpretation of the results.

As indicated earlier, the menopause causes, even in normal subjects, an increase in Ac.f and a negative bone balance. In post-menopausal osteoporosis (PmOP) these effects on Ac.f and W.Th are even stronger, with extreme loss in bone mass as a consequence[17,32,56,57]. Again, given the likely increased presence of underfilled cavities associated with a reduced W.Th, one would expect a reduced average E.De, but an increased ES/BS. In contrast to normal post-menopausal women, a small but not significant increase in resorption depth has been observed[15,17,32,56,57]. Furthermore, ES/BS is reduced or unchanged[56,57]. Given this difference from normal age-related changes, we hypothesize that individual cavity depth might actually have increased in PmOP, but that this increase is not detected with the averaged values for E.De reported in literature. The presence of underfilled cavities and absence of perforating cavities in the measurement, shift this average to lower values, masking the real increase. The increased cavity depth might cause more perforations on already thinner trabeculae and, again, because these perforating cavities are not included in the ES/BS measurement, the real ES is underestimated. Idiopathic (primary) male osteoporosis leads to similar effects but while some studies find similar results as for PmOP[54,58], others found unchanged W.Th and increased resorption parameters (ES/BS)[47].

Prolonged corticoid treatment leads to secondary OP.

Table 1 Normal values for specific eroded surface, erosion depthand wall thickness as reported in literature for healthy patients

Sex	Parameter	Change with age	Mean age	Values
F	ES/BS (%)	↓[2]↑	10-30	2.15 (0.36)[43] 3.23 (2.6-4.02)[22]
			30-60	3.43 (2.68-4.4)[22] 1.85 (0.82-4.21)[27] 1.78"[43]
			60-90 (post-meno)	4.59 (3.72-5.66)[22] 4.2 (1.7)[24] 7.1[1] (2.9-16.9)[56] 4.0 (2.0)[57] 1.66 (0.66)[43]
			All ages	6.2 (2.9)[21]
	E.De (μm)	[2]↓	10-30	56.8 (50.2-63.4)[22]
			30-60	63.4 (57.5-69.3)[22] 33.7 (24.4-46.6)[27]
			60-90 (post-meno)	50.8 (46.9-54.7)[22] 27.21 (2.27)[24] 49.1[1] (38.3-61.7)[56] 49.4 (12.1)[32]
	W.Th (μm)	↓	10-30	62.0 (8)[29]
			30-60	49.0 (9.1)[48] 37.2 (3.8)[51] 38.1 (28.6-68.8)[53] 56.2 (7.1)[50] 50.4 (7.4)[29]
			60-90 (post-meno)	48.8[1] [37.8-62.2][56] 33.9 (4.7)[51] 32.2 (23.2-39.3)[53] 39.5 (2.0)[32] 32.1 (4.13)[57] 44.3 (4.9)[50] 40.2 (4.6)[29]
			All ages	31-43.9[13] 49.0 (2.5)[21]
M and F	ES/BS(%)	↓[2]	10-30	16.3 (11.6-18.1)[102] 16.6 (5.6)[23]
			30-60	4.03 (1.42)[11]
			All ages	1.35 (0.39)[31] 1.94 (0.76-4.93)[103]
	E.De (μm)	[2]↓	30-60	62.6[11]
			All ages	28.9 (23.4-39.3)[31] 34.2 (22.8-51.3)[103]
	W.Th (μm)	↓	10-30	44.2 (5.7)[102] 41.4 (5.7)[23]
			30-60	61.9 (6.8)[11]
			60-90	59.4[13]
			All ages	51.6 (35.8-74.4)[103]
M	ES/BS(%)	↓[2]↑	10-30	3.32 (2.34-4.7)[22] 6.3 (0.6)[49] 2.84 (1.27)[43]
			30-60	3.55 (2.55-4.95)[22] 3.7 (0.9)[24] 1.81 (0.72-4.56)[27] 6.6[2][51] 1.72[2][43]
			60-90	3.99 (3.11-5.13)[22] 3.7 (0.6)[24] 6.4+[49] 1.91 (0.42)[43]
	E.De (μm)	[2]↓	10-30	66.1 (57.1-75.1)[22]
			30-60	64.1 (48.0-60.2)[22] 33.0 (3.16)[24] 35.6 (23.2-54.7)[27]
			60-90	46.3 (44.3-48.3)[22] 28.94 (1.78)[24]
	W.Th (μm)	↓	10-30	62.0 (8.1)[29] 32.8 (2.6)[49]
			30-60	50.2 (8.7)[48] 53 (8.6)[50] 49.2 (4.6)[29] 35.0[2][49]
			60-90	48.5 (8.6)[50] 43.8 (2.8)[29] 32.8[2][49]
			All ages	40.6[13]

[1]Median; [2]Indicates recalculation to age groups. Data ordered by sex [Female (F), Female and male (FM), Male (M)] and age groups (10-30 year, 30-60 year, 60-90 year or all ages mixed). Values presented as mean ± SD, mean [95% confidence interval (CI)], mean [10th-90th percentile], mean [Q 1st-3rd quartile], Also indicated is whether the parameters increase (↑), decrease (↓) with age or stay constant (b). ES/BS: Erosion surface/bone surface; E.De: Erosion depth; W.Th: Wall thickness.

The main effect is osteoblastic dysfunction, with significantly reduced W.Th as a consequence. Next to that, the lifespan of osteoclasts seems to be increased and changes in cavity surface shape have been observed[59]. The change in cavity surface shape might have a different mechanical impact, especially in combination with an increased E.De and ES/BS, as indicated in most studies[5,60-63].

Effect of anti-osteoporotic medication

Treatment for OP interferes with the bone remodelling cycle, hence, may affect osteoclast resorption cavities. This section presents an overview of the effect of some of the major anti-osteoporotic medication for which resorption cavity properties were reported and compared to untreated PmOP patients (Table 3).

Bisphosphonates (BP) reduce bone resorption by reducing the Ac.f: the number of new BMU's that initiate and thus the remodelling space decreases[28,52,60,64-66]. The W.Th is reduced as well but no evidence of changes in ES/BS was found[52,60,64,66,67]. It is debated whether osteoclasts are only prevented from starting new BMU's or that the amount of bone resorbed by a BMU is reduced as well; also the number and size of the resorption cavities might be reduced[28,68,69]. The impact on resorption cavity properties would be similar: either only underfilled and thus shallow cavities remain or only new shallow cavities are resorbed. Indeed, superficial cavities have been observed next to giant hypernucleated osteoclasts[70]. BPs thus prevent a significant increase in erosion depth and prevent further progression of the resorption pits[67].

The trends observed for resorption parameters in other treatments are less clear and few studies found conflicting results. In contrast to BPs, both parathyroid hormone (PTH 1-84) and the cyclic hPTH(1-34) (Teriparatide), caused an increase in ES/BS, next to an increased Ac.f and W.Th, although it was not always significant[71-73]. A larger surface is thus occupied by cavities, but the increased W.Th may keep them superficial. For patients treated with strontium Ranelate, a dual action bone agent, some studies found no significant differences in Ac.f or ES/BS while others found a significantly reduced ES/BS[52,74].

In a recent three-dimensional dynamic bone histomorphometric study, Matheny *et al*[75] showed reductions in resorption cavity size (depth, width and volume) with antiresorptive agents (Raloxifene and Risondrenate) while the ES/BS was unchanged.

Table 2 Change of eroded surface, erosion depth and wall thickness in common bone diseases (postmenopausal osteoporosis, male idiopathic osteoporosis, glucocorticoid induced osteoporosis) as reported in literature

Disease	Parameter	Change	Values[1] [1]Significantly lower than control [2]Significantly higher than control
PmOP	W.Th (μm)	↓	40.74[a] (31.6-54.3)[1][56] 36.2 (6.4)[1][21] 28.3 (20.1-34.8)[1][53] 35.3 (2.0)[1][32] 28.0 (4.44)[1][57] 29.3 (1.4)[73] 31.2 (0.4)-32.1 (0.5)[64] 41.8 (4.25)-49.0 (8.93)[67]
	ES/BS (%)	[b]↓	5.3[a] (1.7-18.1)[56] 6.0 (3.0)[21] 4.8 (2.7)[57] 1.67 (0.48)[73] 4.9 (2.9)[71] 1.89 (0.12)-3.41 (0.5)[64] 4.49 (1.6) - 6.55 (1.62)[65] 2.18 (1.24)[61] 2.42 (Q 1.31-2.93)[72] 4.7 (Q 3.3-5.7)-5.2 (Q 3.2-6.9)[67]
	E.De (μm)	[b]	55[a] (37.3-82)[56] 48.5 (43.8-53.2)[8] 50.0 (13.4)[32] 22 (5)[71] 13.5 (0.43)-15.8 (0.91)[64]
	EV/BV (%)		0.46 (0.04)-1.21 (0.29)[64]
MIOP	ES/BS (%)	↑	9.7 (1.7)[55] 7.5 (1.3-17.7)[58]
	E.De (μm)	[b]	44.7 (9.3)[58]
	W.Th (μm)	[b]↓	35.3 (7.5)[1][58]
GC	EV/BV (%)		0.44 (0.1)[60]
induced	ES/BS (%)	[b]↑	2.3 (0.4)[60] 4.06 (2.45)[61]
OP	E.De (μm)	↑	15.0 (1.3)[60]
	W.Th (μm)	↓	30.6 (0.8)[60]

Significant difference *vs* control indicated ([1]Significantly lower than control; [2]Significantly higher than control); [a]Median; Values presented as mean ± SD, mean (95%CI), mean [10th-90th percentile], mean [Q 1st-3rd quartile]; [b]Also indicated in table is whether the parameters increase (↑), decrease (↓) due to the disease or stay constant. When more then one value is reported for the same reference, it concerns measurements at different time points. ES/BS: Erosion surface/bone surface; E.De: Erosion depth; W.Th: Wall thickness; PmOP: Postmenopausal osteoporosis.

Table 3 Change of eroded surface, erosion depth and wall thickness with treatment for postmenopausal osteoporosis as reported in literature

Treatment for PmOP	Parameter	Change	Values[1] [1]Significantly lower then no treatment [2]Significantly higher then no treatment
Bisphosphonates (oral/IV ibandronate, alendronate, risendronate)	EV/BV (%)	[b]	0.40 (0.1)-0.50 (0.1)[60]
	ES/BS (%)	[b]	2.2 (0.4)-2.6 (0.5)[60]
			5.3 (2.75)[67]
			1.29 (90%CI: 1.04-1.95)-1.62 (90%CI: 1.32-1.88)[66]
	E.De (μm)	[b]	13.4 (1.0)-16.2 (1.0)[60]
			45.6 (9.45)[67]
	W.Th (μm)	[b]	30.0 (1.0)-31.4 (1.0)[60]
			41.6 (4.86)[67]
Strontium ranelate	ES/BS (%)	[b]	2.92 (1.48-3.89)[52]
Strontium ranelate 6 m	ES/BS (%)	↓	1.21 (0.21)[1][74]
hPTH (1-34) (teriparatide)	ES/BS (%)	↑	0.78 (0.11)[74]
			10.1 (4.9)[2]-11.8 (7.1)[2][71]
			3.51 (Q 2.67-5.64)-4.0 (Q 2.8-6.0)[72]
	W.Th (μm)	[b]	22 (5)-28 (7)[71]
PTH (1-84)	ES/BS (%)	[b]↑	1.75 (0.35)[73]
	W.Th (μm)	[b]	33.1 (1.4)[73]

Significant difference vs control (no treatment) indicated ([1]Significantly lower than control; [2]Significantly higher than control). Values as mean ± SD, mean (95%CI), mean [10th-90th percentile], mean[Q 1st-3rd quartile]; [b]Also indicated in table is whether the parameters increase (↑), decrease (↓) due to the treatment or stay constant. When more than one value is reported for the same reference, it concerns measurements at different time points or different doses. ES/BS: Erosion surface/bone surface; E.De: Erosion depth; W.Th: Wall thickness; PmOP: Postmenopausal osteoporosis.

BIOMECHANICAL CONSEQUENCES OF RESORPTION CAVITIES

Resorption by osteoclasts, as part of the bone remodelling cycle, causes cavities on the bone surface, since the cells reach their location through the bone marrow. During resorption and the following reversal phase, these cavities form structural defects, that weaken the bone[6]. With a normal bone balance, this mechanical effect is quasi-constant, since an equal amount of cavities is refilled simultaneously. If this balance is disrupted, the changes cause a structural and thus mechanical effect[4,12].

Three main possible mechanisms have been identified by which bone turnover in general can influence bone biomechanics[36]. These mechanisms are related to bone mass, yet they have effects that go beyond their direct impact on the bone volume and thus go beyond "standard" density-strength power relationships[76,77]. First, there is the effect of modifications in tissue degree of mineralisation, which is not directly related to resorption. Second, the fenestration or disconnection of individual trabeculae that modify the trabecular architecture is a direct result of resorption[76,78-80]. And third, the resorption cavities also act as stress risers. Experimental evaluation of these effects is difficult, forcing researchers to rely on modelling.

In the next paragraph we focus on different modelling approaches and their findings.

Modelling resorption cavities in finite element analyses

Numerous authors have tried to model the bone remodelling sequence, but few have directly incorporated the 3D microstructural properties of resorption. There have mainly been attempts using analytical models to predict local changes of bone properties like the bone density, based on BMU properties like birth-rate, formation, resorption and mineralisation rates[81,82]. These models don't incorporate the real resorption cavity properties and are thus not further described in this review.

Simplified structural models can give insight in some of the basic mechanism of the effect of cavities on bone mechanical properties. Mechanical analyses of the effect of a cavity on a straight beam shows that the number and size of remodelling cavities may influence the mechanical behaviour of a trabecula independent of bone volume or total amount of bone turnover[36].

Using a mechano-regulation algorithm to model and refill cavities of different depths on a 2D and 3D simplified finite element model of a bone trabeculum, it was shown that beyond a certain cavity depth the remodelling was not able to refill the cavity and a notching effect caused perforation[83,84].

An extension of simple beam models is 2D and 3D lattice structures. Langton proposed a 2D stochastical model of resorption on a lattice structure where resorption was guided by a probability that a surface pixel is activated and a probability for the duration of resorption[85]. Small bone volume losses caused high stiffness losses which are related to 2D nature of that model. Lattice 3D models are more robust, A model presented by Tayyar *et al*[86] used planar structural units to test the effect of increased activation frequency during menopause on bone volume. He used rectangular shaped cavities with a maximum depth of 50 μm and 2% of the cavity volume was not refilled during formation[86]. The volume loss was larger in case of menopause, with almost 40% of the bone loss caused by perforation (disconnection from the network).

Lattice models are unable to capture the complex and heterogeneous nature of trabecular bone. In a trabecular network, the mechanical effect of perforations or ruptures depends on the cavity location and specific trabecular properties. μCT-scans have enabled researchers to take the intricate trabecular structure into account when modelling resorption effects.

The stress-concentrating effect of resorption cavities on real isolated trabeculae was first investigated by McNamara *et al*[87]. Cavities were identified on μCT-scans and the authors found from finite element analysis that micro-damage was inevitable around these lacunae, which might lead to more resorption than 'initially' intended to restore damaged bone[87].

Different cavity-based erosion and formation algorithms have been applied to complete trabecular samples as well, and FE analyses were performed to investigate the mechanical impact[88-93]. These algorithms have been applied iteratively to simulate the effect of a sequence of remodelling cycles, with both formation and resorption, sometimes spanning several decades in the virtual life of the sample. The algorithms used had different grounds. One approach was to remove voxels on the entire bone surface based on a gaussian filter constrained to a certain cavity volume[90,94], which not necessarily erodes individual cavities. Using this method they showed that a negative bone balance and increased activation frequency can cause extreme bone loss[90]. Others considered the local mechanical environment of voxels and removed them based on the nonuniformity of local stress on the surface or a strain signal[91,93]. Both models caused an evolution towards a typical anisotropic bone structure after several cycles, with a higher stiffness in the loading direction.

The approach of Van der Linden *et al*[92] was the first to specifically take the cavity shape into account. They developed a computer simulation of bone remodelling on a 3D-μCT-based structure where voxels of bone matrix were removed as hemispherical cavities located at random locations on the bone surface. In a sequence of bone remodelling cycles, a formation deficit was modelled hence the cavities were not refilled completely. The model was used to simulate several bone loss scenarios[95] as well as the effect of treatment with anti-resorptive agents by gradually changing cavity properties[96]. They clearly showed the complex relationship between bone loss and stiffness loss and that bone loss alone cannot explain the mechanical changes. While Van der Linden *et al* based their amount of remodelling on the remodelling volume, Liu *et al*[89] added hemispherical cavities at random locations according to the activation frequency. They observed a shift to less plate-like trabeculae and more, but thinner, rod-like trabeculae after the simulated menopause.

Hernandez *et al*[88] used a similar 3D model to test the effect of resorption cavities on the trabecular bone strength. They digitally added cavities at regions of high strain or at random locations. For the first time, the cavities were modelled with an ellipsoidal shape. Adding resorption cavities caused a significant reduction in stiffness and yield strength, with even higher reduction for cavities at regions of high strain. The total removed bone volume was however the same, showing that cavities may influence bone mechanics independent of their effect on bone volume. The same research group continued to model the biomechanical effect of (uniform size) resorption cavities on voxel-based models and have shown a larger impact of cavities located in highly strained areas on the trabecular bone structure[97].

Using a new approach that overcomes some of the modelling limitations described above and below, we recently simulated the effect of resorption cavities on the stiffness of a wide variety of trabecular bone structures using a parametric beam-shell finite element model[98]. The reduction in bone stiffness due to cavities was signif-

icantly larger than for homogeneous erosion of the same bone volume and depended on the nature of the bone structure (rod-like *vs* plate-like trabeculae). A more specific study using the same modelling technique showed that glucocorticoid changes in the geometry of osteoclast resorption cavities affect trabecular bone stiffness[99].

Slyfield *et al*[100] were recently able to take the ultimate step in the 3D analysis of the mechanical effect of resorption cavities. They were able to demonstrate the role of resorption cavity size and location on mechanical failure (damage) of bone using 3D imaging of the failure process.

Modelling limitations

As described above, the different modelling approaches have revealed interesting effects of resorption on bone mechanical properties. There are however several disadvantages in the methods and potential flaws in the presented studies.

First, simplified (lattice) models are unable to capture the complex and heterogeneous nature of trabecular bone and are therefore less suited to model the combined mechanical effect of all the interacting structural properties.

Second, detailed μCT-based models of trabecular bone have been used, but so far applied only to a limited number of trabecular bone samples. Given the enormous heterogeneity of trabecular bone structures, related to the anatomical site, the influence of the initial structure should be taken into account. It is as yet unclear whether resorption cavities have a similar impact on plate-like samples then on rod-like bone samples.

Third, state-of-the-art μCT-based models add en remove bone by adding or removing voxels. Cavity shapes and sizes are thus limited to the voxel resolution. As our review of resorption cavity properties shows, a large variation in sizes exists and changes often occur on a sub-voxel-resolution level. High resolution imaginghas shown that resorption cavities have very irregular shapes of which the mechanical impact can possibly not be modelled correctly on a voxel-basis[37]. Potential solutions to this problem lie in the use of tetrahedral-based FE models, where surface nodes can be moved inwards to model cavities or by using parameter-based models of trabecular bone, like beam-shell finite element models[101].

Fourth, state-of-the-art μCT-based models assume, partly due to their voxel-based nature, cavities of a fixed size. However, cavity shapes and sizes are far from constant. *In vivo*, they exist in a skewed distribution of surface area and cavity depth. Moreover, at a certain snapshot in time, not all cavities are in the same remodelling stage: some may have just started while others are already being refilled. Furthermore all simulation studies have shown that the highest mechanical impact occurs when trabeculae are perforated or ruptures, especially when occurring in highly strained locations. The presence of just a few deep perforating cavities can thus change the mechanics decisively, while an averaged cavity depth might not cause perforation. It is thus advisable to use a realistic spread of resorption cavity properties when modelling their mechanical impact.

Fifth, the choice of modelling parameters remains problematic. As we explained above, different measuring methods exist and all have specific disadvantages, requiring careful interpretation of the values before using them as a model basis. Resorption cavity depths used in simulation studies seem to be large compared to literature values, again due to the voxel-based nature of the models. Using dynamic parameters like the total remodelling space or Ac.f as a basis for a static study, might lead to an overestimation of the impact of resorption cavities[88,89]. There is no single timepoint where the entire remodelling space has been removed by osteoclasts. Given the fact that ES/BS is commonly measured and there is less discussion concerning the measurement technique, it is likely the best parameter to quantify the extend of erosion.

CONCLUSION

Osteocyte resorption cavities affect bone competence. Hence, a proper quantification of the cavity dimensions will be beneficial in estimating the effect of metabolic bone diseases on bone mechanical quality. Until recently, the dimensions of osteoclast resorption cavities have been estimated from 2D measures. Their role in affecting bone quality has been analyzed using computational models that, on one hand, provide rather detailed information on trabecular bone structure, but on the other incorporate rather crude assumptions on cavity dimensions. Considering the 3D nature of the cavities this approach has clear limitations, requiring a careful interpretation. The introduction of 3D imaging techniques like μCT and SR-CT has opened the door to quantifying these dimensions in an unbiased manner in 3D space. These data can be included in high-resolution computational models and in parametric descriptions of bone, thereby improving our understanding of their effect on bone competence. Further exploration of this area of research will disclose relevant information on the mechanical consequences of metabolic bone diseases and can aide in the development of (bio)mechanically relevant pharmacological and physical treatments.

REFERENCES

1 **Heaney RP**, Yates AJ, Santora AC. Bisphosphonate effects and the bone remodeling transient. *J Bone Miner Res* 1997; **12**: 1143-1151 [PMID: 9258743 DOI: 10.1359/jbmr.1997.12.8.1143]

2 **Seeman E**, Delmas PD. Bone quality--the material and structural basis of bone strength and fragility. *N Engl J Med* 2006; **354**: 2250-2261 [PMID: 16723616 DOI: 10.1056/NEJMra053077]

3 **Frost HM**. Tetracycline-based histological analysis of bone remodeling. *Calcif Tissue Res* 1969; **3**: 211-237 [PMID: 4894738 DOI: 10.1007/BF02058664]

4 **Rauch F**. Watching bone cells at work: what we can see

from bone biopsies. *Pediatr Nephrol* 2006; **21**: 457-462 [PMID: 16520951 DOI: 10.1007/s00467-006-0025-6]
5 **Recker RR**. Bone biopsy and histomorphometry in clinical practice. *Rheum Dis Clin North Am* 1994; **20**: 609-627 [PMID: 7984781 DOI: 10.1359/prim.2008.0735]
6 **Seeman E**. Structural basis of growth-related gain and age-related loss of bone strength. *Rheumatology* (Oxford) 2008; **47** Suppl 4: iv2-iv8 [PMID: 18556646]
7 **Frost HM**. The skeletal intermediary organization. *Metab Bone Dis Relat Res* 1983; **4**: 281-290 [PMID: 6353132]
8 **Eriksen EF**. Normal and pathological remodeling of human trabecular bone: three dimensional reconstruction of the remodeling sequence in normals and in metabolic bone disease. *Endocr Rev* 1986; **7**: 379-408 [PMID: 3536460 DOI: 10.1210/edrv-7-4-379]
9 **Parfitt AM**. Targeted and nontargeted bone remodeling: relationship to basic multicellular unit origination and progression. *Bone* 2002; **30**: 5-7 [PMID: 11792557 DOI: 10.1016/S8756-3282(01)00642-1]
10 **Baron R**. Importance of the intermediate phases between resorption and formation in the measurement and understanding of the bone remodeling sequence. *Bone Histomorphometry* 1977: 1977
11 **Eriksen EF**, Melsen F, Mosekilde L. Reconstruction of the resorptive site in iliac trabecular bone: a kinetic model for bone resorption in 20 normal individuals. *Metab Bone Dis Relat Res* 1984; **5**: 235-242 [PMID: 6493035 DOI: 10.1016/0221-8747(84)90066-3]
12 **Chavassieux P**, Seeman E, Delmas PD. Insights into material and structural basis of bone fragility from diseases associated with fractures: how determinants of the biomechanical properties of bone are compromised by disease. *Endocr Rev* 2007; **28**: 151-164 [PMID: 17200084 DOI: 10.1210/er.2006-0029]
13 **Compston JE**, Croucher PI. Histomorphometric assessment of trabecular bone remodelling in osteoporosis. *Bone Miner* 1991; **14**: 91-102 [PMID: 1912765 DOI: 10.1016/0169-6009(91)90086-F]
14 **Croucher PI**, Gilks WR, Compston JE. Evidence for interrupted bone resorption in human iliac cancellous bone. *J Bone Miner Res* 1995; **10**: 1537-1543 [PMID: 8686510 DOI: 10.1002/jbmr.5650101015]
15 **Eriksen EF**, Mosekilde L, Melsen F. Trabecular bone remodeling and balance in primary hyperparathyroidism. *Bone* 1986; **7**: 213-221 [PMID: 3768200 DOI: 10.1016/8756-3282(86)90020-7]
16 **Parfitt AM**, Drezner MK, Glorieux FH, Kanis JA, Malluche H, Meunier PJ, Ott SM, Recker RR. Bone histomorphometry: standardization of nomenclature, symbols, and units. Report of the ASBMR Histomorphometry Nomenclature Committee. *J Bone Miner Res* 1987; **2**: 595-610 [PMID: 3455637 DOI: 10.1002/jbmr.5650020617]
17 **Recker RR**, Lappe JM, Davies KM, Heaney RP. Bone remodeling: Biochemical markers or bone biopsy? *J BONE MINER RES* 2006; **21**: 180-180
18 **Vedi S**, Compston J. Bone histomorphometry. *Methods Mol Med* 2003; **80**: 283-298 [PMID: 12728725]
19 **Gundersen HJ**. Stereology--or how figures for spatial shape and content are obtained by observation of structures in sections. *Microsc Acta* 1980; **83**: 409-426 [PMID: 7442556]
20 **Kragstrup J**, Gundersen HJG, Melsen F, Mosekilde L. Estimation of the 3-Dimensional Wall Thickness of Completed Remodeling Sites in Iliac Trabecular Bone. *Metab Bone Dis Relat Res* 1982; **4:** 113-119
21 **Arlot ME**, Delmas PD, Chappard D, Meunier PJ. Trabecular and endocortical bone remodeling in postmenopausal osteoporosis: comparison with normal postmenopausal women. *Osteoporos Int* 1990; **1**: 41-49 [PMID: 2133640]
22 **Eriksen EF**, Mosekilde L, Melsen F. Trabecular bone resorption depth decreases with age: differences between normal males and females. *Bone* 1985; **6**: 141-146 [PMID: 4027092 DOI: 10.1016/8756-3282(85)90362-X]
23 **Glorieux FH**, Travers R, Taylor A, Bowen JR, Rauch F, Norman M, Parfitt AM. Normative data for iliac bone histomorphometry in growing children. *Bone* 2000; **26**: 103-109 [PMID: 10678403 DOI: 10.1016/S8756-3282(99)00257-4]
24 **Palle S**, Chappard D, Vico L, Riffat G, Alexandre C. Evaluation of the osteoclastic population in iliac crest biopsies from 36 normal subjects: a histoenzymologic and histomorphometric study. *J Bone Miner Res* 1989; **4**: 501-506 [PMID: 2816499 DOI: 10.1002/jbmr.5650040408]
25 **Parfitt AM**. Morphometry of bone resorption: introduction and overview. *Bone* 1993; **14**: 435-441 [PMID: 8363889 DOI: 10.1016/8756-3282(93)90176-B]
26 **Vedi S**, Tighe JR, Compston JE. Measurement of total resorption surface in iliac crest trabecular bone in man. *Metab Bone Dis Relat Res* 1984; **5**: 275-280 [PMID: 6493040 DOI: 10.1016/0221-8747(84)90014-6]
27 **Croucher PI**, Garrahan NJ, Mellish RW, Compston JE. Age-related changes in resorption cavity characteristics in human trabecular bone. *Osteoporos Int* 1991; **1**: 257-261 [PMID: 1790413]
28 **Allen MR**, Erickson AM, Wang X, Burr DB, Martin RB, Hazelwood SJ. Morphological assessment of basic multicellular unit resorption parameters in dogs shows additional mechanisms of bisphosphonate effects on bone. *Calcif Tissue Int* 2010; **86**: 67-71 [PMID: 19953232 DOI: 10.1007/s00223-009-9315-x]
29 **Croucher PI**, Mellish RW, Vedi S, Garrahan NJ, Compston JE. The relationship between resorption depth and mean interstitial bone thickness: age-related changes in man. *Calcif Tissue Int* 1989; **45**: 15-19 [PMID: 2504458 DOI: 10.1007/BF02556655]
30 **Roux JP**, Arlot ME, Gineyts E, Meunier PJ, Delmas PD. Automatic-interactive measurement of resorption cavities in transiliac bone biopsies and correlation with deoxypyridinoline. *Bone* 1995; **17**: 153-156 [PMID: 8554923 DOI: 10.1016/S8756-3282(95)00174-3]
31 **Garrahan NJ**, Croucher PI, Compston JE. A computerised technique for the quantitative assessment of resorption cavities in trabecular bone. *Bone* 1990; **11**: 241-245 [PMID: 2242290 DOI: 10.1016/8756-3282(90)90076-B]
32 **Cohen-Solal ME**, Shih MS, Lundy MW, Parfitt AM. A new method for measuring cancellous bone erosion depth: application to the cellular mechanisms of bone loss in postmenopausal osteoporosis. *J Bone Miner Res* 1991; **6**: 1331-1338 [PMID: 1792944 DOI: 10.1002/jbmr.5650061210]
33 **Recker RR**, Kimmel DB, Dempster D, Weinstein RS, Wronski TJ, Burr DB. Issues in modern bone histomorphometry. *Bone* 2011; **49**: 955-964 [PMID: 21810491 DOI: 10.1016/j.bone.2011.07.017]
34 **Yamaguchi K**, Croucher PI, Compston JE. Comparison between the lengths of individual osteoid seams and resorption cavities in human iliac crest cancellous bone. *Bone Miner* 1993; **23**: 27-33 [PMID: 8274877 DOI: 10.1016/S0169-6009(08)80088-8]
35 **Croucher PI**, Wright CD, Garrahan NJ, Kudlac H, Williams AJ, Compston JE. Characteristics of trabecular bone resorption cavities in patients with chronic renal failure. *Bone Miner* 1992; **16**: 139-137 [PMID: 1576489 DOI: 10.1016/0169-6009(92)90884-G]
36 **Hernandez CJ**. How can bone turnover modify bone strength independent of bone mass? *Bone* 2008; **42**: 1014-1020 [PMID: 18373970 DOI: 10.1016/j.bone.2008.02.001]
37 **Mosekilde L**. Consequences of the remodelling process for vertebral trabecular bone structure: a scanning electron microscopy study (uncoupling of unloaded structures). *Bone Miner* 1990; **10**: 13-35 [PMID: 2397325 DOI: 10.1016/0169-6009(90)90046-I]
38 **Tkachenko EV**, Slyfield CR, Tomlinson RE, Daggett JR,

Wilson DL, Hernandez CJ. Voxel size and measures of individual resorption cavities in three-dimensional images of cancellous bone. *Bone* 2009; **45**: 487-492 [PMID: 19482097 DOI: 10.1016/j.bone.2009.05.019]
39 **Goff MG**, Slyfield CR, Kummari SR, Tkachenko EV, Fischer SE, Yi YH, Jekir MG, Keaveny TM, Hernandez CJ. Three-dimensional characterization of resorption cavity size and location in human vertebral trabecular bone. *Bone* 2012; **51**: 28-37 [PMID: 22507299 DOI: 10.1016/j.bone.2012.03.028]
40 **Soysa NS**, Alles N, Aoki K, Ohya K. Three-dimensional characterization of osteoclast bone-resorbing activity in the resorption lacunae. *J Med Dent Sci* 2009; **56**: 107-112 [PMID: 20099473]
41 **Pascaretti-Grizon F**, Mabilleau G, Basle MF, Chappard D. Measurement by vertical scanning profilometry of resorption volume and lacunae depth caused by osteoclasts on dentine slices. *J Microsc* 2011; **241**: 147-152 [PMID: 21118208]
42 **Schulte FA**, Lambers FM, Kuhn G, Müller R. In vivo micro-computed tomography allows direct three-dimensional quantification of both bone formation and bone resorption parameters using time-lapsed imaging. *Bone* 2011; **48**: 433-442 [PMID: 20950723 DOI: 10.1016/j.bone.2010.10.007]
43 **Vedi S**, Compston JE, Webb A, Tighe JR. Histomorphometric analysis of bone biopsies from the iliac crest of normal British subjects. *Metab Bone Dis Relat Res* 1982; **4**: 231-236 [PMID: 7182722 DOI: 10.1016/0221-8747(82)90032-7]
44 **Schnitzler CM**, Biddulph SL, Mesquita JM, Gear KA. Bone structure and turnover in the distal radius and iliac crest: a histomorphometric study. *J Bone Miner Res* 1996; **11**: 1761-1768 [PMID: 8915784 DOI: 10.1002/jbmr.5650111120]
45 **Compston JE**, Mellish RW, Croucher P, Newcombe R, Garrahan NJ. Structural mechanisms of trabecular bone loss in man. *Bone Miner* 1989; **6**: 339-350 [PMID: 2758162 DOI: 10.1016/0169-6009(89)90039-1]
46 **Wakamatsu E**, Sissons HA. The cancellous bone of the iliac crest. *Calcif Tissue Res* 1969; **4**: 147-161 [PMID: 5363270 DOI: 10.1007/BF02279116]
47 **Kelepouris N**, Harper KD, Gannon F, Kaplan FS, Haddad JG. Severe osteoporosis in men. *Ann Intern Med* 1995; **123**: 452-460 [PMID: 7639446 DOI: 10.7326/0003-4819-123-6-199509150-00010]
48 **Lips P**, Courpron P, Meunier PJ. Mean wall thickness of trabecular bone packets in the human iliac crest: changes with age. *Calcif Tissue Res* 1978; **26**: 13-17 [PMID: 737547 DOI: 10.1007/BF02013227]
49 **Clarke BL**, Ebeling PR, Jones JD, Wahner HW, O'Fallon WM, Riggs BL, Fitzpatrick LA. Changes in quantitative bone histomorphometry in aging healthy men. *J Clin Endocrinol Metab* 1996; **81**: 2264-2270 [PMID: 8964862 DOI: 10.1210/jc.81.6.2264]
50 **Charhon SA**, Edouard CM, Arlot ME, Meunier PJ. Effects of parathyroid hormone on remodeling of iliac trabecular bone packets in patients with primary hyperparathyroidism. *Clin Orthop Relat Res* 1985: 255-263 [PMID: 7067220]
51 **Parfitt AM**, Han ZH, Palnitkar S, Rao DS, Shih MS, Nelson D. Effects of ethnicity and age or menopause on osteoblast function, bone mineralization, and osteoid accumulation in iliac bone. *J Bone Miner Res* 1997; **12**: 1864-1873 [PMID: 9383691 DOI: 10.1359/jbmr.1997.12.11.1864]
52 **Arlot ME**, Jiang Y, Genant HK, Zhao J, Burt-Pichat B, Roux JP, Delmas PD, Meunier PJ. Histomorphometric and microCT analysis of bone biopsies from postmenopausal osteoporotic women treated with strontium ranelate. *J Bone Miner Res* 2008; **23**: 215-222 [PMID: 17922612 DOI: 10.1359/jbmr.071012]
53 **Recker R**, Lappe J, Davies KM, Heaney R. Bone remodeling increases substantially in the years after menopause and remains increased in older osteoporosis patients. *J Bone Miner Res* 2004; **19**: 1628-1633 [PMID: 15355557 DOI: 10.1359/JBMR.040710]
54 **Chavassieux P**, Meunier PJ. Histomorphometric approach of bone loss in men. *Calcif Tissue Int* 2001; **69**: 209-213 [PMID: 11730252]
55 **Delichatsios HK**, Lane JM, Rivlin RS. Bone histomorphometry in men with spinal osteoporosis. *Calcif Tissue Int* 1995; **56**: 359-363 [PMID: 7621341]
56 **Eriksen EF**, Hodgson SF, Eastell R, Cedel SL, O'Fallon WM, Riggs BL. Cancellous bone remodeling in type I (postmenopausal) osteoporosis: quantitative assessment of rates of formation, resorption, and bone loss at tissue and cellular levels. *J Bone Miner Res* 1990; **5**: 311-319 [PMID: 2343771 DOI: 10.1002/jbmr.5650050402]
57 **Kimmel DB**, Recker RR, Gallagher JC, Vaswani AS, Aloia JF. A comparison of iliac bone histomorphometric data in post-menopausal osteoporotic and normal subjects. *Bone Miner* 1990; **11**: 217-235 [PMID: 2268749 DOI: 10.1016/0169-6009(90)90061-J]
58 **Pernow Y**, Hauge EM, Linder K, Dahl E, Sääf M. Bone histomorphometry in male idiopathic osteoporosis. *Calcif Tissue Int* 2009; **84**: 430-438 [PMID: 19308628 DOI: 10.1007/s00223-009-9239-5]
59 **Søe K**, Delaissé JM. Glucocorticoids maintain human osteoclasts in the active mode of their resorption cycle. *J Bone Miner Res* 2010; **25**: 2184-2192 [PMID: 20499345 DOI: 10.1002/jbmr.113]
60 **Chavassieux PM**, Arlot ME, Roux JP, Portero N, Daifotis A, Yates AJ, Hamdy NA, Malice MP, Freedholm D, Meunier PJ. Effects of alendronate on bone quality and remodeling in glucocorticoid-induced osteoporosis: a histomorphometric analysis of transiliac biopsies. *J Bone Miner Res* 2000; **15**: 754-762 [PMID: 10780867 DOI: 10.1359/jbmr.2000.15.4.754]
61 **Dalle Carbonare L**, Arlot ME, Chavassieux PM, Roux JP, Portero NR, Meunier PJ. Comparison of trabecular bone microarchitecture and remodeling in glucocorticoid-induced and postmenopausal osteoporosis. *J Bone Miner Res* 2001; **16**: 97-103 [PMID: 11149495 DOI: 10.1359/jbmr.2001.16.1.97]
62 **Dalle Carbonare L**, Bertoldo F, Valenti MT, Zenari S, Zanatta M, Sella S, Giannini S, Cascio VL. Histomorphometric analysis of glucocorticoid-induced osteoporosis. *Micron* 2005; **36**: 645-652 [PMID: 16243531 DOI: 10.1016/j.micron.2005.07.009]
63 **Weinstein RS**, Chen JR, Powers CC, Stewart SA, Landes RD, Bellido T, Jilka RL, Parfitt AM, Manolagas SC. Promotion of osteoclast survival and antagonism of bisphosphonate-induced osteoclast apoptosis by glucocorticoids. *J Clin Invest* 2002; **109**: 1041-1048 [PMID: 11956241 DOI: 10.1172/JCI14538]
64 **Chavassieux PM**, Arlot ME, Reda C, Wei L, Yates AJ, Meunier PJ. Histomorphometric assessment of the long-term effects of alendronate on bone quality and remodeling in patients with osteoporosis. *J Clin Invest* 1997; **100**: 1475-1480 [PMID: 9294113 DOI: 10.1172/JCI119668]
65 **Qiu S**, Phipps RJ, Ebetino FH, Palnitkar S, Sudhaker Rao D. Effect of risedronate on osteocyte viability and bone turnover in paired iliac bone biopsies from early postmenopausal women. *Calcif Tissue Int* 2010; **87**: 392-397 [PMID: 20809096 DOI: 10.1007/s00223-010-9411-y]
66 **Recker RR**, Ste-Marie LG, Langdahl B, Czerwinski E, Bonvoisin B, Masanauskaite D, Rowell L, Felsenberg D. Effects of intermittent intravenous ibandronate injections on bone quality and micro-architecture in women with postmenopausal osteoporosis: the DIVA study. *Bone* 2010; **46**: 660-665 [PMID: 19909829 DOI: 10.1016/j.bone.2009.11.004]
67 **Eriksen EF**, Melsen F, Sod E, Barton I, Chines A. Effects of long-term risedronate on bone quality and bone turnover in women with postmenopausal osteoporosis. *Bone* 2002; **31**: 620-625 [PMID: 12477578 DOI: 10.1016/S8756-3282(02)00869-4]
68 **Allen MR**, Burr DB. Bisphosphonate effects on bone turnover, microdamage, and mechanical properties: what we

think we know and what we know that we don't know. *Bone* 2011; **49**: 56-65 [PMID: 20955825 DOI: 10.1016/j.bone.2010.10.159]
69 **Ott SM**. Bisphosphonates and BMU birth rate. *Osteoporos Int* 2010; **21**: 887; author reply 889-890 [PMID: 19649676]
70 **Weinstein RS**, Roberson PK, Manolagas SC. Giant osteoclast formation and long-term oral bisphosphonate therapy. *N Engl J Med* 2009; **360**: 53-62 [PMID: 19118304 DOI: 10.1056/NEJMoa0802633]
71 **Hodsman AB**, Kisiel M, Adachi JD, Fraher LJ, Watson PH. Histomorphometric evidence for increased bone turnover without change in cortical thickness or porosity after 2 years of cyclical hPTH(1-34) therapy in women with severe osteoporosis. *Bone* 2000; **27**: 311-318 [PMID: 10913928 DOI: 10.1016/S8756-3282(00)00316-1]
72 **Stepan JJ**, Burr DB, Li J, Ma YL, Petto H, Sipos A, Dobnig H, Fahrleitner-Pammer A, Michalská D, Pavo I. Histomorphometric changes by teriparatide in alendronate-pretreated women with osteoporosis. *Osteoporos Int* 2010; **21**: 2027-2036 [PMID: 20135094]
73 **Recker RR**, Bare SP, Smith SY, Varela A, Miller MA, Morris SA, Fox J. Cancellous and cortical bone architecture and turnover at the iliac crest of postmenopausal osteoporotic women treated with parathyroid hormone 1-84. *Bone* 2009; **44**: 113-119 [PMID: 18983947 DOI: 10.1016/j.bone.2008.09.019]
74 **Recker RR**, Marin F, Ish-Shalom S, Möricke R, Hawkins F, Kapetanos G, de la Peña MP, Kekow J, Farrerons J, Sanz B, Oertel H, Stepan J. Comparative effects of teriparatide and strontium ranelate on bone biopsies and biochemical markers of bone turnover in postmenopausal women with osteoporosis. *J Bone Miner Res* 2009; **24**: 1358-1368 [PMID: 19338452 DOI: 10.1359/jbmr.090904]
75 **Matheny JB**, Slyfield CR, Tkachenko EV, Lin I, Ehlert KM, Tomlinson RE, Wilson DL, Hernandez CJ. Anti-resorptive agents reduce the size of resorption cavities: a three-dimensional dynamic bone histomorphometry study. *Bone* 2013; **57**: 277-283 [PMID: 23988275 DOI: 10.1016/j.bone.2013.08.018]
76 **Heaney RP**. Is the paradigm shifting? *Bone* 2003; **33**: 457-465 [PMID: 14555248 DOI: 10.1016/S8756-3282(03)00236-9]
77 **Garnero P**, Hausherr E, Chapuy MC, Marcelli C, Grandjean H, Muller C, Cormier C, Bréart G, Meunier PJ, Delmas PD. Markers of bone resorption predict hip fracture in elderly women: the EPIDOS Prospective Study. *J Bone Miner Res* 1996; **11**: 1531-1538 [PMID: 8889854 DOI: 10.1002/jbmr.5650111021]
78 **Parfitt AM**. What is the normal rate of bone remodeling? *Bone* 2004; **35**: 1-3 [PMID: 15207734 DOI: 10.1016/j.bone.2004.03.022]
79 **Gibson LJ**. Biomechanics of cellular solids. *J Biomech* 2005; **38**: 377-399 [PMID: 15652536 DOI: 10.1016/j.jbiomech.2004.09.027]
80 **Liu XS**, Sajda P, Saha PK, Wehrli FW, Bevill G, Keaveny TM, Guo XE. Complete volumetric decomposition of individual trabecular plates and rods and its morphological correlations with anisotropic elastic moduli in human trabecular bone. *J Bone Miner Res* 2008; **23**: 223-235 [PMID: 17907921 DOI: 10.1359/jbmr.071009]
81 **Hernandez CJ**, Beaupré GS, Carter DR. A theoretical analysis of the relative influences of peak BMD, age-related bone loss and menopause on the development of osteoporosis. *Osteoporos Int* 2003; **14**: 843-847 [PMID: 12904837]
82 **Hernandez CJ**, Beaupré GS, Carter DR. A theoretical analysis of the changes in basic multicellular unit activity at menopause. *Bone* 2003; **32**: 357-363 [PMID: 12689678 DOI: 10.1016/S8756-3282(03)00037-1]
83 **McNamara LM**, Prendergast PJ. Perforation of cancellous bone trabeculae by damage-stimulated remodelling at resorption pits: a computational analysis. *Eur J Morphol* 2005; **42**: 99-109 [PMID: 16123029 DOI: 10.1080/ejom.42.1-2.0099]
84 **Mulvihill BM**, McNamara LM, Prendergast PJ. Loss of trabeculae by mechano-biological means may explain rapid bone loss in osteoporosis. *J R Soc Interface* 2008; **5**: 1243-1253 [PMID: 18348960 DOI: 10.1098/rsif.2007.1341]
85 **Langton CM**, Haire TJ, Ganney PS, Dobson CA, Fagan MJ. Dynamic stochastic simulation of cancellous bone resorption. *Bone* 1998; **22**: 375-380 [PMID: 9556138 DOI: 10.1016/S8756-3282(97)00290-1]
86 **Tayyar S**, Weinhold PS, Butler RA, Woodard JC, Zardiackas LD, St John KR, Bledsoe JM, Gilbert JA. Computer simulation of trabecular remodeling using a simplified structural model. *Bone* 1999; **25**: 733-739 [PMID: 10593419 DOI: 10.1016/S8756-3282(99)00218-5]
87 **McNamara LM**, Van der Linden JC, Weinans H, Prendergast PJ. Stress-concentrating effect of resorption lacunae in trabecular bone. *J Biomech* 2006; **39**: 734-741 [PMID: 16439243 DOI: 10.1016/j.jbiomech.2004.12.027]
88 **Hernandez CJ**, Gupta A, Keaveny TM. A biomechanical analysis of the effects of resorption cavities on cancellous bone strength. *J Bone Miner Res* 2006; **21**: 1248-1255 [PMID: 16869723 DOI: 10.1359/jbmr.060514]
89 **Liu XS**, Huang AH, Zhang XH, Sajda P, Ji B, Guo XE. Dynamic simulation of three dimensional architectural and mechanical alterations in human trabecular bone during menopause. *Bone* 2008; **43**: 292-301 [PMID: 18550463 DOI: 10.1016/j.bone.2008.04.008]
90 **Müller R**. Long-term prediction of three-dimensional bone architecture in simulations of pre-, peri- and postmenopausal microstructural bone remodeling. *Osteoporos Int* 2005; **16** Suppl 2: S25-S35 [PMID: 15340800]
91 **Tsubota K**, Suzuki Y, Yamada T, Hojo M, Makinouchi A, Adachi T. Computer simulation of trabecular remodeling in human proximal femur using large-scale voxel FE models: Approach to understanding Wolff's law. *J Biomech* 2009; **42**: 1088-1094 [PMID: 19403138 DOI: 10.1016/j.jbiomech.2009.02.030]
92 **Van Der Linden JC**, Verhaar JA, Weinans H. A three-dimensional simulation of age-related remodeling in trabecular bone. *J Bone Miner Res* 2001; **16**: 688-696 [PMID: 11315996 DOI: 10.1359/jbmr.2001.16.4.688]
93 **van der Linden JC**, Day JS, Verhaar JA, Weinans H. Altered tissue properties induce changes in cancellous bone architecture in aging and diseases. *J Biomech* 2004; **37**: 367-374 [PMID: 14757456 DOI: 10.1016/S0021-9290(03)00266-5]
94 **Müller R**, Rüegsegger P. Analysis of mechanical properties of cancellous bone under conditions of simulated bone atrophy. *J Biomech* 1996; **29**: 1053-1060 [PMID: 8817372 DOI: 10.1016/0021-9290(96)00006-1]
95 **van der Linden JC**, Homminga J, Verhaar JA, Weinans H. Mechanical consequences of bone loss in cancellous bone. *J Bone Miner Res* 2001; **16**: 457-465 [PMID: 11277263 DOI: 10.1359/jbmr.2001.16.3.457]
96 **van der Linden JC**, Verhaar JA, Pols HA, Weinans H. A simulation model at trabecular level to predict effects of antiresorptive treatment after menopause. *Calcif Tissue Int* 2003; **73**: 537-544 [PMID: 14508627 DOI: 10.1007/s00223-002-2151-x]
97 **Easley SK**, Chang MT, Shindich D, Hernandez CJ, Keaveny TM. Biomechanical effects of simulated resorption cavities in cancellous bone across a wide range of bone volume fractions. *J Bone Miner Res* 2012; **27**: 1927-1935 [PMID: 22576976 DOI: 10.1002/jbmr.1657]
98 **Vanderoost J**, van Lenthe GH. The effect of resorption cavities on bone stiffness is site dependent. *Comput Methods Biomech Biomed Engin* 2014; **17**: 1483-1491 [PMID: 23282095]
99 **Vanderoost J**, Søe K, Merrild DM, Delaissé JM, van Lenthe GH. Glucocorticoid-induced changes in the geometry of osteoclast resorption cavities affect trabecular bone stiffness. *Calcif Tissue Int* 2013; **92**: 240-250 [PMID: 23187898 DOI: 10.1007/s00223-012-9674-6]
100 **Slyfield CR**, Tkachenko EV, Fischer SE, Ehlert KM, Yi IH, Jekir

MG, O'Brien RG, Keaveny TM, Hernandez CJ. Mechanical failure begins preferentially near resorption cavities in human vertebral cancellous bone under compression. *Bone* 2012; **50**: 1281-1287 [PMID: 22426306 DOI: 10.1016/j.bone.2012.02.636]

101 **Vanderoost J**, Jaecques SV, Van der Perre G, Boonen S, D'hooge J, Lauriks W, van Lenthe GH. Fast and accurate specimen-specific simulation of trabecular bone elastic modulus using novel beam-shell finite element models. *J Biomech* 2011; **44**: 1566-1572 [PMID: 21414627 DOI: 10.1016/j.jbiomech.2011.02.082]

102 **Rauch F**, Travers R, Parfitt AM, Glorieux FH. Static and dynamic bone histomorphometry in children with osteogenesis imperfecta. *Bone* 2000; **26**: 581-589 [PMID: 10831929 DOI: 10.1016/S8756-3282(00)00269-6]

103 **Croucher PI**, Garrahan NJ, Compston JE. Assessment of resorption cavity characteristics in trabecular bone: changes in primary and secondary osteoporosis. *Bone* 1993; **14**: 449-454 [PMID: 8363891 DOI: 10.1016/8756-3282(93)90178-D]

P- Reviewer: Kamishima T, Naraghi M, Quattrocchi CC
S- Editor: Ji FF **L- Editor**: A **E- Editor**: Lu YJ

World Journal of Radiology

Submit a Manuscript: http://www.wjgnet.com/esps/
Help Desk: http://www.wjgnet.com/esps/helpdesk.aspx
DOI: 10.4329/wjr.v6.i9.657

World J Radiol 2014 September 28; 6(9): 657-668
ISSN 1949-8470 (online)

REVIEW

Imaging of gaucher disease

William L Simpson, George Hermann, Manisha Balwani

William L Simpson, George Hermann, Department of Radiology, Icahn School of Medicine at Mount Sinai, New York, NY 10029, United States
Manisha Balwani, Department of Genetics and Genomic Sciences, Icahn School of Medicine at Mount Sinai, New York, NY 10029, United States
Author contributions: Simpson WL, Hermann G and Balwani M contributed equally to this work; Simpson WL drafted the manuscript; Hermann G and Balwani M critically revised the manuscript; Simpson WL, Hermann G and Balwani M approved the final version.
Correspondence to: William L Simpson, Jr., MD, Associate professor of Radiology, Department of Radiology, Icahn School of Medicine at Mount Sinai, Box 1234, 1 Gustave L Levy Place, New York, NY 10029,
United States. william.simpson@mountsinai.org
Telephone: +1-212-2413832 Fax: +1-212-4278137
Received: December 28, 2013 Revised: April 9, 2014
Accepted: July 15, 2014
Published online: September 28, 2014

Abstract

Gaucher disease is the prototypical lysosomal storage disease. It results from the accumulation of undegraded glucosylceramide in the reticuloendothelial system of the bone marrow, spleen and liver due to deficiency of the enzyme glucocerebrosidase. This leads to hematologic, visceral and skeletal maifestions. Build up of glucosylceramide in the liver and spleen results in hepatosplenomegaly. The normal bone marrow is replaced by the accumulating substrate leading to many of the hematologic signs including anemia. The visceral and skeletal manifestations can be visualized with various imaging modalities including radiography, computed tomography, magnetic resonance imaging (MRI) and radionuclide scanning. Prior to the development of enzyme replacement therapy, treatment was only supportive. However, once intravenous enzyme replacement therapy became available in the 1990s it quickly became the standard of care. Enzyme replacement therapy leads to improvement in all manifestations. The visceral and hematologic manifestations respond more quickly usually within a few months or years. The skeletal manifestations take much longer, usually several years, to show improvement. In recent years newer treatment strategies, such as substrate reduction therapy, have been under investigation. Imaging plays a key role in both initial diagnosis and routine monitoring of patient on treatment particularly volumetric MRI of the liver and spleen and MRI of the femora for evaluating bone marrow disease burden.

Key words: Gaucher disease; Lysosomal storage disease; Enzyme replacement therapy; Genetics; Medical imaging; Magnetic resonance imaging; Bone marrow

Core tip: Gaucher disease is the most common lysosomal storage disease resulting from accumulation of undegraded glucosylceramide in the reticuloendothelial system of the bone marrow, spleen and liver. Although affecting all three organs, the bone manifestations lead to the most debilitation. Visceral and bone marrow infiltration respond to enzyme replacement therapy however, the bone marrow response typically takes much longer.

Simpson WL, Hermann G, Balwani M. Imaging of gaucher disease. *World J Radiol* 2014; 6(9): 657-668 Available from: URL: http://www.wjgnet.com/1949-8470/full/v6/i9/657.htm DOI: http://dx.doi.org/10.4329/wjr.v6.i9.657

INTRODUCTION

Gaucher disease (GD) is the most common of the lysosomal storage diseases[1]. It results from accumulation of undegraded glucosylceramide in lysosomes within macrophages of the reticuloendothelial cell system due to a deficiency of the enzyme glucocerebrosidase. Consequently

these macrophages, enlarged with a buildup of glycolipids, are called Gaucher cells and are most abundant in the bone marrow, spleen and liver. GD is inherited in an autosomal recessive manner[2].

Three clinical subtypes of GD have been described[3]. Type 1 does not have any involvement of the central nervous system and is the most common. It formerly was referred to as the "adult type". However, this is a misnomer since type 1 can occur at any age and is currently know as the non-neuronopathic type. Although it is most common in the Ashkenazi Jewish population it can occur in all ethnic groups. Type 2 was formerly referred to as the "infantile type". This type manifests with grave involvement of the central nervous system. It is rapidly progressive usually leading to death within 2 years. It is now known as the acute neuronopathic type. Type 3 also has central nervous system involvement but is less severe and is more indolent than type 2 leading to the current terminology, subacute neuronopathic type.

The clinical manifestations of GD are due to the accumulation of Gaucher cells in the reticuloendothelial system of the bone marrow, spleen and liver. There can be marked variability in the severity of symptoms and the course of the disease. This is particularly true for type 1 where some patients can remain asymptomatic through life. Although the visceral changes can be dramatic, the more debilitating symptoms arise from infiltration of the bone marrow and bone changes. Since type 1 is the most common and widely studied variant of Gaucher disease it will be the primary focus of this review.

GENETICS

Gaucher disease is inherited in an autosomal recessive manner. The diagnosis of GD is made by the demonstration of decreased glucocerebrosidase enzymatic activity in peripheral blood leukocytes or fibroblasts cultured from a skin biopsy. Generally there is a 70%-90% reduction in the enzyme activity when compared to normal[4].

Molecular testing by targeted mutation analysis is used for confirmation of diagnosis and may be helpful for genotype-phenotype correlations. There are more than 300 mutations in the glucocerebrosidase gene that cause Gaucher disease[2]. However, four common mutations - N370S, IVS2(+1), 84GG, L444P - account for approximately 96.5% of disease in Ashkenazi Jewish population in the western hemisphere and approximately 50%-60% in non-Jewish populations[5].

Genotyping is helpful to test at risk family members, for genetic counseling as well as for prognosis. However, genotype-phenotype correlations are limited due to the clinical heterogeneity of the disease. Moreover, the majority of the work on genotype-phenotype correlation was based on a heavily Ashkenazi Jewish population which could skew the results since many affected individuals with the N370S/N370S homozygous genotype may remain asymptomatic and not come to medical attention[2]. Never the less a few generalities can be made: (1) the presence of at least one N370S allele precludes development of neuronopathic disease; and (2) the presence of the L444P allele is strongly (but not exclusively) associated with neuronopathic involvement. In general, those homozygous for the N370S allele tend to have less severe manifestations of disease and compound heterozygotes with one copy of N370S and a second mutation being L444P, 84GG or IVS 2 + 1 tend to have more severe disease. In fact, adults homozygous for L444P mutation (L444P/L444P genotype) typically have the type 3 neuronopathic disease. However, these rules are not hard and fast due to the limited genotype-phenotype correlation. Some patients with the N370S/N370S genotype have profound symptomatic disease whereas a type 1 patient with N370S/L444P genotype may have mild symptoms.

HEMATOLOGIC MANIFESTATIONS

Hematologic abnormalities of GD are exceedingly common. Almost all patients with symptoms present with anemia and thrombocytopenia. The etiology can be explained by depressed hematopoiesis resulting from substitution of the bone marrow by Gaucher cells. However, hypersplenism or sequestration within the spleen can be a cause as well. Symptoms that arise due to the hematologic abnormalities include fatigue, easy bruising and frequent nosebleeds. Additional blood chemistries can be elevated in GD including angiotensin converting enzyme, chitotriosidase, and tartrate resistant acid phosphatase[6]. Changes towards normalization of the anemia, thrombocytopenia and blood chemistries can be used to monitor treatment response[7].

VISCERAL MANIFESTATIONS

The viscera most commonly involved with accumulation of Gaucher cells are the liver and spleen. The pulmonary system can be involved as well; although it is very rare. Current recommendation for evaluating and monitoring visceral involvement is volumetric MRI (preferred due to lack of ionizing radiation) or CT every 12 to 24 mo[6].

Gaucher cells accumulate in the Kupfer cells of the liver leading to hepatomegaly (Figure 1). Liver volumes in type 1 patients are typically approximately 2 times normal[8]. It is notable that glycolipid does not accumulate in the hepatocytes[8,9]. The Gaucher cells can conglomerate into nodules that can be seen with sonography or MRI. These nodules may be hypoechoic, hyperechoic, or mixed on sonography[10,11]. On MRI the nodules typically appear isointense or low signal intensity (SI) on T1 weighted imaging (WI) and high SI on T2 WI. Focal areas of extramedullary hematopoiesis can have a similar appearance and can also be seen due the accompanying anemia. Hepatic infiltration can also lead to fibrosis and cirrhosis[12].

Splenomegaly results from accumulation of Gaucher cells within the spleen (Figure 1). Spleen volumes in type 1 GD are typically 5-15 times normal but the spleen size can be significantly enlarged in some cases and may be

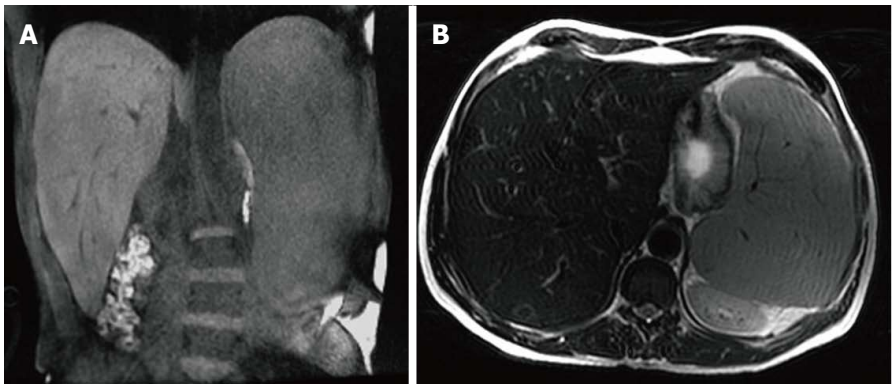

Figure 1 Hepatosplenomegaly. Coronal T1 WI (A) and axial T2 WI (B) images in a male type 1 GD patient with N370S/N370S genotype demonstrate marked hepatosplenomegaly. The liver volume measured 3235 cc. The spleen volume measured 2923 cc.

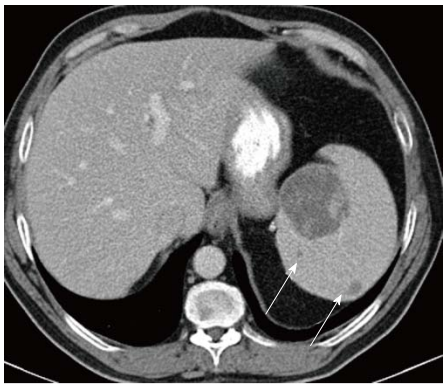

Figure 2 Splenic mass on computed tomography. Axial computed tomography image shows a large low density mass with patchy foci of soft tissue density within it in the medial aspect of the spleen. Additional smaller low density masses are present as well (arrows).

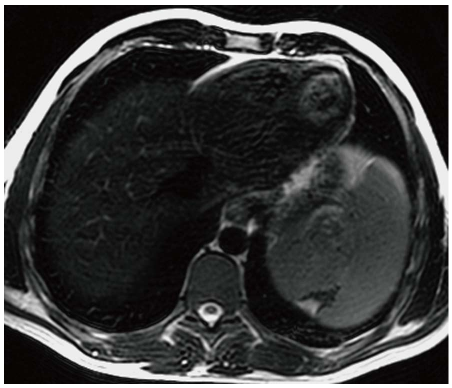

Figure 4 Splenic infarct. Axial T2 WI image demonstrates a wedge shaped defect in a subcapsular region of the spleen in its superior aspect. The defect has low signal intensity (SI) along the edges indicating fibrous tissue. In addition, high SI fat has filled the area left by the retracted capsule.

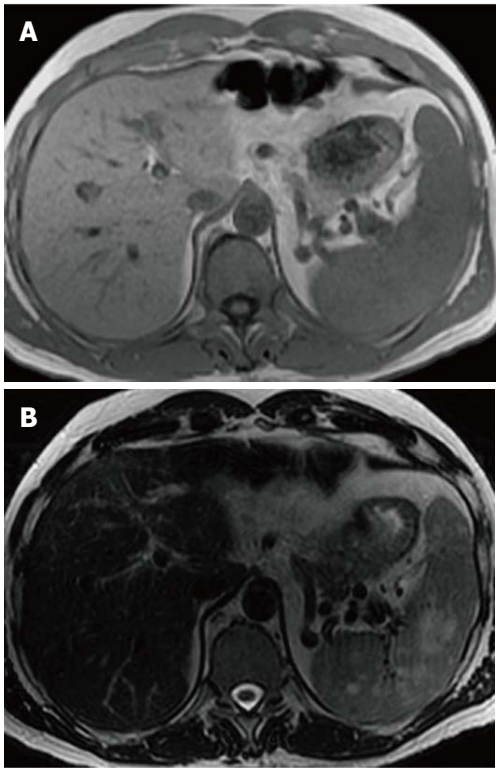

Figure 3 Splenic mass on magnetic resonance. Axial T1WI (A) image shows no apparent abnormality within the spleen consistent with isointense signal intensity (SI) masses. Axial T2WI (B) image at the same level reveals multiple masses in the spleen to be high SI.

over 50 times normal[13]. Focal splenic masses are common and may represent clusters of Gaucher cells or extra-medullary hematopoiesis. They may be detected with sonography, CT or MRI. Similar to the liver, Gaucher masses in the spleen may be hypoechoic, hyperechoic, or mixed echogenicity[11,14]. On CT the masses are low density[15] and occasionally peripherally calcified (Figure 2). These masses are most commonly imaged with MRI. They typically are low SI or isointense on T1 WI and high SI on T2 WI[16] (Figure 3). Low SI on gradient recalled echo imaging in these masses is thought to be secondary to iron contained in the Gaucher cells[17]. Splenic infarcts can occur as well due to massive splenomegaly and can be detected with imaging as well (Figure 4).

An infrequent manifestation of GD is pulmonary involvement which is more commonly seen in type 1 patients who have undergone splenectomy and those with type 3[18]. The lung findings are thought to be secondary to direct infiltration by Gaucher cells into the interstitial spaces, alveolar spaces and capillaries[19] as well as indirect causes secondary to hepatopulmonary syndrome related to the liver manifestations and/or aspiration associated with neurologic manifestations. Chest radiographs generally are normal or demonstrate a reticulo-nodular pattern. The findings are best imaged by high resolution CT and include interstitial thickening (both interlobular and intralobular), ground glass opacity, consolidation and

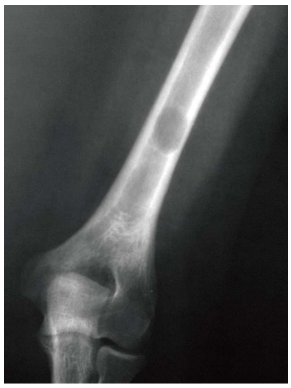

Figure 5 Lytic lesion. Frontal radiograph of the distal right humerus demonstrates a well demarcated lytic lesion that does not show sclerotic borders, endosteal erosion or associated expansion of the humeral shaft.

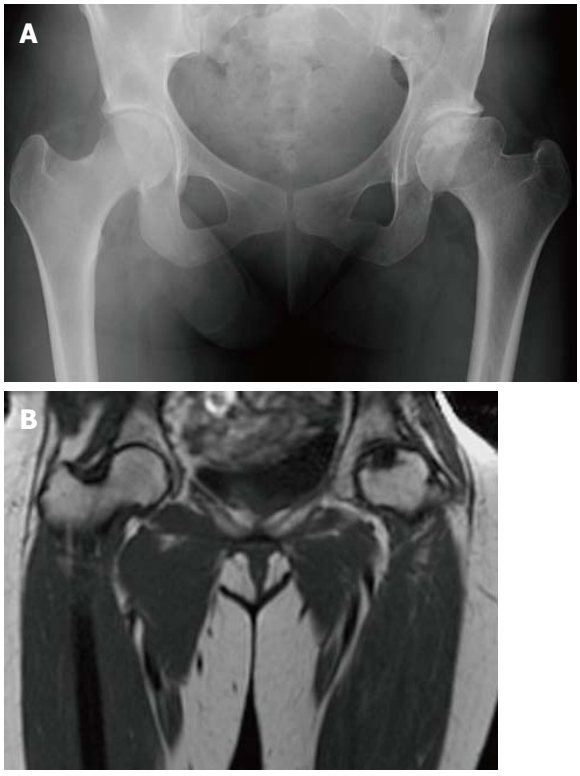

Figure 6 Osteonecrosis. Frontal radiograph of the pelvis (A) shows avascular necrosis of the left femoral head. The femoral head has a flattened contour with sclerosis in the subcapsular areas. Note that the joint space is maintained. Coronal T1 WI (B) in the same patient again demonstrated an abnormal shape of the left femoral head with flattening superiorly. In the same area there is a focus of low SI indicating the devascularized bone.

bronchial wall thickening[20,21]. Pulmonary hypertension can be the result of lung involvement[22-24]. Symptomatic pulmonary involvement is generally seen in patients with more striking visceral and skeletal findings.

SKELETAL MANIFESTATIONS

The skeletal manifestations of GD lead to the most debilitating complications of the disease and significant morbidity. Gaucher cells infiltrate and accumulate in the bone marrow. The pathophysiology of how the infiltration leads to the bone changes is not well understood. Proposed mechanisms include altered bone formation and resorption, as well as increased intra-osseous pressure due to the infiltration leading to vascular occlusion[3,25].

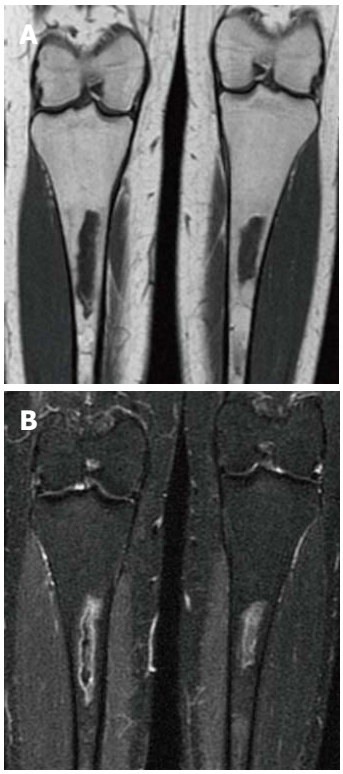

Figure 7 Medullary infarction. Coronal T1 WI (A) image shows irregularly bordered areas of low SI within the medullary cavity of both tibiae. The same areas show peripheral serpigenous high SI on the coronal short tau inversion recovery (STIR) (B) image. The appearance is typical of an infarct.

An array of bone findings are seen in GD, including growth retardation in children, osteopenia, lytic lesions (Figure 5), pathologic fractures, bone pain, osteonecrosis (Figure 6), cortical and medullary infarcts (Figure 7) and evidence of bone crises[3,26]. The severity of bone findings in GD depend on the extent of medullary cavity substitution. Marrow replacement with Gaucher cells can lead to expansion of the medullary cavity with thinning of the cortex and endosteal scalloping (Figure 8) and consequent diffuse osteopenia. In addition, the medullary expansion leads to a failure of remodeling in the distal femurs resulting in the so called Erlenmeyer flask deformity (Figure 9). These manifestations can be imaged using a variety of modalities including radiography, MRI, dual energy X-ray absortiometry (DEXA) and radionuclide imaging. However, the mainstay of skeletal imaging in GD involves MRI.

Bone crises are most common in childhood and adolescence presenting as episodes of severe bone pain associated with fever and leucocytosis. The signs and symptoms are indistinguishable from osteomyelitis, however no infection exists. The terms "pseudo-osteomyelitis" and "aseptic osteomyelitis" have been historically used to

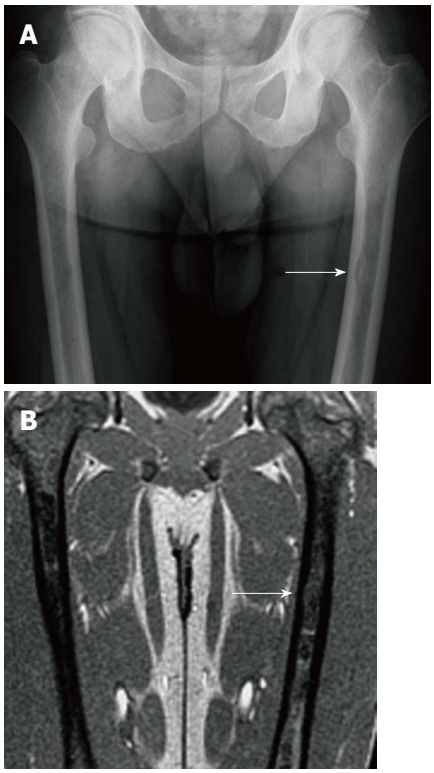

Figure 8 Endosteal scalloping. Frontal radiograph (A) of the femurs shows an area of rounded thinning of the medial cortex of the left femur (arrow). Coronal out of phase image of the femurs in the same patient (B) shows low signal intensity in that same area due to expansion of the medullary cavity due to infiltration. The thinning of the cortex is less apparent on magnetic resonance than on radiography.

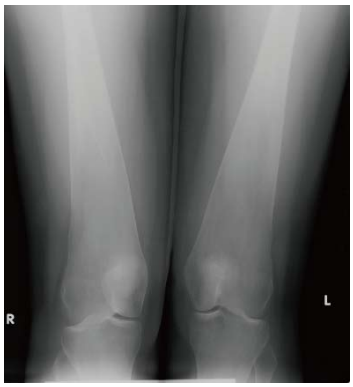

Figure 9 Erlenmeyer flask deformity. Frontal radiograph of the distal femurs demonstrates flaring of the bone and thinning of the cortex due to undertubulation of the metadiaphysis.

characterize this condition[3,27] (Figure 10).

Osteonecrosis, otherwise known as avascular necrosis, is due to lack of blood supply and consequent bone death. It is most commonly seen in the femoral heads (Figure 6), proximal humeri and vertebral bodies. The vertebral body can "cave in" leading to the "H-shaped" vertebra, *i.e.*, Reynolds phenomenon, similar to sickle cell disease (Figure 11). While the end result is similar in both diseases the mechanism of formation is different. In GD the entire vertebral body collapses followed by peripheral regrowth while in sickle cell disease the deformity is secondary to central growth arrest[28]. The necrotic bone crumples and leads to malformation and/or fracture, sometimes requiring treatment with a bone prosthesis or joint replacement.

Radiography is used primarily to image cortical bone. It can detect lytic (Figure 5) or sclerotic lesions within bones. Fractures, both traumatic and pathologic, are readily detected on radiographs. In addition, endosteal scalloping (Figure 8) and the Erlenmeyer flask deformity (Figure 9) due to marrow expansion are also detected with radiography. Although changes in cortical bone secondary to marrow infiltration can be detected with this modality, the marrow space itself is cannot be evaluated by radiography.

Osteopenia is near universal in GD as a representation of decreased bone mineral density. A significant decrease in bone density must occur before osteopenia is perceived on radiography leading to its poor sensitivity for detecting this abnormality. DEXA is the current modality of choice for evaluation of osteopenia and bone mineral density. However, care must be taken to avoid areas of osteonecrosis during DEXA evaluations.

The bone marrow itself is best assessed with MRI. Normal yellow (fatty) marrow is seen as high signal on T1 WI and T2 WI. The infiltration of the marrow by Gaucher cells replaces the normal yellow marrow. Marrow infiltration generally follows the distribution of cellular read marrow progressing from the axial to the peripheral skeleton and from the proximal to the distal aspects of the long bones with a tendency to spare the epiphyses[29]. This is recognized as a change to low SI on both T1 and T2 WI[29,30] (Figure 12). On short tau inversion recovery (STIR) images the infiltration appears slightly high SI[31]. High SI within the marrow on T2 or STIR images suggests edema within the marrow and the presence of an "active" process such as a bone crisis or infection[32]. Evaluation of bone marrow infiltration in children is complicated by the fact that normal red marrow which is seen in this age group manifests with low SI on both T1 and T2 WI.

Radionuclide imaging is useful for evaluating bone changes in GD. Bone scintigraphy utilizing Technicium 99m-methylene diphosphonate (^{99m}Tc-MDP) can be used to evaluate for fractures that are not readily apparent on radiography. In addition, this tracer can be used to help differentiate a bone crisis (aseptic infarction) from osteomyelitis. In a bone crisis bone scintigraphy performed within 1-3 d of the onset of pain will demonstrate decreased tracer uptake at the involved site unlike infection that shows increased uptake[33,34]. The same agent can be used to help evaluate for complication related to joint prostheses such as loosening[31]. Scintigraphy using leucocytes labeled with Indium-111 is commonly used to image areas of suspected infection including osteomyelitis and around joint prostheses.

Prior to the advent of MRI, radionuclide imaging was also used for evaluation of the bone marrow. Technicium 99m sulfur colloid (^{99m}TC-SC) accumulates in normal

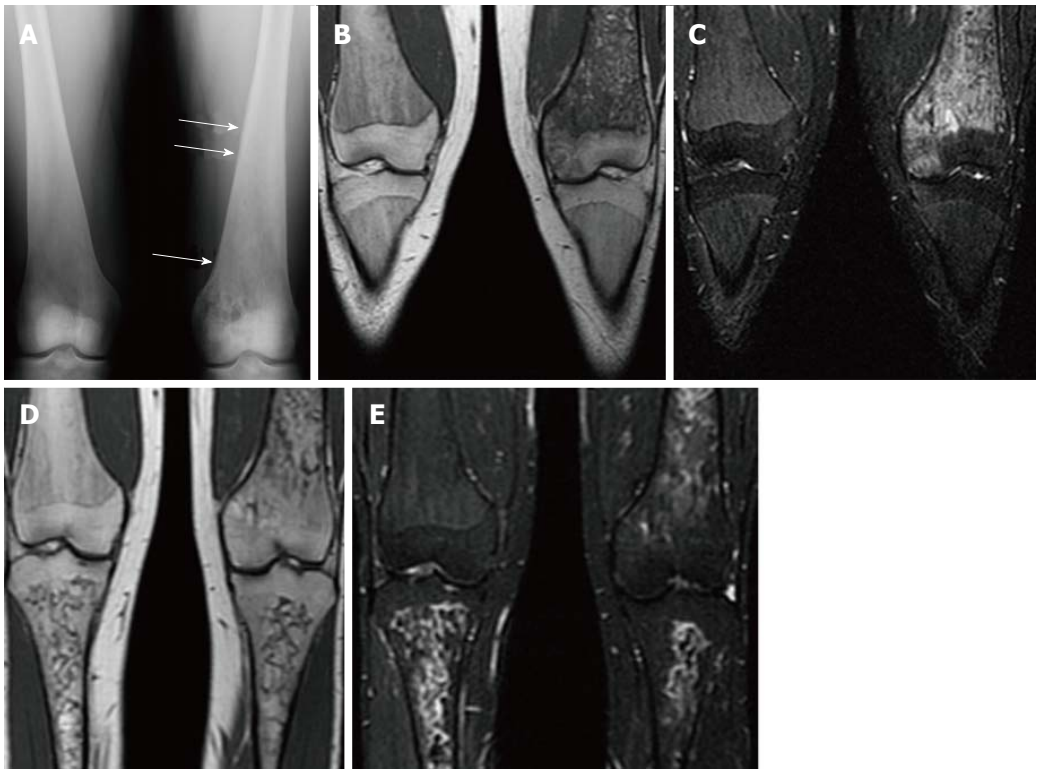

Figure 10 Psuedo-osteomyelitis. Frontal radiograph of both distal femurs in 2009 (A) demonstrates an irregular area of patchy lucency in the medial condyle of the left femur. There is periosteal reaction in this area as well as more superiorly (arrows). Coronal T1 WI (B) image at the same time in 2009 demonstrate low SI in the medial condyle of the femur extending into the medial epiphysis. There is high SI in these areas on coronal STIR (C) image which extends into the adjacent soft tissues where the periosteal reaction is seen on the radiograph. There is no joint effusion. The patient presented with left knee pain and the imaging was suspicious for osteomyelitis involving the medial distal femur. However, the patient has no fever and cultures were negative. Coronal T1 WI (D) of the same area in 2011 shows resolution of the low SI in the medial condyle and epiphysis. The corresponding high SI on the STIR image (E) has resolved as well.

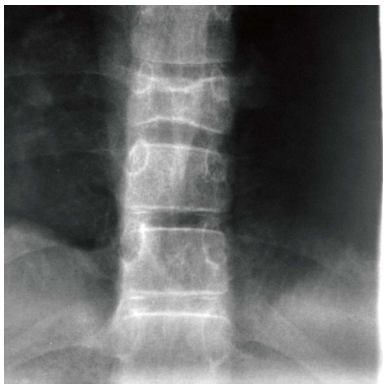

Figure 11 H-shaped vertebra. Cone down frontal radiograph of the lower thoracic spine demonstrates collapse of a lower thoracic vertebral body with bi-concave upper and lower end plates giving the Reynolds phenomenon of Gaucher disease.

bone marrow. Therefore in marrow infiltrated and replaced by Gaucher cells there will be decreased uptake or an abnormal pattern of uptake compared to normal[34]. This gives an indirect sign of infiltration. Another tracer, Technicium 99m sestamibi, has the advantage of being accumulated in areas of Gaucher cell deposition[35,36]. Mariani *et al*[35] imaged 74 Italian patients with Gaucher disease using technetium 99m sestamibi and showed 71 of 74 demonstrated uptake predominantly in the distal femur. An undisclosed number of these patients had MR

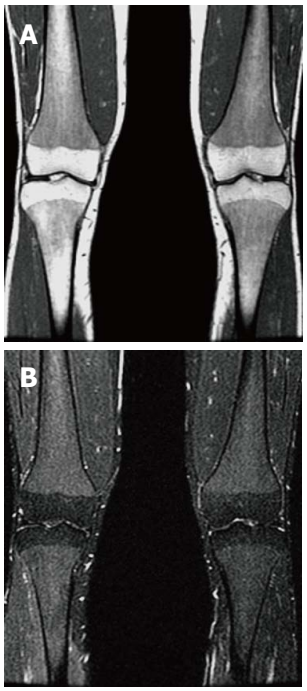

Figure 12 Bone marrow infiltration. Coronal T1 WI (A) of the distal femora and proximal tibiae in a type 1 gaucher disease patient shows low signal intensity (SI) in the bone marrow which spares the epiphyses that demonstrate the normal fatty marrow SI. Coronal short tau inversion recover (STIR) (B) image demonstrates that the low SI on T1 becomes slightly high SI on STIR.

imaging performed at the same approximate time revealing low SI in the same regions. Therefore it is a method of direct visualization of infiltration. Bone marrow sestamibi imaging can be advantageous when imaging children and trying to differentiate Gaucher infiltration from normal red marrow in children. Positron emission tomography has become widely available in recent years. Imaging with the most common radiotracer, fluoride-18 fluorodeoxyglucose, has not proven beneficial for detecting marrow involvement in GD. However, a newer tracer, fluoride-18 L-thymidine, shows promise for imaging bone marrow[37]. Since it is not yet FDA approved its use is limited to clinical trials and its role if any in GD has not been established. Therefore, MRI remains the modality of choice for imaging bone marrow due the poor spatial resolution of scintigraphy as well as the associated radiation dose of radionuclide imaging.

An essential problem of imaging is that it only gives a qualitative assessment of bone marrow infiltration. An MRI shows decreased SI on T1 WI but there is no way to measure the "amount" of signal. A visual assessment of improvement or worsening can be made on the basis of the MR image but that is qualitative and not very useful to clinicians. One way of directly measuring bone marrow disease has been developed, Dixon's quantitative chemical shift imaging[38]. Chemical shift imaging leverages the difference in resonance frequencies between water and fat molecules thereby defining the amount of fat or fat fraction within bone marrow. The fat fraction of normal marrow decreases as the amount of infiltration replaces the triglyceride rich fat cells of normal marrow. Studies have shown a low marrow fat fraction as measured by quantitative chemical sift imaging to correspond to worse clinical disease and more bone complications[39-42]. However, the technique is complex and not widely used outside academic centers. To overcome this problem several semi-quantitative methods have been developed including the Rosenthal staging system[29], the Dusseldorf score[43], the Terk classification[44] and the bone marrow burden (BMB) score[45]. All use conventional MR imaging technology and assign points based on changes in marrow signal intensity at different anatomic locations.

The BMB score is the most widely used and validated[45,46]. The BMB score[45] incorporates both the visual interpretation of SI and the geographic location of the disease on conventional MR images of the lumbar spine and femora. The SI of the bone marrow in the femora is compared to the subcutaneous fat on both T1 and T2 WI sequences. The SI of the bone marrow in the lumbar spine is compared to a non-diseased intervertebral disc on both T1 and T2 WI sequences. The SI is scored as hyper-intense, slightly hyper-intense, iso-intense, slightly hypo-intense, and hypo-intense. A numeric value ranging from 0-2 is assigned based on the SI. Point values are also assigned based on the location/distribution of the marrow infiltration. In the femora, sites of involvement including the diaphysis, proximal epiphysis/apophysis and distal epiphysis are evaluated. In the lumbar spine, the distribution of infiltration is evaluated as patchy or diffuse with special attention given to absence of fat in basivertebral vein region. The score for the femora (0-8) and the lumbar spine (0-8) are added together for a total score which can range from 0 to 16. A higher score indicates more severe the bone marrow involvement. In their study of 12 patients with Gaucher disease[45], Maas *et al*[45] demonstrated good correlation of the BMB score with fat fraction determination by the Dixon technique. That study also showed a decrease in the BMB score in patients on enzyme replacement therapy (ERT), however, it was less sensitive for detection of marrow improvement than Dixon method.

TREATMENT

Only supportive treatment or surgical intervention including splenectomy and joint replacement was available for patients with Gaucher disease into the early 1990s. In 1991 ERT with placentally derived enzyme alglucerase (Ceredase®, Genzyme Corporation, Cambridge, Mass.) came into existence. Following this, in 1994, recombinant mannose-terminated human glucocerebrosidase (Cerezyme®, Genzyme Corporation) received FDA approval. The goal of ERT is to treat the symptoms of the disease as well as to prevent complications particularly the skeletal complications[6].

The visceral and hematologic manifestations of GD respond relatively quickly to ERT[47,48] (Figure 13). The anemia and thrombocytopenia can improve within 6 mo to one year of initialing ERT. The liver and spleen volumes generally can decrease by approximately 50% within the first 2 years but rarely ever return to a normal volume even with long term treatment. Although some improvement in pulmonary involvement has been reported with ERT, response is generally slow, and sometimes no improvement is seen[23,49]. The marrow infiltration responds to ERT as well but takes much longer to be seen[50,51] (Figures 14 and 15). Some skeletal manifestations, such as osteonecrosis, osteosclerosis and vertebral body collapse, remain irreversible. The neurologic manifestations of GD do not respond to ERT since it does not cross the blood-brain barrier[52].

An alternative to ERT for treatment of GD is substrate reduction therapy. Whereas ERT works by replacing the deficient enzyme, substrate reduction works by decreasing the production of the substrate glucosylceramide. Since most type 1 GD patients have some residual enzyme activity, reducing the amount of substrate may allow the native enzyme to succeed. The first medication of this kind was N-butyldeoxynojirimycin (miglustat) approved by the FDA in 2003. It is an oral medication for use in mild to moderate type 1 GD patients who cannot tolerate ERT. Studies have shown improvement of anemia, platelet count, liver volume and spleen volume alone or in combination with ERT[53-55]. One study also showed improvement of bone disease on miglustat[56,57]. However, side effects particularly diarrhea, weight loss and tremors

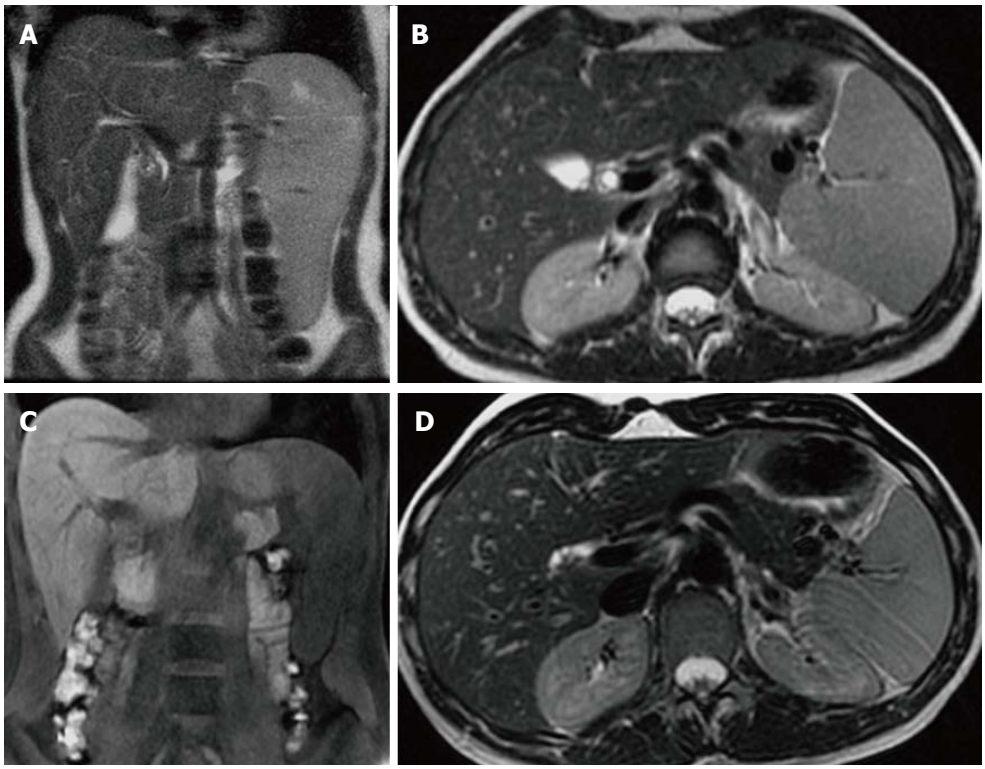

Figure 13 Visceral improvement on enzyme replacement therapy. Female type 3 Gaucher disease patient who began enzyme replacement therapy (ERT) in 2007. Initial evaluation in 2007 before starting ERT shows that the spleen extends down to the iliac crest on the T2 WI coronal image (A). On the axial T2 WI (B) the left lobe of the liver extends across the midline posterior to the lateral aspect of the left rectus abdominus muscle and anterior to the stomach. At that time the liver volume measured 1702 cc and the spleen volume measured 769 cc. After 6 years on treatment, repeat imaging in 2013 reveals the inferior edge of the spleen is now above the iliac crest on the coronal T1 WI (C) and the left lobe of the liver now extends only slightly across the midline to end posterior to the medial aspect of the rectus abdominus muscle and the stomach is now lateral to the liver on the axial T2 WI (D). In 2013, the liver volume measured 1163 cc and the spleen volume measured368 cc.

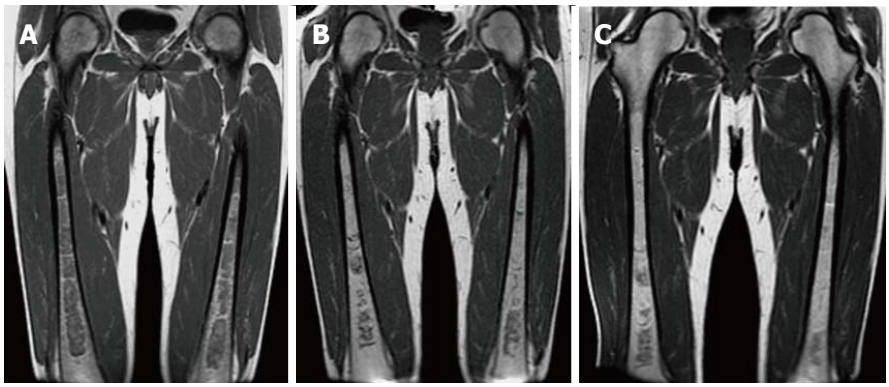

Figure 14 Bone marrow improvement on enzyme replacement therapy. Type 1 GD male patient with N370S/N370S genotype who began enzyme replacement therapy (ERT) in October of 2007 shows relatively rapid improvement of the bone marrow infiltration. Initial coronal T1 WI of the femora (A) demonstrates diffuse low SI throughout the medullary cavity consistent with marked infiltration. Coronal T1 WI in 2009 (B) after only 2 years of treatment shows significant improvement in the infiltration manifest by decreased low SI in the medullary cavity. In 2011, coronal T1 WI (C) shows continued slight decrease in the amount of low SI in the bone marrow.

were significant[52] and its use is limited in the United States Unlike ERT miglustat can cross the blood-brain barrier[52] and has shown promising results in treating neurologic manifestations in combination with ERT[58,59]. A study also shows improvement of pulmonary manifestations with single drug treatment[60]. Currently there is a newer oral substrate reduction therapy agent, eliglustat tartrate, which has demonstrated efficacy in GD type 1 patients with a more favorable side effect profile[61]. It is currently undergoing phase Ⅲ trials.

Both ERT and substrate reduction therapy can lead to improvement in the signs and symptoms of GD. However, there is a significant cost to the treatment ranging from US$100000 to $250000 per year[62]. Thus judicious

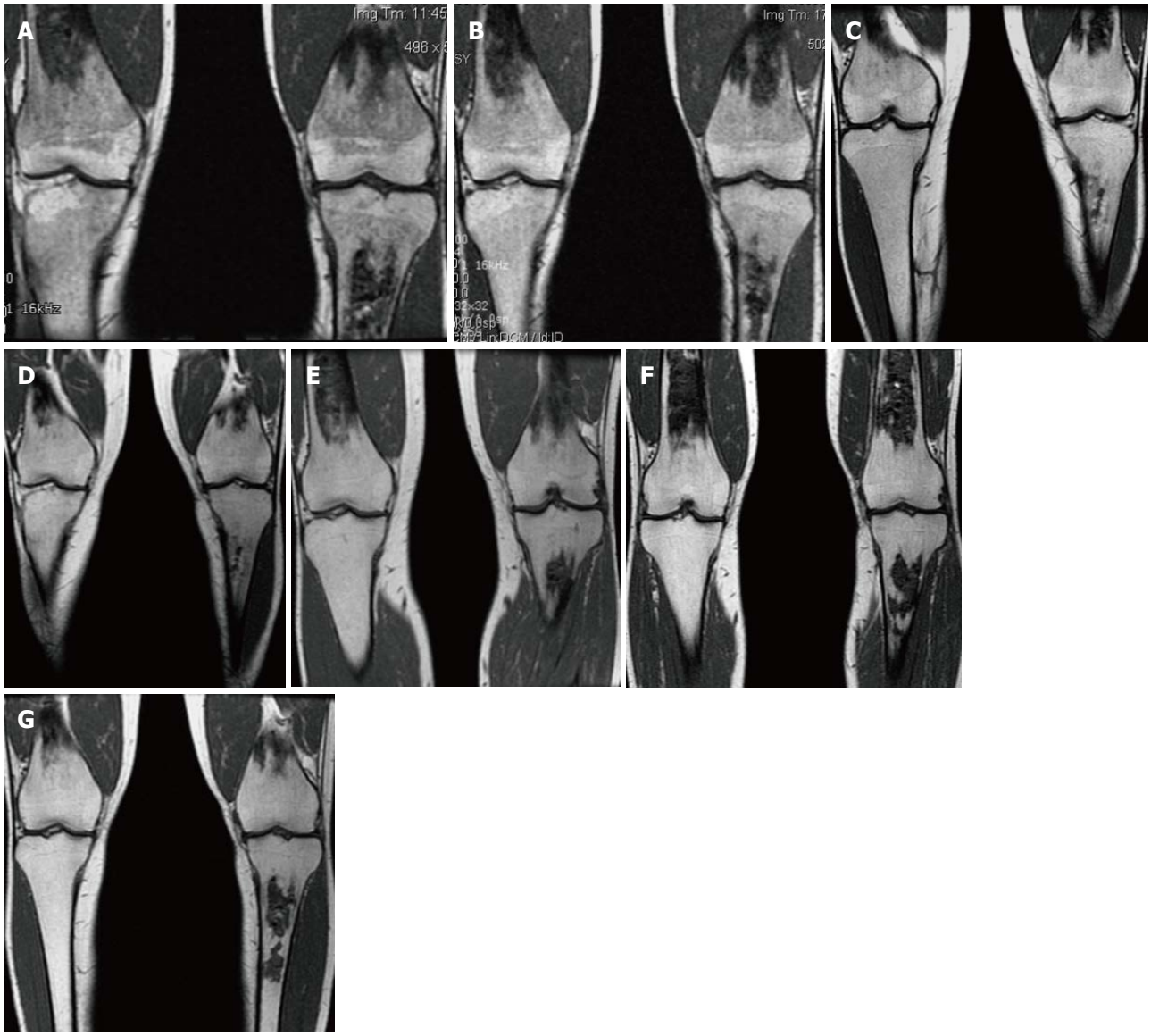

Figure 15 Bone marrow improvement. Gaucher Type 1 patient with N370S/N370S genotype who started enzyme replacement therapy (ERT) in 1997. Coronal T1 WI of the distal femora and proximal tibiae in 1998 (A), 1999 (B), 2002 (C), 2003 (D), 2006 (E), 2008 (F) and 2011 (G). Medullary infarcts are partially seen in both distal femurs and the left tibia. The low T1 SI significantly improves between 1998 and 2002 with near normal marrow signal seen in the noninfarcted areas in 2008 and years later. Although this patient has the same genotype as the patient in Figure 14, there is a longer time to improvement indicating the limited genotype/phenotype correlation.

use is warranted. Imaging plays a significant role in determining which patients need treatment and in surveillance of those on treatment. Current recommendations call for abdominal MRI for determination of liver and spleen volume, MRI of the bilateral femora, radiography of the spine and DEXA of the hips and lumbar spine in the initial assessment[6]. For those patients not on treatment being followed and those on treatment, the same imaging protocol is recommended every 12-24 mo or at the time of a dosage change or significant clinical complication[6].

CONCLUSION

Gaucher disease is the most common lysomal storage disease which affects all ethnic groups. The accumulation of glycolipids in the reticuloendothelial system leads to symptoms. Anemia, thrombocytopenia, and hepatosplenomegaly are commonly seen and respond relatively rapidly to treatment with ERT. The skeletal manifestations are due to build up of the glycolipids in the bone marrow and lead to the most debilitating aspects of GD. Treatment results in improvement of marrow infiltration however it takes much longer than the visceral and hematologic manifestations. Imaging plays a key role in both initial diagnosis and treatment monitoring. MRI of the abdomen is used to monitor liver and spleen volumes. MRI of the femora and lumbar spine is used for evaluation of bone marrow infiltration burden.

REFERENCES

1 **Meikle PJ**, Hopwood JJ, Clague AE, Carey WF. Prevalence

of lysosomal storage disorders. *JAMA* 1999; **281**: 249-254 [PMID: 9918480 DOI: 10.1001/jama.281.3.249]
2 **Grabowski GA**, Petsko GA, Kolodny EH. Gaucher Disease. In: Valle D, Beaudet AL, Vogelstein B, Kinzler KW, Antonarakis SE, Ballabio A, eds. Scriver's Online Metabolic and Molecular Bases of Inherited Disease. Published January 2006. Accessed November 29, 2013 [DOI: 10.1036/ommbid.176]
3 **Wenstrup RJ**, Roca-Espiau M, Weinreb NJ, Bembi B. Skeletal aspects of Gaucher disease: a review. *Br J Radiol* 2002; **75** Suppl 1: A2-12 [PMID: 12036828 DOI: 10.1259/bjr.75.suppl_1.750002]
4 **Beutler E**, Saven A. Misuse of marrow examination in the diagnosis of Gaucher disease. *Blood* 1990; **76**: 646-648 [PMID: 2116196]
5 **Beutler E**, Gelbart T, Kuhl W, Zimran A, West C. Mutations in Jewish patients with Gaucher disease. *Blood* 1992; **79**: 1662-1666 [PMID: 1558964]
6 **Weinreb NJ**, Aggio MC, Andersson HC, Andria G, Charrow J, Clarke JT, Erikson A, Giraldo P, Goldblatt J, Hollak C, Ida H, Kaplan P, Kolodny EH, Mistry P, Pastores GM, Pires R, Prakash-Cheng A, Rosenbloom BE, Scott CR, Sobreira E, Tylki-Szymańska A, Vellodi A, vom Dahl S, Wappner RS, Zimran A. Gaucher disease type 1: revised recommendations on evaluations and monitoring for adult patients. *Semin Hematol* 2004; **41**: 15-22 [PMID: 15468046 DOI: 10.1053/j.seminhematol.2004.07.010]
7 **Charrow J**, Esplin JA, Gribble TJ, Kaplan P, Kolodny EH, Pastores GM, Scott CR, Wappner RS, Weinreb NJ, Wisch JS. Gaucher disease: recommendations on diagnosis, evaluation, and monitoring. *Arch Intern Med* 1998; **158**: 1754-1760 [PMID: 9738604 DOI: 10.1001/archinte.158.16.1754]
8 **James SP**, Stromeyer FW, Chang C, Barranger JA. LIver abnormalities in patients with Gaucher's disease. *Gastroenterology* 1981; **80**: 126-133 [PMID: 7450398]
9 **James SP**, Stromeyer FW, Stowens DW, Barranger JA. Gaucher disease: hepatic abnormalities in 25 patients. *Prog Clin Biol Res* 1982; **95**: 131-142 [PMID: 7122631]
10 **Patlas M**, Hadas-Halpern I, Abrahamov A, Elstein D, Zimran A. Spectrum of abdominal sonographic findings in 103 pediatric patients with Gaucher disease. *Eur Radiol* 2002; **12**: 397-400 [PMID: 11870441 DOI: 10.1007/s003300101031]
11 **Neudorfer O**, Hadas-Halpern I, Elstein D, Abrahamov A, Zimran A. Abdominal ultrasound findings mimicking hematological malignancies in a study of 218 Gaucher patients. *Am J Hematol* 1997; **55**: 28-34 [PMID: 9136914 DOI: 10.1002/(SICI)1096-8652(199705)55: 1<28: : AID-AJH5>3.0.CO; 2-5]
12 **Lee RE**. The pathology of Gaucher disease. *Prog Clin Biol Res* 1982; **95**: 177-217 [PMID: 7122634]
13 **Grabowski GA**, Kolodny EH, Weinreb NJ, Rosenbloom BE, Prakash-Cheng A, Kaplan P, Charrow J, Pastores GM, Mistry PK. Gaucher disease: Phenotypic and Genetic Variation,. In: Valle D, Beaudet AL, Vogelstein B, Kinzler KW, Antonarakis SE, Ballabio A, eds. Scriver's Online Metabolic and Molecular Bases of Inherited Disease. Published January 2006. Accessed November 29, 2013. [DOI: 10.1036/ommbid.177]
14 **Hill SC**, Reinig JW, Barranger JA, Fink J, Shawker TH. Gaucher disease: sonographic appearance of the spleen. *Radiology* 1986; **160**: 631-634 [PMID: 3526400]
15 **Poll LW**, Koch JA, vom Dahl S, Sarbia M, Häussinger D, Mödder U. Gaucher disease of the spleen: CT and MR findings. *Abdom Imaging* 2000; **25**: 286-289 [PMID: 10823453 DOI: 10.1007/s002610000010]
16 **Hill SC**, Damaska BM, Ling A, Patterson K, Di Bisceglie AM, Brady RO, Barton NW. Gaucher disease: abdominal MR imaging findings in 46 patients. *Radiology* 1992; **184**: 561-566 [PMID: 1620865]
17 **Terk MR**, Esplin J, Lee K, Magre G, Colletti PM. MR imaging of patients with type 1 Gaucher's disease: relationship between bone and visceral changes. *AJR Am J Roentgenol* 1995; **165**: 599-604 [PMID: 7645477 DOI: 10.2214/ajr.165.3.7645477]
18 **Hill SC**, Damaska BM, Tsokos M, Kreps C, Brady RO, Barton NW. Radiographic findings in type 3b Gaucher disease. *Pediatr Radiol* 1996; **26**: 852-860 [PMID: 8929296 DOI: 10.1007/BF03178036]
19 **Amir G**, Ron N. Pulmonary pathology in Gaucher's disease. *Hum Pathol* 1999; **30**: 666-670 [PMID: 10374775 DOI: 10.1016/S0046-8177(99)90092-8]
20 **McHugh K**, Olsen E ØE, Vellodi A. Gaucher disease in children: radiology of non-central nervous system manifestations. *Clin Radiol* 2004; **59**: 117-123 [PMID: 14746780 DOI: 10.1016/j.crad.2003.09.010]
21 **Aydin K**, Karabulut N, Demirkazik F, Arat A. Pulmonary involvement in adult Gaucher's disease: high resolution CT appearance. *Br J Radiol* 1997; **70**: 93-95 [PMID: 9059303 DOI: 10.1259/bjr.70.829.9059303]
22 **Theise ND**, Ursell PC. Pulmonary hypertension and Gaucher's disease: logical association or mere coincidence? *Am J Pediatr Hematol Oncol* 1990; **12**: 74-76 [PMID: 2309982 DOI: 10.1097/00043426-199021000-00014]
23 **Mistry PK**, Sirrs S, Chan A, Pritzker MR, Duffy TP, Grace ME, Meeker DP, Goldman ME. Pulmonary hypertension in type 1 Gaucher's disease: genetic and epigenetic determinants of phenotype and response to therapy. *Mol Genet Metab* 2002; **77**: 91-98 [PMID: 12359135 DOI: 10.1016/S1096-7192(02)00122-1]
24 **Pastores GM**, Miller A. Pulmonary hypertension in Gaucher's disease. *Lancet* 1998; **352**: 580 [PMID: 9716094 DOI: 10.1016/S0140-6736(05)79295-3]
25 **Sims KB**, Pastores GM, Weinreb NJ, Barranger J, Rosenbloom BE, Packman S, Kaplan P, Mankin H, Xavier R, Angell J, Fitzpatrick MA, Rosenthal D. Improvement of bone disease by imiglucerase (Cerezyme) therapy in patients with skeletal manifestations of type 1 Gaucher disease: results of a 48-month longitudinal cohort study. *Clin Genet* 2008; **73**: 430-440 [PMID: 18312448 DOI: 10.1111/j.1399-0004.2008.00978.x]
26 **Hermann G**, Goldblatt J, Levy RN, Goldsmith SJ, Desnick RJ, Grabowski GA. Gaucher's disease type 1: assessment of bone involvement by CT and scintigraphy. *AJR Am J Roentgenol* 1986; **147**: 943-948 [PMID: 3490167 DOI: 10.2214/ajr.147.5.943]
27 **Yossipovitch ZH**, Herman G, Makin M. Aseptic osteomyelitis in Gaucher's disease. *Isr J Med Sci* 1965; **1**: 531-536 [PMID: 5842267]
28 **Schwartz AM**, Homer MJ, McCauley RG. „Step-off " vertebral body: Gaucher's disease versus sickle cell hemoglobinopathy. *AJR Am J Roentgenol* 1979; **132**: 81-85 [PMID: 103410 DOI: 10.2214/ajr.132.1.81]
29 **Rosenthal DI**, Scott JA, Barranger J, Mankin HJ, Saini S, Brady TJ, Osier LK, Doppelt S. Evaluation of Gaucher disease using magnetic resonance imaging. *J Bone Joint Surg Am* 1986; **68**: 802-808 [PMID: 3733771]
30 **Lanir A**, Hadar H, Cohen I, Tal Y, Benmair J, Schreiber R, Clouse ME. Gaucher disease: assessment with MR imaging. *Radiology* 1986; **161**: 239-244 [PMID: 3763873]
31 **Katz R**, Booth T, Hargunani R, Wylie P, Holloway B. Radiological aspects of Gaucher disease. *Skeletal Radiol* 2011; **40**: 1505-1513 [PMID: 20658285 DOI: 10.1007/s00256-010-0992-3]
32 **Hermann G**, Shapiro RS, Abdelwahab IF, Grabowski G. MR imaging in adults with Gaucher disease type I: evaluation of marrow involvement and disease activity. *Skeletal Radiol* 1993; **22**: 247-251 [PMID: 8316866 DOI: 10.1007/BF00197668]
33 **Katz K**, Mechlis-Frish S, Cohen IJ, Horev G, Zaizov R, Lubin E. Bone scans in the diagnosis of bone crisis in patients who

have Gaucher disease. *J Bone Joint Surg Am* 1991; **73**: 513-517 [PMID: 2013590]
34 **Mikosch P**, Kohlfürst S, Gallowitsch HJ, Kresnik E, Lind P, Mehta AB, Hughes DA. Is there a role for scintigraphic imaging of bone manifestations in Gaucher disease? A review of the literature. *Nuklearmedizin* 2008; **47**: 239-247 [PMID: 19057797]
35 **Mariani G**, Filocamo M, Giona F, Villa G, Amendola A, Erba P, Buffoni F, Copello F, Pierini A, Minichilli F, Gatti R, Brady RO. Severity of bone marrow involvement in patients with Gaucher's disease evaluated by scintigraphy with 99mTc-sestamibi. *J Nucl Med* 2003; **44**: 1253-1262 [PMID: 12902415]
36 **Mariani G**, Molea N, La Civita L, Porciello G, Lazzeri E, Ferri C. Scintigraphic findings on 99mTc-MDP, 99mTc-sestamibi and 99mTc-HMPAO images in Gaucher's disease. *Eur J Nucl Med* 1996; **23**: 466-470 [PMID: 8612670 DOI: 10.1007/BF01247378]
37 **Agool A**, Schot BW, Jager PL, Vellenga E. 18F-FLT PET in hematologic disorders: a novel technique to analyze the bone marrow compartment. *J Nucl Med* 2006; **47**: 1592-1598 [PMID: 17015893]
38 **Dixon WT**. Simple proton spectroscopic imaging. *Radiology* 1984; **153**: 189-194 [PMID: 6089263]
39 **Maas M**, Hollak CE, Akkerman EM, Aerts JM, Stoker J, Den Heeten GJ. Quantification of skeletal involvement in adults with type I Gaucher's disease: fat fraction measured by Dixon quantitative chemical shift imaging as a valid parameter. *AJR Am J Roentgenol* 2002; **179**: 961-965 [PMID: 12239046 DOI: 10.2214/ajr.179.4.1790961]
40 **Johnson LA**, Hoppel BE, Gerard EL, Miller SP, Doppelt SH, Zirzow GC, Rosenthal DI, Dambrosia JM, Hill SC, Brady RO. Quantitative chemical shift imaging of vertebral bone marrow in patients with Gaucher disease. *Radiology* 1992; **182**: 451-455 [PMID: 1732964]
41 **Maas M**, Poll LW, Terk MR. Imaging and quantifying skeletal involvement in Gaucher disease. *Br J Radiol* 2002; **75** Suppl 1: A13-A24 [PMID: 12036829 DOI: 10.1259/bjr.75.suppl_1.750013]
42 **Maas M**, Akkerman EM, Venema HW, Stoker J, Den Heeten GJ. Dixon quantitative chemical shift MRI for bone marrow evaluation in the lumbar spine: a reproducibility study in healthy volunteers. *J Comput Assist Tomogr* 2001; **25**: 691-697 [PMID: 11584227 DOI: 10.1097/00004728-200109000-00005]
43 **Poll LW**, Koch JA, vom Dahl S, Willers R, Scherer A, Boerner D, Niederau C, Häussinger D, Mödder U. Magnetic resonance imaging of bone marrow changes in Gaucher disease during enzyme replacement therapy: first German long-term results. *Skeletal Radiol* 2001; **30**: 496-503 [PMID: 11587517 DOI: 10.1007/s002560100375]
44 **Terk MR**, Dardashti S, Liebman HA. Bone marrow response in treated patients with Gaucher disease: evaluation by T1-weighted magnetic resonance images and correlation with reduction in liver and spleen volume. *Skeletal Radiol* 2000; **29**: 563-571 [PMID: 11127678 DOI: 10.1007/s002560000276]
45 **Maas M**, van Kuijk C, Stoker J, Hollak CE, Akkerman EM, Aerts JF, den Heeten GJ. Quantification of bone involvement in Gaucher disease: MR imaging bone marrow burden score as an alternative to Dixon quantitative chemical shift MR imaging--initial experience. *Radiology* 2003; **229**: 554-561 [PMID: 14526090 DOI: 10.1148/radiol.2292020296]
46 **DeMayo RF**, Haims AH, McRae MC, Yang R, Mistry PK. Correlation of MRI-Based bone marrow burden score with genotype and spleen status in Gaucher's disease. *AJR Am J Roentgenol* 2008; **191**: 115-123 [PMID: 18562733 DOI: 10.2214/AJR.07.3550]
47 **Weinreb NJ**, Charrow J, Andersson HC, Kaplan P, Kolodny EH, Mistry P, Pastores G, Rosenbloom BE, Scott CR, Wappner RS, Zimran A. Effectiveness of enzyme replacement therapy in 1028 patients with type 1 Gaucher disease after 2 to 5 years of treatment: a report from the Gaucher Registry. *Am J Med* 2002; **113**: 112-119 [PMID: 12133749 DOI: 10.1016/S0002-9343(02)01150-6]
48 **Andersson H**, Kaplan P, Kacena K, Yee J. Eight-year clinical outcomes of long-term enzyme replacement therapy for 884 children with Gaucher disease type 1. *Pediatrics* 2008; **122**: 1182-1190 [PMID: 19047232 DOI: 10.1542/peds.2007-2144]
49 **Goitein O**, Elstein D, Abrahamov A, Hadas-Halpern I, Melzer E, Kerem E, Zimran A. Lung involvement and enzyme replacement therapy in Gaucher's disease. *QJM* 2001; **94**: 407-415 [PMID: 11493717 DOI: 10.1093/qjmed/94.8.407]
50 **Poll LW**, Maas M, Terk MR, Roca-Espiau M, Bembi B, Ciana G, Weinreb NJ. Response of Gaucher bone disease to enzyme replacement therapy. *Br J Radiol* 2002; **75** Suppl 1: A25-A36 [PMID: 12036830 DOI: 10.1259/bjr.75.suppl_1.750025]
51 **Hermann G**, Pastores GM, Abdelwahab IF, Lorberboym AM. Gaucher disease: assessment of skeletal involvement and therapeutic responses to enzyme replacement. *Skeletal Radiol* 1997; **26**: 687-696 [PMID: 9453101 DOI: 10.1007/s002560050313]
52 **Ficicioglu C**. Review of miglustat for clinical management in Gaucher disease type 1. *Ther Clin Risk Manag* 2008; **4**: 425-431 [PMID: 18728838]
53 **Cox T**, Lachmann R, Hollak C, Aerts J, van Weely S, Hrebícek M, Platt F, Butters T, Dwek R, Moyses C, Gow I, Elstein D, Zimran A. Novel oral treatment of Gaucher's disease with N-butyldeoxynojirimycin (OGT 918) to decrease substrate biosynthesis. *Lancet* 2000; **355**: 1481-1485 [PMID: 10801168 DOI: 10.1016/S0140-6736(00)02161-9]
54 **Elstein D**, Dweck A, Attias D, Hadas-Halpern I, Zevin S, Altarescu G, Aerts JF, van Weely S, Zimran A. Oral maintenance clinical trial with miglustat for type I Gaucher disease: switch from or combination with intravenous enzyme replacement. *Blood* 2007; **110**: 2296-2301 [PMID: 17609429 DOI: 10.1182/blood-2007-02-075960]
55 **Pastores GM**, Barnett NL, Kolodny EH. An open-label, non-comparative study of miglustat in type I Gaucher disease: efficacy and tolerability over 24 months of treatment. *Clin Ther* 2005; **27**: 1215-1227 [PMID: 16199246 DOI: 10.1016/j.clinthera.2005.08.004]
56 **Pastores GM**, Elstein D, Hrebícek M, Zimran A. Effect of miglustat on bone disease in adults with type 1 Gaucher disease: a pooled analysis of three multinational, open-label studies. *Clin Ther* 2007; **29**: 1645-1654 [PMID: 17919546 DOI: 10.1016/j.clinthera.2007.08.006]
57 **Mikosch P**, Reed M, Baker R, Holloway B, Berger L, Mehta AB, Hughes DA. Changes of bone metabolism in seven patients with Gaucher disease treated consecutively with imiglucerase and miglustat. *Calcif Tissue Int* 2008; **83**: 43-54 [PMID: 18553043 DOI: 10.1007/s00223-008-9143-4]
58 **Capablo JL**, Franco R, de Cabezón AS, Alfonso P, Pocovi M, Giraldo P. Neurologic improvement in a type 3 Gaucher disease patient treated with imiglucerase/miglustat combination. *Epilepsia* 2007; **48**: 1406-1408 [PMID: 17433057 DOI: 10.1111/j.1528-1167.2007.01074.x]
59 **Cox-Brinkman J**, van Breemen MJ, van Maldegem BT, Bour L, Donker WE, Hollak CE, Wijburg FA, Aerts JM. Potential efficacy of enzyme replacement and substrate reduction therapy in three siblings with Gaucher disease type III. *J Inherit Metab Dis* 2008; **31**: 745-752 [PMID: 18850301 DOI: 10.1007/s10545-008-0873-2]
60 **Schiffmann R**, Fitzgibbon EJ, Harris C, DeVile C, Davies EH, Abel L, van Schaik IN, Benko W, Timmons M, Ries M, Vellodi A. Randomized, controlled trial of miglustat in Gaucher's disease type 3. *Ann Neurol* 2008; **64**: 514-522 [PMID: 19067373 DOI: 10.1002/ana.21491]
61 **Lukina E**, Watman N, Arreguin EA, Dragosky M, Iastreb-

ner M, Rosenbaum H, Phillips M, Pastores GM, Kamath RS, Rosenthal DI, Kaper M, Singh T, Puga AC, Peterschmitt MJ. Improvement in hematological, visceral, and skeletal manifestations of Gaucher disease type 1 with oral eliglustat tartrate (Genz-112638) treatment: 2-year results of a phase 2 study. *Blood* 2010; **116**: 4095-4098 [PMID: 20713962 DOI: 10.1182/blood-2010-06-293902]

62 **Grabowski GA**. Phenotype, diagnosis, and treatment of Gaucher's disease. *Lancet* 2008; **372**: 1263-1271 [PMID: 19094956 DOI: 10.1016/S0140-6736(08)61522-6]

P- Reviewer: Palumbo B **S- Editor**: Ji FF **L- Editor**: A
E- Editor: Lu YJ

World Journal of Radiology

Submit a Manuscript: http://www.wjgnet.com/esps/
Help Desk: http://www.wjgnet.com/esps/helpdesk.aspx
DOI: 10.4329/wjr.v6.i9.669

World J Radiol 2014 September 28; 6(9): 669-676
ISSN 1949-8470 (online)

REVIEW

Role of cardiac CTA in estimating left ventricular volumes and ejection fraction

Robin Man Singh, Balkrishna Man Singh, Jawahar Lal Mehta

Robin Man Singh, Department of Medicine, University of Louisville, Louisville, KY 40202, United States
Balkrishna Man Singh, Baptist Health Heart Institute, 9501 Baptist Health Drive, Little Rock, AR 72205, United States
Jawahar Lal Mehta, Division of Cardiology, University of Arkansas for Medical Sciences, Little Rock, AR 72205, United States
Author contributions: Singh RM performed a thorough review of the subject with initial writing and review; Singh BM helped to review and edit the article; Mehta JL helped to guide the review and make constructive revision in the article.
Correspondence to: Balkrishna Man Singh, MD, FACC, Baptist Health Heart Institute, 9501 Baptist Health Drive, Suite 600, Little Rock, AR 72205, United States. bkmansingh@yahoo.com
Telephone: +1-501-3505242 Fax: +1-501-9781996
Received: January 20, 2014 Revised: July 7, 2014
Accepted: July 17, 2014
Published online: September 28, 2014

Abstract

Left ventricular ejection fraction (LVEF) is an important predictor of cardiac outcome and helps in making important diagnostic and therapeutic decisions such as the treatment of different types of congestive heart failure or implantation of devices like cardiac resynchronization therapy-defibrillator. LVEF can be measured by various techniques such as transthoracic echocardiography, contrast ventriculography, radionuclide techniques, cardiac magnetic resonance imaging and cardiac computed tomographic angiography (CTA). The development of cardiac CTA using multi-detector row CT (MDCT) has seen a very rapid improvement in the technology for identifying coronary artery stenosis and coronary artery disease in the last decade. During the acquisition, processing and analysis of data to study coronary anatomy, MDCT provides a unique opportunity to measure left ventricular volumes and LVEF simultaneously with the same data set without the need for additional contrast or radiation exposure. The development of semi-automated and automated software to measure LVEF has now added uniformity, efficiency and reproducibility of practical value in clinical practice rather than just being a research tool. This article will address the feasibility, the accuracy and the limitations of MDCT in measuring LVEF.

Key words: Stroke volume; Ventricular ejection fraction; Computerized tomography; X ray

Core tip: Left ventricular ejection fraction (LVEF) is an important predictor of cardiac morbidity and mortality. Different noninvasive and invasive techniques are now available to measure LVEF. Multi-detector row CT (MDCT) has seen a very rapid improvement in the technology for identifying coronary artery stenosis. Using the same data set without additional contrast or radiation exposure, MDCT provides a unique opportunity to measure LV volumes and LVEF with great reliability and adds incremental value. This article will address the feasibility, the accuracy and the limitations of MDCT in measuring LVEF.

Singh RM, Singh BM, Mehta JL. Role of cardiac CTA in estimating left ventricular volumes and ejection fraction. *World J Radiol* 2014; 6(9): 669-676 Available from: URL: http://www.wjgnet.com/1949-8470/full/v6/i9/669.htm DOI: http://dx.doi.org/10.4329/wjr.v6.i9.669

INTRODUCTION

Ischemic heart disease (IHD) is the leading cause of morbidity and mortality in developed countries[1]. LVEF can provide valuable diagnostic, prognostic and therapeutic information[2,3]. LVEF, LV volume and mass are inde-

pendent cardiac predictors of morbidity and mortality in patients with IHD[2-4]. LVEF is an important parameter which is needed to make clinical decisions to guide medical or surgical therapy, and assess prognosis and outcome[5]. Various noninvasive and invasive techniques have evolved over time to measure LVEF and cardiac volumes such as echocardiography[6,7], radionuclide ventriculography[8], cardiac MRI[9,10], and contrast ventriculography (CVG) in patients undergoing invasive cardiac catheterization. Echocardiography is the most commonly used technique to measure ventricular dimensions and LVEF in clinical practice, due to its ease, cost, portability, reproducibility, noninvasive nature and lack of radiation or contrast exposure. In patients undergoing cardiac computed tomographic angiography (CTA) to study CAD, it is now feasible to measure LV volume and LVEF using the same data set without the need for additional contrast or radiation exposure. Single detector row helical computed tomography (CT)[11] has been used to measure LVEF. However, this technique has limitations in studying coronary anatomy. Electron beam CT (EBCT)[12,13], with high temporal resolution of 50 milliseconds seems to give good measurement of LVEF, but the superiority of MDCT over EBCT in the detection of coronary stenosis in clinical practice has resulted in MDCT being the preferred imaging modality amongst cardiac CTA to detect coronary artery stenosis due to its ability for retrospective gating and higher spatial resolution despite lower temporal resolution. MDCT has been used to measure LVEF[14,15] and has been shown to be in good agreement with other techniques such as echocardiography, CVG, radionuclide techniques and MRI.

FEASIBILITY OF MDCT TO MEASURE LV VOLUMES AND LVEF

Rapid developments in both the hardware and software in MDCT technology have led to an increase in the use of this technology to detect CAD. The 16 slice CT scanner made it feasible to complete the cardiac scan with 1 breath hold time. However, it was the development of the 64 slice scanner that made it possible to obtain submillimeter slice thickness with a high level of spatial resolution in the X, Y and Z axis along with a significant improvement in temporal resolution. Three-dimensional isometric data sets (voxel) of nearly 0.5 mm each are now possible with the 64 slice or higher scanners due to its ability to post-process and reconstruct images in any plane without image distortion. Electrocardiographic gating during image acquisition and the ability to perform retrospective gating allows acquisition of three-dimensional volumetric data in relation to time reference and cardiac cycle, making it a truly four-dimensional data set. The development of 64 to 312 slice scanners have made it possible to complete the scan not only in one full breath, but also within 1-2 cardiac cycles, making it less prone to registration artifacts due to arrhythmias or breathing.

Developments in software technology have made it possible to post-process and create multi-planar reconstructions from these large numbers of original axial images in a very time efficient manner. This has made it possible to obtain reliable coronary anatomy imaging in most cases. Although limited by both spatial and temporal resolution compared to invasive coronary angiography, this technique of noninvasive coronary angiography by MDCT has come as close as possible to defining coronary anatomy and stenosis without the need for invasive cardiac catheterization in many cases. Hence, MDCT is being increasingly used in the evaluation of chest pain to detect CAD in appropriate subsets of patients.

Excellent visualization of bypass grafts and the 3-dimensional relationship between anomalous coronary artery origin and course have made this the test of choice for evaluation of bypass grafts and coronary anomalies. The study of pulmonary venous anatomy prior to pulmonary vein isolation ablation procedures and the integration of MDCT images in the electrophysiology laboratory help expedite the ablation procedure. Similarly, detailed analysis of the cardiac venous anatomy and identification of the lateral marginal vein are helpful in the implantation of CRT-D.

Noninvasive coronary angiography is the most common indication for cardiac CTA[16-18]. The same data set is now available to measure LV volumes and LVEF using retrospective gating and identify the end-systolic and end-diastolic frames. Typically, 8 phases of cardiac cycles are analyzed for coronary angiography, and this is usually sufficient for LVEF measurement as well. Additional phase analysis can be performed if needed. Reconstruction of the images at 0%, 12.5%, 25%, 37.5%, 50%, 62.5%, 75% and 87.5% phases of the cardiac cycle are automatically post-processed. In the manual technique, the short axis images of the LV cavity (multi-planar reconstruction) are arranged from the 0% to 87.5% phases and usually the 0% phase correlates with the end diastolic phase and the 37.5% phase correlates with the end-systolic phase. Using these multiphase reconstructions, the software can be used to play a cine loop of the LV systolic function.

In the semi-manual method, LV cavity reconstruction is carried out by multi-planar reconstruction in the 4 chamber and 2 chamber views. Using the ellipsoid volumetric calculation by tracing the endocardial border, LV volumes are measured both in end-diastole (LVEDV) and end-systole (LVESV) in 4 chamber, 2 chamber and biplane views. LVEF is measured as LVEDV - LVESV/LVEDV (Figure 1).

Contrast opacification of the LV is excellent during coronary CTA and this allows for good endocardial separation from the contrast filled LV cavity. The development of newer software which identifies the contrast density separation of the LV cavity from the myocardium has allowed semi-automated to fully automated measurements of LV volume and LVEF. One such technique allows an automated recognition and calculation of LVEDV and LVESV (Figure 2).

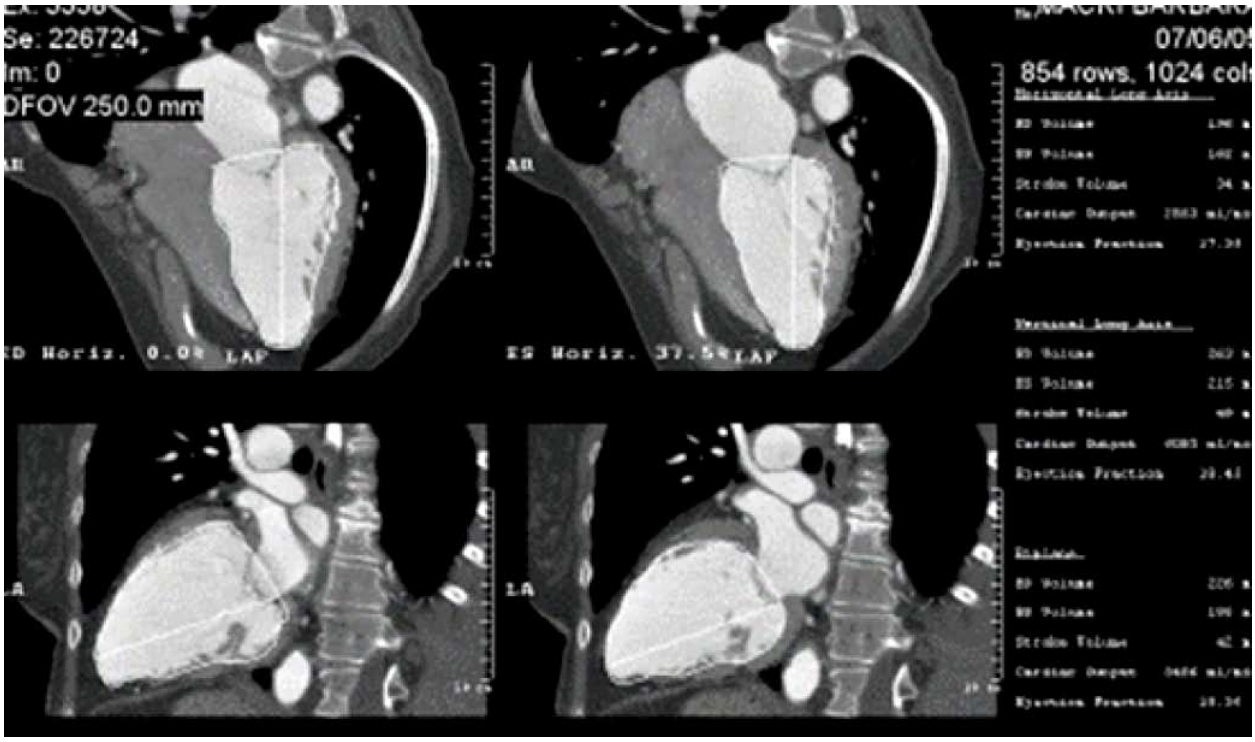

Figure 1 Multi-planar reconstruction of left ventricular cavity in 4 chamber and 2 chamber views and semi-automated calculation of left ventricular volume in both end-systole and end-diastole in biplane and 4 and 2 chamber views by the area length method. Patient with cardiomyopathy and a very low left ventricular ejection fraction of 0.20.

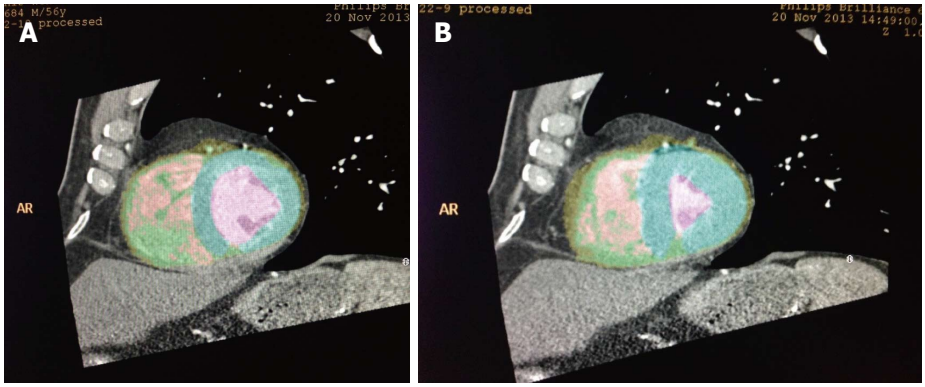

Figure 2 Automatic recognition of left ventricular cavity by automated software to calculate left ventricular volumes in end-diastole (A) and end-systole (B) to calculate left ventricular ejection fraction.

Different vendors have different software to calculate the LV volumes and LVEF. In the example shown in Figure 2, there is automatic endocardial edge detection and the software calculates the LVEDV, LVESV and LVEF as shown in Figure 3. The time-volume curve also shows the quality of the data obtained and good data are characterized by a smooth change in the LVEDV to LVESV and then back to the LVEDV as shown in Figure 3.

Figure 4 shows some compromise in the time volume data.

Radiation exposure is a major concern during cardiac computed tomographic angiography, but it can be substantially diminished by dose modulation. Dose modulation is a technique which minimizes radiation exposure during cardiac computed tomographic angiography by prospective gating at phases which are usually not important for analysis of coronary anatomy. Since most of the coronary anatomy is analyzed around 75% phase (the phase where coronary arteries appear to have the least motion), radiation exposure can be substantially diminished by more than 50% by decreasing the current (milliAmperes) of radiation exposure at phases away from the 75% phase. Despite the use of dose modulation, left ventricular contrast opacification is adequate for endocardial definition even during systole and does not seem to compromise the capacity to measure ventricular volumes both in end-diastole and end-systole, and left ventricular ejection fraction.

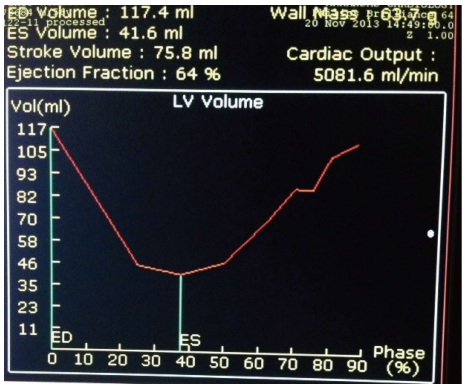

Figure 3 Time-volume curve display of left ventricular volume over different phases of the cardiac cycle (R-R interval) and calculation of left ventricular ejection fraction is displayed automatically. Please note the smooth normal curve without registration artifact.

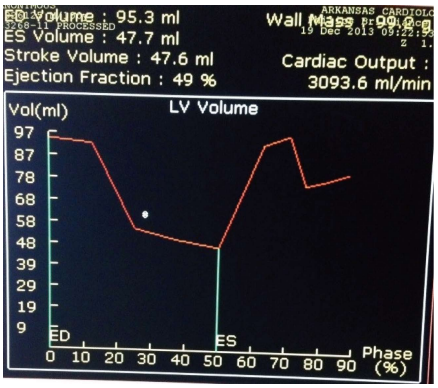

Figure 4 Shows some compromise in the time volume data as shown by the lack of smooth transition of the volume curve, and this likely represents some registration artifact towards the later part of diastole due to arrhythmias such as atrial fibrillation or frequent PVCs. This can lead to errors in the calculation of Left ventricular ejection fraction (LVEF). A quick look at the analysis of this time volume curve data is helpful to assess the quality of the data obtained for LVEF assessment and its limitations.

COMPARISON OF THE TECHNIQUES OF LV VOLUME MEASUREMENT AND LVEF BY VARIOUS METHODS

MDCT using retrospective gating allows for LV volume and LVEF measurements, which appear to have a good correlation with cardiac MRI, currently accepted as the gold standard[14,15,19-22]. LVEF measurement is possible utilizing different noninvasive and invasive techniques such as echocardiography, radionuclide techniques, cardiac MRI, and CVG. Echocardiography is the most commonly used technique to measure LVEF. Echocardiography may have technical, acoustic and operator limitations[23]. It is also subject to alteration in ventricular geometry[6,7]. Nuclear imaging using a SPECT gating also has limitations due to restrictions in both the spatial resolution and the definition of endocardial borders within the myocardium[8,24]. However, for the purpose of LVEF measurement, the estimation of LV endocardial contour is done by radioactive count, and anatomical resolution is not always so important. Prospective gating EBCT has advantages in measuring LVEF because of high temporal resolution, but has limited spatial resolution and is inferior in defining coronary anatomy compared to MDCT. Although cardiac MRI appears to be more accurate in measuring left ventricular volume and LVEF, the technique has limitations in defining coronary anatomy compared to MDCT. This modality also takes a much longer time, is more expensive, and is not feasible in some patients who have implanted devices, non-compatible with MRI. Invasive contrast ventriculography (CVG) has limitations due to the invasive nature of the test. In addition, calculation of the left ventricular volume is based on the assumption of the shape of the ventricle, and this may not be accurate in patients with an altered left ventricular geometry. MDCT is frequently used as a noninvasive coronary angiographic tool to evaluate suspected symptomatic CAD patients. Simultaneous measurement of LVEF using the same data provides a unique opportunity and can add incremental value to the test.

LV volume measurements are possible using various techniques. Current automated software allows LV volume measurement by MDCT based on short axis image reformations as in echocardiography and cardiac MRI. For calculation of LV volume measurement and LVEF, identification of the end-diastolic and end-systolic phases is needed. This is made possible by retrospective gating and post-processing of the images at various phases. In our experience, phase reconstructions at 12.5% phase apart seem to suffice, but reconstructions at every 5% phase of the R-R interval can also be done, but will be more time-consuming. Short axis images at the mid ventricular level are obtained in a semi-automated technique. In the current automated software, end-systolic and end-diastolic short axis images are identified automatically as noted in Figure 2. LV volumes and LVEF are then measured automatically as shown in Figure 3.

The LV volume and EF can be measured by different methods depending on the technique used. The area length method is a technique used primarily in invasive left ventriculography and in echocardiography, as an ellipsoid model is used to measure the LV volume. This technique can also be used in some semi-automated techniques in MDCT using volume measurements in four chamber, two chamber and biplane views. The Simpson method is also commonly used in cardiac MRI, EBCT, MDCT and echocardiography.

The automated technique in MDCT, as shown in Figure 2, employs a threshold-based region growing algorithm. This allows identification of the cardiac chambers and their volume based on the separation of myocardium from LV cavity based on the separation of contrast and tissue signal density. LV volume measurements based on this method do not depend on geometric assumptions and are more accurate than area length method. Since cardiac CTA by MDCT is carried out primarily for coronary angiography, the current technique, volume and timing of contrast injection along with saline bolus allows

for good opacification of the LV. The use of 64 slice or higher MDCT with rapid scan times provide superior results. The automated technique seems to work well even with dose modulation without any limitations of the detection of the contrast edge. Once the LVEDV and LVESV are measured, LVEF is calculated as discussed earlier. The time-volume curve allows the display of LV volume change over the different phases which provide additional qualitative information about the study. It can identify limitations due to arrhythmias, poor contrast opacification or obesity.

ACCURACY OF MDCT IN MEASURING LVEF

In our study of 52 patients, we compared the 16 row detector MDCT with TTE to measure LV volume and LVEF and found MDCT to be a useful tool for measuring LVEF[25]. Biplane measurements by these two techniques correlated better for LV volumes and LVEF, but MDCT gave higher values compared to TTE and this has also been shown in other studies using 64 slice[26,27]. Many other subsequent studies have found MDCT to be a useful tool for measuring LVEF when compared with TTE.

The feasibility of accurate assessment of LVEF and volume has been shown using a single heartbeat 320-row MDCT detector[28]. Similarly in a comparison of 128 slice CT compared to echocardiography, MDCT provided comparable results to echocardiography for LVEF and LV volumes, although LV volume was overestimated by MDCT compared to echocardiography[29]. A recent study using a head to head comparison of LVEF measurement with 64-slice MDCT, biplane LV CVG and both 2D and 3D TTE found 64-slice MDCT to be more accurate than LV CVG and TTE. This study used cardiac MRI as the reference standard for measuring LVEF[30]. However, it should be noted that gadolinium-enhanced cardiac MRI carries a risk of nephrogenic systemic fibrosis in patients with renal failure, and is, thus a limiting factor in this patient population, just as contrast-induced nephropathy would be a concern with MDCT in some patients.

Semi-automatic software to measure LV volume by MDCT has been found to have good reproducibility for LVEF measurement, but it is important to understand the limitations of MDCT in semi-automatic and automatic measurement of LVEF[31].

In a comparison of SPECT versus MDCT to measure LVEF in 292 patients, MDCT gave significantly higher LVEF compared to SPECT and the values may not be interchangeable between different methods of measurement[32]. In another small study of 15 patients, MDCT compared well with biplane LV CVG for measuring LVEF[33]. There appears to be a minor systematic overestimation of LVEDV and LVESV, and underestimation of EF of 2.1% by MDCT compared to cardiac MRI[34]. LVEF measurement in a wide spectrum of LV dysfunction requires further validation compared to other techniques such as EBCT[35]. Studies comparing LVEF measurement by simultaneous multimodality images such as echocardiography, LV CVG and SPECT are limited[36].

A recent systematic review and meta-analysis of 27 eligible studies concluded that MDCT can measure LVEF accurately compared to MRI and TTE[37]. Twelve studies compared MDCT with MRI and 15 studies compared MDCT with TTE to measure LVEF in this meta-analysis, and MDCT appears to be a useful tool for measuring LVEF in patients undergoing coronary CTA. Simultaneous measurement of LVEF at the time of coronary CTA by MDCT seems to provide additional incremental prognostic value[38].

LIMITATIONS OF MDCT IN LVEF MEASUREMENT AND TECHNIQUES TO IMPROVE THESE LIMITATIONS

It should be noted that the current limitations of MDCT do not favor the use of MDCT for the sole purpose of LVEF measurement. This is due to a myriad of reasons, including radiation and contrast exposure, cost, risks of iodine allergy and potential renal failure. The risk of contrast induced-nephropathy is increased in patients with preexisting renal dysfunction, diabetes, heart failure, increased age and other comorbid conditions. The high volume of contrast administered for cardiac CTA may also increase the risk of contrast-induced nephropathy in high risk patients. Pretest risk assessment and good hydration are important in all patients undergoing a contrast study such as cardiac CTA, and for that reason many patients may not be candidates for cardiac CTA for fear of contrast-induced nephropathy and its consequences. The technique has limitations in patients with obesity, renal failure, arrhythmias and difficult breath hold time On the other hand, simultaneous measurements of LVEF in patients undergoing cardiac CTA for noninvasive coronary angiography are feasible, reproducible, and fairly accurate compared to other modalities.

High temporal and spatial resolution is needed for accurate measurement of LVEF[39]. MDCT has good spatial resolution, but has a limited temporal resolution of 125-250 milliseconds compared to EBCT[40] or MRI and can cause motion artifacts[41]. Image quality in patients with higher heart rate may be of poor quality due to limited temporal resolution and may compromise the accuracy[42,43].

MDCT with temporal resolution of 20 milliseconds would be desirable to avoid motion artifacts, but is not yet feasible with current technology[44]. In the early studies using 4 row MDCT, LVEF measurement was underestimated due to poor temporal resolution, and overestimation of LVESV was found as compared to LV CVG and MRI[45,46].

An increase in temporal resolution is a desirable goal to improve the quality of MDCT, and two strategies have been utilized so far. First, gantry rotation time is shortened with the new scanners[16,47,48] and secondly, more

gantry rotations allowing more R-R intervals for image reconstruction are available using multi-segmental image reconstruction algorithms[49,50]. Multiple cardiac cycles are used to create image reconstruction in this method, and thus may improve temporal resolution to less than 100 milliseconds. However, significant variations in the R-R cycle could be a limitation in the multi-segmental image reconstruction due to non-uniformity of ventricular contraction.

Rapid gantry rotations of up to 0.33 s per rotation attained with newer MDCTs can also improve the temporal resolution[51]. Dual source CT can also increase the temporal resolution to 83 milliseconds in single segmental reconstructions[52].

Lower heart rates are needed to obtain better images by MDCT to evaluate coronary anatomy, and consequently beta-blockers are frequently used to slow the heart rate during image acquisition. This introduces the effect of heart rate change and negative inotropic effects on LVEF measurement[42]. Dual-source CT is less dependent on the heart rate and may improve LVEF measurement. The patients with arrhythmia such as atrial fibrillation and frequent premature ventricular complexes may produce significant registration artifacts and may introduce error in the calculation of LVEF. However, with the use of recent higher slice MDCT, this should be less of a concern as most of the data acquisition can be completed within one or two cardiac cycles.

Techniques to reduce radiation exposure are possible using higher detector rows and faster rotation times. Reduced tube current during unnecessary cardiac phase (dose modulation) helps reduce radiation[53]. Since most of the coronary anatomy analysis is done in late diastole close to 75% phase, this normally does not compromise analysis of the coronary anatomy. The degree of contrast density separation of the LV cavity from the myocardium is adequate even with dose modulation in systole for the purpose of LVESV calculation and should not compromise LVEF measurement. Analysis of the quality of data and the LV time volume curve may be helpful in assessing the quality of the study.

LVEF measurement by MDCT is based on a volumetric data set. LVEF measurement should be less susceptible to error in patients with LV enlargement or deformity. LVEF measurement by MDCT correlates well with MRI in patients with LV dysfunction or LV dilation[54].

Cardiac MRI is considered the gold standard for the measurement of LV volume, LVEF and regional wall motion assessment. Lack of radiation and contrast exposure, along with higher temporal resolution are advantageous. However, MDCT requires a short breath hold time, and can be performed even in patients with pacemakers and implanted defibrillators. In contrast to MDCT using single breath hold image acquisition, cardiac MRI needs multiple short breath holds for cine MRI. Both techniques are susceptible to arrhythmias with image degradation. In addition, MDCT is superior to cardiac MRI for coronary imaging due to a higher spatial resolution, and it is in this group of patients that LVEF measurement can be performed to provide additional clinical information. Processing time may also be a limiting factor in some cases, but now with the use of automated software, the LVEF calculation is faster and likely to improve further.

CONCLUSION

LVEF measurement at the time of cardiac CTA for the study of coronary anatomy using MDCT seems reasonable given the feasibility, reproducibility, and accuracy of the data. This information can be obtained at the time of coronary imaging without the need for additional radiation or contrast exposure. Developments in hardware, software and work stations, along with the availability of automated techniques to measure LVESV and LVEDV have made this technique time efficient. The use of MDCT for the sole purpose of LVEF measurement is not reasonable at this time given the radiation exposure, contrast exposure and cost. Instead, this should be used as a complimentary technique to measure LVEF in patients undergoing cardiac CTA for noninvasive coronary angiography.

REFERENCES

1 **Murray CJ**, Lopez AD. Alternative projections of mortality and disability by cause 1990-2020: Global Burden of Disease Study. *Lancet* 1997; **349**: 1498-1504 [PMID: 9167458 DOI: 10.1016/S0140-6736(96)07492-2]

2 **Sanz G**, Castañer A, Betriu A, Magriña J, Roig E, Coll S, Paré JC, Navarro-López F. Determinants of prognosis in survivors of myocardial infarction: a prospective clinical angiographic study. *N Engl J Med* 1982; **306**: 1065-1070 [PMID: 7070402 DOI: 10.1056/NEJM198205063061801]

3 **White HD**, Norris RM, Brown MA, Brandt PW, Whitlock RM, Wild CJ. Left ventricular end-systolic volume as the major determinant of survival after recovery from myocardial infarction. *Circulation* 1987; **76**: 44-51 [PMID: 3594774 DOI: 10.1161/01.CIR.76.1.44]

4 **Hammermeister KE**, DeRouen TA, Dodge HT. Variables predictive of survival in patients with coronary disease. Selection by univariate and multivariate analyses from the clinical, electrocardiographic, exercise, arteriographic, and quantitative angiographic evaluations. *Circulation* 1979; **59**: 421-430 [PMID: 761323]

5 Risk stratification and survival after myocardial infarction. *N Engl J Med* 1983; **309**: 331-336 [PMID: 6866068]

6 **Buck T**, Hunold P, Wentz KU, Tkalec W, Nesser HJ, Erbel R. Tomographic three-dimensional echocardiographic determination of chamber size and systolic function in patients with left ventricular aneurysm: comparison to magnetic resonance imaging, cineventriculography, and two-dimensional echocardiography. *Circulation* 1997; **96**: 4286-4297 [PMID: 9416895 DOI: 10.1161/01.CIR.96.12.4286]

7 **Qin JX**, Jones M, Shiota T, Greenberg NL, Tsujino H, Firstenberg MS, Gupta PC, Zetts AD, Xu Y, Ping Sun J, Cardon LA, Odabashian JA, Flamm SD, White RD, Panza JA, Thomas JD. Validation of real-time three-dimensional echocardiography for quantifying left ventricular volumes in the presence of a left ventricular aneurysm: in vitro and in vivo studies. *J Am Coll Cardiol* 2000; **36**: 900-907 [PMID: 10987618 DOI: 10.1016/S0735-1097(00)00793-2]

8 **Bavelaar-Croon CD**, Kayser HW, van der Wall EE, de Roos A, Dibbets-Schneider P, Pauwels EK, Germano G, Atsma DE. Left ventricular function: correlation of quantitative gated SPECT and MR imaging over a wide range of values. *Radiology* 2000; **217**: 572-575 [PMID: 11058662 DOI: 10.1148/radiology.217.2.r00nv15572]

9 **Pattynama PM**, Lamb HJ, van der Velde EA, van der Wall EE, de Roos A. Left ventricular measurements with cine and spin-echo MR imaging: a study of reproducibility with variance component analysis. *Radiology* 1993; **187**: 261-268 [PMID: 8451425]

10 **Bellenger NG**, Burgess MI, Ray SG, Lahiri A, Coats AJ, Cleland JG, Pennell DJ. Comparison of left ventricular ejection fraction and volumes in heart failure by echocardiography, radionuclide ventriculography and cardiovascular magnetic resonance; are they interchangeable? *Eur Heart J* 2000; **21**: 1387-1396 [PMID: 10952828 DOI: 10.1053/euhj.2000.2011]

11 **Mochizuki T**, Murase K, Higashino H, Koyama Y, Doi M, Miyagawa M, Nakata S, Shimizu K, Ikezoe J. Two- and three-dimensional CT ventriculography: a new application of helical CT. *AJR Am J Roentgenol* 2000; **174**: 203-208 [PMID: 10628479]

12 **Lipton MJ**, Higgins CB, Farmer D, Boyd DP. Cardiac imaging with a high-speed Cine-CT Scanner: preliminary results. *Radiology* 1984; **152**: 579-582 [PMID: 6540463]

13 **Lipton MJ**, Farmer DW, Killebrew EJ, Bouchard A, Dean PB, Ringertz HG, Higgins CB. Regional myocardial dysfunction: evaluation of patients with prior myocardial infarction with fast CT. *Radiology* 1985; **157**: 735-740 [PMID: 4059561]

14 **Juergens KU**, Grude M, Maintz D, Fallenberg EM, Wichter T, Heindel W, Fischbach R. Multi-detector row CT of left ventricular function with dedicated analysis software versus MR imaging: initial experience. *Radiology* 2004; **230**: 403-410 [PMID: 14668428 DOI: 10.1148/radiol.2302030042]

15 **Grude M**, Juergens KU, Wichter T, Paul M, Fallenberg EM, Muller JG, Heindel W, Breithardt G, Fischbach R. Evaluation of global left ventricular myocardial function with electrocardiogram-gated multidetector computed tomography: comparison with magnetic resonance imaging. *Invest Radiol* 2003; **38**: 653-661 [PMID: 14501493 DOI: 10.1097/01.rli.0000077070.40713.76]

16 **Raff GL**, Gallagher MJ, O'Neill WW, Goldstein JA. Diagnostic accuracy of noninvasive coronary angiography using 64-slice spiral computed tomography. *J Am Coll Cardiol* 2005; **46**: 552-557 [PMID: 16053973 DOI: 10.1016/j.jacc.2005.05.056]

17 **Achenbach S**, Giesler T, Ropers D, Ulzheimer S, Derlien H, Schulte C, Wenkel E, Moshage W, Bautz W, Daniel WG, Kalender WA, Baum U. Detection of coronary artery stenoses by contrast-enhanced, retrospectively electrocardiographically-gated, multislice spiral computed tomography. *Circulation* 2001; **103**: 2535-2538 [PMID: 11382719 DOI: 10.1161/01.CIR.103.21.2535]

18 **Ropers D**, Baum U, Pohle K, Anders K, Ulzheimer S, Ohnesorge B, Schlundt C, Bautz W, Daniel WG, Achenbach S. Detection of coronary artery stenoses with thin-slice multi-detector row spiral computed tomography and multiplanar reconstruction. *Circulation* 2003; **107**: 664-666 [PMID: 12578863 DOI: 10.1161/01.CIR.0000055738.31551.A9]

19 **Halliburton SS**, Petersilka M, Schvartzman PR, Obuchowski N, White RD. Evaluation of left ventricular dysfunction using multiphasic reconstructions of coronary multislice computed tomography data in patients with chronic ischemic heart disease: validation against cine magnetic resonance imaging. *Int J Cardiovasc Imaging* 2003; **19**: 73-83 [PMID: 12602485 DOI: 10.1023/A:1021793420007]

20 **Koch K**, Oellig F, Kunz P, Bender P, Oberholzer K, Mildenberger P, Hake U, Kreitner KF, Thelen M. [Assessment of global and regional left ventricular function with a 16-slice spiral-CT using two different software tools for quantitative functional analysis and qualitative evaluation of wall motion changes in comparison with magnetic resonance imaging]. *Rofo* 2004; **176**: 1786-1793 [PMID: 15573290 DOI: 10.1055/s-2004-813730]

21 **Mahnken AH**, Koos R, Katoh M, Spuentrup E, Busch P, Wildberger JE, Kühl HP, Günther RW. Sixteen-slice spiral CT versus MR imaging for the assessment of left ventricular function in acute myocardial infarction. *Eur Radiol* 2005; **15**: 714-720 [PMID: 15682266 DOI: 10.1007/s00330-004-2592-x]

22 **Heuschmid M**, Rothfuss J, Schröder S, Küttner A, Fenchel M, Stauder N, Mahnken AH, Burgstahler C, Miller S, Claussen CD, Kopp AF. [Left ventricular functional parameters: comparison of 16-slice spiral CT with MRI]. *Rofo* 2005; **177**: 60-66 [PMID: 15657821 DOI: 10.1055/s-2004-813768]

23 **Malm S**, Frigstad S, Sagberg E, Larsson H, Skjaerpe T. Accurate and reproducible measurement of left ventricular volume and ejection fraction by contrast echocardiography: a comparison with magnetic resonance imaging. *J Am Coll Cardiol* 2004; **44**: 1030-1035 [PMID: 15337215 DOI: 10.1016/j.jacc.2004.05.068]

24 **Manrique A**, Faraggi M, Véra P, Vilain D, Lebtahi R, Cribier A, Le Guludec D. 201Tl and 99mTc-MIBI gated SPECT in patients with large perfusion defects and left ventricular dysfunction: comparison with equilibrium radionuclide angiography. *J Nucl Med* 1999; **40**: 805-809 [PMID: 10319754]

25 **Bansal D**, Singh RM, Sarkar M, Sureddi R, Mcbreen KC, Griffis T, Sinha A, Mehta JL. Assessment of left ventricular function: comparison of cardiac multidetector-row computed tomography with two-dimension standard echocardiography for assessment of left ventricular function. *Int J Cardiovasc Imaging* 2008; **24**: 317-325 [PMID: 17701445 DOI: 10.1007/s10554-007-9252-6]

26 **Lessick J**, Ghersin E, Abadi S, Yalonetsky S. Accuracy of the long-axis area-length method for the measurement of left ventricular volumes and ejection fraction using multidetector computed tomography. *Can J Cardiol* 2008; **24**: 685-689 [PMID: 18787718 DOI: 10.1016/S0828-282X(08)70666-4]

27 **Ko SM**, Kim YJ, Park JH, Choi NM. Assessment of left ventricular ejection fraction and regional wall motion with 64-slice multidetector CT: a comparison with two-dimensional transthoracic echocardiography. *Br J Radiol* 2010; **83**: 28-34 [PMID: 19546180 DOI: 10.1259/bjr/38829806]

28 **de Graaf FR**, Schuijf JD, van Velzen JE, Nucifora G, Kroft LJ, de Roos A, Schalij MJ, Jukema JW, van der Wall EE, Bax JJ. Assessment of global left ventricular function and volumes with 320-row multidetector computed tomography: A comparison with 2D-echocardiography. *J Nucl Cardiol* 2010; **17**: 225-231 [PMID: 19953354 DOI: 10.1007/s12350-009-9173-y]

29 **Lim SJ**, Choo KS, Park YH, Kim JS, Kim JH, Chun KJ, Jeong DW. Assessment of left ventricular function and volume in patients undergoing 128-slice coronary CT angiography with ECG-based maximum tube current modulation: a comparison with echocardiography. *Korean J Radiol* 2011; **12**: 156-162 [PMID: 21430931 DOI: 10.3348/kjr.2011.12.2.156]

30 **Greupner J**, Zimmermann E, Grohmann A, Dübel HP, Althoff TF, Borges AC, Rutsch W, Schlattmann P, Hamm B, Dewey M. Head-to-head comparison of left ventricular function assessment with 64-row computed tomography, biplane left cineventriculography, and both 2- and 3-dimensional transthoracic echocardiography: comparison with magnetic resonance imaging as the reference standard. *J Am Coll Cardiol* 2012; **59**: 1897-1907 [PMID: 22595410 DOI: 10.1016/j.jacc.2012.01.046]

31 **van Ooijen PM**, de Jonge GJ, Oudkerk M. Informatics in radiology: postprocessing pitfalls in using CT for automatic and semiautomatic determination of global left ventricular function. *Radiographics* 2012; **32**: 589-599 [PMID: 22323618 DOI: 10.1148/rg.322115058]

32 **Abadi S**, Brook OR, Rispler S, Frenkel A, Engel A, Keidar Z. Hybrid cardiac SPECT/64-slice CTA-derived LV function

parameters: correlation and reproducibility assessment. *Eur J Radiol* 2010; **75**: 154-158 [PMID: 19443161 DOI: 10.1016/j.ejrad.2009.04.039]
33 **Chaosuwannakit N**, Rerkpattanapipat P, Wangsuphachart S, Srimahachota S. Reliability of the evaluation for left ventricular ejection fraction by ECG-gated multi-detector CT (MDCT): comparison with biplane cine left ventriculography. *J Med Assoc Thai* 2007; **90**: 532-538 [PMID: 17427532]
34 **Dewey M**, Müller M, Teige F, Hamm B. Evaluation of a semiautomatic software tool for left ventricular function analysis with 16-slice computed tomography. *Eur Radiol* 2006; **16**: 25-31 [PMID: 15965660 DOI: 10.1007/s00330-005-2817-7]
35 **Baik HK**, Budoff MJ, Lane KL, Bakhsheshi H, Brundage BH. Accurate measures of left ventricular ejection fraction using electron beam tomography: a comparison with radionuclide angiography, and cine angiography. *Int J Card Imaging* 2000; **16**: 391-398 [PMID: 11215924 DOI: 10.1023/A:1026536510821]
36 **Yamamuro M**, Tadamura E, Kubo S, Toyoda H, Nishina T, Ohba M, Hosokawa R, Kimura T, Tamaki N, Komeda M, Kita T, Konishi J. Cardiac functional analysis with multidetector row CT and segmental reconstruction algorithm: comparison with echocardiography, SPECT, and MR imaging. *Radiology* 2005; **234**: 381-390 [PMID: 15670995 DOI: 10.1148/radiol.2342031271]
37 **Asferg C**, Usinger L, Kristensen TS, Abdulla J. Accuracy of multi-slice computed tomography for measurement of left ventricular ejection fraction compared with cardiac magnetic resonance imaging and two-dimensional transthoracic echocardiography: a systematic review and meta-analysis. *Eur J Radiol* 2012; **81**: e757-e762 [PMID: 22381439 DOI: 10.1016/j.ejrad.2012.02.002]
38 **de Graaf FR**, van Werkhoven JM, van Velzen JE, Antoni ML, Boogers MJ, Kroft LJ, de Roos A, Schalij MJ, Jukema JW, van der Wall EE, Schuijf JD, Bax JJ. Incremental prognostic value of left ventricular function analysis over noninvasive coronary angiography with multidetector computed tomography. *J Nucl Cardiol* 2010; **17**: 1034-1040 [PMID: 20694585 DOI: 10.1007/s12350-010-9277-4]
39 **Setser RM**, Fischer SE, Lorenz CH. Quantification of left ventricular function with magnetic resonance images acquired in real time. *J Magn Reson Imaging* 2000; **12**: 430-438 [PMID: 10992310]
40 **Lipton MJ**. Quantitation of cardiac function by cine-CT. *Radiol Clin North Am* 1985; **23**: 613-626 [PMID: 3877947]
41 **Hong C**, Becker CR, Huber A, Schoepf UJ, Ohnesorge B, Knez A, Brüning R, Reiser MF. ECG-gated reconstructed multi-detector row CT coronary angiography: effect of varying trigger delay on image quality. *Radiology* 2001; **220**: 712-717 [PMID: 11526271]
42 **Schroeder S**, Kopp AF, Kuettner A, Burgstahler C, Herdeg C, Heuschmid M, Baumbach A, Claussen CD, Karsch KR, Seipel L. Influence of heart rate on vessel visibility in noninvasive coronary angiography using new multislice computed tomography: experience in 94 patients. *Clin Imaging* 2002; **26**: 106-111 [PMID: 11852217]
43 **Sechtem U**, Pflugfelder P, Higgins CB. Quantification of cardiac function by conventional and cine magnetic resonance imaging. *Cardiovasc Intervent Radiol* 1987; **10**: 365-373 [PMID: 3123062]
44 **Ritchie CJ**, Godwin JD, Crawford CR, Stanford W, Anno H, Kim Y. Minimum scan speeds for suppression of motion artifacts in CT. *Radiology* 1992; **185**: 37-42 [PMID: 1523332]
45 **Wintersperger BJ**, Hundt W, Knez A. Left ventricular systolic function assessed by ECG gated multirow-detector spiral computed tomography (multi-detector row CT): comparison to ventriculography. *Eur Radiol* 2002; **12**: S192
46 **Lüders F**, Fischbach R, Seifarth H, Wessling J, Heindel W, Juergens KU. [Dual-source computed tomography: effect on regional and global left ventricular function assessment compared to magnetic resonance imaging]. *Rofo* 2009; **181**: 962-969 [PMID: 19517343]
47 **Leber AW**, Knez A, von Ziegler F, Becker A, Nikolaou K, Paul S, Wintersperger B, Reiser M, Becker CR, Steinbeck G, Boekstegers P. Quantification of obstructive and nonobstructive coronary lesions by 64-slice computed tomography: a comparative study with quantitative coronary angiography and intravascular ultrasound. *J Am Coll Cardiol* 2005; **46**: 147-154 [PMID: 15992649 DOI: 10.1016/j.jacc.2005.03.071]
48 **Heuschmid M**, Küttner A, Flohr T, Wildberger JE, Lell M, Kopp AF, Schröder S, Baum U, Schaller S, Hartung A, Ohnesorge B, Claussen CD. [Visualization of coronary arteries in CT as assessed by a new 16 slice technology and reduced gantry rotation time: first experiences]. *Rofo* 2002; **174**: 721-724 [PMID: 12063601 DOI: 10.1055/s-2002-32227]
49 **Kachelriess M**, Kalender WA. Electrocardiogram-correlated image reconstruction from subsecond spiral computed tomography scans of the heart. *Med Phys* 1998; **25**: 2417-2431 [PMID: 9874836 DOI: 10.1118/1.598453]
50 **Boese JM**, Bahner ML, Albers J, van Kaick G. [Optimizing temporal resolution in CT with retrospective ECG gating]. *Radiologe* 2000; **40**: 123-129 [PMID: 10758625 DOI: 10.1007/s001170050020]
51 **Nieman K**, Cademartiri F, Lemos PA, Raaijmakers R, Pattynama PM, de Feyter PJ. Reliable noninvasive coronary angiography with fast submillimeter multislice spiral computed tomography. *Circulation* 2002; **106**: 2051-2054 [PMID: 12379572 DOI: 10.1161/01.CIR.0000037222.58317.3D]
52 **Achenbach S**, Ropers D, Kuettner A, Flohr T, Ohnesorge B, Bruder H, Theessen H, Karakaya M, Daniel WG, Bautz W, Kalender WA, Anders K. Contrast-enhanced coronary artery visualization by dual-source computed tomography--initial experience. *Eur J Radiol* 2006; **57**: 331-335 [PMID: 16426789 DOI: 10.1016/j.ejrad.2005.12.017]
53 **Jakobs TF**, Becker CR, Ohnesorge B, Flohr T, Suess C, Schoepf UJ, Reiser MF. Multislice helical CT of the heart with retrospective ECG gating: reduction of radiation exposure by ECG-controlled tube current modulation. *Eur Radiol* 2002; **12**: 1081-1086 [PMID: 11976849 DOI: 10.1007/s00330-001-1278-x]
54 **Barkhausen J**, Ruehm SG, Goyen M, Buck T, Laub G, Debatin JF. MR evaluation of ventricular function: true fast imaging with steady-state precession versus fast low-angle shot cine MR imaging: feasibility study. *Radiology* 2001; **219**: 264-269 [PMID: 11274568 DOI: 10.1148/radiology.219.1.r01ap12264]

P- Reviewer: Lai S, Nagamachi S **S- Editor**: Wen LL
L- Editor: Webster JR **E- Editor**: Lu YJ

World Journal of Radiology

Submit a Manuscript: http://www.wjgnet.com/esps/
Help Desk: http://www.wjgnet.com/esps/helpdesk.aspx
DOI: 10.4329/wjr.v6.i9.677

World J Radiol 2014 September 28; 6(9): 677-692
ISSN 1949-8470 (online)

REVIEW

Vascular anomalies: A pictorial review of nomenclature, diagnosis and treatment

John L Nosher, Philip G Murillo, Mark Liszewski, Vyacheslav Gendel, Christopher E Gribbin

John L Nosher, Philip G Murillo, Mark Liszewski, Vyacheslav Gendel, Christopher E Gribbin, Department of Radiology, Rutgers Medical School, Robert Wood Johnson University Hospital, New Brunwick, NJ 08901, United States
Author contributions: All authors contributed textual and illustrative material to this paper.
Correspondence to: John L Nosher, MD, Department of Radiology, Rutgers Medical School, Robert Wood Johnson University Hospital, 1 Robert Wood Johnson Place, MEB404, New Brunswick, NJ 08901, United States. vgendel@gmail.com
Telephone: +1-732-8283000
Received: January 25, 2014 Revised: July 13, 2014
Accepted: July 25, 2014
Published online: September 28, 2014

Abstract

Vascular anomalies, including vascular malformations and tumors, are frequently straightforward to detect; however, accurate diagnosis and appropriate treatment are often challenging. Misdiagnosis of these lesions can lead clinicians in the wrong direction when treating these patients, which can have unfavorable results. This review presents an overview of the classification systems that have been developed for the diagnosis of vascular lesions with a focus on the imaging characteristics. Pictorial examples of each lesion on physical examination, as well as non-invasive and minimally invasive imaging are presented. An overview of the endovascular treatment of these lesions is also given. In some cases, vascular anomalies may be associated with an underlying syndrome and several of the most commonly encountered syndromes are discussed. Understanding of the classification systems, familiarity with the treatment options and knowledge of the associated syndromes are essential for all physicians working with this patient population. The approach to the described entities necessitates an organized multi-disciplinary team effort, with diagnostic imaging playing an increasingly important role in the proper diagnosis and a combined interventional radiologic and surgical treatment method showing promising results.

Key words: Vascular malformation; Lymphatic malformation; Overgrowth syndromes; Arteriovenous malformation; Hemangioma

Core tip: Accurate diagnosis and appropriate treatment of vascular anomalies are challenging endeavors. This review presents a summary of the classification systems for vascular anomalies, a review of endovascular treatment options, and a brief look at several associated syndromes. Understanding of the diagnosis and treatment of these lesions is essential for all physicians working with this patient population.

Nosher JL, Murillo PG, Liszewski M, Gendel V, Gribbin CE. Vascular anomalies: A pictorial review of nomenclature, diagnosis and treatment. *World J Radiol* 2014; 6(9): 677-692 Available from: URL: http://www.wjgnet.com/1949-8470/full/v6/i9/677.htm DOI: http://dx.doi.org/10.4329/wjr.v6.i9.677

INTRODUCTION

Anatomist and obstetrician William Hunter first described vascular anomalies in the mid-18th century in the context of iatrogenic creation of arteriovenous fistulas by phlebotomists[1]. Over the next century, description of these and more complex vascular lesions was furthered by the work of Dupuytren, Virchow, and others but the lack of a cohesive system of classification led to confusion, hampering further understanding of these entities. Since that time, categorization of these lesions has advanced from primitive descriptions and disorganized nomenclatures to a more a structured catalogue of classification. Mulliken

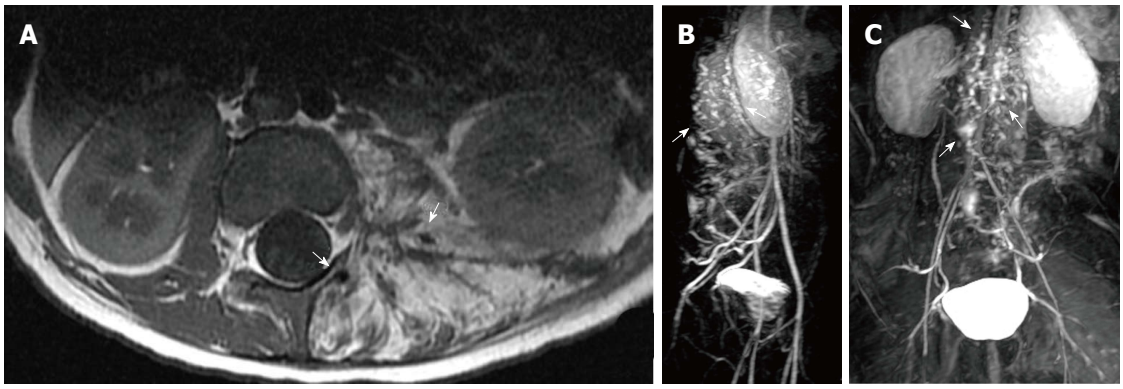

Figure 1 Kaposiform hemangioendothelioma. A: Magnetic resonance (MR) of the retroperitoneum demonstrating infiltrative tumor with fat and interspersed signal void (arrows) consistent with high flow arterial signal; B, C: MR angiogram demonstrating arteriovenous shunting within the tumor (arrows).

and Glowacki pioneered this transformation[2], while the Hamburg classification system further refined it[3].

Early attempts at classification were based on the pathological appearance of the lesions without consideration for underlying biologic behavior. Terms such as "erectile tumors," "naevus maternus," and "stigma metrocelis" were applied without clear delineation[2]. It wasn't until 1982, when Mulliken and Glowacki introduced a classification system rooted in the pathophysiology of these lesions that much of the confusion surrounding these lesions was clarified[2]. This system divided vascular anomalies into two categories: vascular tumors (hemangiomas) and vascular malformations. This standard was adopted by the International Society for the Study of Vascular Anomalies (ISSVA)[3,4] and continues to be embraced by many clinicians in current practice. Subsequent modifications to this classification system have included the addition of other rare vascular tumors distinct from hemangiomas, including tufted angioma, Kaposiform hemangioendothelioma, angiosarcoma and others. With these additions, vascular anomalies continue to be divided into two categories: vascular tumors, which include hemangiomas, and vascular malformations. Several years later, the Hamburg classification system adopted an embryologic perspective to further aid in the classification of vascular malformations[3]. Lesions are identified first based on the prevailing vascular structure involved- arterial, venous, lymphatic, or capillary, also considering arteriovenous shunting and combined vascular defects[3]. The embryological background of the lesion is then considered for additional delineation[5]. Extratruncular lesions result from developmental arrest in the early reticular embryonic stage, prior to the development of vascular trunks. Extratruncular malformations may be infiltrating and diffuse or limited and localized. Truncular lesions result from a defect occurring during the stage of fetal development following the reticular stage, as the vascular trunks are developing. Truncular forms develop from stenosis or obstruction of vascular trunks, with resulting hypoplasia, or dilatation of vascular trunks, which in turn may be localized or diffuse[6].

VASCULAR TUMORS

In their seminal paper, Mulliken and Glowacki[2], reported vascular tumors - then referred to as hemangiomas - to demonstrate specific mitotic activity and eventual involution, setting them apart from vascular malformations. Much has been discovered about vascular tumors, and while beyond the scope of this discussion, this information encompasses a variety of different entities. These include but are not limited to infantile hemangiomas and rapidly involuting and noninvoluting congenital hemangiomas, as well as more aggressive tumors, such as tufted angiomas, Kaposiform hemangioendotheliomas, and angiosarcomas.

Infantile hemangiomas are the most common tumor of infancy and childhood affecting up to 12% of children with a female preponderance[7,8]. Histologically, these lesions stain positively for glucose transporter-1 protein (GLUT-1). Tumors typically appear between 2 wk and 2 mo of life and follow a proliferating phase, an involuting phase, and a state of complete involution[9,10].

Congenital hemangiomas are tumors that demonstrate intrauterine development with growth completed at birth[11]. These lesions more commonly affect the extremities, close to the joint, or on the head and neck, close to the ear[12]. In contrast to infantile hemangiomas, these lesions stain negative for GLUT-1[11,12]. Lesions are divided into two categories based on biologic activity: rapidly involuting congenital hemangiomas (RICHs) and noninvoluting congenital hemangiomas (NICHs). RICHs typically regress within 6-14 mo while NICHs do not regress and have a tendency for progression, usually leading to surgical excision[12].

Kaposiform hemangioendothelioma (Figure 1) is a rare vascular neoplasm, which usually arises in the skin and infiltrates into the deeper tissues over time. Most cases are associated with consumptive coagulopathy or Kasabach-Merritt Syndrome, as well as lymphangiomatosis[13].

VASCULAR MALFORMATIONS

Vascular malformations are structural lesions resulting

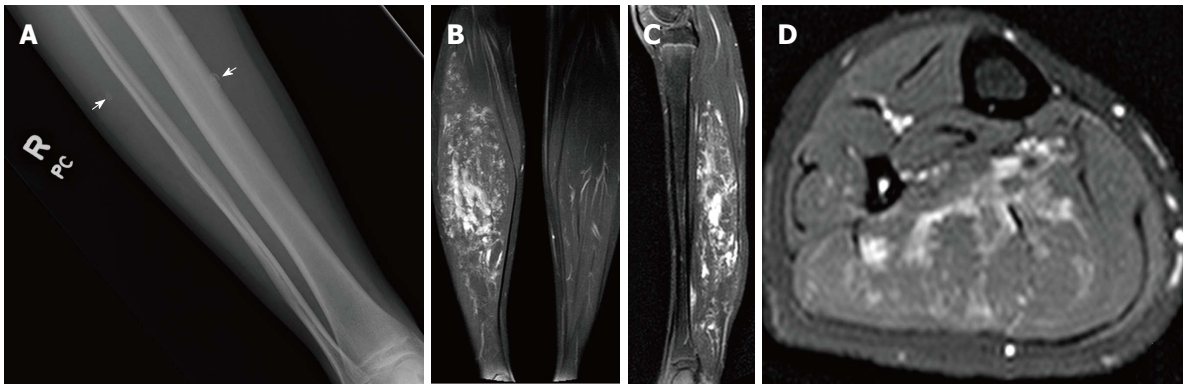

Figure 2 Low flow extratruncular venous malformation. Radiograph of the right lower leg (A) demonstrates phleboliths within the soft tissues (arrows). T2-weighted magnetic resonance images in the coronal (B), sagittal (C), and axial (D) planes demonstrate hyperintense signal within the gastrocnemius muscle due to infiltrative low flow extratruncular venous malformation.

from errors of vascular morphogenesis[2]. Differentiation of vascular malformations into high flow, low flow or mixed lesions is critical in developing treatment strategies. The distinction of truncal from extratruncal may provide insight in predicting response to treatment.

IMAGING OF VASCULAR ANOMALIES

Several noninvasive imaging modalities are useful in characterizing vascular anomalies, contributing information about lesion size, flow characteristics and relationship to adjacent structures[14]. Conventional radiography plays a minor role, though may be valuable in defining bone and joint involvement and presence of phleboliths[14] (Figure 2A). Contrast enhanced computed tomography (CT) and CT angiograph are useful in evaluating osseous involvement and phleboliths, but also provides information about enhancement, thrombosis, calcification, vascular anatomy and involvement of adjacent structures[14]. The use of ionizing radiation and relatively limited ability to provide information about flow dynamics decreases its usefulness. For these reasons ultrasonography (US) and magnetic resonance imaging (MRI) are the primary noninvasive imaging modalities used in the evaluation of vascular anomalies[15].

US is indispensable in the evaluation of superficial vascular lesions given its low cost, ease of use, high temporal and spatial resolution, and ability to evaluate flow dynamics[14,16]. With US, hemangiomas are reliably differentiated from vascular malformations based on depiction of a well-circumscribed solid mass[16]. Hemangiomas and high-flow vascular malformations, including arteriovenous malformations (AVMs) and arteriovenous fistulae (AVFs), demonstrate arterial and venous waveforms on pulsed Doppler US, but are differentiated based on a lack of associated mass in AVMs and AVFs[15,16]. AVMs and AVFs will contain multiple enlarged subcutaneous arteries and veins on grey scale and color Doppler US with associated low-resistance arterial and venous waveforms on pulsed Doppler US[15,16]. Low-flow vascular malformations, including venous and lymphatic malformations, can be differentiated from high flow lesions based on Doppler analysis. Venous malformations contain enlarged subcutaneous vessels without an associated mass, are compressible and demonstrate venous flow on color and pulsed Doppler US[16]. Lymphatic malformations are characterized by macrocystic or microcystic spaces with or without debris separated by septae. On color and pulsed Doppler US these cysts will contain no flow, however the septa may contain small arteries and veins[16]. US is limited in its ability to evaluate deep lesions and lesions that involve bone[14].

MRI is the most valuable modality for imaging vascular anomalies due to its superior contrast resolution, ability to characterize flow dynamics, depiction of deep and adjacent structures and lack of ionizing radiation[14]. Most information needed to characterize a vascular anomaly can be obtained from T1-weighted, fat saturated T2-weighted and gradient echo MR sequences[15]. Basic MR imaging protocols should include each of these sequences in the axial plane along with fast spin echo T2-weighted images in the coronal and sagittal planes[15,17]. Dynamic contrast-enhanced MRI can provide supporting information about flow dynamics[18] and may also be employed. On MRI, hemangiomas will appear as a mass[15,19] with flow voids and intermediate signal on T1-weighted images, flow voids and high signal on T2-weighted images, high signal within vessels on gradient echo sequences and arterial enhancement on contrast enhanced images[15,19]. High-flow vascular malformations including AVMs and AVFs will also demonstrate flow voids and intermediate signal on T1-weighted images, flow voids and high signal on T2-weighted images, high signal within vessels on gradient echo sequences and arterial enhancement on contrast enhanced images, but no associated soft tissue mass[14-19]. Low flow lesions including venous malformations and lymphatic malformations can also be differentiated based on MRI. Venous malformations will appear as multiple serpentine tubular structures or amorphous dilated channels containing intermediate signal on T1 weighted images, high signal on T2 weighted images, intermediate signal on gradient echo sequences and delayed enhancement on dynamic contrast enhanced MRI[14-19]. Flow voids are not seen within venous malformations

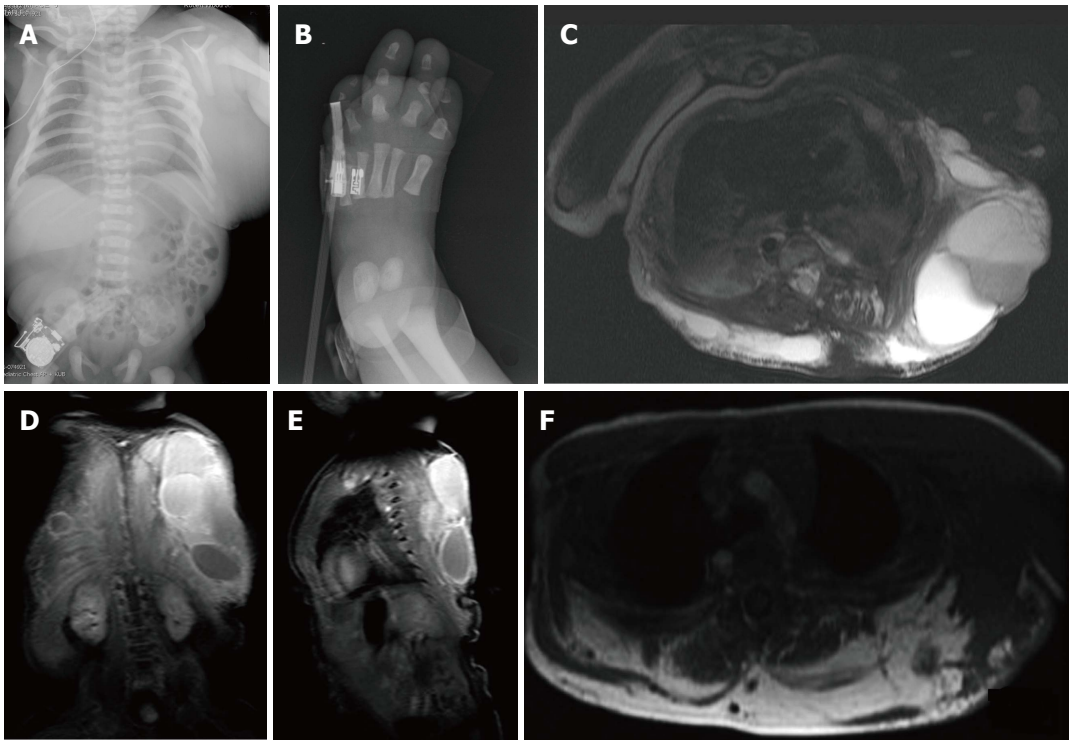

Figure 3 Three-month-old child with CLOVES syndrome. Radiograph of the chest and abdomen (A) demonstrates large soft tissue mass within the left chest and upper abdominal wall. Radiograph of the foot (B) demonstrates overgrowth of the third and fourth digits. Fat suppressed T2 weighted magnetic resonance (MR) images in axial (C), coronal (D) and sagittal (E) planes show the large soft tissue mass within the chest wall contains several loculations, some of which demonstrate hypointense fluid-fluid levels due to hemorrhage. T1 weighted MR image in the axial plane (F) confirms lipomatous overgrowth admixed with muscle.

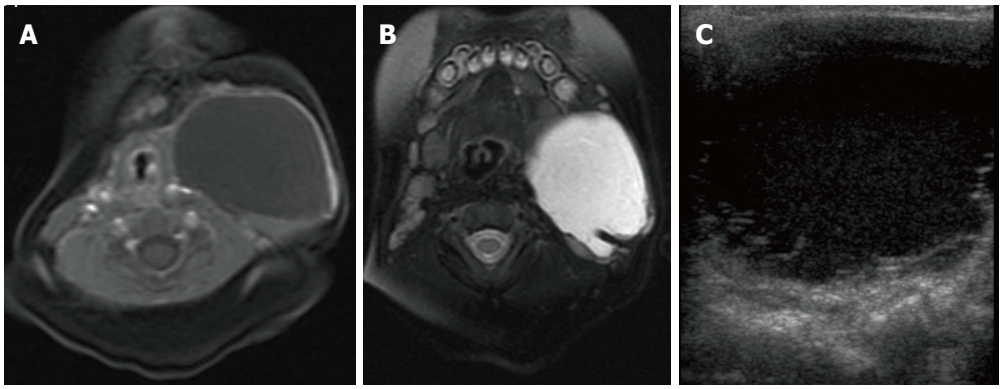

Figure 4 Cervicothoracic macrocystic lymphatic malformation. T1- (A) and T2-weighted (B) fat suppressed magnetic resonance images (MRI) demonstrate a macrocyst within the left neck that is predominantly hypointense on T1-weighted image and hyperintense on T2-weighted image. Trace blood products layering within the posterior aspect of the cyst are hyperintense on the T1 weighted image and hypointense on the T2 weighted image. Transverse ultrasound (C) demonstrates a predominantly anechoic macrocyst with layering low-level echoes, corresponding to blood products seen on MRI.

due to a lack of fast-flowing blood. Lymphatic malformations are characterized by micro- or macrocystic spaces that often contain fluid-fluid levels due to hemorrhage or proteinaceous material within the cysts[15] (Figures 3-5). Cysts will often be hyperintense on T2-weighted images, hypointense on T1 weighted images (though may be iso- to hyperintense depending on proteinaceous contents), and will not enhance[15,19]. When microcystic, the cystic spaces may not be visible with the fibrovascular stroma seen as regions of intermediate signal on T1-weighted images and high signal on T2-weighted images with associated enhancement on post-contrast images (Figure 2).

LOW-FLOW VASCULAR MALFORMATIONS

Capillary malformations present as flat pink or red macules that do not involute. These lesions result from abnormal morphogenesis of superficial dermal blood vessels, which lead to ectatic papillary dermal capillaries and postcapillary venules[20]. Histologically, these lesions stain positive for fibronectin, von Willebrand factor, and collagenous basement membrane proteins[21]. Particularly, in port wine stains, there is increased expression of vascular endothelial growth factor VEGF-A as well as its most

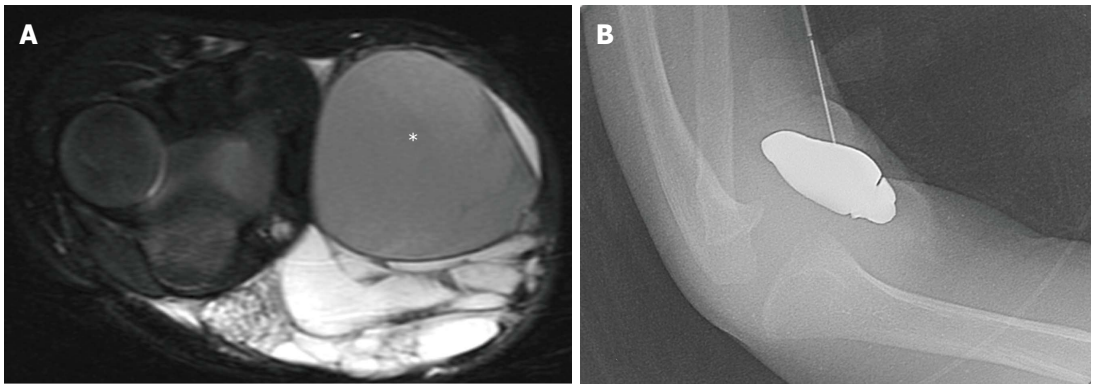

Figure 5 Macrocystic lymphatic malformation with hemorrhage. Axial fat suppressed T2 weighted magnetic resonance image of the elbow (A) demonstrates a predominantly hyperintense malformation with hypointense hemorrhage in a loculation (asterisk). Direct access to the malformation is obtained with a 22-gauge needle for sclerosis (B), subsequently performed with doxycycline.

Table 1 Commonly used sclerosants and liquid embolic agents

Sclerosants and liquid embolic agents	Comments
Sodium tetradecyl sulfate (STS)	Combined with non-ionic contrast for final concentration of 1.5%; foamed according to Tessari's method[39]
Doxycycline	10 mg/mL, maximum dose 1000 mg
Ethanol	95% concentration; Risk of systemic toxicity increases with doses > 1 mL/kg or total volume > 60 mL
Bleomycin	0.3-0.5 mg/kg
OK-432/Picibanil	1-3 intralesional injections of 0.2 mL each dose at 0.01 mg/kg
Polidocanol	0.5-1.0% concentration; Inject 0.1-0.3 mL for a total administered dose of 10 mL
n-BCA glue	Combined with Ethiodol for polymerization
Onyx	Dissolved with DMSO and tantalum; three different concentrations (6%, 6.5%, 8%)

STS: Sotradecol; n-BCA: n-butyl cyanoacrylate.

active receptor VEGF-R2, which is suggestive of an underlying mechanism for pathogenesis[22]. These lesions occur in 0.3% of newborns without preponderance for gender[23]. Detection typically occurs at birth, although acquired capillary malformations are rarely identified. Capillary malformations can be seen with several different syndromes as described later.

LYMPHATIC MALFORMATIONS

Lymphatic malformations arise from abnormal development of the lymphatic system during the early phases of angiogenesis and may be diffuse, often described as lymphedema, or localized, commonly described as a lymphangioma[20]. These malformations are typically large, spongy masses that are non-tender. These lesions can affect any area of the body, but there is a propensity for the head and neck, where they are often referred to as cystic hygromas[20]. Sixty five to 75% of lesions present at birth whereas the remainder of cases appear within 2 years of age[24]. While most lesions are sporadic, some are occur as part of syndromes, such as CLOVES (Figure 3). Complications of these lesions may include bleeding or infection for superficial lesions and encroachment on other anatomic structures such as airways or abdominal viscera for deep lesions.

Lymphatic malformations may be macrocystic (Figures 4, 5), consisting of lymphatic spaces arbitrarily defined as greater than two centimeters in diameter, microcystic, or a combination of macrocystic and microcystic. As these lesions are commonly encountered in infants and children ultrasound plays an important role in the diagnosis, staging, and treatment of lymphatic malformations. MR is useful in determining the type and anatomic relationships of lesions but often requires sedation or general anesthesia in children.

Treatment

Sclerotherapy is the primary form of treatment of macrocystic lymphatic malformations. Lesions are punctured under ultrasound guidance and accessed with 3 to 8. French multiholed drainage catheters. The entire contents of the cysts are aspirated and then 25% to 50% of the volume replaced with a sclerosant. The sclerosant is instilled for several hours and then aspirated. Some remove the catheters at this time and re-access the malformation as required, while others leave the catheters in place for serial sclerosis over 24-48 h. Many sclerosants have been described (Table 1), including doxycycline, sodium tetradecyl sulfate (Sotradecol, STS), ethanol, bleomycin, and OK-432 (picibanil). Using bleomycin as a sclerotherapy agent in macrocystic lymphatic malformations has been reported as successful in up to 72% of patients[25,26]. Using OK-432 (picibanil) has shown success in up to 66.5% of patients, while using doxycycline (Figures 5, 6) has demonstrated success in up to 93% of patients[27].

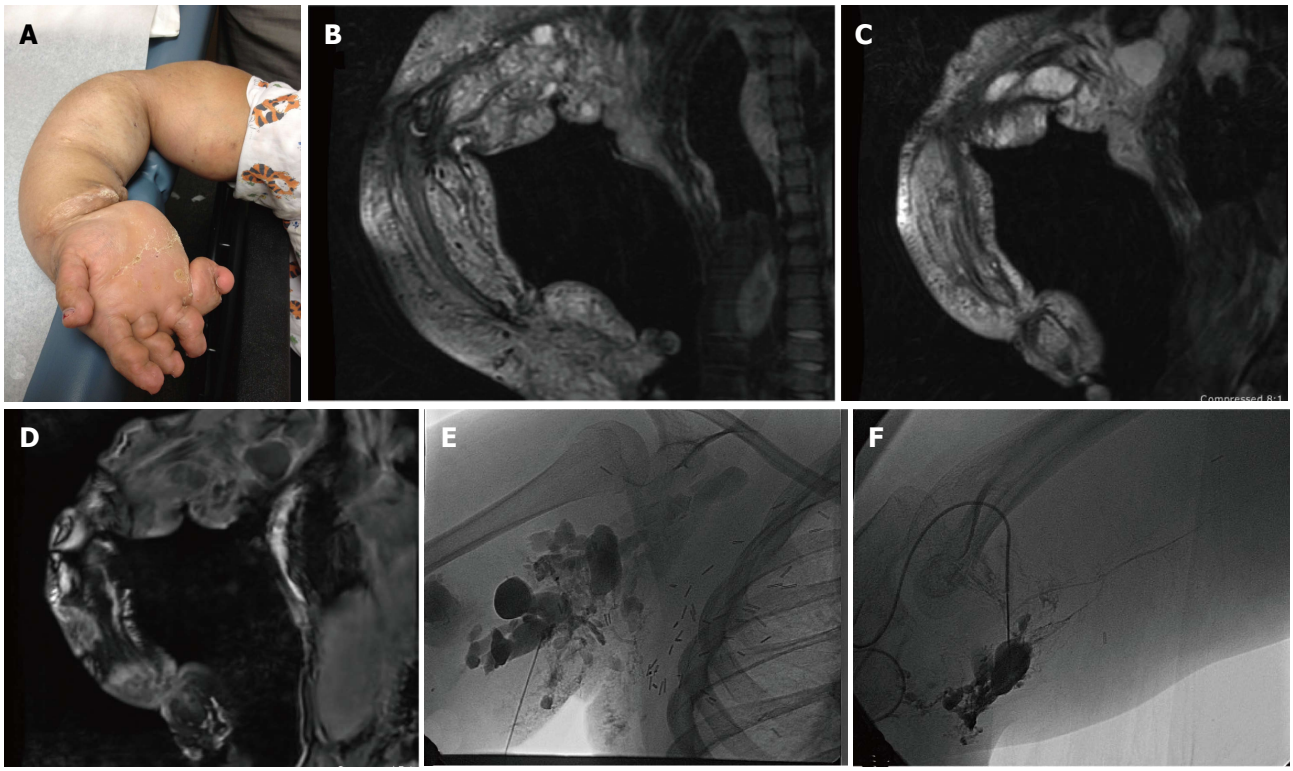

Figure 6 Ten-year-old girl with CLOVES syndrome. Photograph (A) demonstrates right upper extremity overgrowth. Pre-treatment coronal MR images of the right upper extremity (B, C, D) demonstrate a large, combined macro/microcystic lymphatic malformation with venous lakes in the axilla and evidence of lipomatous overgrowth. Angiographic images (E, F) demonstrate direct puncture of the malformation followed by sclerosis with doxycycline.

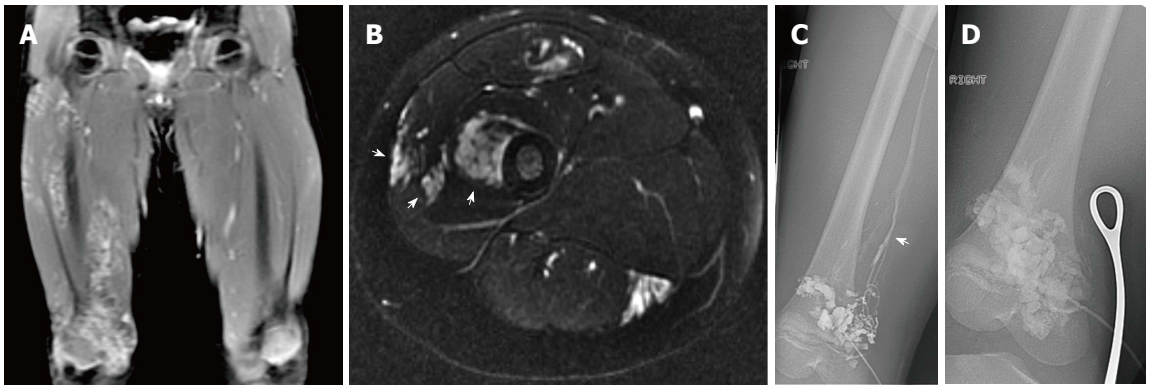

Figure 7 Infiltrative extratruncular low flow vascular malformation of the right leg. Coronal (A) and axial (B) T2-weighted magnetic resonance images demonstrate a high signal intensity infiltrative lesion (arrows). Venography (C) demonstrates filling of the malformation with outflow communication to the femoral vein (arrow). Sclerosis was subsequently performed utilizing 3% STS opacified with contrast (D) with compression of the outflow vein using metal forceps.

LOW-FLOW VENOUS MALFORMATIONS

Venous malformations result from abnormal sprouting or branching during embryonic development. Venous malformations may be focal, multifocal or diffuse and infiltrative. These dysmorphic vascular channels are lined with flattened endothelium[2,20] and defective smooth muscle, leading to progressive expansion under hydrostatic pressure. Stasis promotes *in-situ* thrombosis and lysis. Patients present most often with swelling and pain, worse as the day progresses and exacerbated in the standing position. On physical examination there may be an associated dermal capillary malformation. Clinically, these lesions appear as a soft, compressible, blue mass typically within the cutaneous tissues of the face, trunk, and limbs, although involvement of the viscera and bones has also been described[28,29] (Figure 7). It should be noted that two thirds of all vascular malformations are venous predominant[30]. Although it is felt that there is no gender predisposition, one series did find a female preponderance[29,31].

Treatment

Low flow venous malformations may be treated by compression, surgical excision or sclerosis. Treatment should be reserved for symptomatic or cosmetically disfiguring malformations (Figure 8). Sclerosing agents,

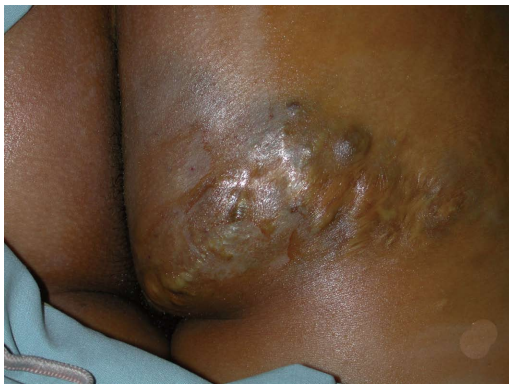

Figure 8 Superficial low flow venous malformation. This soft compressible mass with nodular purple skin discoloration in the buttock is typical of a superficial low flow venous malformation.

which comprise the main form of treatment, include STS, polidocanol, and absolute alcohol. Overall, good to excellent results with sclerotherapy have been reported in 53%-100% patients, depending on the size and definition of the treated lesion[14,32-36]. Technical success rates using absolute alcohol have been reported in up to 95% with no evidence of recurrence[32]. Studies looking at STS have reported moderate to excellent clinical results in 68%-86% of patients[33,37,38]. Polidocanol has shown a treatment benefit in 78%-100% of patients[33,39,40].

Access to the venous vascular malformation is generally achieved by direct puncture, utilizing ultrasound guidance. A butterfly needle is frequently utilized for more superficial malformations. Venography is then performed, and the volume of contrast administered to fill the malformation is noted. The appearance of any outflow into the deep venous structures is also noted. The malformation is emptied of as much blood as possible to increase contact of the sclerosant with the vein wall. Compression of previously visualized outflow veins is applied with tourniquets or direct pressure (Figure 9). Sclerosant is then injected, generally at a volume of 50%-60% of that which was noted to fill the malformation with contrast. Foam sclerotherapy is ideal for treatment of low flow venous vascular malformations (Figure 10). The sclerosant 3% STS is combined on a one-to-one basis with nonionic contrast, for a final concentration of 1.5%, and is then foamed according to Tessari's method[41] with 4 parts of air, or an O_2/CO_2 mixture, with one part sclerosant. Foaming the sclerosant increases the surface contact of the foam micelles with the endothelium of the malformation (Figure 9). Depending upon the size of the malformation, additional access is obtained and the process is repeated. Large truncular malformations may require coil embolization or balloon occlusion of larger outflow veins, in addition to sclerotherapy.

HIGH FLOW VASCULAR MALFORMATIONS

High flow vascular malformations exhibit variable presentation dependent on location (Figures 11, 12). Superficial lesions may present as a warm painless mass with palpable bruit and associated dilated veins. Skin erosion and bleeding is possible (Figure 12). Deeper lesions may present with steal phenomena as the malformation deprives blood flow from downstream structures. Staging of these lesions can be accomplished by scoring according to the Schobinger clinical staging system[20,42]. Within this system, stage Ⅰ describes a phase of quiescence where there is a cutaneous blush and skin warmth. In stage Ⅱ, there is expansion with a darkening blush, lesion pulsation, as well as a bruit or palpable thrill. Stage Ⅲ is defined by destruction, namely pain, dystrophic skin changes, ulceration, distal ischemia, and steal. Finally, stage Ⅳ is marked by decompensation or high output cardiac failure.

High flow vascular malformations include macrofistulas, or truncular malformations, that consist of single or multiple arteries directly communicating with outflow veins without an interposed high resistance capillary system. In contrast, arteriovenous malformations, which are often extratruncular, consist of a low resistance nidus recruiting blood supply from numerous regional inflow arteries and draining by multiple outflow veins.

Treatment

Macrofistulous malformations are treated by coil occlusion of the fistula at the distal arterial end of the communication. Accurate oversizing of the coils is essential to eliminate systemic embolization of the coil. The use of detachable coils, released only when satisfactory placement is achieved, may increase the safety of the procedure (Figure 13). In addition to coils, occlusion devices such as the Amplatzer occluder device (St. Jude Medical, Plymouth, MN, United States) may be considered.

The goal in the treatment of high flow arteriovenous vascular malformations is eradication of the nidus. This is best accomplished with a liquid embolic agent, which will penetrate the feeding vessels into the nidus. A coaxial guiding and microcatheter system is advanced toward the nidus and repeat angiography is performed to determine the volume of embolic agent required to penetrate and fill the nidus.

Particulate agents, such as polyvinyl alcohol (PVA)[43,44] may be used independently or in conjunction with liquid embolic agents. Particulate agents do not generally provide complete occlusion, and recanalization may occur (Figure 14).

A commonly employed embolic agent is n-butyl cyanoacrylate (n-BCA), commonly referred to as "glue." n-BCA is a non-adherent liquid in a nonionic environment that rapidly polymerizes in an ionic environment. Polymerization rate is decreased by mixing with increasing volumes of Ethiodol, permitting progressively distal penetration. Selecting the ideal ratio of n-BCA/ethiodol permits polymerization to occur within the nidus of the AVM rather than the feeding artery (Figure 15).

An alternative to n-BCA as a liquid embolic agent is Onyx (ev3 Endovascular, Inc., Plymouth, MN, United States)[45-47]. Distal microcatheter placement is essential.

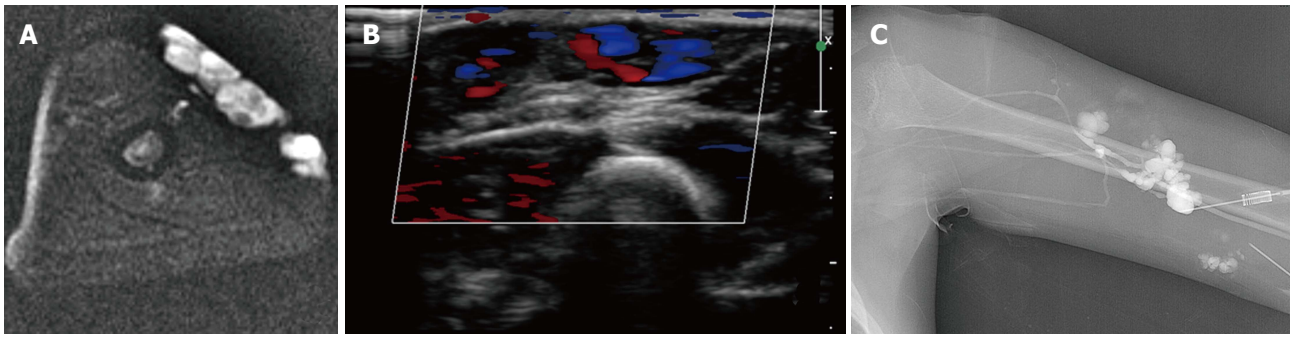

Figure 9 Foaming the sclerosant increases the surface contact of the foam micelles with the endothelium of the malformation. Axial T2 magnetic resonance demonstrating high signal intensity subcutaneous low flow venous malformation of the left upper arm (A). The lower signal small round structure likely represents a phlebolith. Color Doppler ultrasound demonstrates low flow signal in the venous malformation (B). Venography prior to sclerotherapy with tourniquet in place on upper arm demonstrates the venous malformation with no filling of normal deep venous drainage (C). A few faint radio-opaque phleboliths are seen in the venographic image.

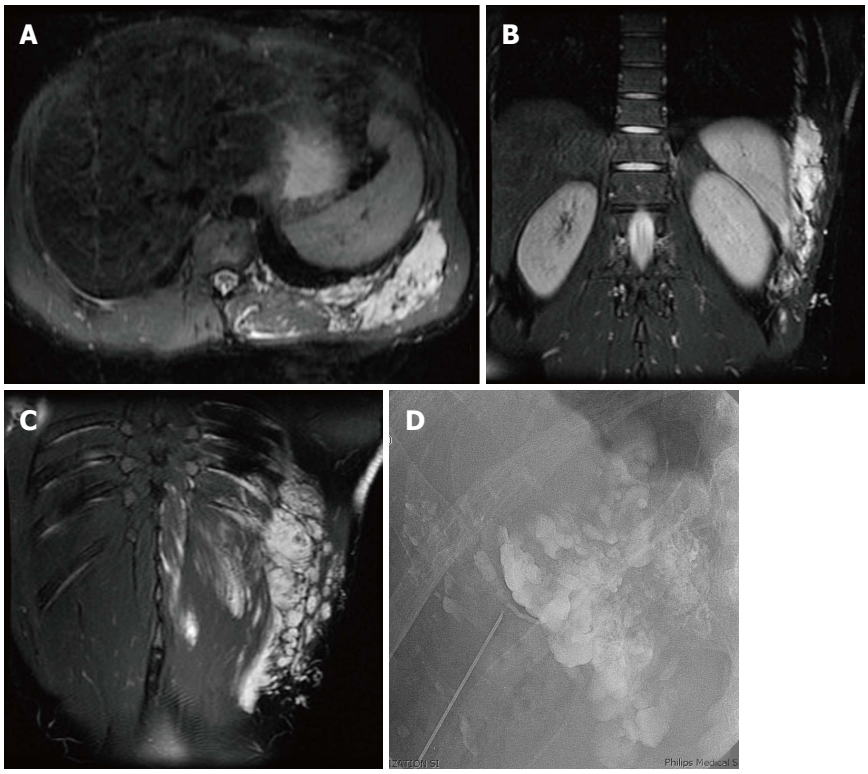

Figure 10 Foam sclerotherapy is ideal for treatment of low flow venous vascular malformations. Axial and coronal T2 weighted magnetic resonance images demonstrate a low flow venous malformation of the chest and upper abdominal wall (A, B, C). Direct access venography with a 22-gauge needle shows foamed STS opacified with contrast filling the malformation (D).

The technique of delivery of Onyx differs from glue in that a "plug" of Onyx is first formed around the tip of the microcatheter, preventing retrograde flow after the agent is forced in the direction of the nidus (Figure 15).

Absolute alcohol is an extremely effective alternative liquid agent, which causes protein denaturation and endothelial cell destruction (Figure 16). The treatment success rate of using ethanol in arteriovenous malformations has been reported up to 68% in certain small series[48]. Its efficacy decreases with decreasing concentration, making it difficult to mix with contrast agents and still achieve the same result. It has a greater tendency for peripheral penetration and a higher incidence of non-target injury such as skin necrosis, nerve injury and related complications (Figure 12). Using a balloon occlusion catheter during ethanol delivery may decrease the incidence of complications. Acute pulmonary hypertension, right heart strain, and sudden death during the administration of alcohol have been reported, urging careful monitoring of pulmonary arterial pressures during procedures involving alcohol sclerosis[49-51].

SYNDROMES ASSOCIATED WITH VASCULAR MALFORMATIONS

While most vascular malformations occur sporadically, some are associated with known syndromes. In some syndromes, the vascular malformation is the predominant source of morbidity, while in the majority of syndromes, the vascular malformation is present in association with

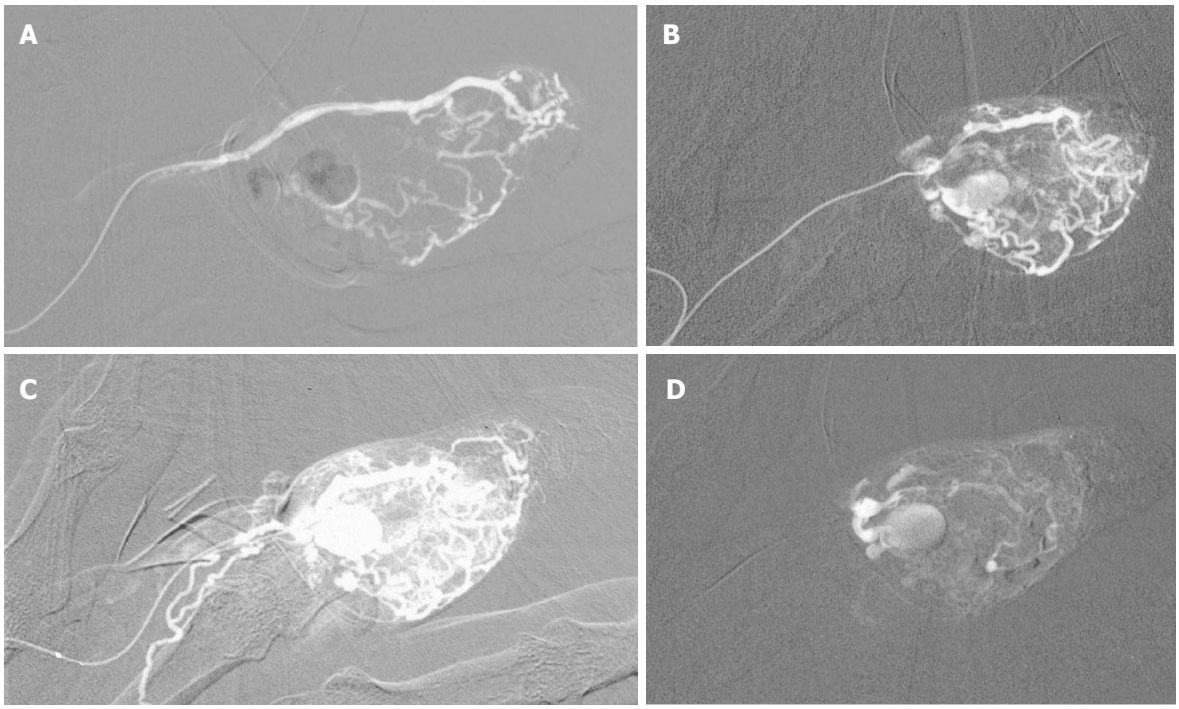

Figure 11 High flow arteriovenous malformation of second digit. This patient scheduled for amputation due to intractable pain under went alcohol embolization as a last resort prior to surgery. Digital arteriography with a microcatheter in the lateral digital artery with the tip at the level of the middle phalanx demonstrating filling of the nidus of the malformation (A, B, C). Following embolizaton, there is stasis of flow in the malformation (D). The medial digital artery remained patent with preservation of arterial flow to the digit.

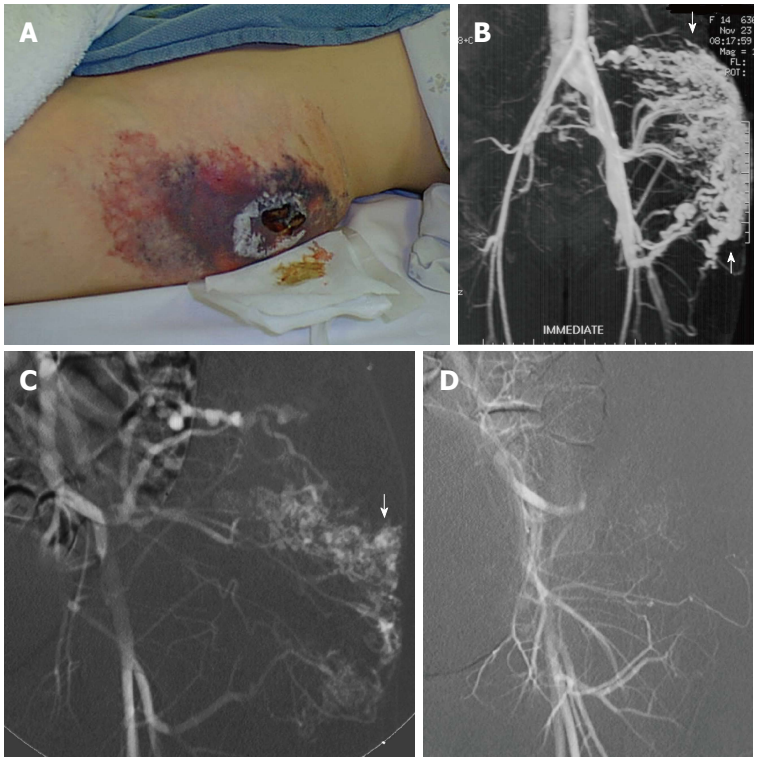

Figure 12 Superficial lesions may present as a warm painless mass with palpable bruit and associated dilated veins. High flow arteriovenous malformation with extensive skin breakdown in the region of this superficial malformation (A). Magnetic resonance angiogram demonstrates a high flow arteriovenous malformation with arteriovenous shunting (arrow) (B). Left internal iliac arteriogram demonstrating filling of the nidus of the malformation (arrow) (C). Arteriography following alcohol embolization shows eradication of the nidus of the malformation (D). As the malformation was located in subcutaneous fat, it was resected en block and skin grafts were created to bridge the area of skin breakdown.

other components, which produce the more significant pathology. When considered from the point of view of the vascular malformation, syndromes associated with vascular malformations may be classified according to their flow characteristics. Syndromes involving predominantly the head and neck or characterized by capillary malformations only are well described within the literature and are not included in this review.

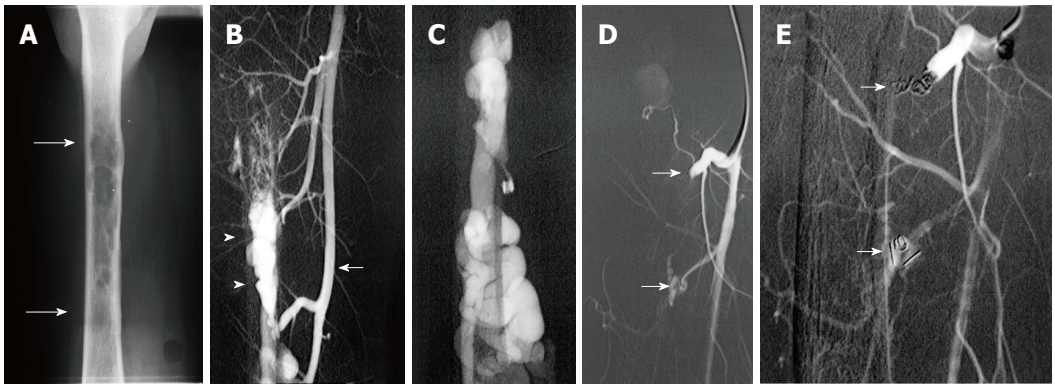

Figure 13 Use of detachable coils, released only when satisfactory placement is achieved, may increase the safety of the procedure. Radiograph of the mid-diaphysis of the femur demonstrates a region of endosteal erosion (arrows) (A). Arteriography demonstrates a multifistulous malformation with arterial supply from two muscular branches of the superficial femoral artery (arrow) with early filling of intraosseous venous drainage (arrowheads) (B, C). Occlusion of the feeding arteries was accomplished with large coils (arrow) eliminating the fistulous communications (D, E).

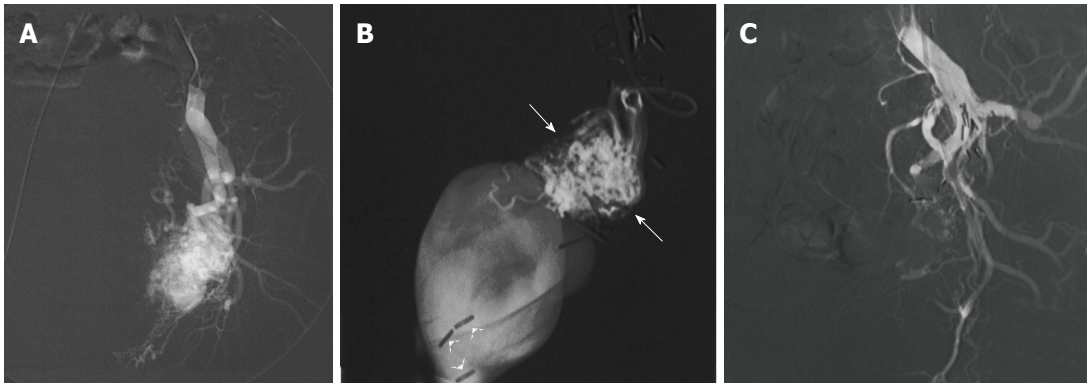

Figure 14 Particulate agents do not generally provide complete occlusion, and recanalization may occur. High flow arteriovenous malformation with nidus and venous aneurysm originating from branches of the left internal iliac artery (A). Following superselective catheterization of the feeding branch of the inferior gluteal artery there is demonstration of the nidus and venous aneurysm (arrow) (B). Following particulate embolization with PVA, there is occlusion of the nidus. Surgical clips are seen overlying internal iliac artery branches from previous unsuccessful attempts at surgical treatment (C).

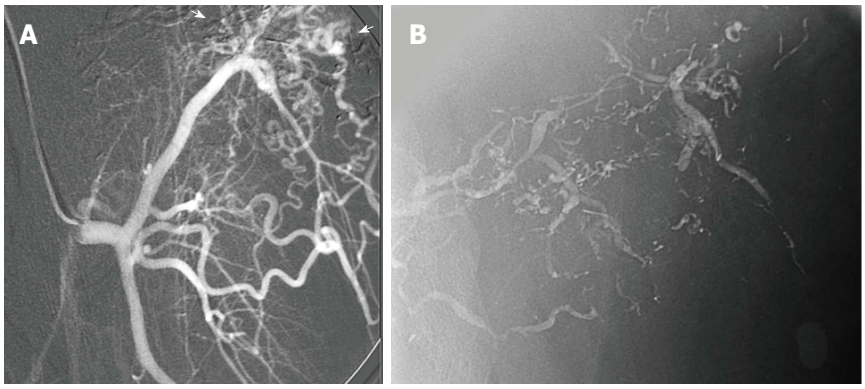

Figure 15 Arteriogram of high flow arteriovenous malformation. A: Arteriogram demonstrates nidus (arrows) of a high flow arteriovenous malformation of the abdominal wall, supplied in part by a muscular branch of the circumflex femoral artery; B: The lesion was treated twice, initially with Onyx, then with n-BCA glue, seen within the arterial feeders of the malformation on post-embolization imaging.

SYNDROMES ASSOCIATED WITH HIGH FLOW AND MIXED VASCULAR MALFORMATIONS

Hereditary hemorrhagic telangiectasia S

Hereditary hemorrhagic telangiectasia (HHT) is an autosomal dominant disorder involving mutations in the transforming growth factor-beta signaling pathway resulting in irregular cytoskeletal architecture and abnormal vascular tubule formation characterized by telangiectasias and fistulous malformations. Incidence is estimated to be between 1 in 5000 to 8000 with males and females affected equally[52,53]. Onset of symptoms most commonly occurs within the second and third decades of life. Telangiectasias are seen on mucosal surfaces and associated with epistaxis and gastrointestinal bleeding. Arteriovenous fistulas, particularly in the lung, liver, brain and

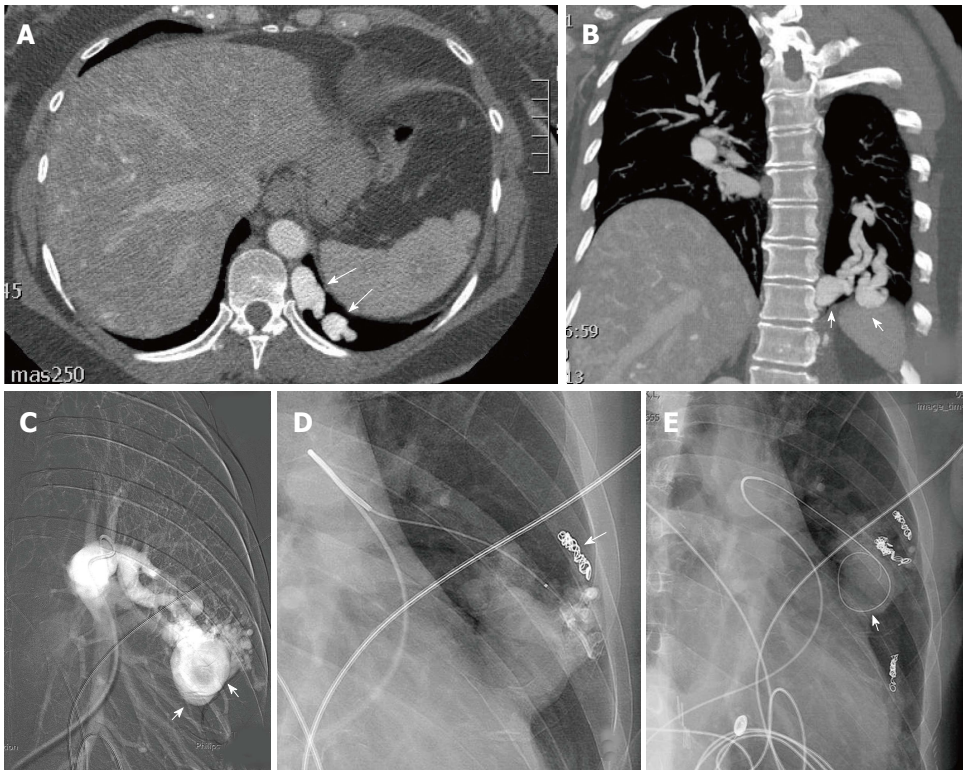

Figure 16 This patient with hereditary hemorrhagic telangiectasia presented with an abnormal chest radiograph. A computed tomography angiogram was performed for further evaluation. Axial CTA demonstrates a left lower lobe high flow vascular malformation (arrows) (A). Coronal reconstruction demonstrates several branches of the left lower lobe pulmonary artery feeding the malformation (arrows) (B). Sequential coil embolization of pulmonary arterial branches feeding the malformation was performed (arrow) (C). A framing coil was then placed in the venous aneurysm (D) followed by coil occlusion of the venous aneurysm and each of the remaining pulmonary arterial feeding branches (arrow) (E).

gastrointestinal tract are a major source of morbidity and mortality.

While 30% of patients with HHT have pulmonary arteriovenous fistulas, 80% of pulmonary arteriovenous fistulas occur in patients with HHT. As these fistulas act as right to left shunts, patients can present with hypoxia, stroke or brain abscess and less frequently hemoptysis or hemothorax. Lesions may be single or multiple. Simple lesions consist of fistulas between a single segmental branch of the pulmonary artery and the pulmonary vein, or complex with multiple segmental pulmonary artery branches supplying the fistula. Fistulas with arterial supply greater than 3 mm in diameter are considered at greatest risk of complication.

Surgical resection of pulmonary arteriovenous fistulas has currently been replaced by transcatheter occlusion. Superselective catheterization of the feeding pulmonary arterial branch close to the site of arteriovenous communication is required for placement of coils. Coil size selection, usually 20% larger than the target artery, is critical to avoid systemic coil embolization. Complete occlusion of each feeding artery is critical. Occasionally, occlusion of the aneurysmal draining vein can precede arterial occlusion in order to prevent systemic coil loss (Figure 17). Success of coil embolization approaches 80% but recanalization of the occluded artery or recruitment of additional feeding arterial supply results in recurrence of the fistula in up to 25% of patients, necessitating retreatment[54]. Careful follow-up of patients, therefore, is essential. Detachable coils or use of the Amplatzer occluder device may increase the safety of the procedure in select cases.

Parkes Weber syndrome

Parkes Weber Syndrome is an OSCVA syndrome[55] (Overgrowth Syndrome with Complex Vascular Anomalies), characterized by extremity overgrowth and vascular anomaly. In contrast to the Klippel Trenaunay syndrome, venous abnormalities are associated with high flow arteriovenous malformations within the hypertrophied extremity. A third component of the syndrome is a cutaneous capillary malformation. Arteriovenous fistulas may form around the time of puberty, and exacerbation of the vascular abnormalities is associated with trauma (Figure 17).

PTEN Hamartoma Syndrome

PTEN mutations promote stimulation of angiogenesis by the Akt/mTOR pathway[56]. PTEN Hamartoma Syndrome (PHTS) usually involves cutaneous lesions, capillary or capillary venous malformations, typically small deep tissue vascular malformations, and multiple high flow AVMs, associated with hamartomatous lesions[55]. Occasionally, lymphatic and venous malformations may

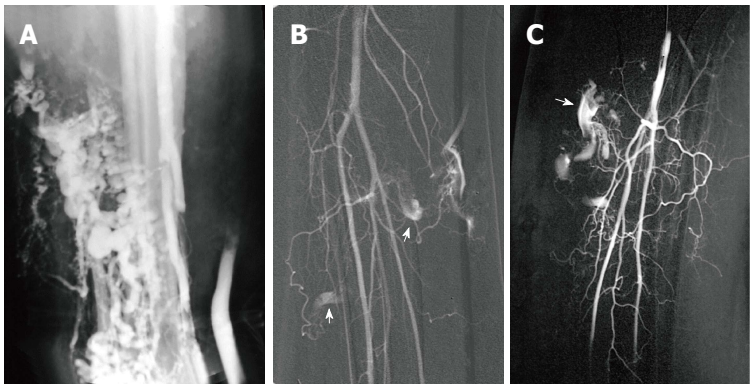

Figure 17 Venogram of low flow venous malformation in Parkes Weber Syndrome. Right lower extremity venogram demonstrates extensive low flow venous malformation in a patient with the Parkes Weber syndrome (A). Right lower extremity arteriogram demonstrating tibial artery shunting to the venous malformation (arrows) (B, C).

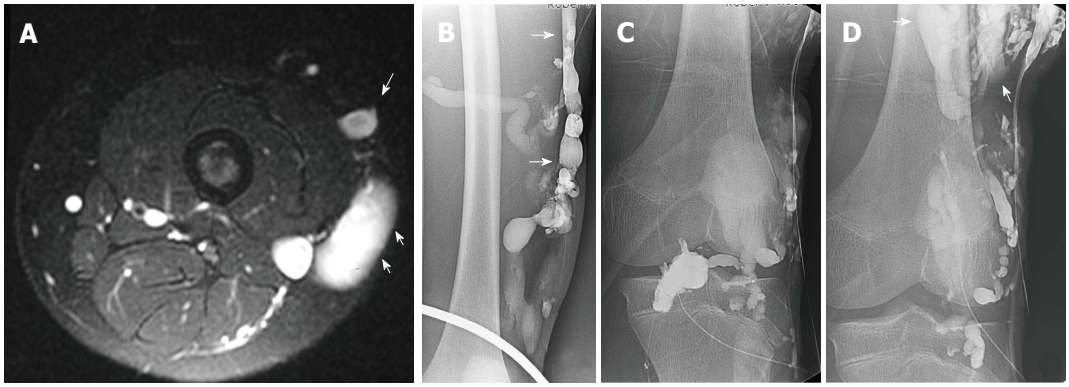

Figure 18 Klippel Trenaunay Syndrome. Axial T2 weighted fat suppressed magnetic resonance image of the thigh (A) in a patient with Klippel Trenaunay syndrome demonstrates a lateral embryonic vein (arrows) and venous malformation (short arrows). Lower extremity venogram demonstrates the lateral embryonic vein (arrows) (B). Direct puncture venography prior to alcohol sclerotherapy demonstrates progressive filling of the low flow truncular venous malformation (arrows) (C, D).

be present. High flow AVMs may be present in the limbs, paraspinal region and dura. They are frequently intramuscular and associated with ectopic fat. The hamartomatous lesion, comprised of vascular clusters, fibrous tissue, large veins and fat, has been termed PTEN hamartoma of soft tissue. Cowden syndrome, Bannayan-Riley-Ruvalcaba syndrome (BRRS) and some instances of Proteus syndrome are classified together with PHTS. More extensive high flow AVMs are occasionally seen in the BRRS.

SYNDROMES ASSOCIATED WITH LOW FLOW VASCULAR MALFORMATIONS

Klippel trenaunay syndrome

Klippel trenaunay syndrome (KTS) is another OSCVA syndrome with extremity overgrowth, associated with a superficial vascular stain, venous malformations, and usually partial aplasia of the deep venous system. The syndrome may also involve lymphatic anomalies. The vascular venous vascular malformations in KTS are characterized as truncal malformations, and may be related to persistence of the embryonic dorsal vein system in the lateral aspect of the extremity (lateral marginal vein in the lower extremity). Large varicosities may result in venous thrombosis and pulmonary embolism. Coagulopathy and gram-negative sepsis are also complications. Limb gigantism is especially prominent when there is an associated lymphatic malformation. MRI is the mainstay of imaging in KTS, with sonography reserved for guiding interventions and for distinguishing venous from lymphatic components of malformations (Figures 18, 19). Catheter based venography is occasionally needed to determine the presence, absence or partial aplasia of the deep venous system, when this is not obvious on other imaging modalities.

CLOVES Syndrome

The congenital lipomatous overgrowth, vascular malformations, epidermal nevi, and scoliosis and other skeletal deformities (CLOVES) syndrome consists of truncal lipomatosis, vascular malformations, and acral/musculoskeletal anomalies. The lipomatous lesions are often infiltrative and tend to recur following resection. Skeletal overgrowth and malformation are common in the extremities, as is scoliosis. Vascular lesions include capillary, lymphatic, venous and arteriovenous malformations (Figures 3, 19). In contrast to the Proteus and BRRS syndrome there is no mental impairment. Treatment includes sclerotherapy of lymphatic and venous malformations and resection of lipomatous lesions[55].

Blue rubber bleb nevus syndrome

This syndrome consists of venous malformations of the skin and those within the gastrointestinal tract. The skin lesions are comprised of a compressible blue subcutaneous nodule, representing a cutaneous venous malforma-

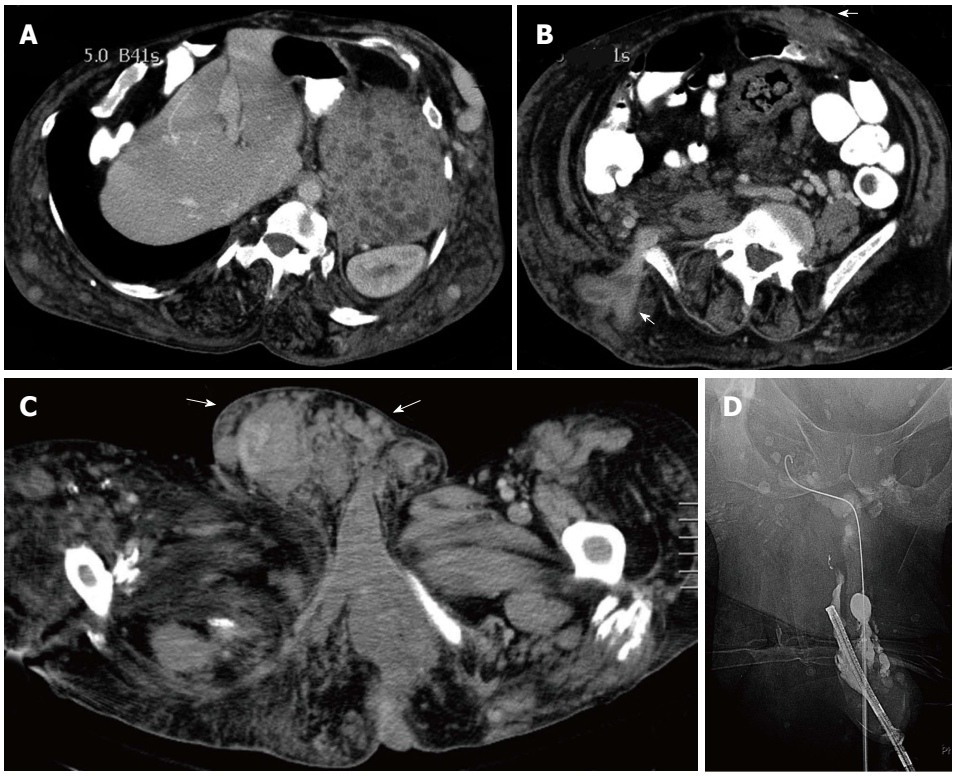

Figure 19 Klippel Trenaunay Syndrome. CT scan of the abdomen in a patient with the Klippel Trenaunay syndrome demonstrating extensive venous malformation in the abdominal wall (arrows) as well as venous malformations in the spleen (asterisk) (A, B). CT scan of the pelvis demonstrating extensive venous malformation in the inguinal canal and scrotum (arrows) (C). Sclerotherapy was performed through the dorsal vein of the penis to treat intractable urethral hemorrhage (D).

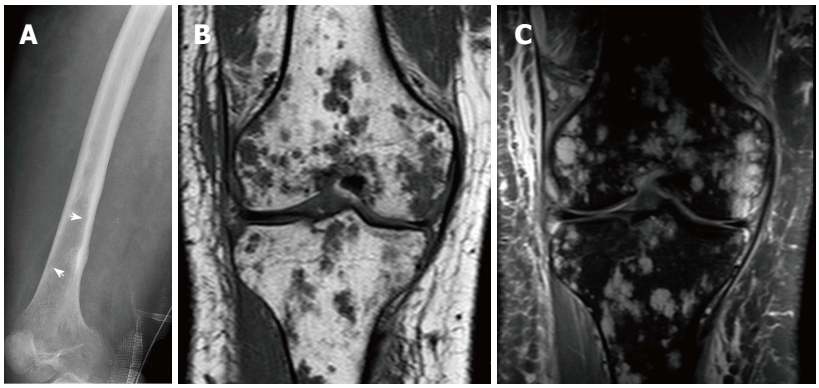

Figure 20 21-year-old man, who presented with pain and swelling of his leg. Radiograph of the femur demonstrates cortical erosion of the distal femur (arrows) (A). T1 weighted coronal magnetic resonance (MR) of the knee demonstrates innumerable focal lesions in the tibia and femur (B). These lesions are high signal intensity on T2 weighted coronal MR (C), however no contrast enhancement was seen within the lesions. Biopsy of the femur demonstrated a lymphatic microcystic lymphatic malformation.

tion. Clinical consequences generally result from gastrointestinal venous malformations, which may lead to occult or frank gastrointestinal bleeding.

Maffucci syndrome

In this syndrome, enchondromas are found in coexistence with venous malformations. There is a high frequency of malignant transformation of the enchondromas into chondrosarcomas.

Generalized Lymphatic Anomaly and Gorham-Stout disease

Generalized Lymphatic Anomaly (GLA) and Gorham-Stout Disease are two different disorders of the lymphatic system with overlapping features[57]. GLA is synonymous with "generalized cystic lymphangiomatosis", "cystic angiomatosis" and "lymphangiomatosis," though the term GLA is preferred based on the ISSVA classification system. GLA is a multisystem disorder characterized by dilated lymphatic vessels[58,59]. Features of GLA may include splenic cysts, hepatic cysts, pleural effusions, and macrocytic lymphatic malformations, which may involve several organ systems, including bone[57-59]. On imaging, osseous lesions in GLA are seen as lucent lesions within the medullary cavity on radiography and display hyperintensity on T2-weighted MR imaging, but do not demonstrate cortical destruction[57,60]. Numerous bones are typically affected in GLA, and the axial and appendicular skeleton are both affected with similar frequency[57]. In cases of osseous involvement, patients may present with pain and pathologic fracture (Figure 20).

Gorham-Stout disease, which has been called "vanish-

ing bone disease," is also a vascular anomaly of the lymphatics characterized by proliferation of lymphatic vessels within bone, resulting in progressive bony destruction[61]. Though the skeletal system is the primary site of disease in GSD, extra-osseous findings are also seen in GSD and include pleural effusions, splenic cysts, hepatic cysts, and infiltrating soft tissue abnormalities, which may extend from the bone into the adjacent soft tissues[57]. On imaging, osseous lesions are lytic, as in GLA, but are characterized by progressive osseous resorption and cortical destruction. On MRI, osseous lesions in GSD are most frequently accompanied by infiltrating soft tissue signal that is iso-to hypointense to muscle on T1-weighted images, hyperintense and heterogeneous on T2 weighted images, and enhances with contrast[57,62]. Infiltrative soft tissue is less common in GLA, which is seen in a minority of cases[57]. Unlike GLA, which affects the appendicular and axial skeleton with similar frequency, the axial skeleton is more commonly affected in GSD, with appendicular involvement seen in a minority of cases[57]. Macrocytic lymphatic malformations are infrequently seen in GSD[57]. As in GLA, patients with GSD may present with pain and pathologic fracture.

CONCLUSION

Accurate diagnosis of vascular malformations and their associated syndromes is often challenging but crucial in the formulation of appropriate treatment. The approach to the described entities requires an organized multidisciplinary team effort, with diagnostic imaging playing an increasingly important role in the proper diagnosis and a combined interventional radiologic and surgical treatment method showing promising results.

REFERENCES

1 **Yaşargil MG**. Microneurosurgery: AVM of the Brain, History, Embryology, Pathological Considerations, Hemodynamics, Diagnostic Studies, Microsurgical Anatomy. Vol. IIIA: Thieme, 1987

2 **Mulliken JB**, Glowacki J. Hemangiomas and vascular malformations in infants and children: a classification based on endothelial characteristics. *Plast Reconstr Surg* 1982; **69**: 412-422 [PMID: 7063565 DOI: 10.1097/00006534-198203000-00002]

3 **Belov S**. Anatomopathological classification of congenital vascular defects. *Semin Vasc Surg* 1993; **6**: 219-224 [PMID: 8305976]

4 **Enjolras O**, Wassef M, Chapot R. Color atlas of vascular tumors and vascular malformations. New York: Cambridge University Press, 2007: 1-11

5 **Lee BB**, Laredo J, Lee TS, Huh S, Neville R. Terminology and classification of congenital vascular malformations. *Phlebology* 2007; **22**: 249-252 [PMID: 18274331 DOI: 10.1258/026835507782655236]

6 **Lee BB**, Lardeo J, Neville R. Arterio-venous malformation: how much do we know? *Phlebology* 2009; **24**: 193-200 [PMID: 19767485 DOI: 10.1258/phleb.2009.009032]

7 **Bree AF**, Siegfried E, Sotelo-Avila C, Nahass G. Infantile hemangiomas: speculation on placental trophoblastic origin. *Arch Dermatol* 2001; **137**: 573-577 [PMID: 11346335 DOI: 10-1001/pubs.Arch]

8 **Chiller KG**, Passaro D, Frieden IJ. Hemangiomas of infancy: clinical characteristics, morphologic subtypes, and their relationship to race, ethnicity, and sex. *Arch Dermatol* 2002; **138**: 1567-1576 [PMID: 12472344 DOI: 10.1001/archderm.138.12.1567]

9 **Moore CW**, Lowe LH. Caffey's Pediatric Diagnostic Imaging. Philadelphia, PA: Mosby Elsevier, 2008: 1929-1948

10 **Haggstrom AN**, Drolet BA, Baselga E, Chamlin SL, Garzon MC, Horii KA, Lucky AW, Mancini AJ, Metry DW, Newell B, Nopper AJ, Frieden IJ. Prospective study of infantile hemangiomas: clinical characteristics predicting complications and treatment. *Pediatrics* 2006; **118**: 882-887 [PMID: 16950977 DOI: 10.1542/peds.2006-0413]

11 **Krol A**, MacArthur CJ. Congenital hemangiomas: rapidly involuting and noninvoluting congenital hemangiomas. *Arch Facial Plast Surg* 2005; **7**: 307-311 [PMID: 16172338 DOI: 10.1001/archfaci.7.5.307]

12 **Mulliken JB**, Enjolras O. Congenital hemangiomas and infantile hemangioma: missing links. *J Am Acad Dermatol* 2004; **50**: 875-882 [PMID: 15153887 DOI: 10.1016/j.jaad.2003.10.670]

13 **Fernández Y**, Bernabeu-Wittel M, García-Morillo JS. Kaposiform hemangioendothelioma. *Eur J Intern Med* 2009; **20**: 106-113 [PMID: 19327597 DOI: 10.1016/j.ejim.2008.06.008]

14 **Hyodoh H**, Hori M, Akiba H, Tamakawa M, Hyodoh K, Hareyama M. Peripheral vascular malformations: imaging, treatment approaches, and therapeutic issues. *Radiographics* 2005; **25** Suppl 1: S159-S171 [PMID: 16227489 DOI: 10.1148/rg.25si055509]

15 **Donnelly LF**, Adams DM, Bisset GS. Vascular malformations and hemangiomas: a practical approach in a multidisciplinary clinic. *AJR Am J Roentgenol* 2000; **174**: 597-608 [PMID: 10701595 DOI: 10.2214/ajr.174.3.1740597]

16 **Paltiel HJ**, Burrows PE, Kozakewich HP, Zurakowski D, Mulliken JB. Soft-tissue vascular anomalies: utility of US for diagnosis. *Radiology* 2000; **214**: 747-754 [PMID: 10715041 DOI: 10.1148/radiology.214.3.r00mr21747]

17 **Rak KM**, Yakes WF, Ray RL, Dreisbach JN, Parker SH, Luethke JM, Stavros AT, Slater DD, Burke BJ. MR imaging of symptomatic peripheral vascular malformations. *AJR Am J Roentgenol* 1992; **159**: 107-112 [PMID: 1609682 DOI: 10.2214/ajr.159.1.1609682]

18 **van Rijswijk CS**, van der Linden E, van der Woude HJ, van Baalen JM, Bloem JL. Value of dynamic contrast-enhanced MR imaging in diagnosing and classifying peripheral vascular malformations. *AJR Am J Roentgenol* 2002; **178**: 1181-1187 [PMID: 11959728 DOI: 10.2214/ajr.178.5.1781181]

19 **Meyer JS**, Hoffer FA, Barnes PD, Mulliken JB. Biological classification of soft-tissue vascular anomalies: MR correlation. *AJR Am J Roentgenol* 1991; **157**: 559-564 [PMID: 1872245 DOI: 10.2214/ajr.157.3.1872245]

20 **Garzon MC**, Huang JT, Enjolras O, Frieden IJ. Vascular malformations: Part I. *J Am Acad Dermatol* 2007; **56**: 353-370; quiz 371-374 [PMID: 17317485 DOI: 10.1016/j.jaad.2006.05.069]

21 **Finley JL**, Clark RA, Colvin RB, Blackman R, Noe J, Rosen S. Immunofluorescent staining with antibodies to factor VIII, fibronectin, and collagenous basement membrane protein in normal human skin and port wine stains. *Arch Dermatol* 1982; **118**: 971-975 [PMID: 6816146 DOI: 10.1001/archderm.1982.01650240015012]

22 **Vural E**, Ramakrishnan J, Cetin N, Buckmiller L, Suen JY, Fan CY. The expression of vascular endothelial growth factor and its receptors in port-wine stains. *Otolaryngol Head Neck Surg* 2008; **139**: 560-564 [PMID: 18922344 DOI: 10.1016/j.otohns.2008.07.015]

23 **Kanada KN**, Merin MR, Munden A, Friedlander SF. A prospective study of cutaneous findings in newborns in the United States: correlation with race, ethnicity, and gestational status using updated classification and nomenclature. *J Pediatr* 2012; **161**: 240-245 [PMID: 22497908 DOI: 10.1016/

j.jpeds.2012.02.052]
24 **Redondo P**. [Classification of vascular anomalies (tumours and malformations). Clinical characteristics and natural history]. *An Sist Sanit Navar* 2004; **27** Suppl 1: 9-25 [PMID: 15148508]
25 **Sainsbury DC**, Kessell G, Fall AJ, Hampton FJ, Guhan A, Muir T. Intralesional bleomycin injection treatment for vascular birthmarks: a 5-year experience at a single United Kingdom unit. *Plast Reconstr Surg* 2011; **127**: 2031-2044 [PMID: 21532430 DOI: 10.1097/PRS.0b013e31820e923c]
26 **Acevedo JL**, Shah RK, Brietzke SE. Nonsurgical therapies for lymphangiomas: a systematic review. *Otolaryngol Head Neck Surg* 2008; **138**: 418-424 [PMID: 18359347 DOI: 10.1016/j.otohns.2007.11.018]
27 **Nehra D**, Jacobson L, Barnes P, Mallory B, Albanese CT, Sylvester KG. Doxycycline sclerotherapy as primary treatment of head and neck lymphatic malformations in children. *J Pediatr Surg* 2008; **43**: 451-460 [PMID: 18358281 DOI: 10.1016/j.jpedsurg.2007.10.009]
28 **Dubois J**, Soulez G, Oliva VL, Berthiaume MJ, Lapierre C, Therasse E. Soft-tissue venous malformations in adult patients: imaging and therapeutic issues. *Radiographics* 2001; **21**: 1519-1531 [PMID: 11706222 DOI: 10.1148/radiographics.21.6.g01nv031519]
29 **Mazoyer E**, Enjolras O, Bisdorff A, Perdu J, Wassef M, Drouet L. Coagulation disorders in patients with venous malformation of the limbs and trunk: a case series of 118 patients. *Arch Dermatol* 2008; **144**: 861-867 [PMID: 18645137 DOI: 10.1001/archderm.144.7.861]
30 **Eifert S**, Villavicencio JL, Kao TC, Taute BM, Rich NM. Prevalence of deep venous anomalies in congenital vascular malformations of venous predominance. *J Vasc Surg* 2000; **31**: 462-471 [PMID: 10709058 DOI: 10.1067/mva.2000.101464]
31 **Boon LM**, Mulliken JB, Enjolras O, Vikkula M. Glomuvenous malformation (glomangioma) and venous malformation: distinct clinicopathologic and genetic entities. *Arch Dermatol* 2004; **140**: 971-976 [PMID: 15313813 DOI: 10.1001/archderm.140.8.971]
32 **Lee BB**, Do YS, Byun HS, Choo IW, Kim DI, Huh SH. Advanced management of venous malformation with ethanol sclerotherapy: mid-term results. *J Vasc Surg* 2003; **37**: 533-538 [PMID: 12618688 DOI: 10.1067/mva.2003.91]
33 **Legiehn GM**, Heran MK. Venous malformations: classification, development, diagnosis, and interventional radiologic management. *Radiol Clin North Am* 2008; **46**: 545-597, vi [PMID: 18707962 DOI: 10.1016/j.rcl.2008.02.008]
34 **Goyal M**, Causer PA, Armstrong D. Venous vascular malformations in pediatric patients: comparison of results of alcohol sclerotherapy with proposed MR imaging classification. *Radiology* 2002; **223**: 639-644 [PMID: 12034929 DOI: 10.1148/radiol.2233010025]
35 **Rautio R**, Saarinen J, Laranne J, Salenius JP, Keski-Nisula L. Endovascular treatment of venous malformations in extremities: results of sclerotherapy and the quality of life after treatment. *Acta Radiol* 2004; **45**: 397-403 [PMID: 15323391 DOI: 10.1080/02841850410004913]
36 **Rimon U**, Garniek A, Galili Y, Golan G, Bensaid P, Morag B. Ethanol sclerotherapy of peripheral venous malformations. *Eur J Radiol* 2004; **52**: 283-287 [PMID: 15544907 DOI: 10.1016/j.ejrad.2003.09.010]
37 **Tan KT**, Kirby J, Rajan DK, Hayeems E, Beecroft JR, Simons ME. Percutaneous sodium tetradecyl sulfate sclerotherapy for peripheral venous vascular malformations: a single-center experience. *J Vasc Interv Radiol* 2007; **18**: 343-351 [PMID: 17377179 DOI: 10.1016/j.jvir.2006.12.735]
38 **O'Donovan JC**, Donaldson JS, Morello FP, Pensler JM, Vogelzang RL, Bauer B. Symptomatic hemangiomas and venous malformations in infants, children, and young adults: treatment with percutaneous injection of sodium tetradecyl sulfate. *AJR Am J Roentgenol* 1997; **169**: 723-729 [PMID: 9275886 DOI: 10.2214/ajr.169.3.9275886]
39 **Pascarella L**, Bergan JJ, Yamada C, Mekenas L. Venous angiomata: treatment with sclerosant foam. *Ann Vasc Surg* 2005; **19**: 457-464 [PMID: 15981122 DOI: 10.1007/s10016-005-4656-z]
40 **Jain R**, Bandhu S, Sawhney S, Mittal R. Sonographically guided percutaneous sclerosis using 1% polidocanol in the treatment of vascular malformations. *J Clin Ultrasound* 2002; **30**: 416-423 [PMID: 12210459 DOI: 10.1002/jcu.10091]
41 **Tessari L**, Cavezzi A, Frullini A. Preliminary experience with a new sclerosing foam in the treatment of varicose veins. *Dermatol Surg* 2001; **27**: 58-60 [PMID: 11231246 DOI: 10.1111/j.1524-4725.2001.00192.x]
42 **Kohout MP**, Hansen M, Pribaz JJ, Mulliken JB. Arteriovenous malformations of the head and neck: natural history and management. *Plast Reconstr Surg* 1998; **102**: 643-654 [PMID: 9727427]
43 **Simons ME**. Peripheral vascular malformations: diagnosis and percutaneous management. *Can Assoc Radiol J* 2001; **52**: 242-251 [PMID: 11512297]
44 **Patel AA**, Solomon JA, Soulen MC. Pharmaceuticals for Intra-arterial Therapy. *Semin Intervent Radiol* 2005; **22**: 130-138 [PMID: 21326683 DOI: 10.1055/s-2005-871868]
45 **Vanninen RL**, Manninen I. Onyx, a new liquid embolic material for peripheral interventions: preliminary experience in aneurysm, pseudoaneurysm, and pulmonary arteriovenous malformation embolization. *Cardiovasc Intervent Radiol* 2007; **30**: 196-200 [PMID: 17205359 DOI: 10.1007/s00270-006-0071-2]
46 **Castaneda F**, Goodwin SC, Swischuk JL, Wong GC, Bonilla SM, Wang MJ, Abdel-Sayed PS. Treatment of pelvic arteriovenous malformations with ethylene vinyl alcohol copolymer (Onyx). *J Vasc Interv Radiol* 2002; **13**: 513-516 [PMID: 11997360 DOI: 10.1016/S1051-0443(07)61532-2]
47 **Rautio R**, Haapanen A. Transcatheter embolization of a renal artery aneurysm using ethylene vinyl alcohol copolymer. *Cardiovasc Intervent Radiol* 2007; **30**: 300-303 [PMID: 17206392 DOI: 10.1007/s00270-005-0238-2]
48 **Do YS**, Yakes WF, Shin SW, Lee BB, Kim DI, Liu WC, Shin BS, Kim DK, Choo SW, Choo IW. Ethanol embolization of arteriovenous malformations: interim results. *Radiology* 2005; **235**: 674-682 [PMID: 15858106 DOI: 10.1148/radiol.2352040449]
49 **Shin BS**, Do YS, Lee BB, Kim DI, Chung IS, Cho HS, Kim MH, Kim GS, Kim CS, Byun HS, Shin SW, Park KB. Multistage ethanol sclerotherapy of soft-tissue arteriovenous malformations: effect on pulmonary arterial pressure. *Radiology* 2005; **235**: 1072-1077 [PMID: 15833991 DOI: 10.1148/radiol.2353040903]
50 **Ko JS**, Kim JA, Do YS, Kwon MA, Choi SJ, Gwak MS, Lee JJ, Yang M. Prediction of the effect of injected ethanol on pulmonary arterial pressure during sclerotherapy of arteriovenous malformations: relationship with dose of ethanol. *J Vasc Interv Radiol* 2009; **20**: 39-45; quiz 45 [PMID: 19028113 DOI: 10.1016/j.jvir.2008.10.012]
51 **Chapot R**, Laurent A, Enjolras O, Payen D, Houdart E. Fatal cardiovascular collapse during ethanol sclerotherapy of a venous malformation. *Interv Neuroradiol* 2002; **8**: 321-324 [PMID: 20594492]
52 **Dakeishi M**, Shioya T, Wada Y, Shindo T, Otaka K, Manabe M, Nozaki J, Inoue S, Koizumi A. Genetic epidemiology of hereditary hemorrhagic telangiectasia in a local community in the northern part of Japan. *Hum Mutat* 2002; **19**: 140-148 [PMID: 11793473 DOI: 10.1002/humu.10026]
53 **Schoen FJ**. Cotran RS, Vinay K, Collins T. Robbins Pathologic Basis of Disease. 5th ed. WB Saunders, 1994: 509
54 **Woodward CS**, Pyeritz RE, Chittams JL, Trerotola SO. Treated pulmonary arteriovenous malformations: patterns of persistence and associated retreatment success. *Radiology* 2013; **269**: 919-926 [PMID: 23912618 DOI: 10.1148/ra-

diol.13122153]
55 **Alomari AI**. Characterization of a distinct syndrome that associates complex truncal overgrowth, vascular, and acral anomalies: a descriptive study of 18 cases of CLOVES syndrome. *Clin Dysmorphol* 2009; **18**: 1-7 [PMID: 19011570 DOI: 10.1097/MCD.0b013e328317a716]
56 **Iacobas** I, Burrows, P. PTEN: Structure, mechanisms-of-action, role in cell signaling and regulation. Nova Science, 2013: 215-217
57 **Lala S**, Mulliken JB, Alomari AI, Fishman SJ, Kozakewich HP, Chaudry G. Gorham-Stout disease and generalized lymphatic anomaly--clinical, radiologic, and histologic differentiation. *Skeletal Radiol* 2013; **42**: 917-924 [PMID: 23371338 DOI: 10.1007/s00256-012-1565-4]
58 **Wunderbaldinger P**, Paya K, Partik B, Turetschek K, Hörmann M, Horcher E, Bankier AA. CT and MR imaging of generalized cystic lymphangiomatosis in pediatric patients. *AJR Am J Roentgenol* 2000; **174**: 827-832 [PMID: 10701634 DOI: 10.2214/ajr.174.3.1740827]
59 **Rasalkar DD**, Chu WC. Generalized cystic lymphangiomatosis. *Pediatr Radiol* 2010; **40** Suppl 1: S47 [PMID: 20574655 DOI: 10.1007/s00247-010-1694-7]
60 **Boyle WJ**. Cystic angiomatosis of bone. A report of three cases and review of the literature. *J Bone Joint Surg Br* 1972; **54**: 626-636 [PMID: 4639439]
61 **Mavrogenis AF**, Zambirinis CP, Dimitriadis PA, Tsakanikas A, Papagelopoulos PJ. Gorham-Stout disease. *J Surg Orthop Adv* 2010; **19**: 85-90 [PMID: 20727303]
62 **Ozbayrak M**, Yilmaz MH, Kantarci F, Ozer H, Harmanci K, Babacan M, Dervisoglu S. A case of an idiopathic massive osteolysis with skip lesions. *Korean J Radiol* 2013; **14**: 946-950 [PMID: 24265571 DOI: 10.3348/kjr.2013.14.6.946]

P- Reviewer: Behr GG **S- Editor**: Wen LL **L- Editor**: A
E- Editor: Lu YJ

World Journal of Radiology

Submit a Manuscript: http://www.wjgnet.com/esps/
Help Desk: http://www.wjgnet.com/esps/helpdesk.aspx
DOI: 10.4329/wjr.v6.i9.693

World J Radiol 2014 September 28; 6(9): 693-707
ISSN 1949-8470 (online)

REVIEW

Expectations from imaging for pre-transplant evaluation of living donor liver transplantation

Tiffany Hennedige, Gopinathan Anil, Krishnakumar Madhavan

Tiffany Hennedige, Gopinathan Anil, Department of Diagnostic Imaging, National University Health and Yong Loo Lin School of Medicine, Singapore 119074, Singapore
Krishnakumar Madhavan, Department of Department of General Surgery, National University Hospital Singapore, Singapore 119074, Singapore
Author contributions: All the three authors have contributed equally to this work.
Correspondence to: Gopinathan Anil, MD, DNB, FRCR (Lon), FAMS, Department of Diagnostic Imaging, National University Health and Yong Loo Lin School of Medicine, 5 Lower Kent Ridge Road, Singapore 119288, Singapore. ivyanil10@gmail.com
Telephone: +65-97296614 Fax: +65-67797101
Received: February 8, 2014 Revised: March 25, 2014
Accepted: July 15, 2014
Published online: September 28, 2014

Abstract

Living donor liver transplant (LDLT) is a major surgical undertaking. Detailed pre-operative assessment of the vascular and biliary anatomy is crucial for safe and successful harvesting of the graft and transplantation. Computed tomography (CT) and magnetic resonance imaging (MRI) are currently the imaging modalities of choice in pre-operative evaluation. These cross-sectional imaging techniques can reveal the vascular and biliary anatomy, assess the hepatic parenchyma and perform volumetric analysis. Knowledge of the broad indications and contraindications to qualify as a recipient for LDLT is essential for the radiologist reporting scans in a pre-transplant patient. Similarly, awareness of the various anatomical variations and pathological states in the donor is essential for the radiologist to generate a meaningful report of his/her observations. CT and MRI have largely replaced invasive techniques such as catheter angiography, percutaneous cholangiography and endoscopic retrograde cholangiopancreatography. In order to generate a meaningful report based on these pre-operative imaging scans, it is also mandatory for the radiologist to be aware of the surgeon's perspective. We intend to provide a brief overview of the common surgical concepts of LDLT and give a detailed description of the minimum that a radiologist is expected to seek and report in CT and MR scans performed for LDLT related evaluation.

Key words: Liver transplantation; Pre-living donor liver transplant imaging; Vascular anatomy and variants; Biliary anatomy and variants; Computed tomography; Magnetic resonance imaging

Core tip: Living donor liver transplantation (LDLT) has evolved to a widely accepted therapeutic option. As a radiologist, knowledge of the various anatomical variations and pathological states in both the donor and recipient are imperative to generating a meaningful report in pre-operative evaluation. This paper provides a brief overview of the common surgical concepts of LDLT and gives a detailed description of the minimum that a radiologist is expected to seek and report in computed tomography and magnetic resonance scans performed for LDLT related evaluation.

Hennedige T, Anil G, Madhavan K. Expectations from imaging for pre-transplant evaluation of living donor liver transplantation. *World J Radiol* 2014; 6(9): 693-707 Available from: URL: http://www.wjgnet.com/1949-8470/full/v6/i9/693.htm DOI: http://dx.doi.org/10.4329/wjr.v6.i9.693

INTRODUCTION

Living donor liver transplantation (LDLT) has evolved into a widely accepted therapeutic option to ease the persistent shortage of cadaveric livers for deceased donor liver transplantantion (DDLT)[1]. Together with improved surgical techniques and advances in immunology, the

outcome in terms of LDLT recipient survival is as good as those attained after DDLT with full-sized deceased donor organs[2]. LDLT enables healthy volunteers to donate a portion of their liver to compatible recipients. Resection of a portion of the liver from a donor is an immense personal and surgical under-taking; hence a detailed knowledge of the vascular and biliary anatomy and the presence of variants are imperative to ensure safe and successful harvesting of the graft and transplantation[3]. The risk to the donor from LDLT is estimated to be 0.5% mortality and up to 21% post-operative morbidity[4].

In the past, semi-invasive techniques such as catheter angiography and endoscopic retrograde cholangiopancreatography were used to delineate vascular and biliary anatomy respectively. Liver biopsies were commonly performed for ruling out diffuse parenchymal changes such as steatosis. With the exponential progress in computed tomography (CT) and MR techniques, today it is possible to obtain the same information non-invasively. Some of the major limitations of conventional invasive techniques such as morbidity and mortality, high cost, higher radiation exposure as well as sub-optimal demonstration of venous anatomy have been overcome by shifting to pre-operative evaluation with CT and MRI[5].

INDICATIONS FOR TRANSPLANT

The major indications for liver transplantation (LT) are irreversible hepatic failure and hepatocellular carcinoma (HCC)[6]. Advanced cirrhosis secondary to chronic viral hepatitis or alcohol abuse is the most frequent cause of hepatic failure that leads to transplantation[1]. Cholestatic and metabolic diseases are the other pathologies that often result in end-stage liver disease. The usual cholestatic diseases that end up in LT are primary biliary cirrhosis, primary sclerosing cholangitis and biliary atresia[1]. Several metabolic diseases like non-alcoholic steatohepatitis, Wilson's disease, haemachromatosis, cystic fibrosis and glycogen storage disease may eventually need a LT for patient survival[1,7].

RECIPIENT CRITERIA

Various criteria have been described to assess the eligibility of a recipient to obtain a liver transplant. The rationale of these criteria is to ensure that LT is done for those patients who need it the most and in those who are most likely to benefit from it. The guidelines on ensuring fair allocation of the cadaveric graft, a scarce resource, among transplant candidates, have gone through various stages of evolution. Features of decompensated cirrhosis such as ascites, encephalopathy, refractory variceal hemorrhage and hepatorenal syndrome are accounted for while triaging a patient for transplantation[6]. Before 2002, Child-Turcotte-Pugh (CTP) Score was the primary basis for prioritization of candidates for LT. Currently, priority is assigned to a patient on the transplantation list on the basis of his/her highest estimated short-term mortality risk determined using the Model for End-Stage Liver Disease (MELD) score[6]. The MELD is a multiparameteric mathematical score that utilizes the patient's serum bilirubin, serum creatinine and the international normalized ratio to predict survival with higher scores indicating a sicker patient; hence in more urgent need of LT. The MELD was initially developed to predict death within three months of the procedure in patients who had undergone a transjugular intrahepatic portosystemic shunt. As it was found to be a reliable measure in estimation of short-term mortality risk, it was adopted over CTP for determining and prioritizing recipients of LT[8]. Compared to CTP, MELD is a more objective scoring system that avoids potential inter-observer bias and also takes into account renal dysfunction, a common problem among cirrhotics. Adjustments to MELD scores are made for patients with HCC depending on the stage of the disease.

Although HCC is an indication for LT in the appropriate setting, extensive disease can be a contraindication. In 1998 Mazaferro *et al*[9] reported excellent outcomes after LT in patients with a solitary HCC less than 5 cm in diameter or with up to 3 HCC nodules that were each less than 3 cm in diameter; these tumor characteristics and an absence of involvement of the main and primary branches of the portal vein by tumour formed the Milan criteria. Patients outside these criteria are generally believed to have poor tumor biology with high chances of recurrence and hence less likely to benefit from a liver transplant. Strict adherence to Milan Criteria may however preclude patients with a slightly more advanced HCC who may have acceptable, if not excellent long term outcomes from undergoing a transplant. This was the rationale behind the development of the University of California San Francisco (UCSF) criteria. According to UCSF criteria, patients with a single hepatoma < 6.5 cm in diameter or less than 4 hepatomas, with the largest < 4.5 cm in diameter and the sum of the diameters of all the tumors < 8 cm have a recurrence-free survival rate after LT close to that achieved with the Milan criteria[10]. The Milan and UCSF criteria provide broad guidelines to cadaveric liver allocation in many countries. However, every case still merits individual evaluation in a multidisciplinary meeting before being subjected to surgery.

Some of the absolute contraindications to transplantation include active extra-hepatic malignancy, non-hepatic active or uncontrolled infection, thrombosis of the entire portal and superior mesenteric venous system, active substance abuse, advanced cardiopulmonary disease or other co-morbidities that would compromise post-surgical recovery[6].

DONOR CRITERIA

The initial steps in the assessment of a potential liver donor include blood type compatibility, biochemical tests, viral markers and relevant co-morbidities. If these are satisfactory, radiological evaluation follows. If indicated,

a liver biopsy may have to be performed[11]. Variation in anatomy of potential donors can alter surgical approach or even preclude surgery[12,13]. Adequate liver volume with respect to both the graft for the recipient and remnant liver for the donor also needs to be assessed.

SURGICAL CONSIDERATIONS

For the reporting radiologist, understanding the surgeon's perspective on LDLT is imperative so that the necessary information can be conveyed pre-operatively. The three most often harvested grafts for LDLT are the right lobe, left lobe and left lateral segment grafts. The type of hepatectomy is based on the vascular and biliary anatomy as well as the estimated graft and remnant liver volume[14].

Traditionally, liver surgery relies on Couinaud's liver segment classification that divides the liver into eight functionally independent segments[15]. The right hepatic vein (RHV) divides the right lobe into anterior (V and Ⅷ) and posterior (Ⅵ and Ⅶ) sectors, the middle hepatic vein (MHV) divides the liver into right (V-Ⅷ) and left lobes (Ⅱ to Ⅳ) and the left hepatic vein (LHV) divides the left lobe into a medial (Ⅳa and Ⅳb) and lateral part (Ⅱ and Ⅲ). The portal vein divides the liver into superior (Ⅶ, Ⅷ, Ⅳa and Ⅱ) and inferior (Ⅵ, Ⅴ, Ⅳb and Ⅲ) segments.

Left lateral hepatectomy that harvests segment Ⅱ and Ⅲ is the most common LDLT technique and usually used for paediatric recipients or recipients of small size. Most of the adult recipients need a left or right liver graft; this decision depends on the residual volume of donor liver and size of the recipient. The techniques of right or left hepatectomy are fairly standardized worldwide[16-18]. Some controversy exists regarding the inclusion of the middle hepatic vein (MHV) with right or left sided grafts. When the donor's left lobe volume is more than 30% of total hepatic volume, a right hepatectomy (segments V-Ⅷ) can be done[19]. Left lobe is usually small; hence left hepatectomy generally includes the middle hepatic vein so as to obtain a reasonably large graft volume and to maintain good tissue viability for transplantation. However, if the middle hepatic vein is the dominant vein with a small right hepatic vein, this may not be advisable. Right hepatic grafts are often harvested without the MHV trunk. Such grafts are at risk for congestion of right paramedian sector with subsequent graft dysfunction and septic complications. To avoid such outcomes, MHV drainage to recipient IVC may be reconstructed with vascular grafts for segment V and Ⅷ veins[19]. The caudate lobe is generally left behind because of its direct venous drainage in to the IVC. However, for smaller left sided grafts the caudate lobe may need to be harvested together with rest of the left lobe and separate venous drainage reconstruction for the caudate lobe may be required.

IMAGING OVERVIEW

In the past, B mode ultrasound (US) in conjunction with Doppler and color flow imaging formed a routine part of preoperative evaluation of LDLT. However, it is highly operator dependent and subject to factors which are difficult to control and affect image quality such as a large body habitus, a high-riding liver and overlying bowel gas. A key limitation lies in the fact that US has limited ability to estimate liver volume[20]. In current practice, CT and MRI have largely displaced ultrasound from preoperative assessment for LDLT candidates.

In general, the spatial resolution of CT is superior to that of MR. CT is also relatively less expensive, requires a shorter scan time and is more easily assessable. However, CT involves exposure to ionizing radiation. MR on the other hand requires a longer scan time and high degree of patient compliance (*e.g.*, during breath hold sequences). Often normal patients (as these donors always are) do not comply well with these requirements leading to image degradation. Similarly, patients with pacemakers, metallic hardware or claustrophobia may not be able to undergo MR imaging. There is no ionizing radiation involved in MR imaging and it has better contrast resolution than CT scan. In addition, the Gadolinium-based contrast agents used for MR imaging are generally safer compared to the iodinated CT contrast agents with no nephrotoxicity and extremely rare anaphylactic reactions[21].

Source images from both modalities can be post processed for multi-planar reformation and three-dimensional (3D) reconstruction with maximum intensity projection (MIP) and volume rendering (VR) at commercially available workstations. This enables the branching points of the vessels and biliary ducts in relation to their intended site of incision to be viewed with little or no interruption between consecutive sections or on 3D images. 3D imaging with VR gives a stereoscopic view of the anatomy while MIP images may accentuate the visualization of smaller segmental vessels or ducts[22].

In the following sections of this article we will describe the role of CT and MR imaging in the evaluation of the vascular and biliary anatomy along with their variants as well as assessment of the hepatic parenchyma and volumetric analysis. We shall then address the impact of these factors in the selection of potential donors and the surgical decision-making. In our practice, multidetector CT and MRI are used as a compliment to each other in pre-LDLT donor evaluation. Initially the donor undergoes a CT scan that primarily evaluates the vascular anatomy and looks for any gross parenchymal abnormalities; if there is no contra-indication for donor selection on CT scan, further evaluation with MRI is performed for assessing the biliary anatomy and hepatic fat content.

HEPATIC ARTERIAL SYSTEM

According to Couinaud[23], the liver develops in 3 sectors with each one having its own embryological artery; the left gastric artery irrigates the left lateral segment, the common hepatic artery supplies the paramedian segments, and the superior mesenteric artery feeds the right

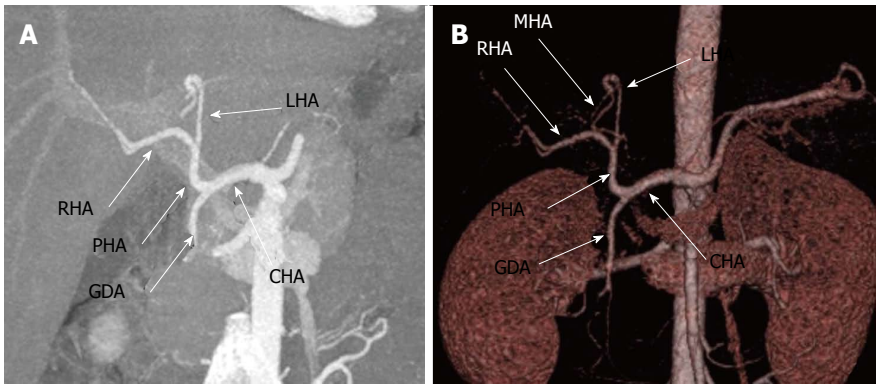

Figure 1 Conventional hepatic arterial anatomy depicted in (A) maximum intensity projection and (B) 3D volume-rendered images generated from a computed tomography angiogram. The CHA comes off the celiac axis, gives off the GDA to become the PHA which then bifurcates into the RHA and LHA. Note the MHA (the slender branch arising from left hepatic artery as seen in 1B) arising from LHA. CHA: Common hepatic artery; GDA: Gastroduodenal artery; PHA: Proper hepatic artery; RHA: Right hepatic artery; LHA: Left hepatic artery; MHA: Middle hepatic artery.

Table 1 Michel's classification of hepatic arterial variants

Type	Frequency of occurrence (%)	Description
I	55	RHA and LHA from the CHA
II	10	Replaced LHA from LGA
III	11	Replaced RHA from SMA
IV	1	Replaced RHA and LHA
V	8	Accessory LHA from LGA
VI	7	Accessory RHA from SMA
VII	1	Accessory RHA and LHA
VIII	4	Accessory RHA and LHA and replaced LHA or RHA
IX	4.5	CHA from SMA
X	0.5	CHA from LGA

RHA: Right hepatic artery; LHA: Left hepatic artery; CHA: Common hepatic artery; LGA: Left gastric artery; SMA: Superior mesenteric artery.

lateral segment. In early fetal life, the liver is large and gut is small; but as the fetus grows, the liver stays relatively small while the gut grows rapidly. The three hepatic arteries fuse at the hilum of the liver, and some of them regress while the enteric branches expand. Thus emerges the conventional hepatic arterial anatomy where the liver is supplied by right and left hepatic arteries after bifurcation of a proper hepatic artery, a branch of the common hepatic artery (CHA) beyond the origin of gastro duodenal artery (Figure 1). This pattern is seen in slightly more than 50% of individuals with many other possible variations[5]. If some of the embryonic hepatic arteries do not regress or fail to detach from their embryonic source, it may result in "aberrant" (variant) hepatic arteries. An aberrant hepatic artery is an artery supplying the liver but arising from a source outside the conventional anatomy (*i.e.,* proper hepatic artery located in the celiac circulation). An aberrant hepatic artery may be "replacing" or "accessory". An aberrant replacing hepatic artery substitutes the normal (usual) hepatic artery that is absent. An aberrant accessory hepatic artery is present in addition to one that is normally (usually) present. Some sort of aberrant (variable) hepatic artery, either replacing or accessory, occurs in approximately 42% of individuals. The Michel classification of hepatic arterial anatomy describes ten subtypes with the variants II, III, V and IX being the most significant ones with respect to LDLT. Table 1 describes the different subtypes and their frequency of occurrence[24].

Both arterial-phase CT and MRI have a diagnostic accuracy comparable to that of catheter angiography and intra-operative finding[13,25,26]. However, Schroeder *et al*[4] found CT to be more accurate in detecting variations in vascular anatomy. This is probably related to the inherently superior spatial resolution of CT compared to MR. Hepatic artery thrombosis (HAT) is one of the most dreaded complications of LT and can be drastically decreased by excluding grafts with unfavorable anatomy[27]. In the past, a potential graft with a narrow hepatic artery of less than 2 mm in diameter was regarded as a contraindication for LDLT due to the high risk of HAT. However, with developments in microvascular surgical techniques, this rarely disqualifies a potential donor from providing the graft[28]. Grafts with multiple arteries and several arterial variants are often not preferred by the surgeon. Grafts with multiple arterial feeders are often found to perfuse poorly in the recipient and may need an alternative inflow source such as an aorto-hepatic interposition graft[29]. A short right hepatic artery is another variant that may often make the anastomosis technically difficult and need extensive reconstructive surgery.

In right lobe grafts, it is important to determine the origin of the segment IV artery[30]. There is some inconsistency in the nomenclature and origin of this artery; it has been variably described as middle hepatic artery (MHA), medial segment artery, left medial artery, and segment IV artery. Anatomical studies suggest that MHA most often arise from the left hepatic artery (LHA) (approximately 60%) while CT based studies show 62.5% of the arterial supply to segment 4 originating from the right hepatic artery (RHA[31]. While harvesting a right-sided graft, it is mandatory to preserve MHA to ensure adequate regeneration and function of the residual liver in the donor. Prior knowledge of MHA variation is especially important since its origin is very difficult to identify intra-operatively unless extensive dissection is done around the porta hepatis. During right lobectomy, the surgeon transects the right hepatic artery, distal to the branches to segment IV and hence it is also prudent to seek the length of the RHA beyond the origin of the segment IV artery so as to ensure there is adequate length of graft hepatic artery to anastomose with the recipient

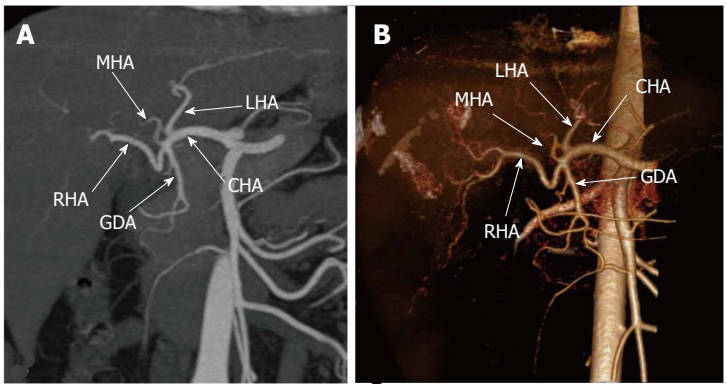

Figure 2 Maximum intensity projection (A) and volume rendered (B) images generated from a computed tomography angiogram shows a variant arterial anatomy. The CHA arises from the celiac trunk, it gives off the LHA followed by the GDA and MHA; thereafter it continues as the RHA in (A) MIP and (B) volume rendered images generated from a CT angiogram. CHA: Common hepatic artery; LHA: Left hepatic artery; GDA: Gastroduodenal artery; RHA: Right hepatic artery; MHA: Middle hepatic artery.

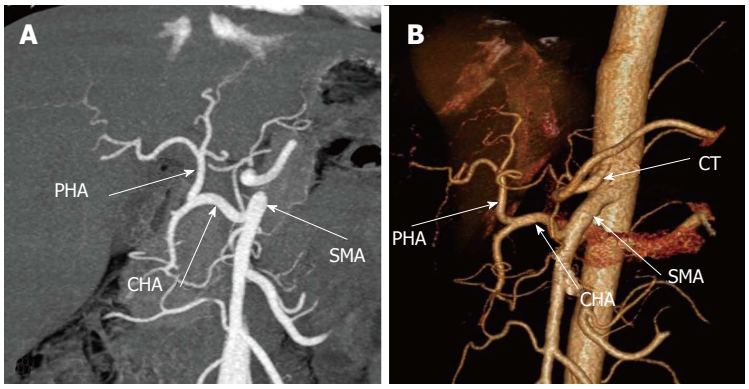

Figure 3 Michel type IX variant is shown in the (A) maximum intensity projection and (B) volume rendered images generated from a computed tomography angiogram. There is a replaced CHA that comes off the SMA. CHA: Common hepatic artery; SMA: Superior mesenteric artery; PHA: Proper hepatic artery; CT-celiac trunk).

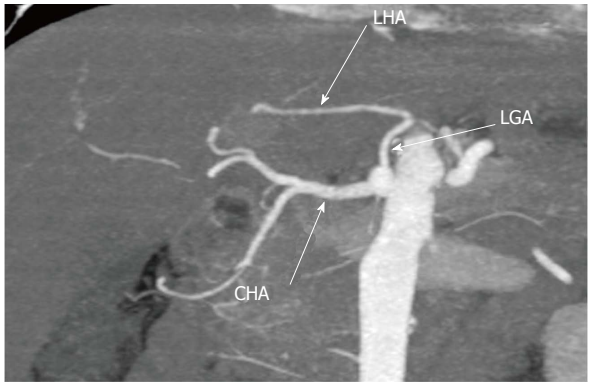

Figure 4 Coronal maximum intensity projection generated from a computed tomography angiogram shows Michel type II variant with a replaced left hepatic artery coming off the left gastric artery. LHA: Left hepatic artery; LGA: Left gastric artery; CHA: Common hepatic artery.

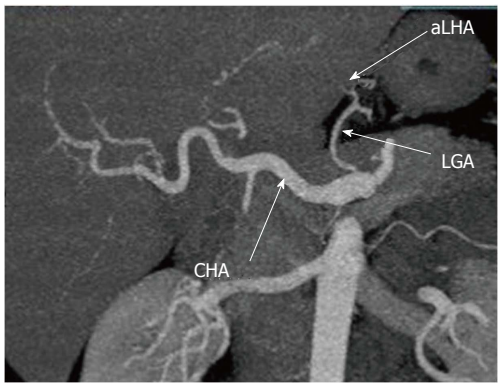

Figure 5 Coronal maximum intensity projection generated from a computed tomography angiogram shows Michel type V variant where an accessory left hepatic artery arises from the left gastric artery. LHA: Left haptic artery; LGA: Left gastric artery; aLHA: Accessory left hepatic artery.

hepatic artery. In left lobe resection, MHA arising from RHA will necessitate two anastomoses: one for the LHA and another one for the MHA.

When the RHA or LHA take off before the origin of the gastroduodenal artery (Figure 2) or if there is a trifurcation of the CHA into the gastroduodenal, RHA and LHA, clamping of the CHA can compromise perfusion to the stomach and duodenum. Such an anomaly can even preclude the subject from being a donor[5]. The main hepatic artery may take an aberrant course deep to the portal vein if it arises from the superior mesenteric artery instead of the celiac trunk (Michel type IX, Figure 3). This variation, when present in the recipient often mandates a change in the usual sequence of vascular anastomoses, such that the portal venous anastomosis will have to follow (rather than precede) the arterial anastomosis[29]. A similar significant variation to be sought in the recipient is a replaced or accessory LHA arising from the left gastric artery (Michel type Ⅱ and Ⅴ, Figure 4 and 5 respectively); this artery would require to be ligated at its origin while removing the native liver to avoid major bleeding. A replaced right hepatic artery arising from the SMA (Michel type Ⅲ, Figure 6) is a significant variation when present in the donor or the recipient as it means additional steps are required for both harvesting and reimplanting the graft[5].

Left lateral segment and left lobe grafts are associated with a higher incidence of arterial complications[32].

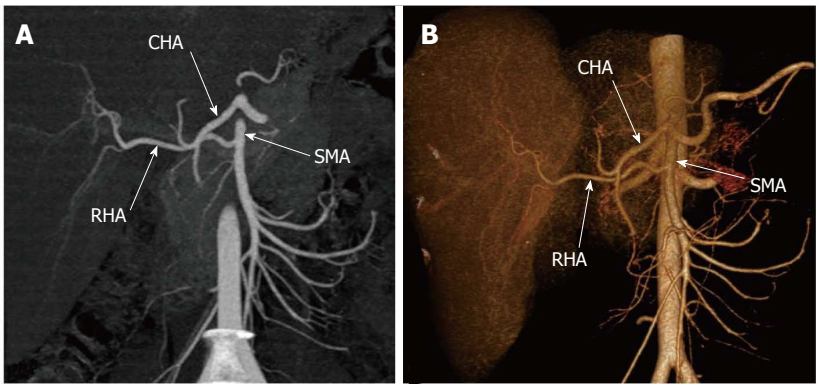

Figure 6 Maximum intensity projection (A) and volume rendered (B) images generated from a computed tomography angiogram shows Michel type III variant with a replaced right hepatic artery arising from the superior mesenteric artery. RHA: Right hepatic artery; SMA: Superior mesenteric artery; CHA: Common hepatic artery.

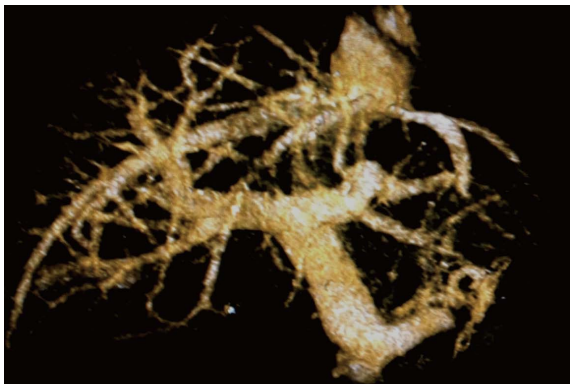

Figure 7 Normal portal and hepatic venous anatomy is demonstrated in this 3D volume rendered image. The MPV divides into RPV and LPV. The RPV then divides into the RAPV and RPPV. The three hepatic veins open into the IVC. MPV: Main portal vein; LPV: Left portal vein; RPV: Right portal vein; RAPV: Right anterior portal vein; RPPV: Right posterior portal vein.

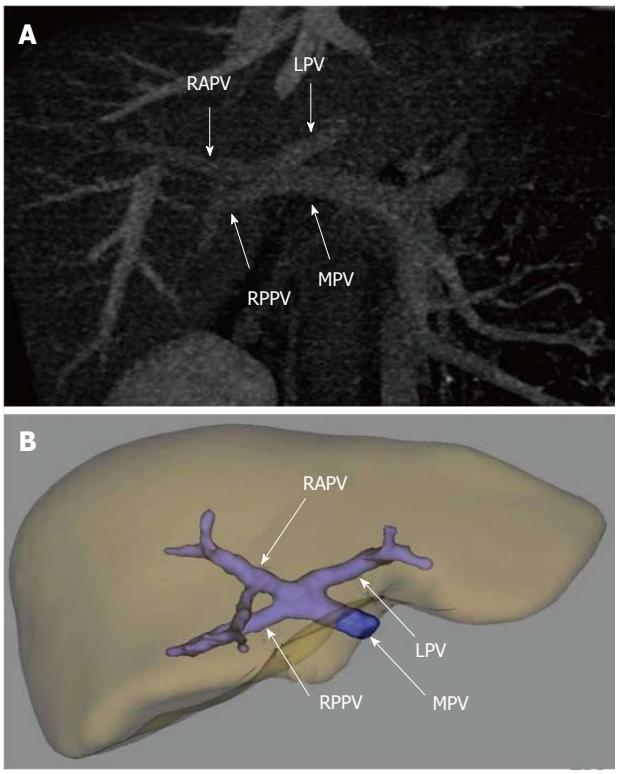

Figure 8 (A) Maximum intensity projection and (B) 3 D volume rendered image generated using dedicated software demonstrates trifurcation of the main portal vein into the right anterior portal vein, right posterior portal vein and left portal vein. MPV: Main portal vein; RAPV: Right anterior portal vein; RPPV: Right posterior portal vein; LPV: Left portal vein.

Complications such as HAT that results in hepatic infarction and bile duct ischemia are more frequent with such grafts[32]. Anastomotic bleeding, stenosis and pseudoaneurysm formation are some of the other common arterial complications. Significant difference in caliber between donor and recipient arteries, small caliber of the anastomosed vessels, clamp injury and presence of an interpositional conduit are among the usual causes for anastomotic stenosis and HAT[33].

PORTAL VENOUS SYSTEM

The normal portal venous anatomy (Figure 7) consists of the main portal vein and its two branching vessels, the right and left portal veins[34]. The right portal vein is a short trunk that further divides into anterior and posterior branches. The left portal vein has a horizontal segment that turns at right angles at the base of the umbilical fissure to form the umbilical segment. The umbilical segment then gives branches to segments II to IV while the caudate lobe receives direct supply from the transverse segment.

The portal venous anatomy is best appreciated in the coronal images[5]. Portal venous variants account for approximately 20% of all significant vascular variants[34]. Up to 20% of potential donors may get excluded from surgery due to variations in portal vein anatomy[35]. The angle of portal vein branching is significant to the recipient. If the angle is too acute, the graft may surround and consume the vein during the regeneration process leading to ischemia and infarction[5]. In such cases, vascular reconstruction may have to be performed. Adequate length of the portal vein is also important for satisfactory anastomosis. A significant portal venous variant to note in a right lobe graft is the presence of portal venules to segment IV as they are important collateral pathways. This knowledge is important for anastomosis and to avoid bleeding and ischemia.

A vital variation is the absence of the right portal vein that is seen in 16.5% of right anterior, right poste-

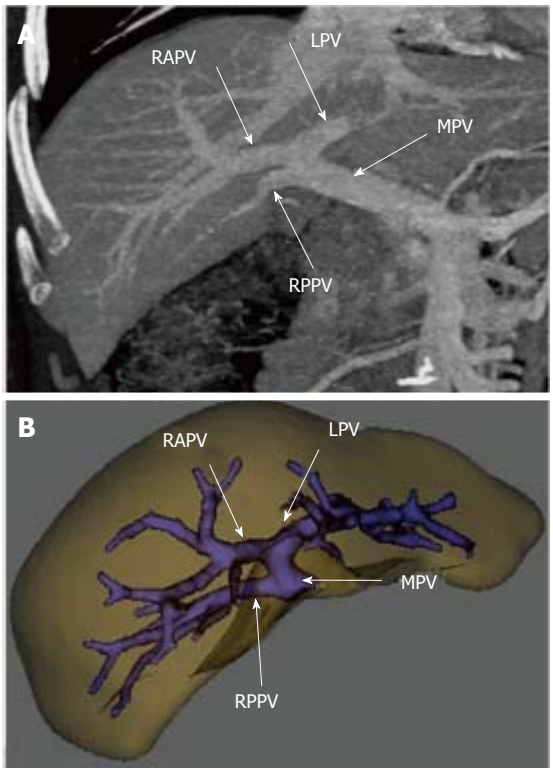

Figure 9 (A) maximum intensity projection and (B) 3 D volume rendered image generated using dedicated software shows an early origin of right posterior portal vein from the main portal vein that later bifurcates in to the right anterior portal vein and left portal vein. RPPV: Right posterior portal vein; MPV: Main portal vein; RAPV: Right anterior portal vein; LPV: Left portal vein.

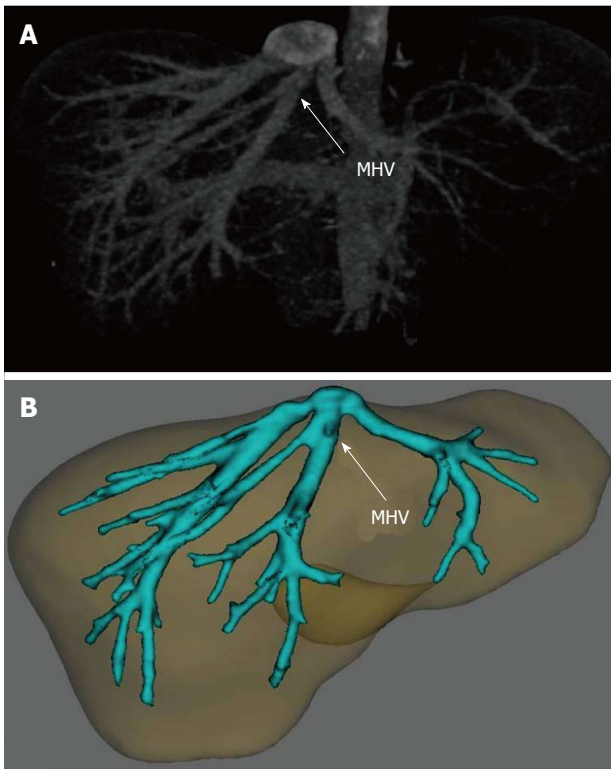

Figure 10 (A) maximum intensity projection and (B) 3 D volume rendered image generated using dedicated software demonstrates early bifurcation of the middle hepatic vein with large veins draining into it from the right hepatic lobe. MHV: Middle hepatic vein.

rior and left portal venous branches (Figure 8) or direct origin of the right posterior portal vein (RPPV) from the main portal vein (Figure 9) or a right anterior portal vein (RAPV) arising from the left portal vein[36]. Trifurcation of the portal vein is important to note pre-operatively as it can often be a contra-indication for surgery or may need alternate surgical planning. For instance, in a right lobe graft, this variant as well as a direct origin of RPPV would necessitate anastomosis of two portal veins, which increases the risk of post-operative portal vein thrombosis[35]. If the RAPV is arising from the left portal vein, the distance of its origin from the bifurcation should be noted. Such donors need the portal vein to be transected distal to the RAPV. Hence there is a possibility that this plane of transection may be intraparenchymal leading to an extra-parenchymal length insufficient for anastomosis to the recipient's portal vein. A left portal vein arising from the RAPV may cause a technical problem during right lobe transplant due to the short length of the graft portal vein.

Diameter of the portal vein is also important and should be measured at the level of the expected anastomosis. The presence or absence of portal vein thrombosis in the recipient can also impact the suitability for a transplant[37]. Acute thrombus may be recanalized by intra-operative thrombectomy. However in case of chronic thrombosis or cavernoma formation, careful scrutiny is required to identify a suitable vein for anastomosis.

Both CT and MR are equally good in providing anatomical information on the portal venous system[4]. Complications that may occur with respect to the portal veins in the recipient are stenosis and thrombosis. Portal vein stenosis tends to develop at the anastomosis while thrombosis is seen with vessel malalignment, differences in caliber of the anastomosed vessels causing turbulent flow or prior thrombosis in the recipient[33].

HEPATIC VENOUS SYSTEM

The plane of transection is determined by the anatomy of the hepatic veins. Hence a detailed hepatic venous mapping that includes the number, size and drainage pattern of the hepatic veins is imperative in CT/MR evaluation of the donor. The normal hepatic venous system comprises of three main venous tributaries that drain into the inferior vena cava (IVC) (Figure 7). Usually, the right hepatic vein (RHV) drains liver segments V-Ⅶ, the MHV drains segments Ⅳ, V and Ⅷ and the LHV drains segments Ⅱ and Ⅲ[38]. Variations in hepatic venous anatomy have been reported in up to 30% of patients[35]. The site of drainage of the middle hepatic vein is particularly relevant. In 60% of cases, the MHV and LHV form a common trunk that drains into the IVC[38].

In right lobe dissection, the surgical plane typically courses 1 cm to the right of the MHV[12]. Early bifurca-

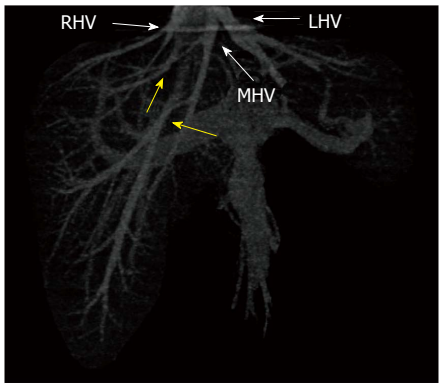

Figure 11 Three-dimensional volume rendered image generated from venous phase computed tomography scan show a relatively small right hepatic vein draining only the dome of the right lobe and two accessory right hepatic veins (yellow arrows). In this case, the caudal accessory right hepatic vein drains the bulk of the right lobe. RHV: Right hepatic vein; MHV: Middle hepatic vein; LHV: Left hepatic vein.

tion of the MHV and large branching veins draining into it from the right lobe (Figure 10) will necessitate alteration of the transection plane as well as separate anastomosis of segment V and Ⅷ branches to the IVC using conduits. Early confluence of the hepatic veins may also result in a small graft that may not be adequate to maintain the metabolic function in the recipient[5,35]. In case of left lobe grafts, the anatomy of segment Ⅳ venous drainage is particularly important. If the segment Ⅳ vein is not patent, the graft would get congested with hepatofugal portal venous flow and eventual graft atrophy. The draining veins of segment Ⅳ can be highly variable, multiple in number and small in caliber often draining into the middle hepatic vein.

In LDLT, special attention must be paid to the presence of accessory hepatic veins draining directly into the IVC that have to be dissected separately and can be a source of excessive haemorrhage if not identified preoperatively[5]. An accessory RHV occurs in 52.5% of patients, two accessory veins in 12% (Figure 11) and an accessory vein draining the caudate lobe in 12% with the most common being the accessory inferior RHV[39,40]. The size of the accessory hepatic vein and its distance from the confluence of the hepatic veins into the IVC should be reported. If this distance is more than 4 cm, it may be difficult to surgically implant both veins in the recipient with a single partially occluded clamp on the IVC[5]. Small accessory veins, usually less than 3 mm in size may be suitable for ligation while a similar treatment of the larger ones can lead to congestion of the graft.

The hepatic veins are best evaluated in the axial plane with the MHV as the landmark. In case of multiple hepatic veins, the vein that extends from hepatic venous confluence with the IVC towards the gall bladder fossa is considered the MHV. CT and MRI are equally good in venous mapping[4]. However, the authors feel most confident about this interpretation when reading non-contrast T1W images. Complications that may occur with respect to the hepatic veins are stenosis and thrombosis,

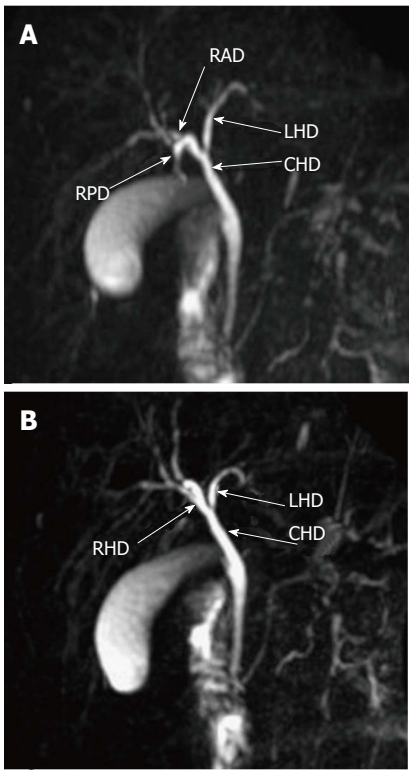

Figure 12 Thick slab magnetic resonance cholangiopancreatography images in different coronal planes demonstrates the normal biliary anatomy where right hepatic duct is formed by fusion of the right anterior duct and right posterior duct. The RHD then joins the LHD to form the CHD. RHD: Right hepatic duct; RAD: Right anterior duct; RPD: Right posterior duct; LHD: Left hepatic duct; CHD: Common hepatic duct.

usually at the site of anastomosis. Again, size discrepancy between the anastomosed vessels is a predisposing factor. Post transplant regeneration of the graft can compresses short and narrow venous anastomoses leading to graft congestion and dysfunction[41]. Various graft materials have been used to create hepatic venous reconstructions allowing for wide ostium anastomoses that can then withstand compression during regeneration[42].

BILIARY SYSTEM

Conventional biliary tract anatomy (Figure 12) is as follows: The right anterior duct drains segments V and Ⅷ, and the right posterior duct drains segments Ⅵ and Ⅶ. The right hepatic duct is formed by fusion of the anterior duct and the posterior duct. The left hepatic duct drains segments Ⅱ, Ⅲ and Ⅳ. The duct draining the caudate lobe usually joins the origin of the right or left hepatic ducts[43]. The right and left hepatic bile ducts merge to form the common hepatic duct (CHD). The cystic duct drains into the CHD below the confluence of right and left hepatic ducts to form the common bile duct. This normal biliary anatomy is seen in only 58% of individuals[44]. The frequency of variations is very high in biliary anatomy[45]. The more frequently encountered and clinically significant variations of biliary anatomy are (1) right posterior duct draining into the left hepatic

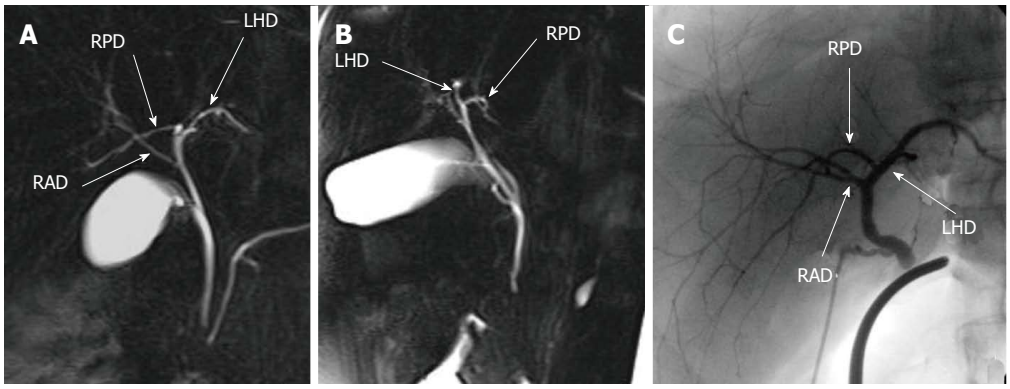

Figure 13 Thick slab coronal magnetic resonance cholangiopancreatography images at 15 degrees left anterior oblique (A) and 80 degrees right anterior oblique (B) projections demonstrate a variant biliary anatomy- the magnetic resonance cholangiopancreatography drains into the magnetic resonance cholangiopancreatography, note the intra-operative cholangiographic appearance of the same variant (C). RHD: Right hepatic duct; RAD: Right anterior duct; RPD: Right posterior duct; LHD: Left hepatic duct; CHD: Common hepatic duct.

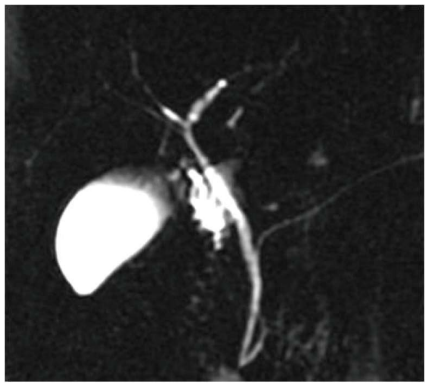

Figure 14 Thick slab magnetic resonance cholangiopancreatography shows a variant biliary anatomy- trifurcation pattern with a common confluence of the right posterior duct right anterior duct and left hepatic duct. RPD: Right posterior duct; RAD: Right anterior duct; LHD: Left hepatic duct.

duct (Figure 13) seen in 13%-19% of individuals[43]; (2) trifurcation pattern where there is confluence of the right posterior, right anterior, and left hepatic ducts (Figure 14) that is seen in 11 % of the population[44]; and (3) the right posterior duct draining directly into the common hepatic duct (Figure 15) or common bile duct. Several other biliary variations involving aberrant and accessory ducts have been described in the literature. An aberrant duct is the only duct draining a particular hepatic segment while an accessory duct is an additional duct draining the same area of liver. Failure to recognize even minor variations can cause post-operative complications like bilomas or biliary leaks that can be extremely difficult to manage.

CT and MR imaging assessment of the biliary tract in potential liver donors include magnetic resonance cholangiopancreatography (MRCP), intravenous administration of liver-specific contrast agents in excretory MR (eMRCP) and CT cholangiogram (CTCh). As the contrast agent used in CTCh is limited to a few countries and not yet available at our institution, MR remains the imaging modality of choice in assessing the biliary tree. The main stay of MRCP in the donor evaluation is a high quality respiratory-triggered thin slice coronal 3D MRCP sequence. In patients with irregular breathing, thin slice 2D MRCP acquisitions in dead coronal as well as right anterior oblique and left anterior oblique projections may be obtained with breath hold. Each of these breath-hold sequences typically takes 15-20 s. Thick slab MRCP in multiple radial planes is optional. We perform eMRCP with gadoxetate disodium (a hepatocyte-specific MR contrast agent) administration followed by three dimensional image acquisitions, 20 min from injection, in all the three orthogonal planes using a 3D fast spoiled gradient echo sequence.

CTCh involves the use of ionizing radiation and the slow infusion of a dilute biliary contrast agent (cholografin). Although acquisition of images is quicker compared to MR, it needs a longer preparation time and there is higher potential for adverse drug reactions with CTCh. The advantages of CTCh include higher spatial resolution (Figure 16) and a lower cost[46]. CTCh allows for depiction to at least the second order intrahepatic biliary ducts. Schroeder *et al*[4] found that MRCP revealed only about one third of the biliary variants found on CTCh. Yeh *et al*[46] also found eMRCP inferior to CTCh in visualization of second order bile ducts. Some studies have shown complete agreement between CTCh and endoscopic retrograde cholangiopancreatography[47,48]. MR imaging of the biliary ducts in general is better suited in the evaluation of pathological states wherein biliary ductal dilatation occurs secondary to obstructing calculi or masses[49] while normal caliber bile ducts of potential donors are better demonstrated with CTCh. The limitations of MR-specific artifacts (*e.g.*, pseudo-obstruction of the common hepatic duct caused by pulsatile vascular compression by the right hepatic artery) do not exist for CTCh[50].

Variations in biliary anatomy have a statistically significant association with variations in portal venous anatomy[51]. Biliary tract complications after liver transplantation have been reported in 10%-25% of cases, proving fatal in up to 10% of complicated cases[52,53]. Biliary complications essentially occur in the form of biliary leaks and anastomotic strictures with the presence of more

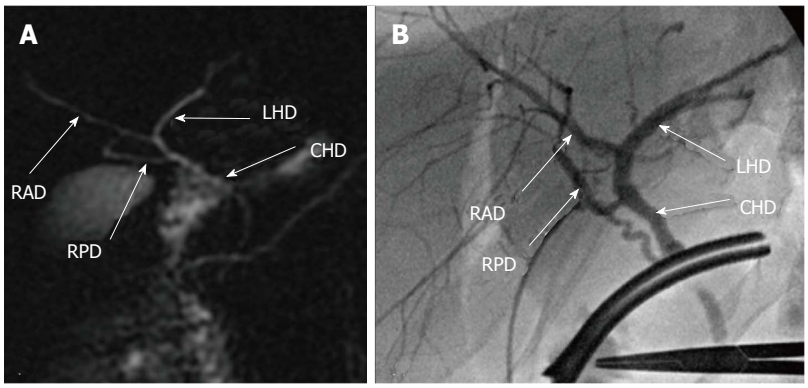

Figure 15 (A) Magnetic resonance cholangiopancreatography and (B) intra-operative cholangiogram in the same patient demonstrates a variant biliary anatomy-the right posterior duct drains directly into the common hepatic duct. RPD: Right posterior duct; RAD: Right anterior duct; LHD: Left hepatic duct; CHD: Common hepatic duct.

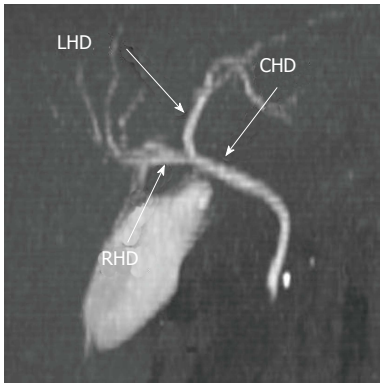

Figure 16 Maximum intensity projection image generated from a computed tomography cholangiogram. Normal biliary anatomy is demonstrated here. LHD: Left hepatic duct; RHD: Right hepatic duct; CHD: Common hepatic duct.

than one graft bile duct and more than one anastomosis increasing the frequency of biliary complications[54]. A bile leak from the cut surface of a graft is typically self-limiting. Biliary strictures may develop at the anastomosis or may occur at non-anastomotic sites secondary to ischaemia caused by hepatic artery compromise[55].

HEPATIC PARENCHYMA

Evaluation of the hepatic parenchyma is mainly to identify and characterize focal liver lesions and exclude diffuse liver disease. Focal lesions have been identified in up to 18% of donor liver evaluations[25]; however most of them are benign cysts or haemangiomas. MR is superior in characterization of focal liver lesions[56,57]. Fatty liver is the most common diffuse liver disease that may preclude an outwardly healthy patient from being a donor. Grafts with more than 30% fatty change carries high risk of graft non-function in the recipient and liver dysfunction in the donor[58]. Hence pre-operative detection and quantification of fatty liver is vital. Uniform fatty change of the liver is easier to quantify; however hepatic steatosis can often be heterogeneous. Generally, fatty changes are more pronounced in the right lobe than in the left as former receives greater amount of portal venous blood flow.

Hepatic steatosis is identified on CT scan as reduced attenuation relative to the spleen (Figure 17). This is best evaluated on a non-contrast study as relative densities of the liver and spleen can vary on post contrast scans depending on the phase of image acquisition[27]. The attenuation value of normal liver on unenhanced CT ranges between 55 and 65 Hounsfield units (HU) and is generally at least 8 HU higher relative to the spleen; the liver is regarded as fatty when the liver attenuation is at least 10 HU less than the spleen[59]. This method has high sensitivity (88%-95%) and specificity (90%-99%)[60]. Liver attenuation values also reflect the severity of fatty change. Hepatic CT attenuation value below 48 HU may be considered as fatty liver and a value of 40 HU represents approximately 30% fatty change[61]. With more than 30% macrovesicular steatosis the hepatic parenchyma appears hypoattenuating compared to the hepatic vessels on non-enhanced CT scan[62]. Similarly, a hepatic to splenic attenuation ratio of 0.8 is almost 100% specific for moderate to severe (> 30%) macrovesicular steatosis[63]. According to Limanond *et al*[64], a hepatic-splenic attenuation difference of more than 5 HU was consistent with absence of significant macrovesicular steatosis (0%-5%), a difference of -10 to 5 HU was suggestive of mild to moderate steatosis (6%-30%). The same authors reported a specificity of 100% for the detection of moderate to severe (> 30%) macrovesicular steatosis when the hepatic-splenic attenuation difference was less than -10 HU. Dual energy CT can also be used in detecting and quantifying hepatic steatosis but there is limited literature to validate its utility in this context.

MR is an extremely sensitive modality in detection and characterization of hepatic steatosis. Fatty liver is seen as increased signal intensity on conventional T1W spin echo sequence. However, these sequences are seldom used for hepatic fat evaluation due to their poor sensitivity. Detection and quantification of fatty liver is much better performed with chemical shift imaging or MR proton spectroscopy[27]. Chemical shift imaging utilizes the differences of resonance frequencies between water and fat

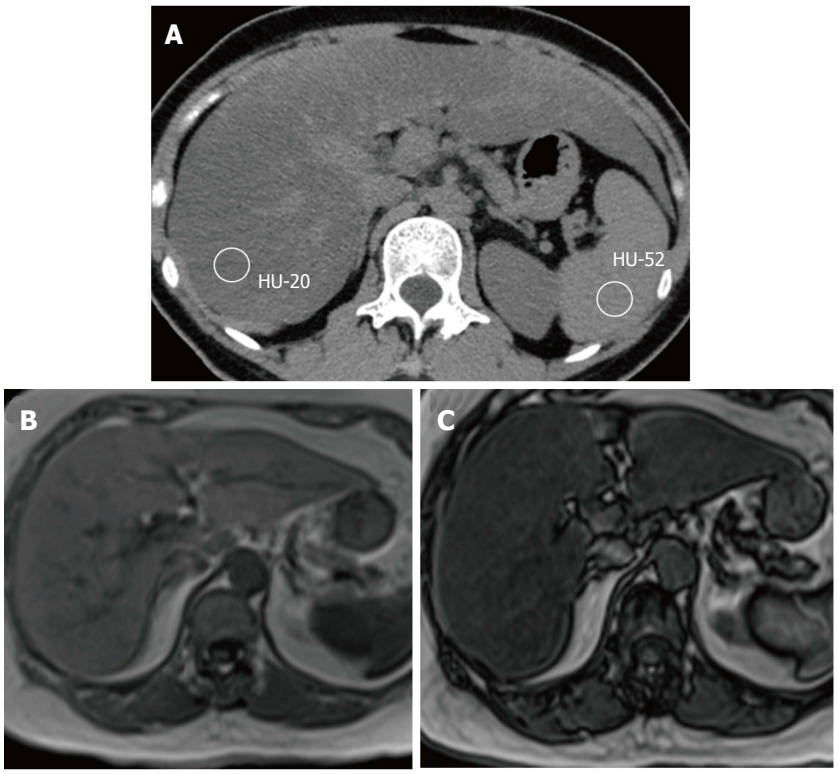

Figure 17 Diffuse hepatic steatosis is demonstrated here. In the non-enhanced computed tomography scan (A) the hepatic parenchyma has significantly lower attenuation than spleen. The out phase magnetic resonance imaging image (C) shows a drop in the hepatic signal intensity compared to that in the in-phase image (B).

proton signals to quantify fat accumulation. By acquiring images at echo times when water and fat signals are in-phase and out-of-phase, the extent of hepatic steatosis can be quantified based on signal change[65]. Loss of signal on out-of-phase images suggests fatty liver (Figure 17). Nowadays, the in-phase and out-of-phase images are obtained near simultaneously (*i.e.,* less than a few milliseconds apart) using breath-hold gradient-echo sequences. The spleen or skeletal muscle can be used as an internal standard for calculating the percentage of relative signal loss of the liver[66]. This technique provides a relatively simple way of estimating the degree of steatosis. Three circular regions of interest (ROI) can be placed in the liver; two in the right lobe and one in the left with three ROI placed within the spleen at anatomically matched levels. The mean signal intensity can then be calculated using the formula: $[(SI_{\text{in-phase}} - SI_{\text{out-of-phase}})/SI_{\text{in-phase}}] \times 100$ where SI = average liver signal intensity/average spleen intensity[67]. Fischer *et al*[68] found that this dual echo MR imaging technique for liver fat quantification was actually superior to histopathological analysis. This method is accurate in detection of hepatic fat fraction when it is in the 15%-50% range. Although this method is technically simple and highly sensitive, absolute quantification of hepatic fat is not possible with this technique. Fast spin echo T2 weighted sequences with and without fat saturation may be used in a similar fashion to estimate fat fraction of the liver.

MR spectroscopy is the most accurate non-invasive method of evaluating fatty liver. It can quantify the absolute fat concentration in the liver and is highly sensitive to small changes in hepatic triglyceride levels.

LIVER VOLUME

The size of the graft is one of the most crucial factors that have to be taken into account when considering LDLT[69]. The normal liver weighs between 2%-2.7% of the total body weight; for LDLT, a graft that is at least 0.8% of the recipient's body weight ratio is considered adequate. Liver remnant volume of 30%-40% of the total liver volume is adequate for donor survival, this is provided the liver parenchyma is normal[70]. The minimum graft volume required to provide sufficient functional hepatocytes to the recipient is about 40% of the standard liver mass[71], which can be calculated using the body surface area[72].

If the graft is too large, haemostasis, vascular anastomosis and abdominal closure may prove problematic[20]. A graft that is too small has increased likelihood of dysfunction secondary to inadequate functional hepatic mass and possible excessive portal perfusion[73]. A small for size graft is also prone to torsion and may necessitate additional surgical maneuvers like fixation of falciform ligament to anterior aspect of the peritoneal cavity[27].

For volumetric analysis, any cross-sectional imaging that provides sufficient contrast between the liver parenchyma and the surrounding tissues can be used. This is achievable both with portal venous phase CT and T1-weighted MR, with CT being marginally superior due to inherently sharper images obtained with it[4]. Hepatic volumes can be determined by manually tracing the contours of the entire liver and the intended graft excluding the large vessels, major fissures and the gallbladder fossa using contiguous CT or MR images[70]. The cross-sectional area within the region of interest is determined on

each slice and the sum of all the slices estimates the liver volume. 3D software reconstruction of the liver can be performed which allows the surgeon to better determine the size and shape of the intended graft by performing virtual hepatectomies. Dedicated software programs also allow calculation of the potential residual volume in the donor and the potential volume in the recipient by clicking a few buttons[74]. Studies have shown that automated volumetric results are comparable to manual volumetric results with the former being more efficient[75,76]. Usually the calculated liver volume over-estimates the weight of the graft[70], this is most likely due to lack of perfusion of the graft when it is weighed intra-operatively.

CONCLUSION

As discussed above, CT and MR are complementary modalities that allow for a comprehensive non-invasive assessment of a potential liver donor while either of these modalities is adequate for pre-transplant radiological assessment of a potential recipient. Knowledge of the broad indications and contraindications to qualify as a recipient for LDLT is essential for the radiologist reporting scans in a pre-transplant patient. Similarly, awareness of the various anatomical variations and pathological states in the donor is essential for the radiologist to generate a meaningful report of his/her observations. A radiologist oblivious to these facts would not be able to effectively harness the immense potential of non invasive imaging modalities in contributing towards a LT program.

Both CT and MR are comparable in terms of illustration of vascular anatomy. MRCP and in particular eMRCP are extensively used for evaluating the biliary anatomy of the potential donor. Few studies have shown CTCh to be superior to MRI for this purpose, but limited availability of the CT cholangiographic contrast agent limits the application of this technique. MR outperforms CT in evaluation of focal liver lesions and diffuse parenchymal disease. Volumetric analysis is marginally better with CT compared to MRI.

In most successful LDLT programs the radiologist is an integral part of the transplant team and is present during transplant planning discussions. Only a cross-fertilization of knowledge in their respective areas can lead to a high level of predictability of transplant results and an ongoing increase in success of the program.

ACKNOWLEDGMENTS

Dr. Anand Kumar Singh, Department of Radiology, Massachusetts General Hospital, Boston, United States; and Ajith AV, CT applications specialist, Philips Healthcare, Singapore.

REFERENCES

1 **Adam R**, McMaster P, O'Grady JG, Castaing D, Klempnauer JL, Jamieson N, Neuhaus P, Lerut J, Salizzoni M, Pollard S, Muhlbacher F, Rogiers X, Garcia Valdecasas JC, Berenguer J, Jaeck D, Moreno Gonzalez E. Evolution of liver transplantation in Europe: report of the European Liver Transplant Registry. *Liver Transpl* 2003; **9**: 1231-1243 [PMID: 14625822 DOI: 10.1016/j.lts.2003.09.018]

2 **Settmacher U**, Neuhaus P. [Innovations in liver surgery through transplantation from living donors]. *Chirurg* 2003; **74**: 536-546 [PMID: 12883803 DOI: 10.1007/s00104-003-0675-x]

3 **Zhuang ZG**, Qian LJ, Gong HX, Zhou Y, Chai WM, Li QG, Xu JR. Multidetector computed tomography angiography in the evaluation of potential living donors for liver transplantation: single-center experience in China. *Transplant Proc* 2008; **40**: 2466-2477 [PMID: 18929770 DOI: 10.1016/j.transproceed.2008.08.031]

4 **Schroeder T**, Malagó M, Debatin JF, Goyen M, Nadalin S, Ruehm SG. "All-in-one" imaging protocols for the evaluation of potential living liver donors: comparison of magnetic resonance imaging and multidetector computed tomography. *Liver Transpl* 2005; **11**: 776-787 [PMID: 15973711 DOI: 10.1002/lt.20429]

5 **Sahani D**, Mehta A, Blake M, Prasad S, Harris G, Saini S. Preoperative hepatic vascular evaluation with CT and MR angiography: implications for surgery. *Radiographics* 2004; **24**: 1367-1380 [PMID: 15371614 DOI: 10.1148/rg.245035224]

6 **O'Leary JG**, Lepe R, Davis GL. Indications for liver transplantation. *Gastroenterology* 2008; **134**: 1764-1776 [PMID: 18471553 DOI: 10.1053/j.gastro.2008.02.028]

7 **Farrell GC**. Non-alcoholic steatohepatitis: what is it, and why is it important in the Asia-Pacific region? *J Gastroenterol Hepatol* 2003; **18**: 124-138 [PMID: 12542595 DOI: 10.1046/j.1440-1746.2003.02989.x]

8 **Kamath PS**, Wiesner RH, Malinchoc M, Kremers W, Therneau TM, Kosberg CL, D'Amico G, Dickson ER, Kim WR. A model to predict survival in patients with end-stage liver disease. *Hepatology* 2001; **33**: 464-470 [PMID: 11172350 DOI: 10.1053/jhep.2001.22172]

9 **Mazzaferro V**, Regalia E, Doci R, Andreola S, Pulvirenti A, Bozzetti F, Montalto F, Ammatuna M, Morabito A, Gennari L. Liver transplantation for the treatment of small hepatocellular carcinomas in patients with cirrhosis. *N Engl J Med* 1996; **334**: 693-699 [PMID: 8594428 DOI: 10.1056/NEJM199603143341104]

10 **Yao FY**, Ferrell L, Bass NM, Watson JJ, Bacchetti P, Venook A, Ascher NL, Roberts JP. Liver transplantation for hepatocellular carcinoma: expansion of the tumor size limits does not adversely impact survival. *Hepatology* 2001; **33**: 1394-1403 [PMID: 11391528 DOI: 10.1053/jhep.2001.24563]

11 **Valentín-Gamazo C**, Malagó M, Karliova M, Lutz JT, Frilling A, Nadalin S, Testa G, Ruehm SG, Erim Y, Paul A, Lang H, Gerken G, Broelsch CE. Experience after the evaluation of 700 potential donors for living donor liver transplantation in a single center. *Liver Transpl* 2004; **10**: 1087-1096 [PMID: 15349997 DOI: 10.1002/lt.20223]

12 **Marcos A**, Ham JM, Fisher RA, Olzinski AT, Posner MP. Surgical management of anatomical variations of the right lobe in living donor liver transplantation. *Ann Surg* 2000; **231**: 824-831 [PMID: 10816625 DOI: 10.1097/00000658-200006000-00006]

13 **Lee VS**, Morgan GR, Teperman LW, John D, Diflo T, Pandharipande PV, Berman PM, Lavelle MT, Krinsky GA, Rofsky NM, Schlossberg P, Weinreb JC. MR imaging as the sole preoperative imaging modality for right hepatectomy: a prospective study of living adult-to-adult liver donor candidates. *AJR Am J Roentgenol* 2001; **176**: 1475-1482 [PMID: 11373217 DOI: 10.2214/ajr.176.6.1761475]

14 **Tanaka K**, Uemoto S, Tokunaga Y, Fujita S, Sano K, Nishizawa T, Sawada H, Shirahase I, Kim HJ, Yamaoka Y. Surgical techniques and innovations in living related liver transplantation. *Ann Surg* 1993; **217**: 82-91 [PMID: 8424706 DOI: 10.1097/00000658-199301000-00014]

15 **Couinaud C**. Surgical anatomy of the liver revisited. Paris, France: Coinaud, 1989: 130-132
16 **Nadalin S**, Bockhorn M, Malagó M, Valentin-Gamazo C, Frilling A, Broelsch CE. Living donor liver transplantation. *HPB* (Oxford) 2006; **8**: 10-21 [PMID: 18333233 DOI: 10.1080/13651820500465626]
17 **Tüzüner A**, Ersöz S, Hazinedaroğlu S, Karayalçin K, Yerdel MA, Anadol E. Technical implications of living donor liver transplantation: a single-center experience. *Transplant Proc* 2004; **36**: 212-213 [PMID: 15013349 DOI: 10.1016/j.transproceed.2003.11.068]
18 **Chen WH**, Xin W, Wang J, Huang QJ, Sun YF, Xu Q, Yu SN. Multi-slice spiral CT angiography in evaluating donors of living-related liver transplantation. *Hepatobiliary Pancreat Dis Int* 2007; **6**: 364-369 [PMID: 17690030]
19 **Makuuchi M**, Sugawara Y. Technical progress in living donor liver transplantation for adults. *HPB* (Oxford) 2004; **6**: 95-98 [PMID: 18333057 DOI: 10.1080/13651820410032914]
20 **Redvanly RD**, Nelson RC, Stieber AC, Dodd GD. Imaging in the preoperative evaluation of adult liver-transplant candidates: goals, merits of various procedures, and recommendations. *AJR Am J Roentgenol* 1995; **164**: 611-617 [PMID: 7863881 DOI: 10.2214/ajr.164.3.7863881]
21 **Shellock FG**, Kanal E. Safety of magnetic resonance imaging contrast agents. *J Magn Reson Imaging* 1999; **10**: 477-484 [PMID: 10508312 DOI: 10.1002/(SICI)1522-2586(199909)10:3<477: : AID-JMRI33>3.3.CO; 2-5]
22 **Hyodo T**, Kumano S, Kushihata F, Okada M, Hirata M, Tsuda T, Takada Y, Mochizuki T, Murakami T. CT and MR cholangiography: advantages and pitfalls in perioperative evaluation of biliary tree. *Br J Radiol* 2012; **85**: 887-896 [PMID: 22422383 DOI: 10.1259/bjr/21209407]
23 **Couinaud C**. Surgical anatomy of the liver revisited: Embryology. Paris: Couinaud, 1989: 11-24
24 **Michel NA**. Blood supply and anatomy of the upper abdominal organs with a descriptive atlas. Philadelphia, Pa: Lippincott, 1955: 64-69
25 **Fulcher AS**, Szucs RA, Bassignani MJ, Marcos A. Right lobe living donor liver transplantation: preoperative evaluation of the donor with MR imaging. *AJR Am J Roentgenol* 2001; **176**: 1483-1491 [PMID: 11373218 DOI: 10.2214/ajr.176.6.1761483]
26 **Schroeder T**, Nadalin S, Stattaus J, Debatin JF, Malagó M, Ruehm SG. Potential living liver donors: evaluation with an all-in-one protocol with multi-detector row CT. *Radiology* 2002; **224**: 586-591 [PMID: 12147860 DOI: 10.1148/radiol.2242011340]
27 **Mortelé KJ**, Cantisani V, Troisi R, de Hemptinne B, Silverman SG. Preoperative liver donor evaluation: Imaging and pitfalls. *Liver Transpl* 2003; **9**: S6-14 [PMID: 12942472 DOI: 10.1053/jlts.2003.50199]
28 **Mori K**, Nagata I, Yamagata S, Sasaki H, Nishizawa F, Takada Y, Moriyasu F, Tanaka K, Yamaoka Y, Kumada K. The introduction of microvascular surgery to hepatic artery reconstruction in living-donor liver transplantation--its surgical advantages compared with conventional procedures. *Transplantation* 1992; **54**: 263-268 [PMID: 1496539 DOI: 10.1097/00007890-199208000-00014]
29 **Nghiem HV**. Imaging of hepatic transplantation. *Radiol Clin North Am* 1998; **36**: 429-443 [PMID: 9520993 DOI: 10.1016/S0033-8389(05)70033-6]
30 **Kamel IR**, Kruskal JB, Raptopoulos V. Imaging for right lobe living donor liver transplantation. *Semin Liver Dis* 2001; **21**: 271-282 [PMID: 11436577 DOI: 10.1055/s-2001-15399]
31 **Mizumoto R**, Suzuki H. Surgical anatomy of the hepatic hilum with special reference to the caudate lobe. *World J Surg* 1988; **12**: 2-10 [PMID: 3344582 DOI: 10.1007/BF01658479]
32 **Haberal M**, Sevmis S, Karakayali H, Moray G, Yilmaz U, Ozcay F, Torgay A, Aydogan C, Arslan G. A novel technique for hepatic arterial reconstruction in living-donor liver transplant. *Exp Clin Transplant* 2007; **5**: 585-589 [PMID: 17617047]
33 **Caiado AH**, Blasbalg R, Marcelino AS, da Cunha Pinho M, Chammas MC, da Costa Leite C, Cerri GG, de Oliveira AC, Bacchella T, Machado MC. Complications of liver transplantation: multimodality imaging approach. *Radiographics* 2007; **27**: 1401-1417 [PMID: 17848699 DOI: 10.1148/rg.275065129]
34 **Cheng YF**, Huang TL, Lee TY, Chen TY, Chen CL. Variation of the intrahepatic portal vein; angiographic demonstration and application in living-related hepatic transplantation. *Transplant Proc* 1996; **28**: 1667-1668 [PMID: 8658830]
35 **Kamel IR**, Kruskal JB, Pomfret EA, Keogan MT, Warmbrand G, Raptopoulos V. Impact of multidetector CT on donor selection and surgical planning before living adult right lobe liver transplantation. *AJR Am J Roentgenol* 2001; **176**: 193-200 [PMID: 11133565 DOI: 10.2214/ajr.176.1.1760193]
36 **Soyer P**, Bluemke DA, Choti MA, Fishman EK. Variations in the intrahepatic portions of the hepatic and portal veins: findings on helical CT scans during arterial portography. *AJR Am J Roentgenol* 1995; **164**: 103-108 [PMID: 7998521 DOI: 10.2214/ajr.164.1.7998521]
37 **Matsuura T**, Yanagi Y, Saeki I, Hayashida M, Taguchi T. Outcome of modified portal vein anastomosis for recipients with portal vein thrombosis or stenosis before living donor liver transplantation. *J Pediatr Surg* 2011; **46**: 2291-2295 [PMID: 22152867 DOI: 10.1016/j.jpedsurg.2011.09.015]
38 **Soyer P**, Heath D, Bluemke DA, Choti MA, Kuhlman JE, Reichle R, Fishman EK. Three-dimensional helical CT of intrahepatic venous structures: comparison of three rendering techniques. *J Comput Assist Tomogr* 1996; **20**: 122-127 [PMID: 8576462 DOI: 10.1097/00004728-199601000-00023]
39 **Pomfret EA**, Pomposelli JJ, Lewis WD, Gordon FD, Burns DL, Lally A, Raptopoulos V, Jenkins RL. Live donor adult liver transplantation using right lobe grafts: donor evaluation and surgical outcome. *Arch Surg* 2001; **136**: 425-433 [PMID: 11296114 DOI: 10.1001/archsurg.136.4.425]
40 **Fan ST**, Lo CM, Liu CL. Technical refinement in adult-to-adult living donor liver transplantation using right lobe graft. *Ann Surg* 2000; **231**: 126-131 [PMID: 10636112 DOI: 10.1097/00000658-200001000-00018]
41 **Akbulut S**, Yilmaz M, Eris C, Kutlu R, Yilmaz S. Living-donor liver transplant using the right hepatic lobe without the right hepatic vein: solving the drainage problem. *Exp Clin Transplant* 2013; **11**: 278-282 [PMID: 23767945 DOI: 10.6002/ect.2012.0060]
42 **Lee SG**. Techniques of reconstruction of hepatic veins in living-donor liver transplantation, especially for right hepatic vein and major short hepatic veins of right-lobe graft. *J Hepatobiliary Pancreat Surg* 2006; **13**: 131-138 [PMID: 16547674 DOI: 10.1007/s00534-005-1019-7]
43 **Puente SG**, Bannura GC. Radiological anatomy of the biliary tract: variations and congenital abnormalities. *World J Surg* 1983; **7**: 271-276 [PMID: 6868640 DOI: 10.1007/BF01656159]
44 **Mortelé KJ**, Ros PR. Anatomic variants of the biliary tree: MR cholangiographic findings and clinical applications. *AJR Am J Roentgenol* 2001; **177**: 389-394 [PMID: 11461869 DOI: 10.2214/ajr.177.2.1770389]
45 **Testa G**, Malagò M, Broelseh CE. Complications of biliary tract in liver transplantation. *World J Surg* 2001; **25**: 1296-1299 [PMID: 11596893 DOI: 10.1007/s00268-001-0113-5]
46 **Yeh BM**, Breiman RS, Taouli B, Qayyum A, Roberts JP, Coakley FV. Biliary tract depiction in living potential liver donors: comparison of conventional MR, mangafodipir trisodium-enhanced excretory MR, and multi-detector row CT cholangiography--initial experience. *Radiology* 2004; **230**: 645-651 [PMID: 14990830 DOI: 10.1148/radiol.2303021775]
47 **Cheng YF**, Lee TY, Chen CL, Huang TL, Chen YS, Lui CC. Three-dimensional helical computed tomographic cholangiography: application to living related hepatic transplanta-

tion. *Clin Transplant* 1997; **11**: 209-213 [PMID: 9193844]
48 **Fleischmann D**, Ringl H, Schöfl R, Pötzi R, Kontrus M, Henk C, Bankier AA, Kettenbach J, Mostbeck GH. Three-dimensional spiral CT cholangiography in patients with suspected obstructive biliary disease: comparison with endoscopic retrograde cholangiography. *Radiology* 1996; **198**: 861-868 [PMID: 8628884]
49 **Romagnuolo J**, Bardou M, Rahme E, Joseph L, Reinhold C, Barkun AN. Magnetic resonance cholangiopancreatography: a meta-analysis of test performance in suspected biliary disease. *Ann Intern Med* 2003; **139**: 547-557 [PMID: 14530225 DOI: 10.7326/0003-4819-139-7-200310070-00006]
50 **Watanabe Y**, Dohke M, Ishimori T, Amoh Y, Okumura A, Oda K, Hayashi T, Hiyama A, Dodo Y. Pseudo-obstruction of the extrahepatic bile duct due to artifact from arterial pulsatile compression: a diagnostic pitfall of MR cholangiopancreatography. *Radiology* 2000; **214**: 856-860 [PMID: 10715058 DOI: 10.1148/radiology.214.3.r00mr09856]
51 **Lee VS**, Morgan GR, Lin JC, Nazzaro CA, Chang JS, Teperman LW, Krinsky GA. Liver transplant donor candidates: associations between vascular and biliary anatomic variants. *Liver Transpl* 2004; **10**: 1049-1054 [PMID: 15390332 DOI: 10.1002/lt.20181]
52 **Kapoor V**, Baron RL, Peterson MS. Bile leaks after surgery. *AJR Am J Roentgenol* 2004; **182**: 451-458 [PMID: 14736680 DOI: 10.2214/ajr.182.2.1820451]
53 **Suhocki PV**, Meyers WC. Injury to aberrant bile ducts during cholecystectomy: a common cause of diagnostic error and treatment delay. *AJR Am J Roentgenol* 1999; **172**: 955-959 [PMID: 10587128 DOI: 10.2214/ajr.172.4.10587128]
54 **Alawi K**, Khalaf H, Medhat Y, Allam N, Al-Saghier M, Al-Sofayan M, Al-Bahili H, Al-Hamoudi W, Abdo A, Sebayel M. Risk factors for biliary complications after living-donor liver transplant: a single-center experience. *Exp Clin Transplant* 2008; **6**: 101-104 [PMID: 18816235]
55 **Bhargava P**, Vaidya S, Dick AA, Dighe M. Imaging of orthotopic liver transplantation: review. *AJR Am J Roentgenol* 2011; **196**: WS15-WS25, Quiz WS15-WS25 [PMID: 21343537]
56 **Petersein J**, Spinazzi A, Giovagnoni A, Soyer P, Terrier F, Lencioni R, Bartolozzi C, Grazioli L, Chiesa A, Manfredi R, Marano P, Van Persijn Van Meerten EL, Bloem JL, Petre C, Marchal G, Greco A, McNamara MT, Heuck A, Reiser M, Laniado M, Claussen C, Daldrup HE, Rummeny E, Kirchin MA, Pirovano G, Hamm B. Focal liver lesions: evaluation of the efficacy of gadobenate dimeglumine in MR imaging--a multicenter phase III clinical study. *Radiology* 2000; **215**: 727-736 [PMID: 10831691 DOI: 10.1148/radiology.215.3.r00jn14727]
57 **Hawighorst H**, Schoenberg SO, Knopp MV, Essig M, Miltner P, van Kaick G. Hepatic lesions: morphologic and functional characterization with multiphase breath-hold 3D gadolinium-enhanced MR angiography--initial results. *Radiology* 1999; **210**: 89-96 [PMID: 9885592 DOI: 10.1148/radiology.210.1.r99ja1489]
58 **Marsman WA**, Wiesner RH, Rodriguez L, Batts KP, Porayko MK, Hay JE, Gores GJ, Krom RA. Use of fatty donor liver is associated with diminished early patient and graft survival. *Transplantation* 1996; **62**: 1246-1251 [PMID: 8932265 DOI: 10.1097/00007890-199611150-00011]
59 **Piekarski J**, Goldberg HI, Royal SA, Axel L, Moss AA. Difference between liver and spleen CT numbers in the normal adult: its usefulness in predicting the presence of diffuse liver disease. *Radiology* 1980; **137**: 727-729 [PMID: 6934563]
60 **Boll DT**, Merkle EM. Diffuse liver disease: strategies for hepatic CT and MR imaging. *Radiographics* 2009; **29**: 1591-1614 [PMID: 19959510 DOI: 10.1148/rg.296095513]
61 **Kodama Y**, Ng CS, Wu TT, Ayers GD, Curley SA, Abdalla EK, Vauthey JN, Charnsangavej C. Comparison of CT methods for determining the fat content of the liver. *AJR Am J Roentgenol* 2007; **188**: 1307-1312 [PMID: 17449775 DOI: 10.2214/AJR.06.0992]
62 **Lee SW**, Park SH, Kim KW, Choi EK, Shin YM, Kim PN, Lee KH, Yu ES, Hwang S, Lee SG. Unenhanced CT for assessment of macrovesicular hepatic steatosis in living liver donors: comparison of visual grading with liver attenuation index. *Radiology* 2007; **244**: 479-485 [PMID: 17641368 DOI: 10.1148/radiol.2442061177]
63 **Park SH**, Kim PN, Kim KW, Lee SW, Yoon SE, Park SW, Ha HK, Lee MG, Hwang S, Lee SG, Yu ES, Cho EY. Macrovesicular hepatic steatosis in living liver donors: use of CT for quantitative and qualitative assessment. *Radiology* 2006; **239**: 105-112 [PMID: 16484355 DOI: 10.1148/radiol.2391050361]
64 **Limanond P**, Raman SS, Lassman C, Sayre J, Ghobrial RM, Busuttil RW, Saab S, Lu DS. Macrovesicular hepatic steatosis in living related liver donors: correlation between CT and histologic findings. *Radiology* 2004; **230**: 276-280 [PMID: 14695401 DOI: 10.1148/radiol.2301021176]
65 **Reeder SB**, Sirlin CB. Quantification of liver fat with magnetic resonance imaging. *Magn Reson Imaging Clin N Am* 2010; **18**: 337-357, ix [PMID: 21094444 DOI: 10.1016/j.mric.2010.08.013]
66 **Qayyum A**, Goh JS, Kakar S, Yeh BM, Merriman RB, Coakley FV. Accuracy of liver fat quantification at MR imaging: comparison of out-of-phase gradient-echo and fat-saturated fast spin-echo techniques--initial experience. *Radiology* 2005; **237**: 507-511 [PMID: 16244259 DOI: 10.1148/radiol.2372040539]
67 **Qayyum A**, Chen DM, Breiman RS, Westphalen AC, Yeh BM, Jones KD, Lu Y, Coakley FV, Callen PW. Evaluation of diffuse liver steatosis by ultrasound, computed tomography, and magnetic resonance imaging: which modality is best? *Clin Imaging* 2009; **33**: 110-115 [PMID: 19237053 DOI: 10.1016/j.clinimag.2008.06.036]
68 **Fischer MA**, Raptis DA, Montani M, Graf R, Clavien PA, Nanz D, Alkadhi H, Scheffel H. Liver fat quantification by dual-echo MR imaging outperforms traditional histopathological analysis. *Acad Radiol* 2012; **19**: 1208-1214 [PMID: 22841289 DOI: 10.1016/j.acra.2012.05.009]
69 **Ishiko T**, Inomata Y, Beppu T, Asonuma K, Okajima H, Takeitchi T, Baba H. Age and donor safety in living-donor liver transplant in 110 consecutive cases at 1 institute. *Exp Clin Transplant* 2008; **6**: 190-193 [PMID: 18954295]
70 **Kamel IR**, Kruskal JB, Warmbrand G, Goldberg SN, Pomfret EA, Raptopoulos V. Accuracy of volumetric measurements after virtual right hepatectomy in potential donors undergoing living adult liver transplantation. *AJR Am J Roentgenol* 2001; **176**: 483-487 [PMID: 11159100 DOI: 10.2214/ajr.176.2.1760483]
71 **Lo CM**, Fan ST, Liu CL, Wei WI, Lo RJ, Lai CL, Chan JK, Ng IO, Fung A, Wong J. Adult-to-adult living donor liver transplantation using extended right lobe grafts. *Ann Surg* 1997; **226**: 261-269; discussion 261-269 [PMID: 9339932 DOI: 10.1097/00000658-199709000-00005]
72 **Urata K**, Kawasaki S, Matsunami H, Hashikura Y, Ikegami T, Ishizone S, Momose Y, Komiyama A, Makuuchi M. Calculation of child and adult standard liver volume for liver transplantation. *Hepatology* 1995; **21**: 1317-1321 [PMID: 7737637 DOI: 10.1002/hep.1840210515]
73 **Emond JC**, Renz JF, Ferrell LD, Rosenthal P, Lim RC, Roberts JP, Lake JR, Ascher NL. Functional analysis of grafts from living donors. Implications for the treatment of older recipients. *Ann Surg* 1996; **224**: 544-552; discussion 552-554 [PMID: 8857858 DOI: 10.1097/00000658-199610000-00012]
74 **Singh AK**, Cronin CG, Verma HA, Boland GW, Saini S, Mueller PR, Sahani DV. Imaging of preoperative liver transplantation in adults: what radiologists should know. *Radiographics* 2011; **31**: 1017-1030 [PMID: 21768236 DOI: 10.1148/rg.314105197]
75 **Nakayama Y**, Li Q, Katsuragawa S, Ikeda R, Hiai Y, Awai K, Kusunoki S, Yamashita Y, Okajima H, Inomata Y, Doi K.

Automated hepatic volumetry for living related liver transplantation at multisection CT. *Radiology* 2006; **240**: 743-748 [PMID: 16857979 DOI: 10.1148/radiol.2403050850]

76 **Suzuki K**, Epstein ML, Kohlbrenner R, Garg S, Hori M, Oto A, Baron RL. Quantitative radiology: automated CT liver volumetry compared with interactive volumetry and manual volumetry. *AJR Am J Roentgenol* 2011; **197**: W706-W712 [PMID: 21940543 DOI: 10.2214/AJR.10.5958]

P- Reviewer: Chen F, Kilickesmez O, Verma S, Yuan Z
S- Editor: Wen LL **L- Editor**: A **E- Editor**: Lu YJ

World Journal of Radiology

Submit a Manuscript: http://www.wjgnet.com/esps/
Help Desk: http://www.wjgnet.com/esps/helpdesk.aspx
DOI: 10.4329/wjr.v6.i9.708

World J Radiol 2014 September 28; 6(9): 708-715
ISSN 1949-8470 (online)

REVIEW

Radiation pneumonitis after stereotactic radiation therapy for lung cancer

Hideomi Yamashita, Wataru Takahashi, Akihiro Haga, Keiichi Nakagawa

Hideomi Yamashita, Wataru Takahashi, Akihiro Haga, Keiichi Nakagawa, Department of Radiology, University of Tokyo Hospital, Tokyo 113-8655, Japan

Author contributions: Yamashita H designed the study and performed the majority of work, including literature review and writing the first draft of the manuscript; Takahashi W, Haga A and Nakagawa K provided advice regarding important intellectual content of the topical discussion.

Correspondence to: Hideomi Yamashita, MD, PhD, Department of Radiology, University of Tokyo Hospital, 7-3-1 Hongo, Bunkyo-ku, Tokyo 113-8655, Japan. yamachan07291973@yahoo.co.jp

Telephone: +81-3-58008667 Fax: +81-3-58008935

Received: December 7, 2013 Revised: July 1, 2014
Accepted: July 15, 2014
Published online: September 28, 2014

Abstract

Stereotactic body radiation therapy (SBRT) has a local control rate of 95% at 2 years for non-small cell lung cancer (NSCLC) and should improve the prognosis of inoperable patients, elderly patients, and patients with significant comorbidities who have early-stage NSCLC. The safety of SBRT is being confirmed in international, multi-institutional Phase Ⅱ trials for peripheral lung cancer in both inoperable and operable patients, but reports so far have found that SBRT is a safe and effective treatment for early-stage NSCLC and early metastatic lung cancer. Radiation pneumonitis (RP) is one of the most common toxicities of SBRT. Although most post-treatment RP is Grade 1 or 2 and either asymptomatic or manageable, a few cases are severe, symptomatic, and there is a risk for mortality. The reported rates of symptomatic RP after SBRT range from 9% to 28%. Being able to predict the risk of RP after SBRT is extremely useful in treatment planning. A dose-effect relationship has been demonstrated, but suggested dose-volume factors like mean lung dose, lung V20, and/or lung V2.5 differed among the reports. We found that patients who present with an interstitial pneumonitis shadow on computed tomography scan and high levels of serum Krebs von den Lungen-6 and surfactant protein D have a high rate of severe radiation pneumonitis after SBRT. At our institution, lung cancer patients with these risk factors have not received SBRT since 2006, and our rate of severe RP after SBRT has decreased significantly since then.

Key words: Radiation pneumonitis; Stereotactic radiation therapy; Dose-volume factors; Krebs von den Lungen-6; Surfactant protein D; Computed tomography changes

Core tip: Radiation pneumonitis (RP) is one of the most common toxicities after stereotactic body radiation therapy (SBRT). Although most RP is Grade 1 or 2 and either asymptomatic or manageable, a few cases are severe and there is a risk for mortality. A dose-effect relationship has been demonstrated that can be used for treatment planning. Other prognostic indicators of severe radiation pneumonitis after SBRT are an interstitial pneumonitis shadow on computed tomography scan and high levels of serum Krebs von den Lungen-6 and surfactant protein D before treatment.

Yamashita H, Takahashi W, Haga A, Nakagawa K. Radiation pneumonitis after stereotactic radiation therapy for lung cancer. *World J Radiol* 2014; 6(9): 708-715 Available from: URL: http://www.wjgnet.com/1949-8470/full/v6/i9/708.htm DOI: http://dx.doi.org/10.4329/wjr.v6.i9.708

INTRODUCTION

Stereotactic body radiotherapy (SBRT) is becoming standard of care therapy for patients with inoperable

early-stage non-small cell peripheral lung cancer or lung cancer with limited demarcated metastases. The delivery of higher doses to smaller lung planning target volumes (PTVs) limits toxicity in the normal lung tissue surrounding the tumor to very limited areas. Local control of up to 95% at 2 years has been reported[1-4].

Given the improved local control and toxicity results reported by recent lung SBRT studies[1-4], future directions for this technique include the treatment of larger lesions. Palma *et al*[5] and Diot *et al*[6] suggest that toxicity might increase with lesion size, and this possibility should be anticipated and closely monitored.

Symptomatic lung toxicity with SBRT is typically less than 10%[7]; however, occurrences up to 25% have been reported[8], highlighting the necessity of developing SBRT treatment parameters that ensure consistently low toxicity levels.

Radiation-induced pneumonitis is the most frequent acute pulmonary toxicity. The majority of patients develop asymptomatic Grade 1 pneumonitis. Clinically symptomatic pneumonitis develops in less than 10% of patients, but most patients develop late pulmonary toxicity characterized by localized pulmonary fibrosis in the high-dose region[9]. Because this fibrosis is usually asymptomatic, we considered post-SBRT pulmonary function changes the clinically relevant endpoint of our review.

A dose-effect relationship has been demonstrated for SBRT that is similar to that observed in conventionally fractionated radiation therapy[10,11]; but a study by Guckenberger *et al*[12] failed to demonstrate this relationship in early-stage non-small cell lung cancer. Gluckenberger's results were based on a large number of patients[12] and confirmed the findings in other studies that post-SBRT pulmonary function was either stable[13-17] or almost asymptomatic[18,19]. These data were encouraging and further supported the safety of SBRT.

SBRT has been widely used as a safe and effective treatment for primary or metastatic lung tumors for a number of years[20]. According to the protocol of the Japan Clinical Oncology Group (JCOG) 0403 study[21,22], the only absolute contraindication to SBRT is pregnancy.

In Japan, medical service fees officially cover SBRT treatment for primary and metastatic lung cancers only if the tumor is under 5 cm in size, there are no more than three tumors, and there is no metastatic disease in other organs. In Japan, surgery is generally the first-line treatment for early primary lung cancer, so primary lung cancer patients who undergo SBRT are in poor condition and either have multiple primary cancers or co-morbidities such as serious cardiovascular disease. Most Japanese patients with primary lung tumors who received SBRT had low pulmonary function from chronic obstructive pulmonary disease due to long smoking histories.

Contraindications to SBRT were (1) a history of irradiation to the concerned site; (2) severe interstitial pneumonitis or pulmonary fibrosis; (3) severe diabetes or connective tissue disease; and (4) common use of steroids.

LOCAL CONTROL RATE OF SBRT

SBRT with 3D conformal or intensity-modulation techniques is an effective treatment for localized early-stage lung cancer, with local control rates of 85.5% to 100% 2 to 3 years following treatment[1-4]. SBRT is also being employed to treat metastatic lung cancer, although the survival rates are not comparable to those for early-stage (T1 - T2, N0) disease[2].

The excellent local control rates for early-stage lung cancer treated with SBRT are leading to extensive use of this technique in clinical practice and to randomized trials comparing surgery to SBRT for Stage I non-small cell lung cancers in operable patients. Two randomized trials to compare SBRT to surgery for operable patients with Stage I lung cancer were launched in 2008: one in the Netherlands [the Randomized Clinical Trial of Either Surgery or Stereotactic Radiotherapy for Early Stage (IA) Lung Cancer trial] and one in the United States (testing the Cyberknife by Accuray Inc., Sunnyvale, CA, United States).

PREVIOUS REPORTS OF TOXICITIES AFTER SBRT

The safety of SBRT is being confirmed in multi-institutional Phase Ⅱ trials for peripheral lung cancer in both inoperable[16,23] and operable patients[22]. In the Radiation Therapy Oncology Group (RTOG) trial 0236[23], protocol-specific, treatment-related Grade 3 and 4 adverse events occurred in 12.7% (7/59) and 3.6% (2/59) of cases, respectively. No Grade 5 adverse events were reported. In the Nordic Phase II study of SBRT[16]. Grade 3 toxicities were seen in 21% (12/57) of cases, but no Grade 4 or 5 toxicities were reported. Nishio *et al*[22] reported Grade 3 toxicities in 6.2% of operable patients in the JCOG 0403 trial.

Severe clinical toxicities after SBRT are fairly uncommon and occur more frequently in cases of centrally located tumors, such as those near the trachea, primary bronchus, major blood vessels and pericardium[3]. Rates of serious toxicities are low in most studies. Previous reports have described skin, chest wall, and brachial plexus toxicities with their associated risk factors[24-27].

This review documents clinically significant radiation pneumonitis (RP) rates for medically inoperable non-small cell lung cancer (NSCLC) patients treated with SBRT, adding to the sparse literature on pulmonary toxicity resulting from hypo-fractionated radiotherapy.

RP AFTER SBRT

RP is one of the most common toxicities after SBRT, as well as after conventional radiotherapy to the lung. Scoring systems should be considered when interpreting RP results. The reported rates of symptomatic RP after SBRT range from 9% to 28%[8,10,11,28-31]. Although most of the RP was Grade 1 or 2 and either asymptomatic or

manageable, a few cases were severe and there was a risk for mortality[8]. It is very important to develop a method to predict the risk of RP after SBRT for lung cancer.

Grade 3 RP was observed in 3.6% of the overall patients in RTOG 0236[23] and in 3.1% of the operable patients in JCOG 0403[22]. Baumann *et al*[16] reported that no one developed Grade 3 pneumonitis in their Phase Ⅱ trial of SBRT.

McGarry *et al*[31] reported that 2% (1/47) of patients developed circulating tumor cells and 6.4% (3/47) of patients developed Grade 2 and 3 RP in the updated Indiana University Phase I trial that included tumors up to 7 cm in size plus central lesions. G2 toxicity occurred at a dose of 48 Gy, and G3 toxicities developed after 54 Gy and 72 Gy in 3 fractions prescribed to the 80% iso-dose line[32]. Using similar criteria, Onishi reported 4.1% G2 (10/245), 1.2% G3 (3/245), and 1.2% G4 (3/245) RP in a multi-institutional trial of SBRT in Japan[33]. Nagata and colleagues reported no G3 or G4 RP using a slightly less potent dose of 48 Gy in 4 fractions delivered to the iso-center[1].

In the RTOG, Ricardi *et al*[32] treated 62 patients to 45 Gy in 3 fractions to the 80% iso-dose line and reported a 3.2% incidence of Grade 3 RP that required steroids or intermittent oxygen. When Stephans *et al*[34] treated (n = 56) patients to 50 Gy in 5 fractions and (n = 38) patients to 60 Gy in 3 fractions, there was a 2.3% incidence of RP that required steroids (for all 94 patients).

Grills *et al*[35] recently published a case–control study comparing SBRT to wedge resection. In that report, there was 11% G2 - 3 RP using a CTC *vs* a grading system based on the Common Terminology of Criteria of Adverse Events. Only 2% of these patients required temporary steroids for management. Finally, G3 RP occurred at a rate of 3.6% (2/55) in RTOG 0236[23].

Although the reported toxicities of lung SBRT have, for the most part, been minor, the dose constraints to use during treatment planning are based on extremely limited clinical data, most of which has not been validated[36]. Even the recent QUANTEC lung article devoted only one paragraph to the risk of pneumonitis in lung SBRT patients[7]. Baker *et al*[37] reported in QUANTEC that the greatest incidence of pneumonitis was Grade 1 (64.2%) (169/263), and there were 26 cases (9.9%) of Grade 2 pneumonitis and 3 cases (1.1%) of Grade 3 pneumonitis.

DOSE-VOLUME FACTORS FOR RP AFTER SBRT

Table 1 summarizes published reports that focused on the dose volumetrics associated with Grade 2 RP or worse after SBRT. The RP rates varied from 9.4% to 28.0%, and the suggested dose-volume factors for RP differed among the reports. This variation might be caused by differences in the PTV volume, dose fractionation schedule, or RP scoring system.

Since most patients with pulmonary metastases had residual or recurrent disease after first-line treatment with chemotherapy, it appeared appropriate to consider a V20 of 30% as the dose restriction in SBRT for metastatic lung cancer.

Borst *et al*[10] evaluated the relationship between the mean lung dose (MLD) and the incidence of RP after SBRT. They calculated the MLD in the normalized total dose form, using the linear-quadratic model with a α/β ratio of 3. A significant dose-response relationship was found between RP and MLD.

According to Baker *et al*[10], the data from their center and the Japanese group demonstrate that a V20 of less than 10% is readily achievable, and at those levels pneumonitis is not statistically predictable. Analogously, an MLD of approximately 5 - 6 Gy is achievable, and at this dosage pneumonitis should not develop. Therefore, dosimetric guidelines of a V20 of less than 10% and an MLD of less than 6 Gy are a reasonable way to reduce the occurrence of Grades 2 - 4 RP. A German article suggested that a higher MLD or higher V2.5 - V50 (V2.5 in particular) was associated with symptomatic RP[9].

The Mayo Clinic recently reported on a series of patients treated at their institution with consecutive daily fractions of SBRT[32]. There was a 12.5% overall incidence of Grade 2 pneumonitis, but a 14.3% incidence in patients treated either with 54 Gy in three fractions for peripheral lesions or 48 Gy in four fractions for central lesions. In a univariate analysis, a PTV maximum dose greater than 60 Gy was predictive of RP (P = 0.016), although the overall number of events was small (n = 4). No other factors were statistically significant[32]. The decline in pulmonary function seemed to be transient, similar to the initial experience at Indiana University[38].

It is unclear exactly how RP correlates with changes in pulmonary function testing. This is an area that requires further research. It is interesting to note, however, that a dose of radiation higher than V_{10} was predictive of RP in the Indiana University patients, at least on univariate analysis. The same findings were reported by the Cleveland Clinic[34]. The conformity index was not predictive under univariate or multivariate modeling.

At our institution, we suppress the patient's respiration during SBRT using abdominal compression in order to reduce lung V20 and MLD[8,39]. We had used irradiation dose of 48 Gy in 4 fractions (Figure 1). We also used 4D cone beam computed tomography (CT) to evaluate internal target volume and tumor motion just before SBRT, with the result that the margin between the internal target volume and the PTV became narrower[40,41].

EXPRESSSION OF KREBS VON DEN LUNGEN-6 IS A PREDICTOR OF RP AFTER SBRT

High levels of the glycoprotein Krebs von den Lungen-6 (KL-6) indicate interstitial pneumonitis (IP), and the levels rise significantly with physical activity in IP cases. In the human body, KL-6 only develops in type II alveolus

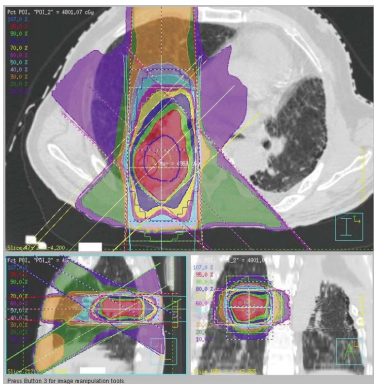

Figure 1 Dose distribution of stereotactic body radiation therapy of 48 Gy in 4 fractions.

epithelial cells, bronchial epithelial cells, and bronchus gland cells. A small quantity of KL-6 is present in the liquid coating the alveoli in normal lungs, but it occurs in higher levels in hyperplastic type II alveolus epithelial cells when IP is present. Inflammation also occurs in IP, which increases the permeability of the blood vessels and allows KL-6 to move into the blood where it can be measured. Blood levels of KL-6, surfactant protein D (SP-D), surfactant protein A (SP-A), and monocyte chemoattractant protein-1 are evaluated whenever there is an injury to the lung stroma, and KL-6 is the most sensitive (93.9%) and specific (96.3%) of these measures where the detection of RP is concerned[42]. SP-D levels at 50 to 60 Gy (midway through radiation therapy) showed greater sensitivity and positive predictive values for RP detection (74% and 68%, respectively) than SP-A (26% and 21%, respectively)[43].

Factors other than dose volumetrics also affect the incidence of pneumonitis after SBRT. Hara *et al*[44] evaluated 16 patients who received single-fraction SBRT from 20 to 35 Gy. Serum KL-6 levels rose significantly between pretreatment presentation and two months after SBRT was administered, and it was significantly correlated with Grade 3 RP by the RTOG criteria.

Iwata *et al*[45] reported that pretreatment serum KL-6 levels, gender, and PTV volume were associated with symptomatic RP in a univariate analysis, and pretreatment KL-6 levels remained significant in a multivariate analysis. They concluded that patients with pretreatment KL-6 levels $\geqslant$ 300 μ/mL should be followed carefully for RP. CT or X-ray imaging of the lung before and after SBRT should also help to predict severe RP.

To limit the risk of severe RP, we recommended to everyone prescreening for interstitial pneumonitis with CT scans and checking serum KL-6 and SP-D levels. After introducing these measures, we reported that the incidence of Grade 4 and 5 RP decreased from 18.8% to 3.5%[45].

Takeda *et al*[46] reported that the sooner RP appeared on chest X-ray after SBRT was administered, the more severe it was. The radiographic appearance of RP during the initial 2 mo after SBRT indicated a 40% risk for Grade 3 RP. The risk was only 1.2% when radiologic changes appeared 3 mo after SBRT.

Evaluating KL-6 and SP-D levels, radiologic imaging before and after treatment, and adjusting dose-volume factors during treatment planning helps lower the risk of severe pneumonitis after SBRT. While the biomarkers are both sensitive and specific for RP, the pathophysiological mechanisms underlying their predictive value are unclear, which makes some clinicians hesitate to use them.

At our institution, Grades 4 and 5 RP occurred in 6 out of 32 patients (18.8%) who received SBRT treatment for lung cancer before 2005 and only 3 out of 85 patients (3.5%) between 2006 and 2013[8,39]. We believe that the significant reduction in the occurrence of Grades 4 - 5 RP is due to our use of prognostic biomarkers and radiography to select appropriate patients for SBRT treatment. After 2006, patients were excluded from SBRT if they had an obvious IP shadow on their CT scan (slice thickness 3.0 mm), and/or if serum KL-6 and SP-D levels were high[39].

RP AFTER SBRT FOR METASTATIC LUNG CANCER

SBRT is also used to treat pulmonary metastases in selected patients and treatment results seem comparable to those obtained by surgical metastasectomy[47]. In this setting, the literature reports that Grade 3 RP occurred in 3% to 5% of cases[2,47,48]. According to Inoue[48], the incidence of G3/4 adverse respiratory events after SBRT for pulmonary metastases was 10%.

GENE EXPRESSION CLASSIFIER

It was reported that radiation pneumonitis after SBRT treatment for lung cancer was associated with pro-inflammatory genes such as TGFB1 or CD44. Accumulating the number of cases appropriate for statistically significant gene analysis might be difficult, and there is no information about predisposing genetic risk factors for lung cancer.

Yuan *et al*[49] reported in 2009 that he and his colleagues at the M.D. Anderson Cancer Center in Houston, Texas, United States, performed an association analysis between pneumonitis onset risk in both Black and White patients who received radiotherapy and/or chemotherapy for NSCLC (94% in both cases). The polymorphism marker on the THFB1 and T869C genes was associated with a low risk of developing RP or IP.

In recent years, many studies have found that SBRT for early stage lung cancer is both effective and safe[1,50], but there are only a few reports about the development of dangerous and lethal radiation pneumonitis that can result from SBRT[8], or the pulmonary fibrosis that may also appear[50].

TIMELINE AND PATTERN OF CT CHANGES

There have been few studies on CT findings in radiation-

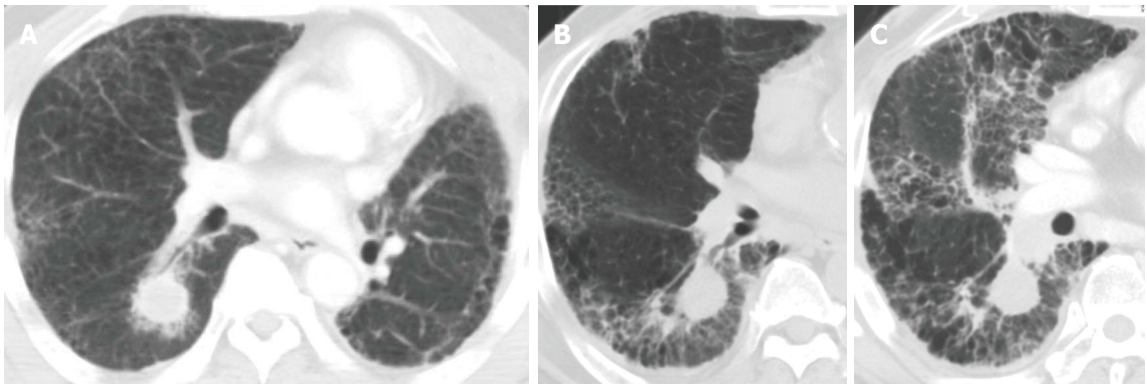

Figure 2 Computed tomography image. A: Before stereotactic body radiation therapy (SBRT) but after surgery for a left lung cancer. The nodule in the lower lobe of the right lung (S6) increased to 23 mm; B: Taken at post-SBRT month 5; C: Taken at post-SBRT month 7. Acute exacerbation of interstitial pneumonitis was found.

Table 1 Summary of reports on Grade 2 radiation pneumonitis after stereotactic body radiation therapy

First author	Ref.	Year	Gy	Pt No.	Median PTV, cc	Median follow-up in months	G2- RP	G3 RP	G4 RP	G5 RP	RP factor 1	RP factor 2
Onishi	[32]	2004	18-75Gy/1-25Fr	245	NA	24	6.50%	1.20%	1.20%	0%		
McGarry	[31]	2005	24Gy/3Fr	47	NA	NA	8.40%	4.30%	2.10%	0%		
Takahashi	[40]	2006	15-30Gy	32	NA	18	12.50%		0%	6%		
Yamashita	[8]	2007	48Gy/4-6Fr	25	43.9	17	28.00%	4%	4%	12%	CI	
Baumann	[16]	2008	45Gy/3Fr	60	NA	23	NA	21%	0%	0%		
Ricardi	[27]	2009	45Gy/3Fr or 26Gy/1Fr	60	NA	30.9	14.30%	3.20%	0%	0%	MLD	
Borst	[10]	2009	35-60Gy/4-8Fr	128	9.6	16.1	10.90%	0.80%	0%	0%	MLD	
Stephans	[13]	2009	60Gy/3Fr or 50Gy/5Fr	86	39.9/30.4	15.3	2.30%	0%	0%	0%		
Rusthoven	[2]	2009	48-60Gy/3Fr	7	NA	15.4	2.60%					
Yamashita	[39]	2010	48Gy/4Fr	117	NA	14.7	NA	1.70%	1.70%	6.00%	KL-6 and SP-D	IP-shadow
Timmerman	[23]	2010	60Gy/3Fr or 54Gy/3Fr	55	NA	34.4	NA	12.70%	3.60%	0%		
Nagata	[20]	2010	48Gy/4Fr	104	NA	46.8	NA	6.20%	0%	0%		
Guckenberger	[9]	2010	26Gy/1Fr or 37.5Gy/3Fr	59	33	13	18.60%	0%	0%	0%	MLD	V2.5-50
Ong	[28]	2010	55Gy/5Fr or 60Gy/8Fr	18	137	12.8	27.80%	11.10%	0%	0%	V5	
Grills	[35]	2010	48Gy/4Fr or 60Gy/5Fr	58	NA	30	11%	2%	0%	0%		
Stauder	[30]	2011	32-60Gy/3-5Fr	74	42.9	15.8	12.50%	2.30%	0%	1.10%	Max dose	
Matsuo	[53]	2012	48Gy/4Fr	74	32.5	31.4	20.30%	1.40%	0%	0%	V25	PTV volume
Barriger	[29]	2012	24-66Gy/3-5Fr	84	48.3	17	9.40%	2%	0.40%	0%	MLD (4Gy)	V20 (4%)
Baker	[37]	2013	Multiple	240	37.6	15.6	11%	1.10%	0%	0%	MLD (6Gy)	V20 (10%)

MLD: Mean lung dose; NA: Not available.

induced lung disease after SBRT for lung cancer[50]. Due to the differences in dose delivery and distribution, biologic effects, and overall treatment time, it is reasonable to expect that any CT changes that occur after SBRT will not have the same appearance, geographic extent, and progression timeline as those following CRT for lung cancers[51].

Like CRT-induced CT changes, CT findings after SBRT have two stages: early acute radiation pneumonitis that occurs within 6 mo of treatment and radiation fibrosis that occurs 6 mo or more after treatment[51,52]. In most cases, radiologic changes in normal lung tissue do not occur until at least 3 mo after SBRT. Clinical symptoms of acute radiation-induced lung injury develop approximately 3 to 6 mo after treatment. All of the severe RP cases in our institution consisted of the acute exacerbation of IP that was spread out over the radiation field (Figure 2)[39].

The analysis of SBRT-induced normal lung density changes by Diot *et al*[6] indicates that self-limiting acute effects in normal lung tissue are more pronounced than late effects, and acute CT changes in patients treated with 3 fractions were considerably less than those in patients treated with 4 or 5 fractions. The changes seemed to be explained by either increased low-dose exposure in normal lung tissue or differences in tumor volume.

CONCLUSION

On the basis of this review, radiation-induced pneumonitis is the most frequent acute pulmonary toxicity following SBRT for lung cancer. The majority of patients develop asymptomatic Grade 1 or asymptomatic and/or manageable Grade 2 pneumonitis, and clinically symptomatic pneumonitis is observed in less than 10%. A dose-effect relationship has been demonstrated that is useful in treatment planning. Since patients with an IP shadow on CT scan and high levels of serum KL-6 and SP-D before SBRT treatment develop severe radiation

pneumonitis at a high rate after treatment, they should not receive SBRT.

REFERENCES

1 **Nagata Y**, Takayama K, Matsuo Y, Norihisa Y, Mizowaki T, Sakamoto T, Sakamoto M, Mitsumori M, Shibuya K, Araki N, Yano S, Hiraoka M. Clinical outcomes of a phase I/II study of 48 Gy of stereotactic body radiotherapy in 4 fractions for primary lung cancer using a stereotactic body frame. *Int J Radiat Oncol Biol Phys* 2005; **63**: 1427-1431 [PMID: 16169670]

2 **Rusthoven KE**, Kavanagh BD, Burri SH, Chen C, Cardenes H, Chidel MA, Pugh TJ, Kane M, Gaspar LE, Schefter TE. Multi-institutional phase I/II trial of stereotactic body radiation therapy for lung metastases. *J Clin Oncol* 2009; **27**: 1579-1584 [PMID: 19255320 DOI: 10.1200/JCO.2008.19.6386]

3 **Timmerman R**, McGarry R, Yiannoutsos C, Papiez L, Tudor K, DeLuca J, Ewing M, Abdulrahman R, DesRosiers C, Williams M, Fletcher J. Excessive toxicity when treating central tumors in a phase II study of stereotactic body radiation therapy for medically inoperable early-stage lung cancer. *J Clin Oncol* 2006; **24**: 4833-4839 [PMID: 17050868]

4 **Xia T**, Li H, Sun Q, Wang Y, Fan N, Yu Y, Li P, Chang JY. Promising clinical outcome of stereotactic body radiation therapy for patients with inoperable Stage I/II non-small-cell lung cancer. *Int J Radiat Oncol Biol Phys* 2006; **66**: 117-125 [PMID: 16765528]

5 **Palma DA**, van Sörnsen de Koste J, Verbakel WF, Vincent A, Senan S. Lung density changes after stereotactic radiotherapy: a quantitative analysis in 50 patients. *Int J Radiat Oncol Biol Phys* 2011; **81**: 974-978 [PMID: 20932655 DOI: 10.1016/j.ijrobp.2010.07.025]

6 **Diot Q**, Kavanagh B, Schefter T, Gaspar L, Stuhr K, Miften M. Regional normal lung tissue density changes in patients treated with stereotactic body radiation therapy for lung tumors. *Int J Radiat Oncol Biol Phys* 2012; **84**: 1024-1030 [PMID: 22583607 DOI: 10.1016/j.ijrobp.2011.11.080]

7 **Marks LB**, Bentzen SM, Deasy JO, Kong FM, Bradley JD, Vogelius IS, El Naqa I, Hubbs JL, Lebesque JV, Timmerman RD, Martel MK, Jackson A. Radiation dose-volume effects in the lung. *Int J Radiat Oncol Biol Phys* 2010; **76**: S70-S76 [PMID: 20171521 DOI: 10.1016/j.ijrobp.2009.06.091]

8 **Yamashita H**, Nakagawa K, Nakamura N, Koyanagi H, Tago M, Igaki H, Shiraishi K, Sasano N, Ohtomo K. Exceptionally high incidence of symptomatic grade 2-5 radiation pneumonitis after stereotactic radiation therapy for lung tumors. *Radiat Oncol* 2007; **2**: 21 [PMID: 17553175]

9 **Huang K**, Dahele M, Senan S, Guckenberger M, Rodrigues GB, Ward A, Boldt RG, Palma DA. Radiographic changes after lung stereotactic ablative radiotherapy (SABR)--can we distinguish recurrence from fibrosis? A systematic review of the literature. *Radiother Oncol* 2012; **102**: 335-342 [PMID: 22305958 DOI: 10.1016/j.radonc.2011.12.018]

10 **Guckenberger M**, Baier K, Polat B, Richter A, Krieger T, Wilbert J, Mueller G, Flentje M. Dose-response relationship for radiation-induced pneumonitis after pulmonary stereotactic body radiotherapy. *Radiother Oncol* 2010; **97**: 65-70 [PMID: 20605245 DOI: 10.1016/j.radonc.2010.04.027]

11 **Borst GR**, Ishikawa M, Nijkamp J, Hauptmann M, Shirato H, Onimaru R, van den Heuvel MM, Belderbos J, Lebesque JV, Sonke JJ. Radiation pneumonitis in patients treated for malignant pulmonary lesions with hypofractionated radiation therapy. *Radiother Oncol* 2009; **91**: 307-313 [PMID: 19321217 DOI: 10.1016/j.radonc.2009.02.003]

12 **Guckenberger M**, Klement RJ, Kestin LL, Hope AJ, Belderbos J, Werner-Wasik M, Yan D, Sonke JJ, Bissonnette JP, Xiao Y, Grills IS. Lack of a dose-effect relationship for pulmonary function changes after stereotactic body radiation therapy for early-stage non-small cell lung cancer. *Int J Radiat Oncol Biol Phys* 2013; **85**: 1074-1081 [PMID: 23154077 DOI: 10.1016/j.ijrobp.2012.09.016]

13 **Stephans KL**, Djemil T, Reddy CA, Gajdos SM, Kolar M, Machuzak M, Mazzone P, Videtic GM. Comprehensive analysis of pulmonary function Test (PFT) changes after stereotactic body radiotherapy (SBRT) for stage I lung cancer in medically inoperable patients. *J Thorac Oncol* 2009; **4**: 838-844 [PMID: 19487961 DOI: 10.1097/JTO.0b013e3181a99ff6]

14 **Bral S**, Gevaert T, Linthout N, Versmessen H, Collen C, Engels B, Verdries D, Everaert H, Christian N, De Ridder M, Storme G. Prospective, risk-adapted strategy of stereotactic body radiotherapy for early-stage non-small-cell lung cancer: results of a Phase II trial. *Int J Radiat Oncol Biol Phys* 2011; **80**: 1343-1349 [PMID: 20708849 DOI: 10.1016/j.ijrobp.2010.04.056]

15 **Fritz P**, Kraus HJ, Blaschke T, Mühlnickel W, Strauch K, Engel-Riedel W, Chemaissani A, Stoelben E. Stereotactic, high single-dose irradiation of stage I non-small cell lung cancer (NSCLC) using four-dimensional CT scans for treatment planning. *Lung Cancer* 2008; **60**: 193-199 [PMID: 18045732]

16 **Baumann P**, Nyman J, Hoyer M, Gagliardi G, Lax I, Wennberg B, Drugge N, Ekberg L, Friesland S, Johansson KA, Lund JS, Morhed E, Nilsson K, Levin N, Paludan M, Sederholm C, Traberg A, Wittgren L, Lewensohn R. Stereotactic body radiotherapy for medically inoperable patients with stage I non-small cell lung cancer - a first report of toxicity related to COPD/CVD in a non-randomized prospective phase II study. *Radiother Oncol* 2008; **88**: 359-367 [PMID: 18768228 DOI: 10.1016/j.radonc.2008.07.019]

17 **Ohashi T**, Takeda A, Shigematsu N, Kunieda E, Ishizaka A, Fukada J, Deloar HM, Kawaguchi O, Takeda T, Takemasa K, Isobe K, Kubo A. Differences in pulmonary function before vs. 1 year after hypofractionated stereotactic radiotherapy for small peripheral lung tumors. *Int J Radiat Oncol Biol Phys* 2005; **62**: 1003-1008 [PMID: 15990001]

18 **Henderson M**, McGarry R, Yiannoutsos C, Fakiris A, Hoopes D, Williams M, Timmerman R. Baseline pulmonary function as a predictor for survival and decline in pulmonary function over time in patients undergoing stereotactic body radiotherapy for the treatment of stage I non-small-cell lung cancer. *Int J Radiat Oncol Biol Phys* 2008; **72**: 404-409 [PMID: 18394819 DOI: 10.1016/j.ijrobp.2007.12.051]

19 **Miyamoto T**, Baba M, Yamamoto N, Koto M, Sugawara T, Yashiro T, Kadono K, Ezawa H, Tsujii H, Mizoe JE, Yoshikawa K, Kandatsu S, Fujisawa T. Curative treatment of Stage I non-small-cell lung cancer with carbon ion beams using a hypofractionated regimen. *Int J Radiat Oncol Biol Phys* 2007; **67**: 750-758 [PMID: 17293232]

20 **Nagata Y**, Negoro Y, Aoki T, Mizowaki T, Takayama K, Kokubo M, Araki N, Mitsumori M, Sasai K, Shibamoto Y, Koga S, Yano S, Hiraoka M. Clinical outcomes of 3D conformal hypofractionated single high-dose radiotherapy for one or two lung tumors using a stereotactic body frame. *Int J Radiat Oncol Biol Phys* 2002; **52**: 1041-1046 [PMID: 11958900]

21 **Matsuo Y**, Takayama K, Nagata Y, Kunieda E, Tateoka K, Ishizuka N, Mizowaki T, Norihisa Y, Sakamoto M, Narita Y, Ishikura S, Hiraoka M. Interinstitutional variations in planning for stereotactic body radiation therapy for lung cancer. *Int J Radiat Oncol Biol Phys* 2007; **68**: 416-425 [PMID: 17363190]

22 **Nishio T**, Kunieda E, Shirato H, Ishikura S, Onishi H, Tateoka K, Hiraoka M, Narita Y, Ikeda M, Goka T. Dosimetric verification in participating institutions in a stereotactic body radiotherapy trial for stage I non-small cell lung cancer: Japan clinical oncology group trial (JCOG0403). *Phys Med Biol* 2006; **51**: 5409-5417 [PMID: 17047260]

23 **Timmerman R**, Paulus R, Galvin J, Michalski J, Straube W, Bradley J, Fakiris A, Bezjak A, Videtic G, Johnstone D, Fowler J, Gore E, Choy H. Stereotactic body radiation therapy for inoperable early stage lung cancer. *JAMA* 2010; **303**:

1070-1076 [PMID: 20233825 DOI: 10.1001/jama.2010.261]
24 **Andolino DL**, Forquer JA, Henderson MA, Barriger RB, Shapiro RH, Brabham JG, Johnstone PA, Cardenes HR, Fakiris AJ. Chest wall toxicity after stereotactic body radiotherapy for malignant lesions of the lung and liver. *Int J Radiat Oncol Biol Phys* 2011; **80**: 692-697 [PMID: 21288656 DOI: 10.1016/j.ijrobp.2010.03.020]
25 **Dunlap NE**, Cai J, Biedermann GB, Yang W, Benedict SH, Sheng K, Schefter TE, Kavanagh BD, Larner JM. Chest wall volume receiving & gt; 30 Gy predicts risk of severe pain and/or rib fracture after lung stereotactic body radiotherapy. *Int J Radiat Oncol Biol Phys* 2010; **76**: 796-801 [PMID: 19427740 DOI: 10.1016/j.ijrobp.2009.02.027]
26 **Hoppe BS**, Laser B, Kowalski AV, Fontenla SC, Pena-Greenberg E, Yorke ED, Lovelock DM, Hunt MA, Rosenzweig KE. Acute skin toxicity following stereotactic body radiation therapy for stage I non-small-cell lung cancer: who's at risk? *Int J Radiat Oncol Biol Phys* 2008; **72**: 1283-1286 [PMID: 19028267 DOI: 10.1016/j.ijrobp.2008.08.036]
27 **Ricardi U**, Filippi AR, Guarneri A, Giglioli FR, Mantovani C, Fiandra C, Anglesio S, Ragona R. Dosimetric predictors of radiation-induced lung injury in stereotactic body radiation therapy. *Acta Oncol* 2009; **48**: 571-577 [PMID: 19031164 DOI: 10.1080/02841860802520821]
28 **Ong CL**, Palma D, Verbakel WF, Slotman BJ, Senan S. Treatment of large stage I-II lung tumors using stereotactic body radiotherapy (SBRT): planning considerations and early toxicity. *Radiother Oncol* 2010; **97**: 431-436 [PMID: 20971523 DOI: 10.1016/j.radonc.2010.10.003]
29 **Barriger RB**, Forquer JA, Brabham JG, Andolino DL, Shapiro RH, Henderson MA, Johnstone PA, Fakiris AJ. A dose-volume analysis of radiation pneumonitis in non-small cell lung cancer patients treated with stereotactic body radiation therapy. *Int J Radiat Oncol Biol Phys* 2012; **82**: 457-462 [PMID: 21035956 DOI: 10.1016/j.ijrobp.2010.08.056]
30 **Stauder MC**, Macdonald OK, Olivier KR, Call JA, Lafata K, Mayo CS, Miller RC, Brown PD, Bauer HJ, Garces YI. Early pulmonary toxicity following lung stereotactic body radiation therapy delivered in consecutive daily fractions. *Radiother Oncol* 2011; **99**: 166-171 [PMID: 21571384 DOI: 10.1016/j.radonc.2011.04.002]
31 **McGarry RC**, Papiez L, Williams M, Whitford T, Timmerman RD. Stereotactic body radiation therapy of early-stage non-small-cell lung carcinoma: phase I study. *Int J Radiat Oncol Biol Phys* 2005; **63**: 1010-1015 [PMID: 16115740]
32 **Ricardi U**, Filippi AR, Guarneri A, Giglioli FR, Ciammella P, Franco P, Mantovani C, Borasio P, Scagliotti GV, Ragona R. Stereotactic body radiation therapy for early stage non-small cell lung cancer: results of a prospective trial. *Lung Cancer* 2010; **68**: 72-77 [PMID: 19556022 DOI: 10.1016/j.lungcan.2009.05.007]
33 **Onishi H**, Araki T, Shirato H, Nagata Y, Hiraoka M, Gomi K, Yamashita T, Niibe Y, Karasawa K, Hayakawa K, Takai Y, Kimura T, Hirokawa Y, Takeda A, Ouchi A, Hareyama M, Kokubo M, Hara R, Itami J, Yamada K. Stereotactic hypofractionated high-dose irradiation for stage I nonsmall cell lung carcinoma: clinical outcomes in 245 subjects in a Japanese multiinstitutional study. *Cancer* 2004; **101**: 1623-1631 [PMID: 15378503]
34 **Stephans KL**, Djemil T, Reddy CA, Gajdos SM, Kolar M, Mason D, Murthy S, Rice TW, Mazzone P, Machuzak M, Mekhail T, Videtic GM. A comparison of two stereotactic body radiation fractionation schedules for medically inoperable stage I non-small cell lung cancer: the Cleveland Clinic experience. *J Thorac Oncol* 2009; **4**: 976-982 [PMID: 19633473 DOI: 10.1097/JTO.0b013e3181adf509]
35 **Grills IS**, Mangona VS, Welsh R, Chmielewski G, McInerney E, Martin S, Wloch J, Ye H, Kestin LL. Outcomes after stereotactic lung radiotherapy or wedge resection for stage I non-small-cell lung cancer. *J Clin Oncol* 2010; **28**: 928-935 [PMID: 20065181 DOI: 10.1200/JCO.2009.25.0928]
36 **Timmerman RD**. An overview of hypofractionation and introduction to this issue of seminars in radiation oncology. *Semin Radiat Oncol* 2008; **18**: 215-222 [PMID: 18725106 DOI: 10.1016/j.semradonc.2008.04.001]
37 **Baker R**, Han G, Sarangkasiri S, DeMarco M, Turke C, Stevens CW, Dilling TJ. Clinical and dosimetric predictors of radiation pneumonitis in a large series of patients treated with stereotactic body radiation therapy to the lung. *Int J Radiat Oncol Biol Phys* 2013; **85**: 190-195 [PMID: 22929858 DOI: 10.1016/j.ijrobp.2012.03.041]
38 **Timmerman R**, Papiez L, McGarry R, Likes L, DesRosiers C, Frost S, Williams M. Extracranial stereotactic radioablation: results of a phase I study in medically inoperable stage I non-small cell lung cancer. *Chest* 2003; **124**: 1946-1955 [PMID: 14605072]
39 **Yamashita H**, Kobayashi-Shibata S, Terahara A, Okuma K, Haga A, Wakui R, Ohtomo K, Nakagawa K. Prescreening based on the presence of CT-scan abnormalities and biomarkers (KL-6 and SP-D) may reduce severe radiation pneumonitis after stereotactic radiotherapy. *Radiat Oncol* 2010; **5**: 32 [PMID: 20459699 DOI: 10.1186/1748-717X-5-32]
40 **Takahashi W**, Yamashita H, Kida S, Masutani Y, Sakumi A, Ohtomo K, Nakagawa K, Haga A. Verification of planning target volume settings in volumetric modulated arc therapy for stereotactic body radiation therapy by using in-treatment 4-dimensional cone beam computed tomography. *Int J Radiat Oncol Biol Phys* 2013; **86**: 426-431 [PMID: 23562767 DOI: 10.1016/j.ijrobp.2013.02.019]
41 **Nakagawa K**, Haga A, Kida S, Masutani Y, Yamashita H, Takahashi W, Sakumi A, Saotome N, Shiraki T, Ohtomo K, Iwai Y, Yoda K. 4D registration and 4D verification of lung tumor position for stereotactic volumetric modulated arc therapy using respiratory-correlated cone-beam CT. *J Radiat Res* 2013; **54**: 152-156 [PMID: 22843380 DOI: 10.1093/jrr/rrs058]
42 **Ohnishi H**, Yokoyama A, Kondo K, Hamada H, Abe M, Nishimura K, Hiwada K, Kohno N. Comparative study of KL-6, surfactant protein-A, surfactant protein-D, and monocyte chemoattractant protein-1 as serum markers for interstitial lung diseases. *Am J Respir Crit Care Med* 2002; **165**: 378-381 [PMID: 11818324]
43 **Kong FM**, Ao X, Wang L, Lawrence TS. The use of blood biomarkers to predict radiation lung toxicity: a potential strategy to individualize thoracic radiation therapy. *Cancer Control* 2008; **15**: 140-150 [PMID: 18376381]
44 **Hara R**, Itami J, Komiyama T, Katoh D, Kondo T. Serum levels of KL-6 for predicting the occurrence of radiation pneumonitis after stereotactic radiotherapy for lung tumors. *Chest* 2004; **125**: 340-344 [PMID: 14718465]
45 **Iwata H**, Shibamoto Y, Baba F, Sugie C, Ogino H, Murata R, Yanagi T, Otsuka S, Kosaki K, Murai T, Miyakawa A. Correlation between the serum KL-6 level and the grade of radiation pneumonitis after stereotactic body radiotherapy for stage I lung cancer or small lung metastasis. *Radiother Oncol* 2011; **101**: 267-270 [PMID: 21640420 DOI: 10.1016/j.radonc.2011.05.031]
46 **Takeda A**, Ohashi T, Kunieda E, Enomoto T, Sanuki N, Takeda T, Shigematsu N. Early graphical appearance of radiation pneumonitis correlates with the severity of radiation pneumonitis after stereotactic body radiotherapy (SBRT) in patients with lung tumors. *Int J Radiat Oncol Biol Phys* 2010; **77**: 685-690 [PMID: 20510193 DOI: 10.1016/j.ijrobp.2009.06.001]
47 **Hof H**, Hoess A, Oetzel D, Debus J, Herfarth K. Stereotactic single-dose radiotherapy of lung metastases. *Strahlenther Onkol* 2007; **183**: 673-678 [PMID: 18040611]
48 **Norihisa Y**, Nagata Y, Takayama K, Matsuo Y, Sakamoto T, Sakamoto M, Mizowaki T, Yano S, Hiraoka M. Stereotactic body radiotherapy for oligometastatic lung tumors. *Int J Ra-*

diat Oncol Biol Phys 2008; **72**: 398-403 [PMID: 18374506 DOI: 10.1016/j.ijrobp.2008.01.002]

49 **Yuan X**, Liao Z, Liu Z, Wang LE, Tucker SL, Mao L, Wang XS, Martel M, Komaki R, Cox JD, Milas L, Wei Q. Single nucleotide polymorphism at rs1982073: T869C of the TGFbeta 1 gene is associated with the risk of radiation pneumonitis in patients with non-small-cell lung cancer treated with definitive radiotherapy. *J Clin Oncol* 2009; **27**: 3370-3378 [PMID: 19380441 DOI: 10.1200/JCO.2008.20.6763]

50 **Takeda A**, Enomoto T, Sanuki N, Nakajima T, Takeda T, Sayama K, Kunieda E. Acute exacerbation of subclinical idiopathic pulmonary fibrosis triggered by hypofractionated stereotactic body radiotherapy in a patient with primary lung cancer and slightly focal honeycombing. *Radiat Med* 2008; **26**: 504-507 [PMID: 18975053 DOI: 10.1007/s11604-008-0261-8]

51 **Guckenberger M**, Heilman K, Wulf J, Mueller G, Beckmann G, Flentje M. Pulmonary injury and tumor response after stereotactic body radiotherapy (SBRT): results of a serial follow-up CT study. *Radiother Oncol* 2007; **85**: 435-442 [PMID: 18053602]

52 **Kimura T**, Matsuura K, Murakami Y, Hashimoto Y, Kenjo M, Kaneyasu Y, Wadasaki K, Hirokawa Y, Ito K, Okawa M. CT appearance of radiation injury of the lung and clinical symptoms after stereotactic body radiation therapy (SBRT) for lung cancers: are patients with pulmonary emphysema also candidates for SBRT for lung cancers? *Int J Radiat Oncol Biol Phys* 2006; **66**: 483-491 [PMID: 16904838]

53 **Matsuo Y**, Shibuya K, Nakamura M, Narabayashi M, Sakanaka K, Ueki N, Miyagi K, Norihisa Y, Mizowaki T, Nagata Y, Hiraoka M. Dose--volume metrics associated with radiation pneumonitis after stereotactic body radiation therapy for lung cancer. *Int J Radiat Oncol Biol Phys* 2012; **83**: e545-e549 [PMID: 22436782 DOI: 10.1016/j.ijrobp.2012.01.018]

P- Reviewer: Can MM, Storto G, Sun Z **S- Editor**: Wen LL
L- Editor: A **E- Editor**: Lu YJ

World Journal of Radiology

Submit a Manuscript: http://www.wjgnet.com/esps/
Help Desk: http://www.wjgnet.com/esps/helpdesk.aspx
DOI: 10.4329/wjr.v6.i9.716

World J Radiol 2014 September 28; 6(9): 716-725
ISSN 1949-8470 (online)

REVIEW

MRI in central nervous system infections: A simplified patterned approach

Krithika Rangarajan, Chandan J Das, Atin Kumar, Arun Kumar Gupta

Krithika Rangarajan, Chandan J Das, Atin Kumar, Arun Kumar Gupta, Department of Radiodiagnosis, All India Institute of Medical Sciences, Ansari Nagar East, New Delhi 110029, India
Author contributions: Rangarajan K and Das CJ wrote most of the manuscript text as well as edited the images; Kumar A and Gupta AK provided valuable inputs, edited the manuscript and approved the content.
Correspondence to: Chandan J Das, MD, Department of Radiodiagnosis, All India Institute of Medical Sciences, Ansari Nagar, Room number 60, New Delhi 110029, India. dascj@yahoo.com
Telephone: +91-11-26594868
Received: January 9, 2014 Revised: July 13, 2014
Accepted: July 27, 2014
Published online: September 28, 2014

Abstract

Recognition and characterization of central nervous system infections poses a formidable challenge to the neuro-radiologist. Imaging plays a vital role, the lesions typically being relatively inaccessible to tisue sampling. The results of an accurate diagnosis are endlessly rewarding, given the availability of excellent pharmacological regimen. The availability of numerous magnetic resonance (MR) sequences which provide functional and molecular information is a powerful tool in the hands of the radiologist. However, the plethora of sequences and the possibilities on each sequence is also intimidating, and often confusing as well as time consuming. While a large number of reviews have already described in detail the possible imaging findings in each infection, we intend to classify infections based on their imaging characteristics. In this review we describe an algorithm for first classifying the imaging findings into patterns based on basic MR sequences (T1, T2 and enhancement pattern with Gadolinium), and then subclassify them based on more advanced molecular and functional sequences (Diffusion, Perfusion, Susceptibility imaging, MR Spectroscopy). This patterned approach is intended as a guide to radiologists in-training and in-practice for quickly narrowing their list of differentials when faced with a clinical challenge. The entire content of the article has also been summarised in the form of flow-charts for the purpose of quick reference.

Key words: Central nervous system; Infection; Magnetic resonance imaging; Magnetic resonance spectroscopy; Perfusion weighted magnetic resonance imaging; Diffusion weighted magnetic resonance imaging

Core tip: The plethora of magnetic resonance sequences available with the radiologist today provides a wealth of information about anatomical, pathological, physiological, functional and molecular aspects of the brain. While this provides an opportunity to transform patient management, the vast number of possibilities can be bewildering, particularly for the radiologist in-training. It is often easy to get lost in the details while forgetting the larger picture. In this article we first classify the infections into broad imaging patterns, and subsequently sub-classify them based on more advanced sequences (molecular and functional imaging). The flow-charts in the article are intended as a source of quick reference to the radiologist when faced with a clinical challenge.

Rangarajan K, Das CJ, Kumar A, Gupta AK. MRI in central nervous system infections: A simplified patterned approach. *World J Radiol* 2014; 6(9): 716-725 Available from: URL: http://www.wjgnet.com/1949-8470/full/v6/i9/716.htm DOI: http://dx.doi.org/10.4329/wjr.v6.i9.716

INTRODUCTION

Central nervous system (CNS) infections are a significant

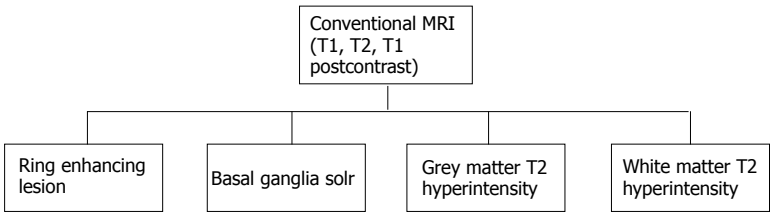

Figure 1 Classification of abnormalities on conventional magnetic resonance imaging sequences in suspected central nervous system infections.

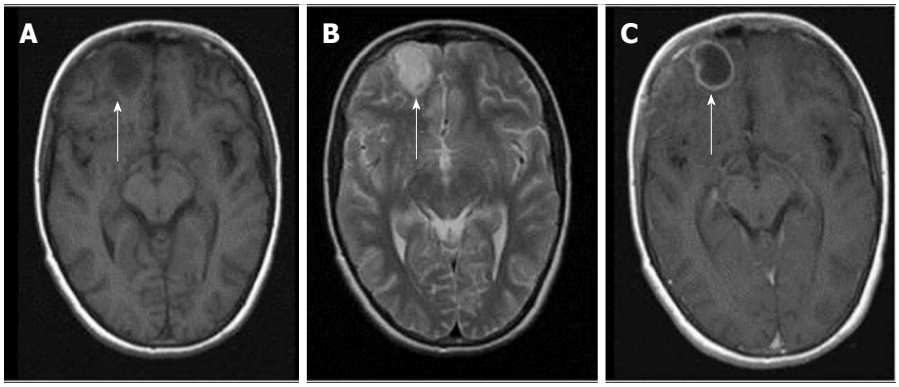

Figure 2 Ring enhancing lesions. T1 (A), T2 (B) and T1 (C) post gadolinium images from the magnetic resonance of an acutely ill child with fever. A ring enhancing lesion is seen in the right frontal lobe. This patient had a bacterial brain abscess. The differential diagnosis of this appearance would include a brain abscess of any etiology.

cause of mortality and morbidity world-wide. This is particularly true owing to its association with conditions of immunological compromise and the increasing incidence of human immunodeficiency virus (HIV) infection is further adding to the problem[1]. Today with the availability of excellent antimicrobials, many of these disorders are potentially treatable, making early recognition imperative. Like in other disorders of the CNS, non-invasive imaging based diagnosis is the key as possibility of a tissue diagnosis by means of fine needle aspiration cytology (FNAC) or biopsy is difficult. Early diagnosis will also help to minimize long term complications related to the disease and its treatment.

The primary imaging modality, like in most CNS disorders is magnetic resonance imaging (MRI)[2]. Coming to an exact etiological agent on the basis of conventional MRI sequences with Gadolinium enhancement is always difficult due to overlapping imaging characteristics. With the possibility of molecular and functional imaging with newer MRI techniqueshowever, the radiologist today is better equipped to handle this dilemma. Though the use of such multiple MRI sequences adds lots of information to narrow the differential possibilities, this vast information is difficult to recall when faced with a clinical problem.

The purpose of this review is to provide a rational MRI approach to narrow the list of differentials, to quickly classify and characterize CNS infections. The flow-charts presented in this review guides the radiologist to first recognize the pattern of findings on routine MRI sequences and subsequently narrow the differential diagnosis based on the addition of other MR parameters such as diffusion weighted imaging (DWI) and MR spectroscopy (MRS).

CLASSIFICATION

Most infections in the CNS may be classified in one of the following categories based on their T1, T2 and contrast enhancement characteristics (Figure 1) as follows (an image demonstrating a typical lesion in each category has been provided in Figures 2-5): Ring enhancing lesions (Figure 2), Basal ganglia space occupying lesions (Figure 3), Grey matter hyperintensities (Figure 4), White matter hyperintensities (Figure 5).

RING ENHANCING LESIONS

Peripheral ring-like enhancement is a common finding in CNS imaging. Ring enhancing lesions on conventional MRI sequences have a long list of differentials ranging from infectious processes to high grade necrotic neoplasm. Glioblastoma multiforme represents the most important condition. Abscesses are usually associated with a thin smooth rim, in contrast to the nodular irregular rim seen in Glioblastoma multiforme. Satellite lesions are commonly seen in abscesses, unlike necrotic neoplasm[1]. Recent work by some investigators has suggested a role for susceptibilityweighted imaging (SWI) in this differentiation. They found that a smooth, complete rim of susceptibility is seen in abscesses in contrast to incomplete irregular rims seen in necrotic neoplasm[3].

All mature abscesses whether bacterial, fungal or pyogenic are hypointense on T1, hyperintense on T2 and show ring enhancement following intravenous Gado-

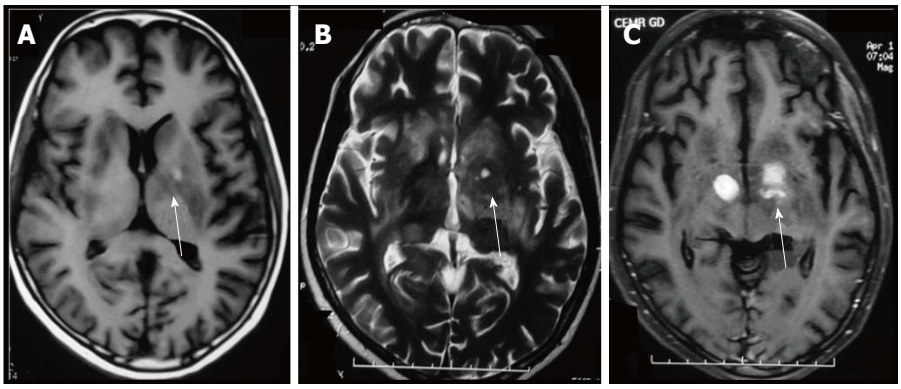

Figure 3 T1 (A), T2 (B) and Post gadolinium T1 (C) weighted images in an human immunodeficiency virus-positive patient with space occupying lesions in bilateral basal ganglia. Differentials for this appearance in such a patient would include Toxoplasmosis, Cryptococcosis as well as central nervous system (CNS) lymphoma. This patient had CNS lymphoma.

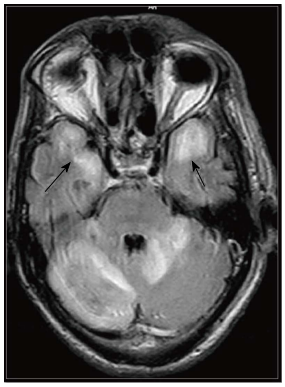

Figure 4 Fluid Attenuated Inversion Recovery Sequence in a patient with fever and altered sensorium shows hyperintensity predominantly in the grey matter of both temporal lobes and also in cerebellum. This patient was diagnosed with Japanese B Encephalitis. A similar picture may be seen in other viral encephalitis including herpes encephalitis.

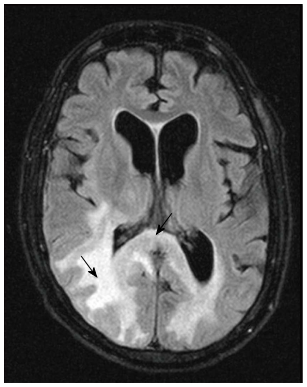

Figure 5 Fluid Attenuated Inversion Recovery Sequence image of a human immunodeficiency virus-positive patient shows hyperintensity predominantly involving the occipital white matter and splenium. The differential diagnosis for such an appearance would include human immunodeficiency virus encephalopathy, progressive multifocal leukoencephalopathy (PML) well as other demyelinating conditions. This patient had PML.

linium injection. Further differentiation of abscesses for possible etiological cause may be made as follows.

DIFFUSSION WEIGHTED IMAGING

DWI explores the molecular characteristic of diffusivity of particles within a region. It is based on the application of two gradients at a set interval of time, in such a way that only a molecule that experiences both gradients at the same position (does not exhibit motion between the two gradients) produces signal. Therefore regions of the brain that show "restricted diffusion" are hyperintense on DWI. This restricted diffusion appears as hyperintense area on DWI and needs to be corroborated with computer generated apparent diffusion coefficient (ADC) maps which show corresponding hypointense area. This corroboration rules out T2-shine through effect. Bacterial as well as tubercular abscesses show central diffusion restriction[4,5] due to highly viscous necrotic tissue within (Figure 6). Fungal abscesses show intracavitary projections. The wall of abscess and the projections may demonstrate diffusion restriction[5,6], though no restriction is seen in the abscess core (Figure 7).

DWI plays an important role in the differentiation of these abscesses from necrotic neoplasms, which usually demonstrate high ADC values within the core[7].

MR SPECTROSCOPY

Spectroscopy provides information about metabolic alterations within a voxel by exploiting changes in the microenvironment produced by unique chemical characteristics of specific metabolites. Thus using this technique it is possible to infer the presence of a microorganism, based on the expected products of the microorganisms metabolism reflected in the metabolic signature.

The characteristic of the spectrum in bacterial abscesses is the presence of amino acid peak at 0.9 parts per million (ppm) [inverted peak at an time of echo (TE) 136 ms] representing valine, leucine and isoleucine (Figure 8)[2]. The detection of succinate (2.4 ppm) and acetate (1.92 ppm) is proposed to indicate anaerobic organisms[2].

Tuberculosis is characterised by lipid peaks at 0.9, 1.3, 2.0 and 2.8 ppm. The presence of lipids in the absence of other amino acids, lactate and succinate is strongly suggestive of tubercular abscess (Figure 9)[5,8]. 0.9, 1.3, 2.0, 2.8, and 3.7 peaks correspond to specific chemical groups within metabolites found in these infections- 0.9 corresponds to a terminal methyl group, 1.3 to a methylene group, 2.0 and 2.8 to specific groups in fatty acyl chains and 3.7 to phosphoserine.

While lactate, acetate and succinate can all be seen

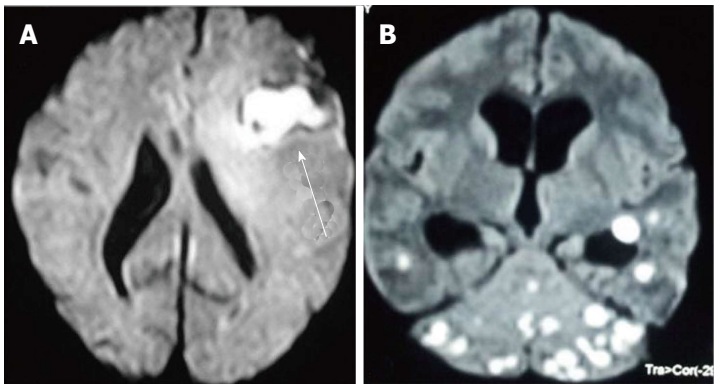

Figure 6 Diffusion weighted images show central restriction of diffusion in bacterial abscess (A) and tuberculomas (B) arrow.

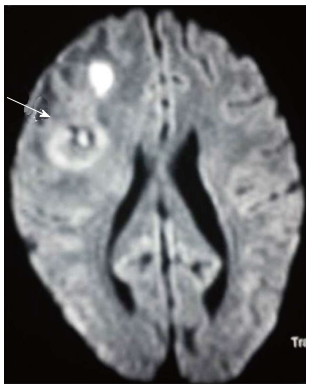

Figure 7 Diffusion weighted image in a diabetic patient shows diffusion restriction in the wall and intra-cavitary projection (arrow) in the centre of a fungal abscess.

in fungal abscesses, the presence of multiple signals between 3.6 and 3.8 ppm (representing Trehalose) has been seen in some forms of fungal abscesses (Figure 10)[5]. The absence of choline peak on MRS provides important supportive evidence for an infective etiology as compared to neoplasms which show increased choline[7,9].

MR ANGIOGRAPHY

Tubercular vasculitis results in extensive infarction due to inflammation of vessels coursing through the basal exudates (Figure 11)[10]. Vascular involvement with formation of aneurysms is seen in fungal infections. These aneurysms are seen as irregular dilatation of vessel wall on MRA.

SUSCEPTIBILITY WEIGHTED IMAGING

The principle underlying SWI is the alteration of local magnetic field by substances that show paramagnetic properties. This is a gradient sequence, so molecules in the vicinity of a paramagnetic substance dephase rapidly, thus do not contribute to signal production. Voxels containing molecules with different magnetic susceptibilities are imaged when they are exactly out-of-phase, such that the whole voxel appears to be of low signal intensity[2]. This is seen as an area of "blooming". The presence of haemorrhage is often a clue to underlying fungal cause of

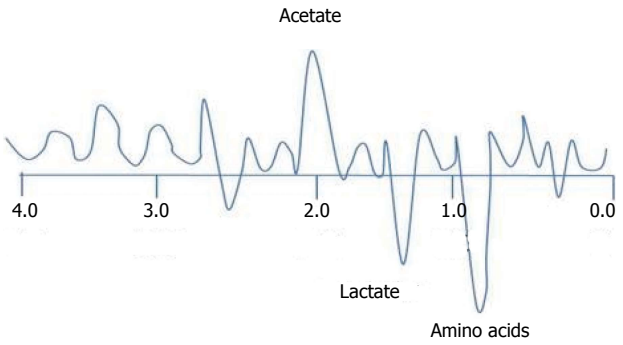

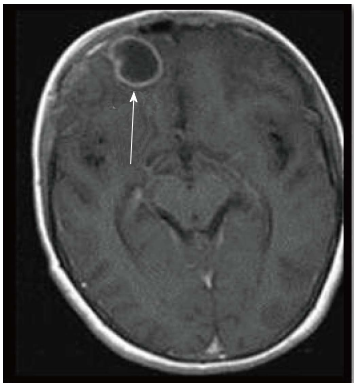

Figure 8 Representation of spectrum of metabolites in a bacterial abscess. Proton magnetic resonance spectroscopy obtained at a time of echo of 30 milliseconds shows the presence of amino acids. Succinate and acetate are seen in anaerobic abscesses.

infection (Figure 12) due to its angioinvasive nature[11].

The presence of a complete, smooth hypointense rim on SWI favours a diagnosis of an abscess against a necrotic neoplasm. A brief summary of approach to a peripherally enhancing lesion is presented as a flowchart (Figure 13).

BASAL GANGLIA SPACE OCCUPYING LESIONS

A number of CNS lesions are seen characteristically involving the region of basal ganglia. The differential diagnosis in this category includes cryptococcosis, toxoplasmosis and primary CNS lymphoma. Cryptococcosis usually does not show enhancement after gadolinium injection.Further characterisation often requires additional

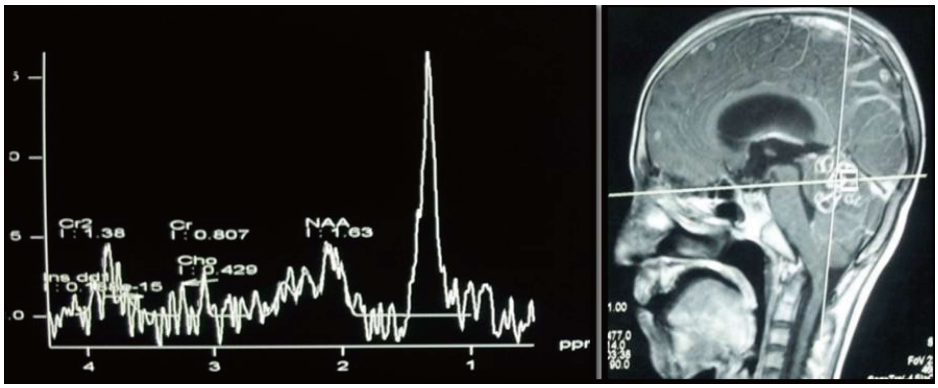

Figure 9 Proton spectroscopy at echo time of 135 ms from a tuberculoma shows a lipid peak at 1.3 ppm.

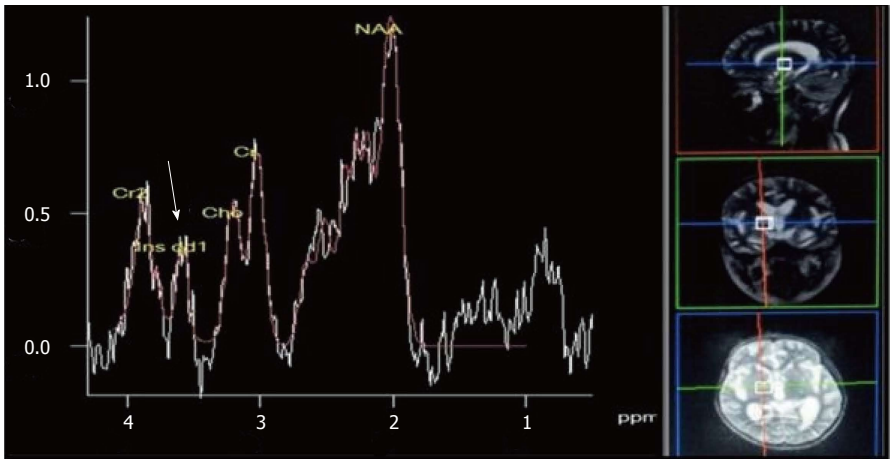

Figure 10 Proton magnetic resonance spectroscopy at time of echo of 30 ms shows multiple peaks between 3.6 and 3.8 ppm in the spectrum obtained from a cryptococcoma (fungus) representative oftrehalose peak (arrow).

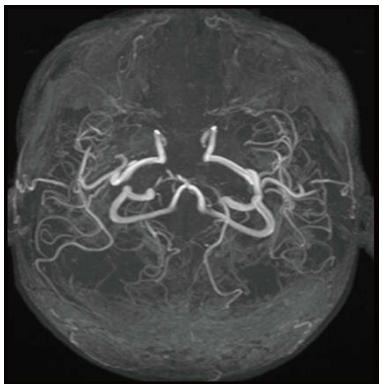

Figure 11 Time of Flight magnetic resonance angiography in a patient with tubercular meningitis. Bilateral anterior cerebral arteries are not seen whereas bilateral middle cerebral arteries aremarkedly attenuated suggesting vasculitis. The patient presented with extensive cerebral infarction.

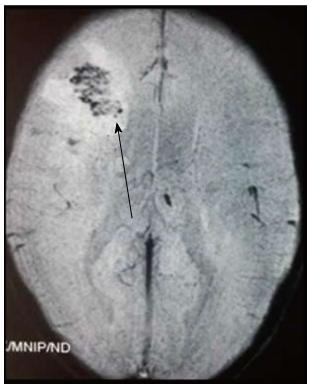

Figure 12 Foci of blooming (arrow) noted within the abscess is suggestive of haemorrhage and points to a fungal cause.

sequences.

DWI

Toxoplasmosis does not usually show significant restriction of diffusion, though a wide range of ADC value have been encountered[2,12]. A proposed explanation is the lack of viscous contents within these lesions. Peripheral areas may show hyperintensity due to the presence of haemorrhage[13]. Lymphoma which usually are highly cellular, shows restricted diffusion[2,12], helping differentiation from toxoplasmosis (Figure 14). The paucity of intercellular spaces results in a decreased diffusivity of water molecules within these lesions. Cryptococcosis is also known to show restricted diffusion within the pseu-

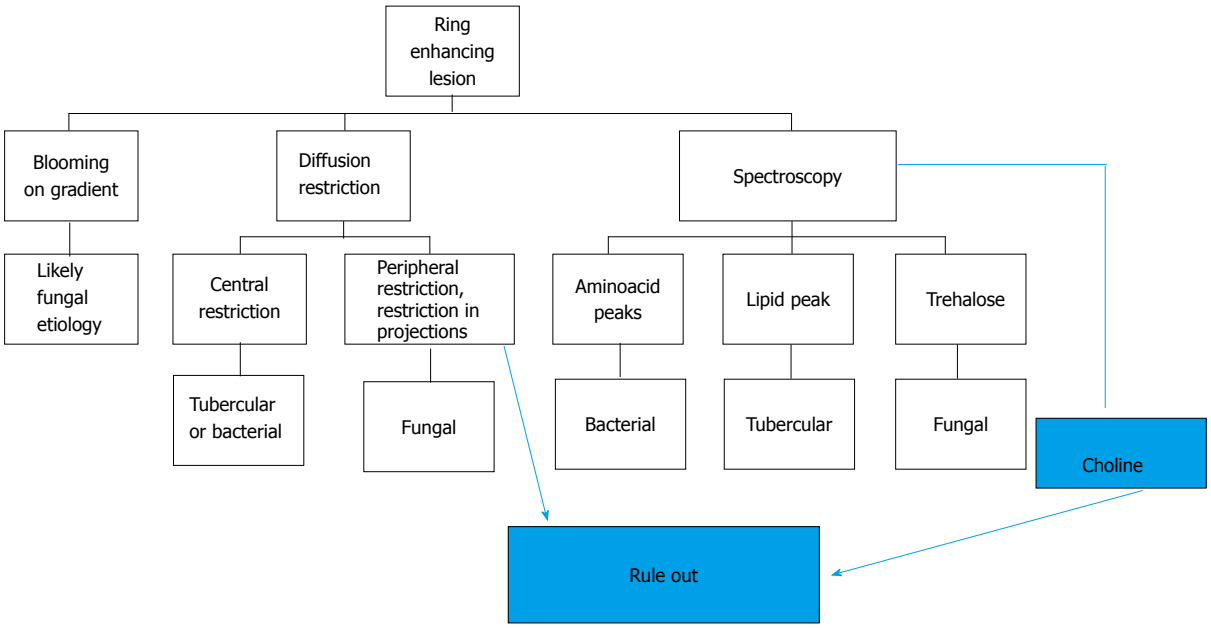

Figure 13 Approach to ring enhancing lesions.

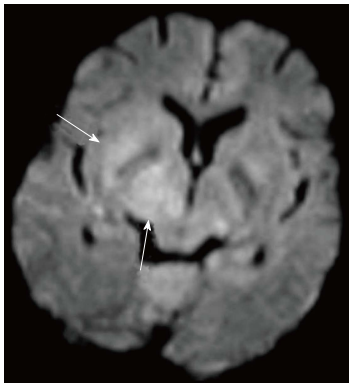

Figure 14 Diffusion weighted image from the Brain magnetic resonance imaging of an human immunodeficiency virus-positive patient with lymphoma shows restriction in the right lentiform nucleus and the thalamus (arrow).

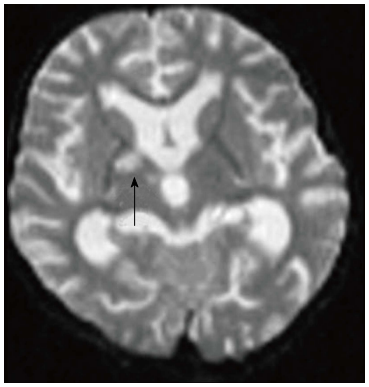

Figure 15 Apparent diffusion coefficient map showing free diffusion within a cryptococcoma (arrow) in a human immunodeficiency virus-positive patient.

docysts[2] owing to the viscosity of gelatinous material. Cryptococcomas have been shown to exhibit peripheral diffusion restriction akin to a necrotic brain tumour[14], though often they may not show any restricted diffusion[12] (Figure 15).

MRS

Presence of peak between 3.6 to 3.8 ppm (trehalose) has been observed in cryptococcosis (which is a fungus)[5] (Figure 10). Toxoplasma lesions (Figure 16) show markedly elevated lipid and lactate with diminished levels of all other metabolites[2]. Lymphoma (Figure 17) shows mild to moderate increase in lipid and lactate with markedly elevated choline peak[2].

MR perfusion

Toxoplasmosis shows normal or decreased cerebral blood volume (CBV). Primary CNS lymphoma on the other hand shows elevated CBV[12].

SWI

Presence of hemorrhage (blooming on gradient echo sequences) points towards toxoplasmosis, as lymphoma rarely showhemorrhage before treatment[12,15] (Figure 18). A brief summary of the approach to space occupying lesions in the basal ganglia is presented as a flowchart in Figure 19.

GREY MATTER HYPERINTENSITY

T2/ FLAIR hyperintensity involving the grey matter may be seen in encephalitis as well as infarction. This differentiation is aided by diffusion and perfusion sequences (Table 1).

Diffusion and perfusion

Reduced diffusion with increased perfusion points to an

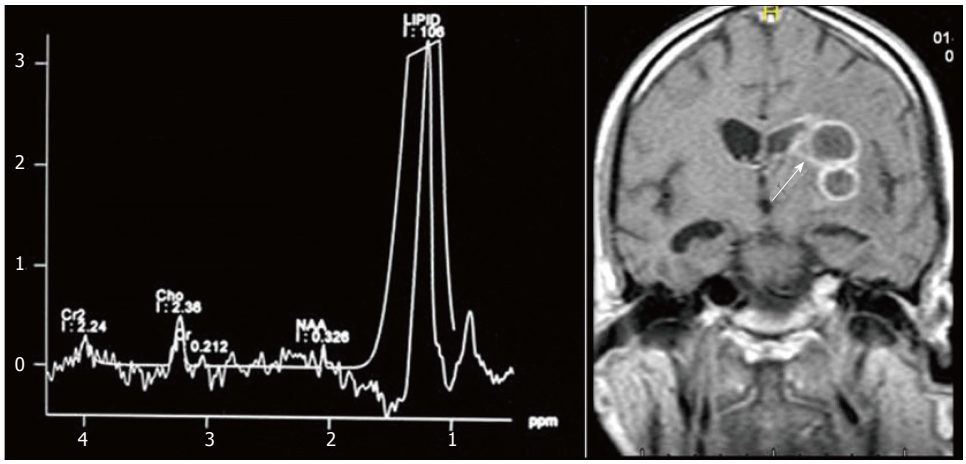

Figure 16 Proton magnetic resonance spectroscopy at echo time of 30 ms in a patient with toxoplasmosis shows a lipid lactate peak with diminished levels of all other metabolites (arrow).

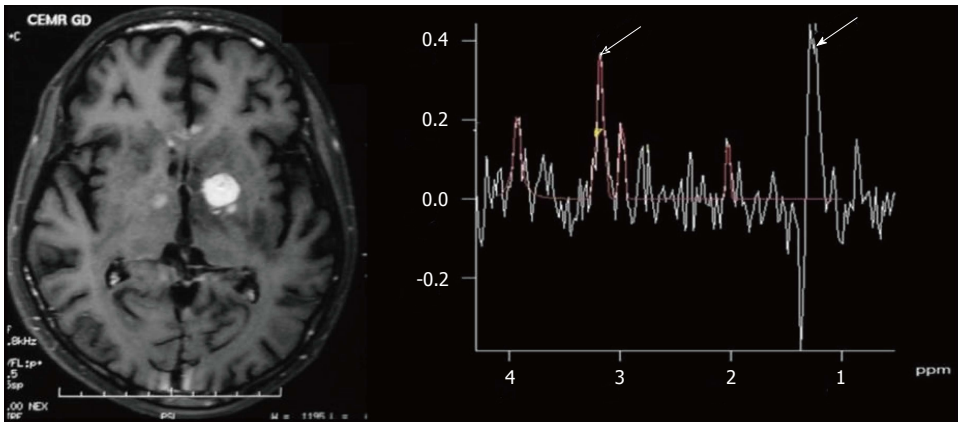

Figure 17 Proton magnetic resonance spectroscopy at echo time of 135 ms in a patient with primary central nervous system Lymphoma of basal ganglia showing elevated lipid, lactate (white arrow) and choline (open arrow).

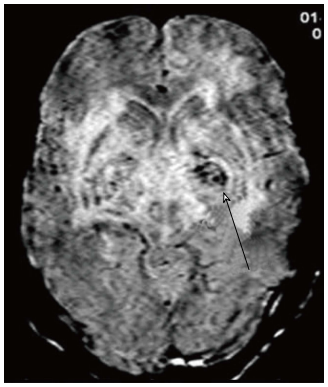

Figure 18 Gradient echo image in a patient with toxoplasmosis shows foci of blooming (arrow) suggestive of haemorrhage.

infective etiology. Reduced diffusion with decreased perfusion characterizes ischemic events. The further characterization of infection is typically based on characteristic neuro-anatomic location of the lesion on T2/FLAIR/DWI (Figure 20)[2,16]. Prion disease can also show similar imaging manifestation. The imaging appearance of these encephalitis may be fairly non-specific. The dengue virus has been reported to show imaging features similar to Japanese encephalitis[17] in regions where this virus is common. Cytomegalovirus can also show non-specific manifestations, though the predominant involvement of grey matter (more than white matter) is an important differentiating feature[1]. The presence of a pencil-thin rim of enhancement in the subependymal region is considered to be a specific finding[1]. Approach to lesions presenting with hyperintensity predominantly involving the Grey matteris presented as a flowchart in Figure 21.

Table 1 This differentiation is aided by diffusion and perfusion sequences

	Diffusion	Perfusion
Infection	Restricted	Increased
Infarction	Restricted	Decreased

WHITE MATTER HYPERINTENSITIES

The major diagnostic considerations are HIV encephalopathy (HIVE) and progressive multifocal leukoen-

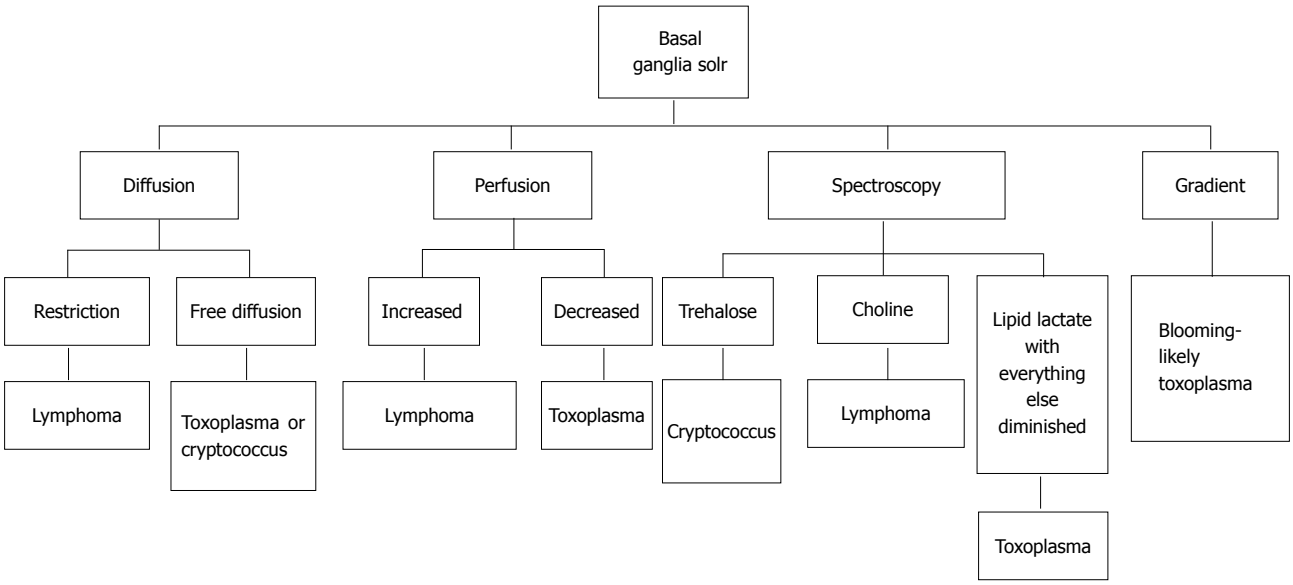

Figure 19 Approach to space occupying lesions in the basal ganglia.

Table 2 Role of additional sequences

	T1	T2	T1 + contrast
HIV Encephalopathy	Isointense	Bilaterally symmetrical periventricular white matter hyperintensities	No enhancement
PML	Hypointense	Asymmetrical lesions involving subcortical and periventricular white matter	Faint peripheral areas of enhancement may sometimes be seen

HIV: Human immunodeficiency virus; PML: Progressive multifocal leukoencephalopathy.

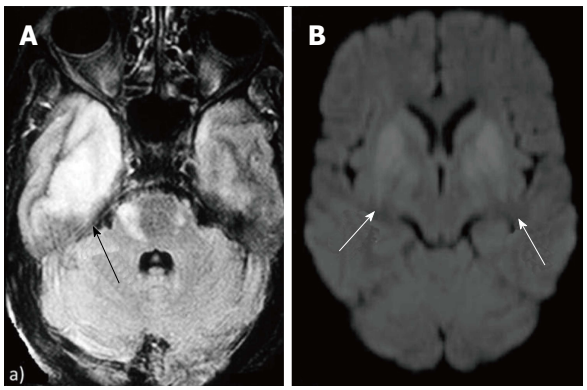

Figure 20 Fluid Attenuated Inversion Recovery Sequence hyperintensity (A) involving right temporal lobe (black arrow) in a patient with Herpes simplex virus encephalitis, diffusion weighted imaging (B) in a patient with Japanese encephalitis showing restricted diffusion in bilateral basal ganglia.

cephalopathy (PML) (Figure 22). Though both entities have characteristic imaging features on conventional MR sequences (Table 2), they may be difficult to differentiate due to overlapping features.

Magnetization transfer

Magnetization transfer (MT) reduction is seen in both PML and HIVE. In PML, it is due to demyelination whereas in HIVE it is primarily related to gliosis. Thus

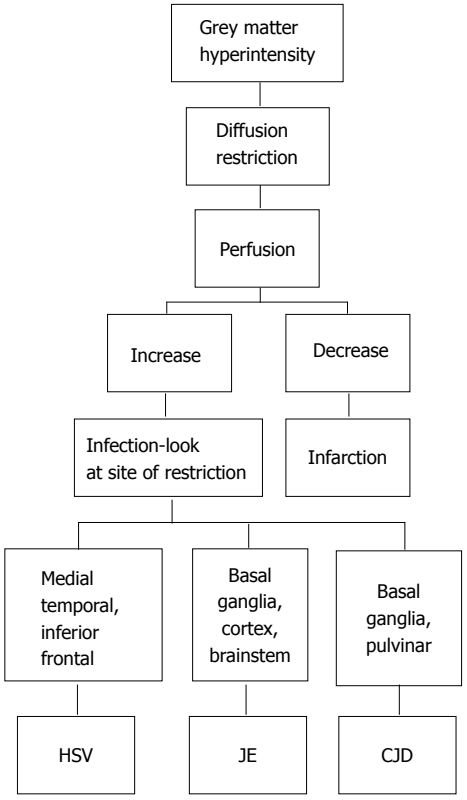

Figure 21 Approach to lesions presenting with hyperintensity predominantly involving the Grey matter.

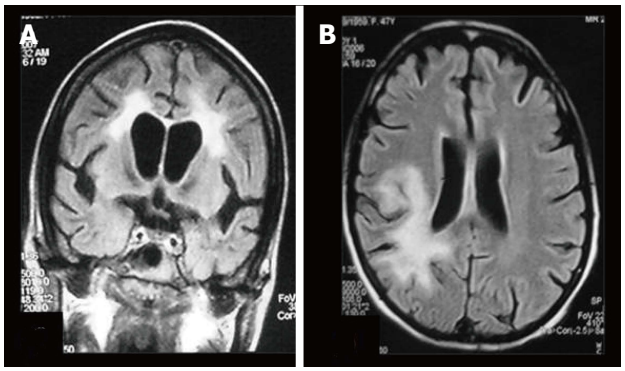

Figure 22 Fluid Attenuated Inversion Recovery Sequence image of a patient with (A) human immunodeficiency virus encephalopathy showing symmetrical periventricular white matter hyperintensity and (B) progressive multifocal leukoencephalopathy showing asymmetrical involvement of white matter, predominantly posterior subcortical white matter, with extension into the periventricularregion.

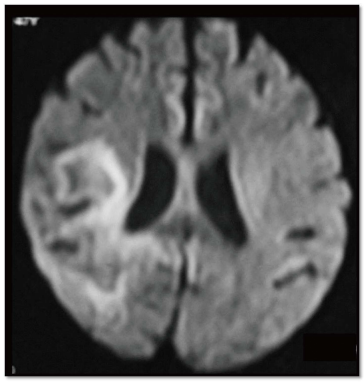

Figure 23 Diffusion weighted image in a patient with progressive multifocal leukoencephalopathy showing peripheral diffusion restriction.

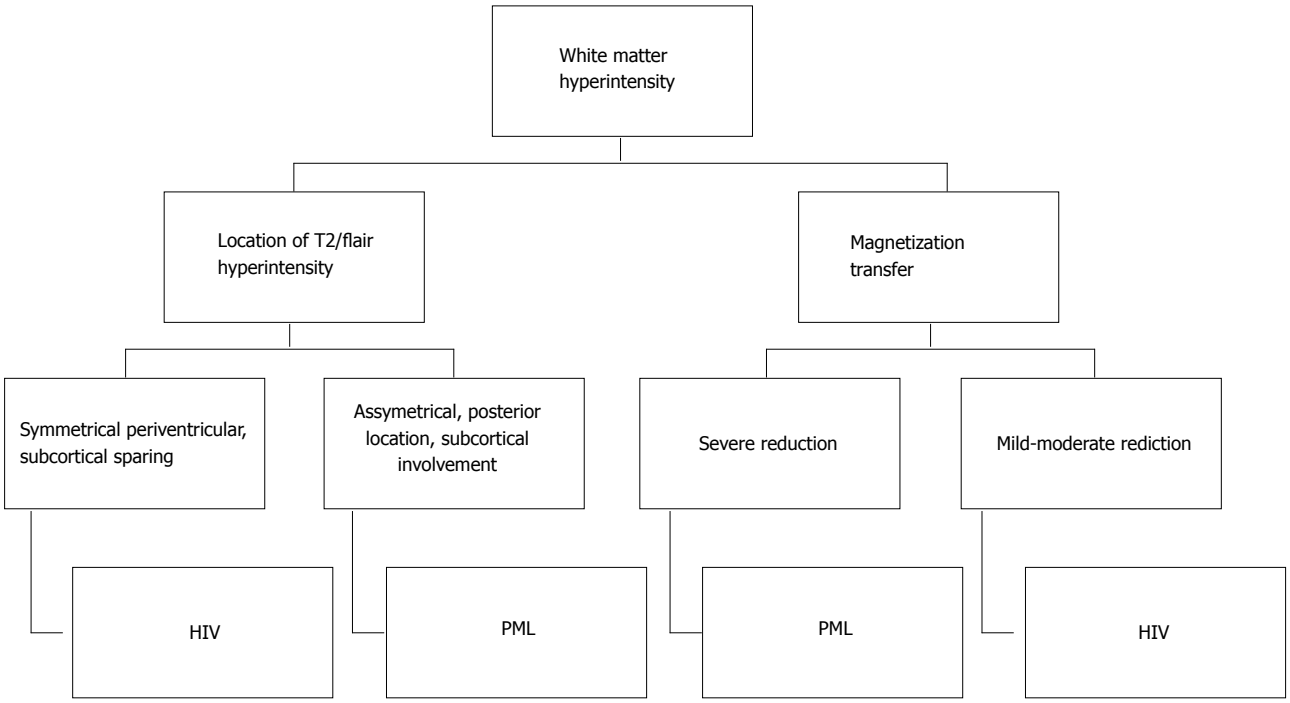

Figure 24 Approach to lesions presenting with hyperintensity predominantly involving the white matter. PML: Progressive multifocal leukoencephalopathy; HIV: Human immunodeficiency virus.

larger reduction in MT has been observed in PML as compared to HIVE[18]. The major role of MT sequence in this setting is in early detection of disease.

Diffusion and diffusion tensor imaging

Fractional anisotropy is seen to be reduced in HIVE and PML before the morphologic changes in conventional sequences[19]. Reduced diffusion is seen in the periphery and free diffusion in the centre of PML lesions[12] (Figure 23).

MRS

Reduction of N-acetylaspartate is seen in HIVE even before the onset of symptoms. Raised choline and myoinositol is also seen in the spectra. A summary of suggested approach to these white matter lesions is presented as a flowchart in Figure 24.

CONCLUSION

Imaging features of CNS infections constitute a complex myriad. Their classification based on conventional MRI sequences, may provide a quick guide to narrowing the differential diagnosis followed by further sub-differentiation into single etiology using advanced MRI sequences

and techniques.

REFERENCES

1 **Aiken AH**. Central nervous system infection. *Neuroimaging Clin N Am* 2010; **20**: 557-580 [PMID: 20974376 DOI: 10.1016/j.nic.2010.07.011]

2 **Whiteman ML**, Bowen BC, Post MJ, Bell MD. Intracranial infections. In Scott W Atlas, editor. Magnetic Resonance Imaging of Brain and Spine. 3rd ed. Philadelphia: Lippincott Williams and Wilkins, 2002: 1099-177

3 **Toh CH**, Wei KC, Chang CN, Hsu PW, Wong HF, Ng SH, Castillo M, Lin CP. Differentiation of pyogenic brain abscesses from necrotic glioblastomas with use of susceptibility-weighted imaging. *AJNR Am J Neuroradiol* 2012; **33**: 1534-1538 [PMID: 22422181 DOI: 10.3174/ajnr.A2986]

4 **Desprechins B**, Stadnik T, Koerts G, Shabana W, Breucq C, Osteaux M. Use of diffusion-weighted MR imaging in differential diagnosis between intracerebral necrotic tumors and cerebral abscesses. *AJNR Am J Neuroradiol* 1999; **20**: 1252-1257 [PMID: 10472982]

5 **Luthra G**, Parihar A, Nath K, Jaiswal S, Prasad KN, Husain N, Husain M, Singh S, Behari S, Gupta RK. Comparative evaluation of fungal, tubercular, and pyogenic brain abscesses with conventional and diffusion MR imaging and proton MR spectroscopy. *AJNR Am J Neuroradiol* 2007; **28**: 1332-1338 [PMID: 17698537 DOI: 10.3174/ajnr.A0548]

6 **Gaviani P**, Schwartz RB, Hedley-Whyte ET, Ligon KL, Robicsek A, Schaefer P, Henson JW. Diffusion-weighted imaging of fungal cerebral infection. *AJNR Am J Neuroradiol* 2005; **26**: 1115-1121 [PMID: 15891169]

7 **Lai PH**, Ho JT, Chen WL, Hsu SS, Wang JS, Pan HB, Yang CF. Brain abscess and necrotic brain tumor: discrimination with proton MR spectroscopy and diffusion-weighted imaging. *AJNR Am J Neuroradiol* 2002; **23**: 1369-1377 [PMID: 12223380]

8 **Gupta RK**, Roy R, Dev R, Husain M, Poptani H, Pandey R, Kishore J, Bhaduri AP. Finger printing of Mycobacterium tuberculosis in patients with intracranial tuberculomas by using in vivo, ex vivo, and in vitro magnetic resonance spectroscopy. *Magn Reson Med* 1996; **36**: 829-833 [PMID: 8946348]

9 **Lai PH**, Weng HH, Chen CY, Hsu SS, Ding S, Ko CW, Fu JH, Liang HL, Chen KH. In vivo differentiation of aerobic brain abscesses and necrotic glioblastomas multiforme using proton MR spectroscopic imaging. *AJNR Am J Neuroradiol* 2008; **29**: 1511-1518 [PMID: 18499784 DOI: 10.3174/ajnr.A1130]

10 **Trivedi R**, Saksena S, Gupta RK. Magnetic resonance imaging in central nervous system tuberculosis. *Indian J Radiol Imaging* 2009; **19**: 256-265 [PMID: 19881100 DOI: 10.4103/0971-3026.57205]

11 **Jain KK**, Mittal SK, Kumar S, Gupta RK. Imaging features of central nervous system fungal infections. *Neurol India* 2007; **55**: 241-250 [PMID: 17921653]

12 **Smith AB**, Smirniotopoulos JG, Rushing EJ. From the archives of the AFIP: central nervous system infections associated with human immunodeficiency virus infection: radiologic-pathologic correlation. *Radiographics* 2008; **28**: 2033-2058 [PMID: 19001657 DOI: 10.1148/rg.287085135]

13 **Lee GT**, Antelo F, Mlikotic AA. Best cases from the AFIP: cerebral toxoplasmosis. *Radiographics* 2009; **29**: 1200-1205 [PMID: 19605667 DOI: 10.1148/rg.294085205]

14 **Ho TL**, Lee HJ, Lee KW, Chen WL. Diffusion-weighted and conventional magnetic resonance imaging in cerebral cryptococcoma. *Acta Radiol* 2005; **46**: 411-414 [PMID: 16134319]

15 **Trenkwalder P**, Trenkwalder C, Feiden W, Vogl TJ, Einhäupl KM, Lydtin H. Toxoplasmosis with early intracerebral hemorrhage in a patient with the acquired immunodeficiency syndrome. *Neurology* 1992; **42**: 436-438 [PMID: 1736179]

16 **Ukisu R**, Kushihashi T, Tanaka E, Baba M, Usui N, Fujisawa H, Takenaka H. Diffusion-weighted MR imaging of early-stage Creutzfeldt-Jakob disease: typical and atypical manifestations. *Radiographics* 2006; **26** Suppl 1: S191-S204 [PMID: 17050516 DOI: 10.1148/rg.26si065503]

17 **Borawake K**, Prayag P, Wagh A, Dole S. Dengue encephalitis. *Indian J Crit Care Med* 2011; **15**: 190-193 [PMID: 22013316 DOI: 10.4103/0972-5229.84896]

18 **Ernst T**, Chang L, Witt M, Walot I, Aronow H, Leonido-Yee M, Singer E. Progressive multifocal leukoencephalopathy and human immunodeficiency virus-associated white matter lesions in AIDS: magnetization transfer MR imaging. *Radiology* 1999; **210**: 539-543 [PMID: 10207441]

19 **Pomara N**, Crandall DT, Choi SJ, Johnson G, Lim KO. White matter abnormalities in HIV-1 infection: a diffusion tensor imaging study. *Psychiatry Res* 2001; **106**: 15-24 [PMID: 11231096]

P- Reviewer: Asensi VC, Mueller WC, Radenovic L
S- Editor: Wen LL **L- Editor**: A **E- Editor**: Lu YJ

World Journal of Radiology

Submit a Manuscript: http://www.wjgnet.com/esps/
Help Desk: http://www.wjgnet.com/esps/helpdesk.aspx
DOI: 10.4329/wjr.v6.i9.726

World J Radiol 2014 September 28; 6(9): 726-729
ISSN 1949-8470 (online)

MINIREVIEWS

Low dose four-dimensional computerized tomography with volume rendering reconstruction for primary hyperparathyroidism: How I do it?

Timothy A Platz, Moshim Kukar, Rania Elmarzouky, William Cance, Ahmed Abdelhalim

Timothy A Platz, Moshim Kukar, William Cance, Ahmed Abdelhalim, Department of Surgical Oncology, Roswell Park Cancer Institute, Buffalo, NY 14263, United States
Rania Elmarzouky, Department of Neuroradiology, Roswell Park Cancer Institute, Buffalo, NY 14263, United States
Author contributions: All authors contributed to this paper.
Correspondence to: Moshim Kukar, MD, Department of Surgical Oncology, Roswell Park Cancer Institute, Elm and Carlton Streets, Buffalo, NY 14263, United States. moshim.kukar@roswellpark.org
Telephone: +1-716-8458972 Fax: +1-716-8453828
Received: May 9, 2014 Revised: June 25, 2014
Accepted: July 25, 2014
Published online: September 28, 2014

Abstract

Modification of 4-dimensional computed tomography (4D-CT) technique with volume rendering reconstructions and significant dose reduction is a safe and accurate method of pre-operative localization for primary hyperparathyroidism. Modified low dose 4D-CT with volume rendering reconstructions provides precise preoperative localization and is associated with a significant reduction in radiation exposure compared to classic preoperative localizing techniques. It should be considered the preoperative localization study of choice for primary hyperparathyroidism.

Key words: Radiology; Nuclear medicine; Medical imaging

Core tip: To our knowledge, this is the first paper detailing the technical aspects of a low dose 4-dimensional computed tomography with volume rendering reconstruction. It is our aim to share our institute's technique and experience in the hope of improved utilization of this modality. With this technique, our results are comparable to those published in the literature for diagnostic accuracy regarding correlation to intraoperative pathology. The 3D Volume rendering reconstruction of the parathyroid pathology shown in relation to the clavicle, thyroid gland, and skin provide superior surgical guidance and an essentially "cut here" approach for directed parathyroidectomy.

Platz TA, Kukar M, Elmarzouky R, Cance W, Abdelhalim A. Low dose four-dimensional computerized tomography with volume rendering reconstruction for primary hyperparathyroidism: How I do it? *World J Radiol* 2014; 6(9): 726-729 Available from: URL: http://www.wjgnet.com/1949-8470/full/v6/i9/726.htm DOI: http://dx.doi.org/10.4329/wjr.v6.i9.726

INTRODUCTION

Improvements in imaging techniques for primary hyperparathyroidism have been critical in the ability to transition from formal cervical four-gland exploration to minimally invasive/directed parathyroidectomy. A precise anatomic localization study is the key to the success of minimally invasive parathyroidectomy. Traditionally, sestamibi single photon emission computed tomography (SPECT) and ultrasound (US) have been used with varying success rates from 29%-79%[1-10]. With advent of 4-dimensional computed tomography (4D-CT) technology, there is improved sensitivity and a higher intraoperative correlation rate ranging from 70%-89% demonstrated by multiple institutions[1-5,11-15]. Despite this clear advantage, the use of 4D-CT has been limited. Numerous factors including the concern of higher cost, increased radiation exposure and a lack of expertise/knowledge have been

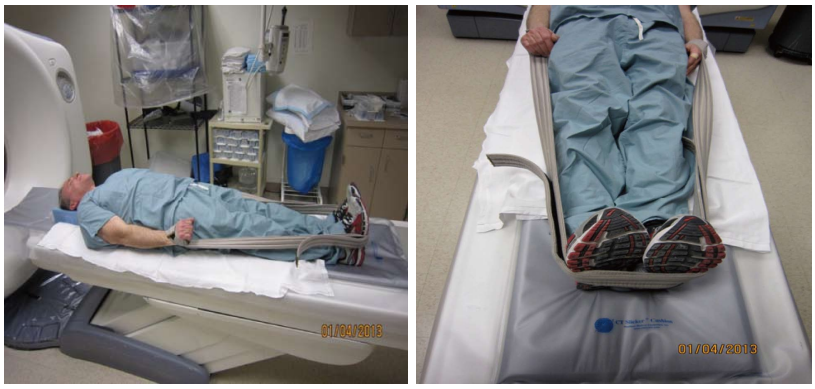

Figure 1 Position of patient for 4-dimensional computed tomography utilizing manufacture shoulder straps.

proposed. At our institution we have modified our technique to address some of these concerns. In this manuscript, we detail our modified 4D-CT technique providing an in-depth review of technical aspects, image processing and adaptations to decrease the effective radiation exposure. The term 4D is used to describe the combination of cross-sectional imaging and basic functional analysis through perfusion information of parathyroid adenomas. The first three dimensions refer to multiplanar CT: axial acquisitions, sagittal and coronal reformatted images. The fourth dimension is the change in enhancement overtime from non-contrast images to arterial and delayed phase imaging.

RESEARCH

Workup

At our institution all patients diagnosed with primary hyperparathyroidism undergo low dose 4D-CT with volume rendering reconstructions. Additional workup includes history/physical, laboratories (serum calcium, intact parathyroid hormone level, 24-h urine calcium, vitamin D), and review of existing imaging modalities if performed (United States, sestamibi SPECT). After confirmation with localization studies, parathyroidectomy is performed *via* standard minimally invasive/directed technique or formal four-gland exploration.

TECHNIQUE DESCRIPTION

CT technique

All imaging is performed on a 64 multi-slice CT scanner (VCT 64; GE Medical Systems, Milwaukee, Wis). The patient is positioned supine in the CT scanner. The patient enters head first with the upper extremities at their side. The manufacturer-supplied head holder is used for all scans. The patient's arms are pulled caudally to minimize shoulder artifact using the manufacturer-supplied shoulder straps (Figure 1). This is very well tolerated by most patients. IV access is obtained in the right or left antecubital vein with an 18-gauge cannula and flushed with heparinized saline. The scanning protocol consists of three phases of CT imaging performed from the hard palate to the level of the carina in all phases using a 0.625 mm slice width. Scanning parameters include a voltage of 120 peak kilovolts (kVp), 200 milliamperes (mA) for the pre-contrast and delayed post-contrast phases (venous), 400 mA for the early post contrast phase (arterial), pitch of 1, and a rotation time of 0.7 s. A 64 mm × 0.625 mm detector configuration with a 10-mm beam width and a table speed of 39.37 cm per gantry rotation is utilized. Imaging is initiated with the non-contrast phase with the anticipation of the normal thyroid tissue being brighter than any parathyroid tissues due to the fact of its increased iodine concentration. The non-contrast phase is followed by intra-venous injection of 90 mL (4 mL/s) of non-ionic contrast medium (iohexol 350, 350 mg of iodine per milliliter; GE health care; Princeton, NJ). A 25 s delay is followed by repeat imaging which constitutes the arterial phase. A delay of 25 s is chosen to coincide with peak enhancement of the parathyroid adenoma as compared to enhancement of the thyroid gland and any regional lymph nodes. A higher mA (400 mA) is used in this phase to facilitate detection of small adenomas including possible multiple gland disease. Approximately 90 s after the injection, a delayed phase scan is performed. This final phase is utilized to confirm the presence of the parathyroid adenoma as it rapidly washes out the IV contrast material compared to the adjacent thyroid tissue. The duration of each phase is dependent on the distance between the hard palate and the carina as well as the table speed. Each phase takes approximately 15-17 s to complete based on the patient's body habitus.

Radiation exposure

A major dose reduction is achieved by reducing the tube current to 200 mA in precontrast and delayed phases. This allows us to detect attenuation differences in lesions adjacent to thyroid gland without compromising imaging quality while achieving significant dose reduction. The effective radiation dose administered utilizing this modification was 11-13 millisieverts (mSv). This dose was calculated from the dose-length product provided by the scanner at the end of each exam[16]. Confirmatory CT dose index measurements using standard 16 cm head phantom and standard CT ionization chamber were also performed yielding the same numbers. Recently, our institution has implemented ASIR technology (Adaptive Statistical Iterative Reconstruction), which incorporates a new reconstructive CT algorithm with an average effec-

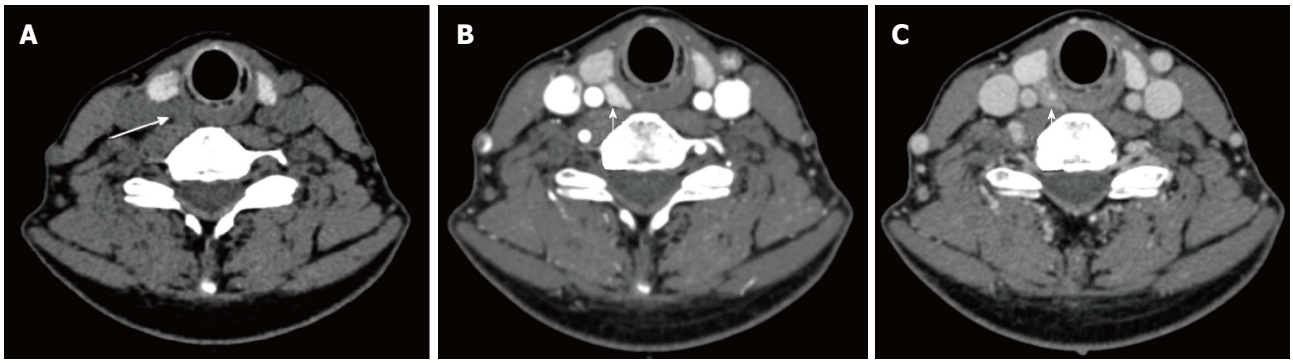

Figure 2 Four-dimensional computed tomography. Axial noncontrast (A), axial arterial phase post contrast (B) and axial delayed phase post contrast (C) images show a hypodense nodule contiguous with the right thyroid gland, which demonstrates avid early contrast enhancement and rapid washout.

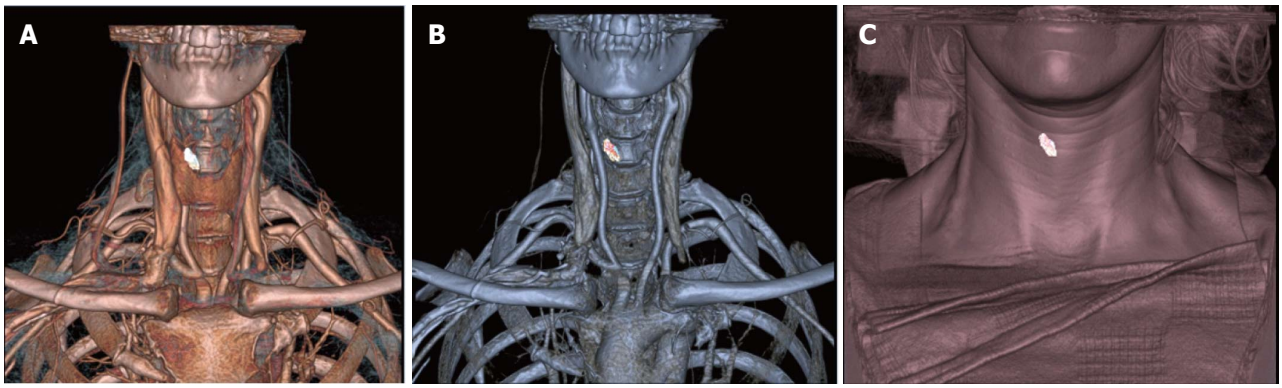

Figure 3 Three-dimensional volume rendering images in 3 different thresholds showing the presumed adenoma in relation to thyroid gland (A), bony landmarks (B) and skin (C).

tive radiation dose of 9-10 mSv.

Image processing

Standard post processing of imaging is performed by a fellowship-trained neuroradiologist on a separate workstation (Advantage Windows Workstation, version 4.5; GE Medical Systems). Two-dimensional sagittal, coronal and oblique multi-planar reformations are obtained from the arterial phase images. This is followed by 3-D reconstruction with volume rendering. The parathyroid adenoma is segmented from the axial images creating a 3-D volume of the adenoma that is merged with the original 3-D volume of the arterial phase of the study. The adenoma is assigned a different color and is shown against the original 3-D volume in three different thresholds and shown in relation to the thyroid gland, skin, and bony landmarks. Measurements are performed from the presumed parathyroid abnormality to the clavicular head and the overlying skin to aid the surgeon in operative guidance (Figures 2 and 3). Images processed on the workstation take an average of 8-10 min. The resulting images are interpreted by the attending neuroradiologist on a PACS workstation and a formal report is issued.

DISCUSSION

Multiple studies including our institute's experience have shown excellent diagnostic accuracy of 4D-CT as a preoperative localization study for primary hyperparathyroidism ranging from 70%-89%[1-5,11-13]. Despite these promising results, many institutions continue to utilize sestamibi SPECT and US as the primary modalities for preoperative localization for directed parathyroidectomy. Despite superiority, 4D-CT has not gained widespread acceptance for reasons unclear to us. Plausible explanations include technical challenges, fear of increased radiation exposure and added costs.

We have utilized this technique in 150 consecutive patients undergoing parathyroidectomy for primary hyperparathyroidism. The true positive rate for modified 4D-CT with volume rendering for this cohort was 133 (89%) of 150 with a false negative (FN) of 17 (11%) of 150. In addition, utilizing our technique, the effective radiation exposure dose is 11-13 mSv. This essentially is an equivalent radiation exposure dose to that of sestamibi SPECT (9-11 mSv) but lower than that previously published for 4D-CT (27 mSv)[17]. To put this in perspective, radiation exposure from some commonly performed procedures such as CT scan of abdomen and pelvis is 14 mSv or CT angiogram is 15 mSv. This reduced effective radiation exposure of our technique is most likely due to the fact that we utilize a lower tube current for noncontrast and delayed images. The most recent implementation of ASIR technology has further reduced the radia-

tion exposure from 4D-CT to essentially equivalent levels to that of sestamibi SPECT.

4D CT is especially useful to identify parathyroid glands in ectopic locations as the axial imaging extends from the hard palate to the level of the pulmonary artery. It is also very useful in recurrent/persistent hyperparathyroidism and improves the success rate of minimally invasive parathyroidectomy in the reoperative setting. Despite these advantages it has some limitations especially in patients with short obese necks, multinodular goiters and multiple exophytic nodules. Another limitation is the observer experience with post image processing and reconstructing 3D images.

To our knowledge, this is the first paper detailing the technical aspects of a low dose 4D-CT with volume rendering reconstruction. It is our aim to share our institute's technique and experience in the hope of improved utilization of this modality. With this technique, our results are comparable to those published in the literature for diagnostic accuracy regarding correlation to intraoperative pathology. The 3D volume rendering reconstruction of the parathyroid pathology shown in relation to the clavicle, thyroid gland, and skin provide superior surgical guidance and an essentially "cut here" approach for directed parathyroidectomy.

In conclusion, low dose 4D-CT with volume rendering reconstruction provides superior quality images while minimizing radiation exposure. The technique is easily reproducible and in our opinion should be the diagnostic modality of choice in patients with primary hyperparathyroidism.

REFERENCES

1 **Eichhorn-Wharry LI**, Carlin AM, Talpos GB. Mild hypercalcemia: an indication to select 4-dimensional computed tomography scan for preoperative localization of parathyroid adenomas. *Am J Surg* 2011; **201**: 334-338; discussion 338 [PMID: 21367374 DOI: 10.1016/j.amjsurg.2010.08.033]

2 **Mortenson MM**, Evans DB, Lee JE, Hunter GJ, Shellingerhout D, Vu T, Edeiken BS, Feng L, Perrier ND. Parathyroid exploration in the reoperative neck: improved preoperative localization with 4D-computed tomography. *J Am Coll Surg* 2008; **206**: 888-895; discussion 895-896 [PMID: 18471717 DOI: 10.1016/j.jamcollsurg.2007.12.044]

3 **Cheung K**, Wang TS, Farrokhyar F, Roman SA, Sosa JA. A meta-analysis of preoperative localization techniques for patients with primary hyperparathyroidism. *Ann Surg Oncol* 2012; **19**: 577-583 [PMID: 21710322 DOI: 10.1245/s10434-011-1870-5]

4 **Starker LF**, Mahajan A, Björklund P, Sze G, Udelsman R, Carling T. 4D parathyroid CT as the initial localization study for patients with de novo primary hyperparathyroidism. *Ann Surg Oncol* 2011; **18**: 1723-1728 [PMID: 21184187 DOI: 10.1245/s10434-010-1507-0]

5 **Rodgers SE**, Hunter GJ, Hamberg LM, Schellingerhout D, Doherty DB, Ayers GD, Shapiro SE, Edeiken BS, Truong MT, Evans DB, Lee JE, Perrier ND. Improved preoperative planning for directed parathyroidectomy with 4-dimensional computed tomography. *Surgery* 2006; **140**: 932-940; discussion 940-941 [PMID: 17188140 DOI: 10.1016/j.surg.2006.07.028]

6 **Glynn N**, Lynn N, Donagh C, Crowley RK, Smith D, Thompson CJ, Hill ADK, Keeling F, Agha A. The utility of 99mTc-sestamibi scintigraphy in the localisation of parathyroid adenomas in primary hyperparathyroidism. *Ir J Med Sci* 2011; **180**: 191-194 [DOI: 10.1007/s11845-010-0641-9]

7 **Witteveen JE**, Kievit J, Stokkel MP, Morreau H, Romijn JA, Hamdy NA. Limitations of Tc99m-MIBI-SPECT imaging scans in persistent primary hyperparathyroidism. *World J Surg* 2011; **35**: 128-139 [PMID: 20957360 DOI: 10.1007/s00268-010-0818-4]

8 **Gómez-Ramírez J**, Sancho-Insenser JJ, Pereira JA, Jimeno J, Munné A, Sitges-Serra A. Impact of thyroid nodular disease on 99mTc-sestamibi scintigraphy in patients with primary hyperparathyroidism. *Langenbecks Arch Surg* 2010; **395**: 929-933 [PMID: 20625763 DOI: 10.1007/s00423-010-0680-8]

9 **Swanson TW**, Chan SK, Jones SJ, Bugis S, Irvine R, Belzberg A, Levine D, Wiseman SM. Determinants of Tc-99m sestamibi SPECT scan sensitivity in primary hyperparathyroidism. *Am J Surg* 2010; **199**: 614-620 [PMID: 20466104 DOI: 10.1016/j.amjsurg.2010.02.001]

10 **Thomas DL**, Bartel T, Menda Y, Howe J, Graham MM, Juweid ME. Single photon emission computed tomography (SPECT) should be routinely performed for the detection of parathyroid abnormalities utilizing technetium-99m sestamibi parathyroid scintigraphy. *Clin Nucl Med* 2009; **34**: 651-655 [PMID: 19893394 DOI: 10.1097/RLU.0b013e3181b591c9]

11 **Stark DD**, Gooding GA, Moss AA, Clark OH, Ovenfors CO. Parathyroid imaging: comparison of high-resolution CT and high-resolution sonography. *AJR Am J Roentgenol* 1983; **141**: 633-638 [PMID: 6604407 DOI: 10.2214/ajr.141.4.633]

12 **Beland MD**, Mayo-Smith WW, Grand DJ, Machan JT, Monchik JM. Dynamic MDCT for localization of occult parathyroid adenomas in 26 patients with primary hyperparathyroidism. *AJR Am J Roentgenol* 2011; **196**: 61-65 [PMID: 21178047 DOI: 10.2214/AJR.10.4459]

13 **Randall GJ**, Zald PB, Cohen JI, Hamilton BE. Contrast-enhanced MDCT characteristics of parathyroid adenomas. *AJR Am J Roentgenol* 2009; **193**: W139-W143 [PMID: 19620416 DOI: 10.2214/AJR.08.2098]

14 **Chazen JL**, Gupta A, Dunning A, Phillips CD. Diagnostic accuracy of 4D-CT for parathyroid adenomas and hyperplasia. *AJNR Am J Neuroradiol* 2012; **33**: 429-433 [PMID: 22135127 DOI: 10.3174/ajnr.A2805]

15 **Gafton AR**, Glastonbury CM, Eastwood JD, Hoang JK. Parathyroid lesions: characterization with dual-phase arterial and venous enhanced CT of the neck. *AJNR Am J Neuroradiol* 2012; **33**: 949-952 [PMID: 22241395 DOI: 10.3174/ajnr.A2885]

16 **Huda W**, Ogden KM, Khorasani MR. Converting dose-length product to effective dose at CT. *Radiology* 2008; **248**: 995-1003 [PMID: 18710988 DOI: 10.1148/radiol.2481080042]

17 **Hunter GJ**, Schellingerhout D, Vu TH, Perrier ND, Hamberg LM. Accuracy of four-dimensional CT for the localization of abnormal parathyroid glands in patients with primary hyperparathyroidism. *Radiology* 2012; **264**: 789-795 [PMID: 22798226 DOI: 10.1148/radiol.12110852]

P- Reviewer: Fulop T **S- Editor**: Ji FF **L- Editor**: A
E- Editor: Lu YJ

World Journal of Radiology

Submit a Manuscript: http://www.wjgnet.com/esps/
Help Desk: http://www.wjgnet.com/esps/helpdesk.aspx
DOI: 10.4329/wjr.v6.i9.730

World J Radiol 2014 September 28; 6(9): 730-736
ISSN 1949-8470 (online)

Malrotation: Current strategies navigating the radiologic diagnosis of a surgical emergency

John J Tackett, Eleanor D Muise, Robert A Cowles

John J Tackett, Eleanor D Muise, Robert A Cowles, Section of Pediatric Surgery, Department of Surgery, Yale University School of Medicine, New Haven, CT 06520, United States
Author contributions: Tackett JJ, Muise ED and Cowles RA contributed to this work and wrote the paper.
Correspondence to: Robert A Cowles, MD, Associate Professor of Surgery, Section of Pediatric Surgery, Department of Surgery, Yale University School of Medicine, Box 208062, New Haven, CT 06520, United States. robert.cowles@yale.edu
Telephone: +1-203-7852701 Fax: +1-203-7853820
Received: December 31, 2013 Revised: June 20, 2014
Accepted: July 17, 2014
Published online: September 28, 2014

Abstract

The most accurate and practical imaging algorithm for the diagnosis of intestinal malrotation can be a complex and sometimes controversial topic. Since 1900, significant advances have been made in the radiographic assessment of infants and children suspected to have anomalies of intestinal rotation. We describe the current methods of abdominal imaging of malrotation along with their pros and cons. When associated with volvulus, malrotation is a true surgical emergency requiring rapid diagnosis and treatment. We emphasize the importance of close cooperation and communication between radiology and surgery to perform an effective and efficient diagnostic evaluation allowing prompt surgical decision making.

Key words: Malrotation; Midgut volvulus; Treitz; Ladd; Heterotaxy; Infant

Core tip: Malrotation, especially when associated with midgut volvulus, is a surgical emergency that must be astutely recognized, quickly diagnosed, and emergently treated operatively. While the diagnosis depends heavily on clinical acumen and suspicion, radiologic imaging is critical in determining which patients need surgery. Surgeons and radiologists must cooperate and communicate effectively during the radiographic evaluation of a child with malrotation. Additionally, the algorithm for imaging malrotation must be adapted based upon the tools and staff available at any given institution.

Tackett JJ, Muise ED, Cowles RA. Malrotation: Current strategies navigating the radiologic diagnosis of a surgical emergency. *World J Radiol* 2014; 6(9): 730-736 Available from: URL: http://www.wjgnet.com/1949-8470/full/v6/i9/730.htm DOI: http://dx.doi.org/10.4329/wjr.v6.i9.730

INTRODUCTION

Surgeons are often consulted for evaluation of pediatric abdominal problems presenting to the emergency department. It is common for these patients to be evaluated by radiographic imaging in addition to a focused history and physical examination. The surgeon and radiologist must always have a particularly high-level of suspicion in cases of possible malrotation that may require emergency surgery after evaluation.

CASE PRESENTATION

A 5-day-old full term male infant presents to the emergency department with continuous bilious non-bloody vomiting and irritability after his last three feeds. He was born by normal spontaneous vaginal delivery without complications and was noted to be breast-feeding well prior to discharge on day-of-life 2; he continued breast-feeding and passing stools at home for the past 4 d until this evening. On exam, his abdomen is minimally distended and he is crying constantly. The clinical picture suggests an obstruction distal to the ampulla of Vater,

and the surgeon has a heightened concern for malrotation with midgut volvulus. Before subjecting this infant to the morbidity of surgery, the surgeon calls a colleague in the Radiology Department to discuss appropriate imaging workup for malrotation.

Embryology

Anomalies of intestinal rotation, commonly referred to as malrotation, are a result of errors during embryologic development. In malrotation, the midgut does not complete its normal lengthening and rotation, and thus is incorrectly positioned within the peritoneal cavity. Normally the process of lengthening and rotation begins between the 4th and 5th wk of gestation. From this time until about week 10, the midgut is outgrowing the abdominal cavity and is forced to herniate through the umbilicus to continue unhindered growth[1]. During weeks 10 and 11, the intestine returns to the peritoneal cavity. From the 11th wk forward, the small bowel undergoes fixation.

The small intestine is a straight tube early in development that derives its blood primarily from the superior mesenteric artery (SMA). This vessel divides the midgut into two parts: the cephlad or prearterial portion, and the caudad or postarterial portion[2]. The prearterial portion is made up of duodenojejunal loops, while the postarterial portion are cecocolic loops[3]. The SMA is important not only because it supplies the majority of blood flow to the small intestine, but also because it serves as the axis for the normal embryologic rotation of the bowel during development.

When the bowel herniates through the umbilicus, the prearterial portion rotates 180° counterclockwise around the axis of the SMA, while the postarterial portion rotates 90° counterclockwise. During the 10th and 11th wk, the prearterial portion of the gut reenters first followed by the postarterial portion. While the bowel returns into the abdominal cavity, both segments complete a total turn of 270°. This configuration places the normal anatomy of the C-loop of the duodenum posterior to the SMA and the transverse colon anterior to the SMA.

The blood from the SMA is distributed throughout smaller vessels running within the mesentery of the bowel. In normal development, the mesenteric root passes along the retroperitoneum from the ligament of Treitz to the proximal cecum[4]. When normal rotation of the small bowel is not completed in embryologic development, the mesenteric root is foreshortened[5]. The small bowel is then supported only by this foreshortened pedicle containing the SMA. The small bowel may then twist (volvulus), about this narrow axis[6]. There are two major types of rotational abnormalities that have been described as malrotation and result in this foreshortening: incomplete rotation and non-rotation[7]. During *incomplete rotation*, neither the cranial nor the caudal portion rotates more than 180°. The proximal midgut becomes fixed to the right of the SMA and the cecum becomes fixed directly anterior to the SMA. This pattern has the classic features of Ladd's bands covering and impinging upon the anterior portion of the duodenum and the close proximity of the fixation points for the cranial and caudal midgut along with the SMA. In *non-rotation,* neither portion rotates more than 90°. Under-rotation leaves the proximal midgut fixed anterior to the right of the SMA and the cecum anterior to the left of the SMA, and the mesentery is still narrowed and foreshortened.

History

Two individuals recognized for their descriptions of small bowel anatomy and malrotation are Václav Treitz and William Ladd. Treitz (1819-1872), a professor of anatomy in Prague, described the area of tissue which we now recognize as the Ligament of Treitz[3]. This area that bears his name gives physicians a common point to localize where the duodenum becomes the jejunum after exiting the retroperitoneum. Some have described the ligament as a "weak thin membranous structure" that is seldom demonstrated on CT[8].

William Ladd (1880-1967) is considered the father of pediatric surgery in North America. During World War 1, Ladd dedicated his career to the surgical care of children and became surgeon-in-chief at Boston Children's Hospital[3]. First in 1932 and then again in 1936, he published articles describing his approach to duodenal obstruction and malrotation with midgut volvulus. In these articles, he described a procedure involving detorsion of the volvulized bowel in a counterclockwise fashion, dividing the bands of tissue extending from the cecum across the duodenum and into the lateral peritoneal gutter, and finally spreading the mesentery from the cecum in the left upper quadrant to the small bowel in the right hemi-abdomen. This procedure later became known as Ladd's procedure[9]. Rather than attempting to restore normal intestinal rotation, Ladd's operation aimed to convert malrotation to an arrangement of broadened nonrotation with the goal of minimizing the chance of recurrent volvulus[7]. While historically Ladd had the availability of flat plate radiography to guide his work-up of children with malrotation, many different imaging modalities have become available to help guide diagnosis and treatment of this surgical emergency.

Imaging modalities

Plain X-ray: Radiographs are often the first step in the imaging evaluation of pediatric patients with suspected malrotation. This relatively inexpensive and widely available test allows the radiologist and surgeon to quickly exclude other potential diagnoses. Unfortunately, the most common finding on plain film of a patient with malrotation is "normal bowel gas pattern"[2]. While abdominal radiographs in a newborn cannot rule-out malrotation, they can occasionally demonstrate findings that are concerning enough to prompt the surgeon to consider operative exploration: "double bubble" sign of duodenal obstruction, lack of bowel gas distal to the duodenum, bowel malposition (small intestine on the right and large intestine on the left, found in *non-rotation*, Figure 1), or pneumatosis intes-

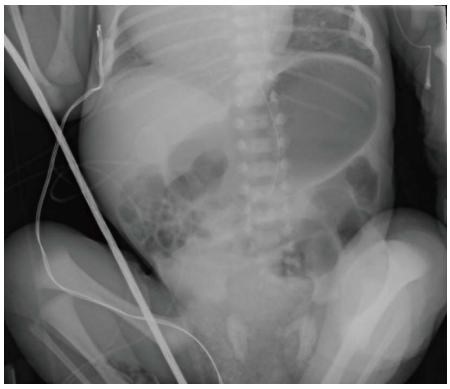

Figure 1 This plain film illustrates an infant with malposition of the small bowel on the right and large bowel on the left suggesting malrotation.

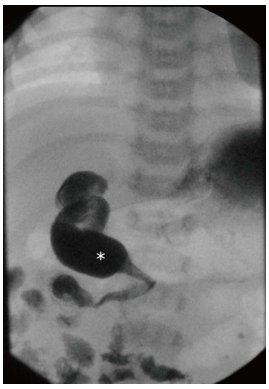

Figure 2 This Upper gastrointestinal demonstrates abnormal position of the duodenal-jejunal junction (white star) to the right of the spine. Normally the duodenum should sweep across from right to left across the spine.

tinalis with or without portal venous gas.

Ultrasound: Ultrasonography can be used as an adjunct to plain film radiography by determining the position of the superior mesenteric vessels and the relationship to the third portion of the duodenum. In normal anatomy, the SMA lies left of the superior mesenteric vein (SMV); reversal of this relationship may suggest malrotation[10]. Orzech *et al*[10] state that ultrasound can serve as an excellent screening tool for malrotation especially when complete inversion of the mesenteric vessels along with a "whirlpool" appearance of the mesentery around the SMA is found, prompting urgent exploration. They further suggest that "normal" positioning of the vessels may exist on a spectrum, and thus deviation from the classic position does not always imply malrotation, therefore clinical correlation and pretest probability should direct further studies including possible confirmative upper gastrointestinal studies.

Acknowledging the variation in normal SMA/SMV anatomy, some have supported the use of graded compression ultrasonography as a tool to assess the retroperitoneal position of the third portion of the duodenum (D3). Menten *et al*[11] state that "based on anatomical and embryological arguments, a retromesenteric D3 excludes intestinal malrotation". They proposed that the utilization of gradual compression to obtain transverse and sagittal images of the aortomesenteric angle could demonstrate truly normal rotation if D3 was visualized between the aorta and the SMA. Senior pediatric radiologists with over 26 years of combined experience performed the study that affirmed the use of ultrasound over upper gastrointestinal series recommended by Yousefzadeh *et al*[12] two years earlier based on his own series of pediatric cases.

Upper gastrointestinal imaging: Thought of as the "gold standard" test to detect malrotation by most of the pediatric community, upper gastrointestinal imaging series (UGI) utilizes enteral contrast to obtain imaging of the prearterial gastrointestinal tract. An UGI involves administration of contrast orally or into the stomach and capturing images as the contrast traverses the esophagus, stomach, duodenal c-loop, and eventually the duodenal-jejunal junction (DJJ). UGI findings suggestive of malrotation or volvulus include low DJJ position, absence of the DJJ from its typical anatomical position to the left of the vertebral body pedicle, jejunum located on the right (Figure 2), duodenal redundancy, and DJJ corkscrew appearance[13].

Imaging quality depends on the position of the patient during the study, a not insignificant challenge in the pediatric population. In 2013, a group in South Africa published their technique to optimize UGI results[14]. They used external metal markers along the child's midline to aid in orienting the anatomical position of the patient during the study; they further invested in a three-person team to control the child's positioning during the entirety of the study. They describe their techniques as follows: "study commences with the child swallowing contrast on their left side (to prevent duodenal filling) to evaluate the esophagus…the child is then placed on its right side to allow duodenal filling and to observe the course of the duodenum…once a sufficient contrast bolus is visualized in the duodenum, the child must be turned rapidly to an unrotated supine position…to capture the c-loop[14]".

Barium enema: The cecum may be malpositioned in malrotation as is the case with the DJJ; thus, a barium enema can be used to visualize the position of the cecum. Abnormal position of the cecum on preoperative imaging can be found in 80% and 87% of surgically proven cases of malrotation[15]. The normally rotated cecum is found in the right lower quadrant of the abdomen and up to 20% of patients with malrotation will have a normally positioned cecum[2]. No radiographic findings related to the cecum can unequivocally rule-out risk of malrotation[16]. As such, the barium enema is rarely used alone, but may prompt surgical exploration if a patient presents acutely and cecal malpositioning clinically correlates with the patient's exam.

Computed tomography: Like ultrasound, computed to-

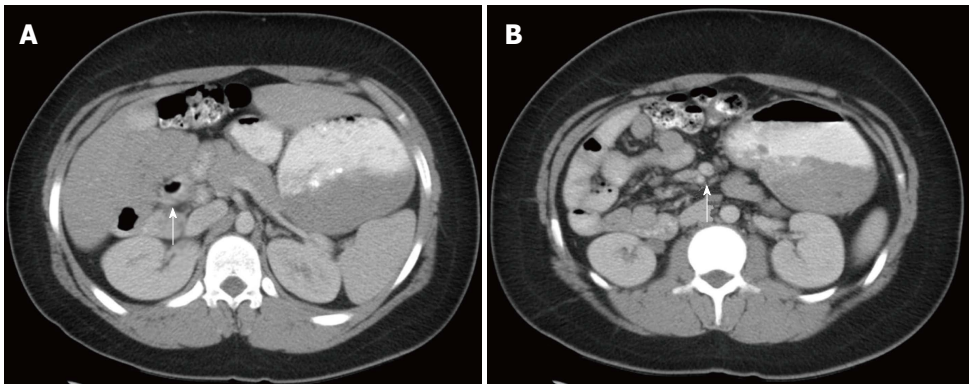

Figure 3 This axial view of an abdominal computed tomography. A: Illustrates the duodenal-jejunal junction (white arrow) in the right hemi-abdomen suggesting malrotation; B: Illustrates superior mesenteric artery Superior Mesenteric Artery (SMA)/Superior Mesenteric Vein (SMV) inversion (white arrow) with the SMA to the right of the SMV. This inversion suggests malrotation.

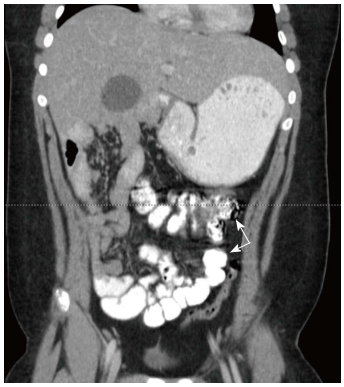

Figure 4 This coronal view of an abdominal computed tomography illustrates the terminal ileum and cecum (white arrows). Positioning of the cecum in the left hemi-abdomen is suggestive of malrotation.

mography (CT) imaging can be used to evaluate the position of D3, the DJJ (Figure 3A), and the anatomical relationship between the SMA and SMV (Figure 3B). Based on a study by Taylor, CT imaging of abnormal D3 position had a sensitivity and specificity of diagnosing malrotation of 97.3% and 99% respectively[17]. Due to the variation in normal SMA/SMV anatomy as previously discussed, the accuracy of identifying "abnormal" SMA/SMV relation in making the diagnosis of malrotation was 76.8%[17]. One unique aspect of a CT is that when used with contrast enhancement it can recognize perfusion abnormalities that may be missed on laboratory studies[18]. CT can be performed quickly on a child with extremely minimal invasiveness, but does subject the child to a significant dose of radiation when compared to an UGI (Figure 4).

MRI: Magnetic resonance imaging (MRI) can be used, much like CT, as a cross-sectional imaging modality to identify findings of malrotation including: dilation of the proximal duodenum, non-retroperitoneal positioning of the duodenum, bowel malpositioning, and inversion of the SMA/SMV relationship[2]. The MRI avoids radiation but relies on the patient holding still for the duration of the lengthier exam. Additionally, the MRI is the most expensive imaging modality available to aid in diagnosing malrotation.

Current controversies

Some believe that localizing the DJJ with UGI cannot give reliable data to rule-out malrotation. One author touts that ultrasonographic imaging in the hands of an experienced technician may demonstrate a retromesenteric D3, which alone can prove that a patient "will not have malrotation and will not develop midgut volvulus[12]". Menten *et al*[11] support this assertion, describing a graded compression-technique to demonstrate positioning between the SMA and aorta. These techniques rely on availability of experienced radiology staff, and some hospitals may not have this capability or around-the-clock availability to allow for this focused ultrasound exam. Furthermore, at least one case of normal D3 retroperitoneal positioning on cross-sectional CT imaging in a child with malrotation has been reported, thus calling to question the conclusion that normal positioning always rules out malrotation[17].

One group of infants in particular has added controversy to the approach of workup for malrotation: infants with heterotaxy (Figure 5). Anomalies of intestinal rotation are common in these infants; unfortunately, these children can also suffer from life-threatening cardiac anomalies. There is debate whether these children should undergo elective surgery to broaden the mesentery and prevent volvulus even if an anomaly of rotation is identified[19]. Some have suggested that watchful waiting may be appropriate as volvulus appears to be rare in this population[20]. Importantly, Tashjian *et al*[21] stated that if a surgeon decides to perform a Ladd's procedure on a patient with heterotaxia it should occur only when the congenital heart disease is well controlled. Additionally, during operative planning when imaging children with heterotaxia, it is difficult to determine the width of the mesenteric root since there is often insufficient data on the location of the cecum relative to the DJJ[3]. This debate still has yet to be studied in detail with long-term follow-up analysis.

Table 1 Positive and negative attributes of commonly used imaging modalities when applied to cases of suspected malrotation

Imaging modality	Pros	Cons
Plain film	Inexpensive, quick, may demonstrate classic appearance of duodenal obstruction, may give earlier indication for operative exploration	May masquerade as other abnormalities, may delay treatment (especially when read as "normal"), cannot exclude malrotation
Ultrasound	Avoids radiation exposure, may demonstrate "whirlpool sign" indicative of volvulus, duplex to determine relationship of D3 and superior mesenteric vessels, Possibility to evaluate normal abdominal anatomy	Normal sonogram may not exclude malrotation, quality related to technician experience
Upper GI	Currently considered the "gold standard", relatively non-invasive, available at pediatric centers, easily demonstrates duodenal obstruction, allows for visualization of the duodenojejunal junction, delayed imaging may show position of the cecum	Small amount of radiation, challenge to position patient for optimal imaging, may be distorted by bowel distention or indwelling tubes, duodenojejunal junction may have normal variation in position
Barium Enema	Easily demonstrates position of entire large bowel (especially cecum) quickly	Small amount of radiation, normal cecum position does not rule out proximal malrotation
CT	Quick, allows for viewing position of SMA/SMV, may demonstrate "whirlpool sign" indicative of volvulus, visualization of all abdominal anatomy	High radiation exposure, requires patient to remain still for short period of time, normal relationship between SMA/SMV does not exclude malrotation
MRI	No radiation exposure, allows for viewing position of SMA/SMV, may demonstrate "whirlpool sign", visualization of all abdominal anatomy	Requires patient to remain still for a longer period of time, expensive, not accessible

CT: Computed tomography; MRI: Magnetic resonance imaging; GI: Gastrointestinal imaging; SMA: Superior mesenteric artery; SMV: Superior mesenteric vein.

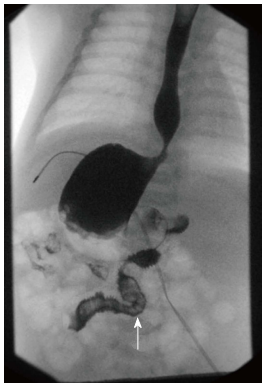

Figure 5 This Upper gastrointestinal in an infant with heterotaxia demonstrates abnormal positioning of the stomach to the right, the liver near the midline, and the duodenum running left to right. The duodenal-jejunal junction (white arrow) is seen inferior to the duodenum demonstrating malrotation.

DISCUSSION

Cooperation

The most important factor in the evaluation of a child with bilious emesis and abdominal tenderness is cooperation between the surgery and radiology teams. Malrotation with volvulus is a surgical emergency in which immediate operative intervention to untwist the volvulus and prevent bowel loss is imperative. Even given prompt diagnosis and preoperative optimization, surgery still carries morbidity and mortality risks associated with anesthesia and the operation itself.

Close communication between the examining surgeon and the radiologist is critical to determine the imaging study best suited to evaluate the given clinical presentation of the child, and to discuss possible limitations of certain studies at specific institutions. Whether initially utilizing radiography/fluoroscopy or cross sectional imaging, lapses in communication should not introduce delay from the time of initial evaluation to the time a decision to operate is made. As discussed, not all imaging results will be straightforward or immediately diagnostic in the evaluation of malrotation, so the coordination of multiple studies should be anticipated and discussed to optimize imaging for the patient.

Proposed decision algorithm

Knowing the importance of cooperation between the surgeon and the radiologist, we propose below a decision algorithm for an infant or child with possible malrotation. It has been discussed that "negative" radiographic results for most imaging modalities are not 100% reliable in ruling out malrotation. Whenever imaging results are positive for malrotation, we recommend considering operative exploration. It is important to keep in mind that even "positive" radiographic results suggesting malrotation must always be correlated with the clinical picture before committing to an operation.

We suggest beginning with the history and physical along with laboratory results; if there is strong evidence of an emergent ischemic process, the patient may need urgent operative exploration without the delay of imaging. If this is not the case, we recommend starting with easily accessible and inexpensive plain radiography. If the radiograph is negative for evidence of malrotation, the surgeon-radiologist team should discuss whether the hospital is equipped to perform experienced gradual-compression ultrasonography. If there is an experienced radiologist available, the non-irradiating imaging can be performed. If this imaging modality is negative or not available to the team, then an UGI should be performed. Negative UGI results should pause the imaging decision pathway.

Based on the discussed sensitivity and accuracy of the ultrasound and UGI, negative results may strongly suggest that the patient does not have malrotation either

my demonstrating normal anatomy or by elucidating evidence of a different diagnosis. At this point, we recommend reassessing the clinical concern for possible malrotation. If the concern is lower, then watchful waiting may be acceptable. If there is still high clinical suspicion, then the imaging should proceed with a barium enema. This pause for decision-making should be short and cooperatively communicated between the surgeon and radiologist, as it would be ideal to obtain a barium enema while the patient is still on the X-ray table from the UGI. A negative barium enema in a patient with high clinical suspicion should prompt a discussion about CT imaging. At this point, do the risks of irradiation with CT imaging outweigh the risks of negative operative exploration or delaying surgery for close observation? If the perceived benefits of the CT outweigh the risks, then CT should be obtained. In the setting of CT results negative for evidence of malrotation, we recommend close observation with low threshold to repeat UGI or consider operation if the exam or labs worsen.

Due to its cost, both in time and dollars, we do not feel that an MRI can give additional information over the previous imaging studies without significantly delaying the diagnosis. Additionally, due to the length of time the patient must remain still, the patient would almost certainly need to be sedated and intubated in order to obtain imaging. We feel the risk of anesthesia for this imaging modality is not acceptable for the benefit of the imaging results gathered.

We recognize that the above algorithm is based on the expectation that plain film radiography, ultrasound, fluoroscopy, and advanced radiography are easily and readily available. Many centers around the world may not have access to these imaging modalities, and the algorithm should be adjusted as such. Additionally, it should be considered that a patient may have intermittent volvulus that, depending on the time of the imaging, may cause false negative results. These cases rely on the clinical evaluation to determine if imaging studies should be repeated.

In conclusion, malrotation presenting in the newborn or older child can become a surgical emergency. Delay in diagnosis, specifically in the setting of a midgut volvulus, can lead to intestinal necrosis, increased mortality, and intestinal failure with dependence on parenteral nutrition. When malrotation is being considered, it is important that pediatric surgeons and pediatric radiologists work closely to discuss available imaging options and communicate a clear workflow of studies while making the decision of whether or not an operation is needed. In the heterotaxy population, even positive imaging can be difficult to interpret clinically and little consensus exists regarding the treatment of this subset of patients.

We have proposed an imaging algorithm based on the current literature and an evaluation of the pros and cons of the different imaging modalities (Table 1). Our algorithm begins with a plain film radiograph followed by either ultrasound or UGI series depending on resources available. However, it is important to stress that any algorithm is useless without the communication and cooperation of the surgery and radiology teams. Teamwork in diagnosis is the key to optimal outcomes in children with malrotation.

ACKNOWLEDGEMENTS

We would like to acknowledge Dr. Lauren Ehrlich (Department of Radiology, Yale University School of Medicine) for providing us with de-identified radiographic images.

REFERENCES

1 **Frazer JE**, Robbins RH. On the Factors concerned in causing Rotation of the Intestine in Man. *J Anat Physiol* 1915; **50**: 75-110 [PMID: 17233053 DOI: 10.1053/j.sempedsurg.2003.08.009]
2 **Strouse PJ**. Malrotation. *Semin Roentgenol* 2008; **43**: 7-14 [PMID: 18053823 DOI: 10.1053/j.ro.2007.08.002]
3 **Lampl B**, Levin TL, Berdon WE, Cowles RA. Malrotation and midgut volvulus: a historical review and current controversies in diagnosis and management. *Pediatr Radiol* 2009; **39**: 359-366 [PMID: 19241073 DOI: 10.1007/s00247-009-1168-y]
4 **McVay MR**, Kokoska ER, Jackson RJ, Smith SD. Jack Barney Award. The changing spectrum of intestinal malrotation: diagnosis and management. *Am J Surg* 2007; **194**: 712-717; discussion 712-717 [PMID: 18005759 DOI: 10.1016/j.amjsurg.2007.08.035]
5 **Daneman A**. Malrotation: the balance of evidence. *Pediatr Radiol* 2009; **39** Suppl 2: S164-S166 [PMID: 19308379 DOI: 10.1007/s00247-009-1152-6]
6 **Irish MS**, Pearl RH, Caty MG, Glick PL. The approach to common abdominal diagnosis in infants and children. *Pediatr Clin North Am* 1998; **45**: 729-772 [PMID: 9728184 DOI: 10.1016/S0031-3955(05)70043-2]
7 **Shew SB**. Surgical concerns in malrotation and midgut volvulus. *Pediatr Radiol* 2009; **39** Suppl 2: S167-S171 [PMID: 19308380 DOI: 10.1007/s00247-008-1129-x]
8 **Kim SK**, Cho CD, Wojtowycz AR. The ligament of Treitz (the suspensory ligament of the duodenum): anatomic and radiographic correlation. *Abdom Imaging* 2008; **33**: 395-397 [PMID: 17653583 DOI: 10.1007/s00261-007-9284-3]
9 **Ladd WE**. Surgical disease of the alimentary tract in infants. *New Eng J Med* 1936; **215**: 705-708 [DOI: 10.1056/NEJM193610152151604]
10 **Orzech N**, Navarro OM, Langer JC. Is ultrasonography a good screening test for intestinal malrotation? *J Pediatr Surg* 2006; **41**: 1005-1009 [PMID: 16677901 DOI: 10.1016/j.jpedsurg.2005.12.070]
11 **Menten R**, Reding R, Godding V, Dumitriu D, Clapuyt P. Sonographic assessment of the retroperitoneal position of the third portion of the duodenum: an indicator of normal intestinal rotation. *Pediatr Radiol* 2012; **42**: 941-945 [PMID: 22684229 DOI: 10.1007/s00247-012-2403-5]
12 **Yousefzadeh DK**. The position of the duodenojejunal junction: the wrong horse to bet on in diagnosing or excluding malrotation. *Pediatr Radiol* 2009; **39** Suppl 2: S172-S177 [PMID: 19308381 DOI: 10.1007/s00247-008-1116-2]
13 **Sizemore AW**, Rabbani KZ, Ladd A, Applegate KE. Diagnostic performance of the upper gastrointestinal series in the evaluation of children with clinically suspected malrotation. *Pediatr Radiol* 2008; **38**: 518-528 [PMID: 18265969 DOI: 10.1007/s00247-008-0762-8]
14 **Dekker G**, Andronikou S, Greyling J, Louw B, Brandt A. Contrast meals and malrotation in children-metal mark-

ers for improved accuracy. *Pediatr Radiol* 2013; **43**: 115-118 [PMID: 23160646 DOI: 10.1007/s00247-012-2503-2]
15 **Applegate KE**. Evidence-based diagnosis of malrotation and volvulus. *Pediatr Radiol* 2009; **39** Suppl 2: S161-S163 [PMID: 19308378 DOI: 10.1007/s00247-009-1177-x]
16 **Slovis TL**, Strouse PJ. Malrotation: some answers but more questions. *Pediatr Radiol* 2009; **39**: 315-316 [PMID: 19241072 DOI: 10.1007/s00247-009-1169-x]
17 **Taylor GA**. CT appearance of the duodenum and mesenteric vessels in children with normal and abnormal bowel rotation. *Pediatr Radiol* 2011; **41**: 1378-1383 [PMID: 21594544 DOI: 10.1007/s00247-011-2118-z]
18 **Aidlen J**, Anupindi SA, Jaramillo D, Doody DP. Malrotation with midgut volvulus: CT findings of bowel infarction. *Pediatr Radiol* 2005; **35**: 529-531 [PMID: 15536561 DOI: 10.1007/s00247-004-1355-9]
19 **Chang J**, Brueckner M, Touloukian RJ. Intestinal rotation and fixation abnormalities in heterotaxia: early detection and management. *J Pediatr Surg* 1993; **28**: 1281-1284; discussion 1285 [PMID: 8263687 DOI: 10.1016/S0022-3468(05)80313-6]
20 **Choi M**, Borenstein SH, Hornberger L, Langer JC. Heterotaxia syndrome: the role of screening for intestinal rotation abnormalities. *Arch Dis Child* 2005; **90**: 813-815 [PMID: 15890694 DOI: 10.1136/adc.2004.067504]
21 **Tashjian DB**, Weeks B, Brueckner M, Touloukian RJ. Outcomes after a Ladd procedure for intestinal malrotation with heterotaxia. *J Pediatr Surg* 2007; **42**: 528-531 [PMID: 17336193 DOI: 10.1016/j.jpedsurg.2006.10.060]

P- Reviewer: Shen L **S- Editor**: Wen LL **L- Editor**: A
E- Editor: Lu YJ

World Journal of Radiology

Submit a Manuscript: http://www.wjgnet.com/esps/
Help Desk: http://www.wjgnet.com/esps/helpdesk.aspx
DOI: 10.4329/wjr.v6.i9.737

World J Radiol 2014 September 28; 6(9): 737-740
ISSN 1949-8470 (online)

CASE REPORT

Magnetic resonance imaging correlates of bee sting induced multiple organ dysfunction syndrome: A case report

Sushant K Das, Li-Chuan Zeng, Bing Li, Xiang-Ke Niu, Jing-Liang Wang, Anup Bhetuwal, Han-Feng Yang

Sushant K Das, Li-Chuan Zeng, Xiang-Ke Niu, Jing-Liang Wang, Anup Bhetuwal, Han-Feng Yang, Department of Radiology, Affiliated Hospital of North Sichuan Medical College, Nanchong 63700, Sichuan Province, China
Bing Li, Han-Feng Yang, Department of Interventional Pain Management, Affiliated Hospital of North Sichuan Medical College, Nanchong 63700, Sichuan Province, China
Author contributions: Das SK and Niu XK designed the report; Wang JL, Zeng LC and Bhetuwal A collected the patient's clinical data and radiological images; Das SK, Niu XK and Yang HF analyzed the data; and Das SK wrote the paper. All authors contributed to this work and wrote the paper
Correspondence to: Han-Feng Yang, MD, PhD, Department of Radiology, Affiliated Hospital of North Sichuan Medical College, 63 Wenhua Road, Nanchong 63700, Sichuan Province, China. hanfengyang168@163.com
Telephone: +86-817-2262089 Fax: +86-817-2262236
Received: March 13, 2014 Revised: July 6, 2014
Accepted: August 27, 2014
Published online: September 28, 2014

Abstract

Occasionally systemic complications with high risk of death, such as multiple organ dysfunction syndrome (MODS), can occur following multiple bee stings. This case study reports a patient who presented with MODS, i.e., acute kidney injury, hepatic and cardiac dysfunction, after multiple bee stings. The standard clinical findings were then correlated with magnetic resonance imaging (MRI) findings, which demonstrates that MRI may be utilized as a simpler tool to use than other multiple diagnostics.

Key words: Bee sting; Multiple organ dysfunction syndrome; Magnetic resonance imaging; Rhabdomyolysis; Acute kidney injury; Myocarditis

Core tip: Multiple bee stings can cause multiple organ dysfunction and lead to a clinical picture that can be accurately depicted by magnetic resonance imaging alone, which thus prevents several imaging tests being administered for evaluating the extent and range of the disease.

Das SK, Zeng LC, Li B, Niu XK, Wang JL, Bhetuwal A, Yang HF. Magnetic resonance imaging correlates of bee sting induced multiple organ dysfunction syndrome: A case report. *World J Radiol* 2014; 6(9): 737-740 Available from: URL: http://www.wjgnet.com/1949-8470/full/v6/i9/737.htm DOI: http://dx.doi.org/10.4329/wjr.v6.i9.737

INTRODUCTION

Cases of multiple bee stings are reported from all parts of the world as accidents or after occupational exposure, especially in rural areas[1]. Sting may result in a wide range of clinical spectra ranging from localized pain to systemic anaphylaxis reactions, organ dysfunction and multiple organ failure[2]. Bee venom contains histamine-like active amines, serotonin, quinines, phospholipase A2, hyaluronidase, melittin, and apamin[3,4] which have hemolytic, neurotoxic, and vasoactive characteristics that may cause intravascular hemolysis and rhabdomyolysis as well as other rare severe conditions like myocardial necrosis and infarction, centrilobular necrosis of the liver, and thrombocytopenia due to direct platelet toxicity[3,5,6]. Herein presented is a case of multiple organ dysfunction secondary to multiple bee stings, which has a clinical picture correlating with magnetic resonance imaging (MRI) findings.

CASE REPORT

A female patient, 56 years of age, was accidentally stung multiple times by bees on her head, neck, face, and upper limbs while working in her farmyard. She complained of pain and mild swelling over the stung areas along with

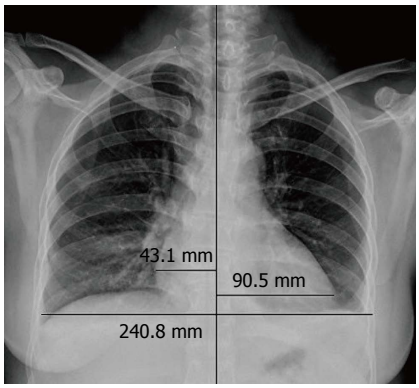

Figure 1 Posteroanterior chest radiograph showing an increased cardio-thoracic ratio [(43.1+90.5)/240.8 > 0.5] demonstrating enlargement of the heart. Bilateral pleural effusion is also evident.

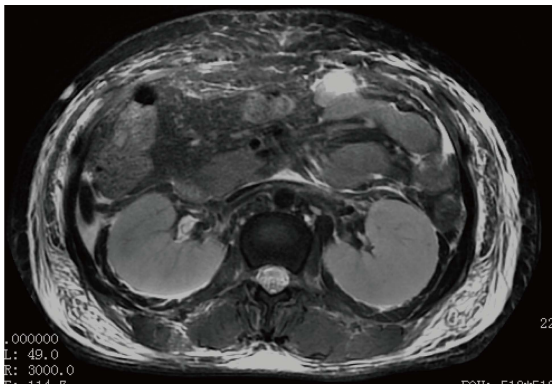

Figure 2 Axial Fat Suppressed T2 Weighted Periodically Rotated Overlapping Parallel Lines with Enhanced Reconstruction FSE image of the abdomen shows bilaterally enlarged kidneys with loss of corticomedullary differentiation. Anterior, posterior renal fascia along with lateral coanal fascia is thickened. High signal intensity within the abdominal cavity represents ascites and those in abdominal soft tissue represent soft tissue edema.

small amount of bleeding. She was taken to the local hospital where her condition deteriorated. She developed nausea, watery vomiting and several bouts of loose stool and was referred to our hospital where, by the next day, her symptoms were further aggravated. Her urine output progressively decreased and was pale yellow in color. Her medical history was unremarkable with no known allergies. Upon examination, she was conscious, cooperative and had approximately 20+ bee sting wounds on her head, neck and upper limbs. The pulse rate was 64 beats/min, the respiratory rate was 20/min, and the blood pressure 182/93 mmHg. Her ECG was recorded as normal sinus rhythm. Hematological studies revealed the following: a total RBC count of 2.50 million/μL (2.80-5.10 million/μL) and a hemoglobin level of 8.70 g/dL (11.50-15.00 g/dL). The levels of biochemical parameters were as follows: serum creatinine 533.30 μmol/L (33.0-96.00 μmol/L), blood urea 15.99 mmol/L (2.1-7.15 μmol/L), creatine kinase 27.80 ng/mL (0-3.8.00 ng/mL), B-type natriuretic peptide 1578.30 pg/mL (0.00-100.00 pg/mL), troponin I 0.229 ng/mL (0.000-0.033 ng/mL), potassium (K) 3.18 mmol/L (3.5 0-5.30 mmol/L), sodium (Na) 136.00 mmol/L (137.00-147.00 mmol/L), myoglobin 1200.00 ng/mL (0.00-116.30 ng/mL), aspartate aminotransferase 55.40 U/L (5.00-35.00 U/L), and alanine aminotransferase 42.50 U/L (5.00-40.00 U/L).

The patient was diagnosed with multiple organ dysfunction syndrome (MODS) (acute kidney injury, myocarditis, hepatic dysfunction, and rhabdomyolysis) and was managed accordingly.

She received alternate-day hemodialysis for two weeks. During this period, her urine output improved gradually, and she became dialysis independent. At the time of discharge, her serum creatinine had stabilized at 88.00 μmol/L.

Imaging findings

Ultrasonography of the kidneys showed bilaterally hypoechoic enlarged kidneys. Chest X-ray revealed bilateral pleural effusion, along with an enlarged one dimensional cardio-thoracic ratio (Figure 1) demonstrating the enlargement of the heart. Head CT was normal. The patient also underwent abdominal MRI, obtaining images in the axial and coronal planes using both T1 and T2 weighted images. The Periodically Rotated Overlapping Parallel Lines with Enhanced Reconstruction (PROPELLER) sequence was used for T2 weighted images, and in and out-of-phase Axial LAVA Flex sequences were used for T1 weighted images. The bilaterally enlarged kidneys with loss of cortico-medullary differentiation were seen on the T2 weighted images (Figure 2). Septal thickening in the perinephric space along with anterior, posterior renal and lateral conal fascia thickening was also noted (Figure 2). Fluid collection in the peritoneal space around the liver and bilateral plural space was evident. Soft tissues around the peritoneal and pelvic cavity showed increased signal on T2 weighted image (Figure 2). Low signal intensity was seen in the splenic parenchyma on LAVA-Flex in-phase sequences as compared to out-phase image (Figure 3). On PROPELLER T2 weighted image the spleen, as well as liver signal intensity was decreased as compared to para-spinal muscle. This represented an iron overload (Figure 4).

DISCUSSION

It was evident from the hematological and biochemical markers observed in the patient that multiple organ dysfunction was secondary to rhabdomyolysis and hemolysis. The MRI findings were accurately concordant with the clinical picture.

The sensitivity of MRI in detecting abnormal muscles is higher than that of CT or ultrasound (100%, 62% and 42%, respectively)[7-9]. While the affected muscles show an increased signal intensity on T2 weighted spin echo images and decreased signal intensity on T1 weighted images[7,8,10], STIR images display good contrast between normal and abnormal muscles and better differentiation of the damaged muscles from the adjacent fat due to its fat suppression (at our hospital, ROPELLER sequence

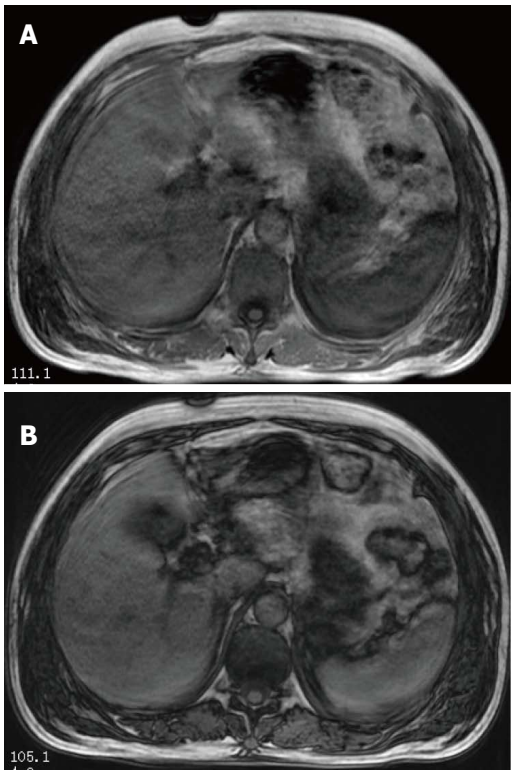

Figure 3 Axial LAVA-Flex T1 Weighted In-Phase image (A) and gradient echo T1 Weighted Out-of-Phase image (B) of the abdomen show decreased signal intensity of the spleen on In-Phase image (A) as compared to Out-of-Phase image (B).

T2 is used to measure fat suppression). At the same time, gradient-echo images are helpful in the detection of hemosiderotic rests in case of hemorrhagic transformation, not in the acute stage, but in chronic long standing disease[11]. Kakuda *et al*[12] described that gadolinium enhanced post-contrast T1 weighted imaging demonstrated lesions more definitively than T2 weighted imaging in the chronic phase of rhabdomyolysis.

In case of acute kidney failure, globular swelling of the kidneys, good cortico-medullary differentiation on T1 weighted images, and loss of cortico-medullary differentiation on T2 weighted images can be observed[13]. In this case study, bilaterally enlarged kidneys with loss of cortico-medullary differentiation on T2 weighted image (Figure 2) were correlated with acute kidney injury as evidenced by increased blood urea and creatinine.

During the last decade, MRI techniques have been developed which allow safe, noninvasive detection and quantitation of iron in body tissues such as the liver, heart, pancreas, and spleen. MRI-based methods for assessing iron overload can be classified into: (1) relaxometry methods measuring absolute T2; (2) relaxometry methods measuring T2*, which is also an absolute value but measured with gradient echo sequences; and (3) signal intensity ratio measurement; where methods A and B show low signal intensity of organs overloaded with iron, and method C measures signal intensity ratio between the iron deposited organs and other tissues in which

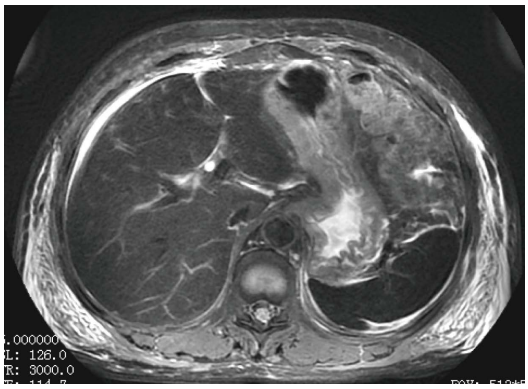

Figure 4 Axial Fat Suppressed T2 Weighted Periodically Rotated Overlapping Parallel Lines with Enhanced Reconstruction FSE image of the abdomen shows decreased signal intensity of the spleen as well as the liver as compared to that of paraspinal muscle.

iron is not generally deposited, usually in the paraspinal muscles[14]. Myoglobin, an iron-containing protein that is released from muscle into the circulation in rhabdomyolysis, is metabolized by the liver and spleen[15], and thus is deposited on them as a result of an overload. In our patient, while LAVA Flex T1 weighted in-phase image showed decreased splenic signal as compared to LAVA Flex T1 weighted out-phase image (Figure 3), the liver signal intensity was decreased on PROPELLER T2 weighted images as compared to its signal intensity with para-spinal muscles (Figure 4). These findings correlated with iron deposition in these organs secondary to hemolysis as evident by the hematological tests.

Cardiac MRI (CMRI) has emerged as a sensitive modality for confirming the myocarditis as well as differentiating acute from chronic. CMRI includes several techniques that can be used in various combinations to assess left ventricular (LV) functional parameters, morphology, myocardial perfusion, and myocardial disorders within one examination[16,17]. In our patient, cardiac dysfunction was confirmed by elevated cardiac enzymes. Apart from chest radiography, neither CMRI nor echocardiography was performed. Chest radiography showed enlargement of the cardio-thoracic ratio which could be due to LV wall thickening secondary to acute myocarditis. Left ventricular hypertrophy can be ruled out when considering the patient's negative history of long term hypertension. Moreover, Hiramitsu *et al*[18] in their study described 25 cases of biopsy proven acute myocarditis with transient thickening of both the interventricular septum and left ventricular wall which was associated with the presence of histologically confirmed interstitial edema. CMR T2-weighted images are sensitive in detecting interstitial edema[17].

Thus, from the presented case, it is concluded that MRI is to be a preferable imaging modality for assessing a patient who presents with multiple organ dysfunction. The MRI only requires one setup, thereby avoiding several imaging procedures which would expose the patient to unnecessary radiation and inconvenience in order to

get a clear picture of the extent of the disease.

COMMENTS

Case characteristics

A 56-year-old female with a history of multiple bee stings presented with mild swelling and pain over the stung area.

Clinical diagnosis

Multiple bee stings along with progressive decrease in urine output and hypertension.

Differential diagnosis

Multiple organ dysfunction syndrome, *i.e.*, acute kidney injury, myocarditis, liver dysfunction, and rhabdomyolysis.

Laboratory diagnosis

Serum creatinine 533.30 μmol/L, blood urea 15.99 mmol/L, creatine kinase 27.80 ng/mL, B-type natriuretic peptide 1578.30 pg/mL, troponin I 0.229 ng/mL, potassium (K) 3.18 mmol/L, sodium (Na) 136.0 mmol/L, myoglobin 1200.0 ng/mL, aspartate aminotransferase 55.4 U/L, alanine aminotransferase 42.5 U/L.

Imaging diagnosis

Magnetic resonance imaging (MRI) showed bilaterally enlarged kidneys with loss of cortico-medullary differentiation, and iron overload in the liver parenchyma with increased signal intensity of the muscles and soft tissues around the peritoneal and pelvic cavity on T2 weighted image.

Treatment

The patient received alternate-day hemodialysis for two weeks.

Experiences and lessons

The case report shows that MR findings are concordant with lab findings and can be preferably used as a single imaging modality to assess multiple organ dysfunction syndrome.

Peer review

It is a well written study for a patient who presented with multiple organ dysfunction syndrome, after multiple bee bites, with acute kidney injury, hepatic and cardiac dysfunction, and had clinical findings correlating with MRI findings.

REFERENCES

1 **Diaz JH**. Recognition, management, and prevention of hymenopteran stings and allergic reactions in travelers. *J Travel Med* 2009; **16**: 357-364 [PMID: 19796109 DOI: 10.1111/J.1708-8305.2009.00316.X]

2 **Sharmila RR**, Chetan G, Narayanan P, Srinivasan S. Multiple organ dysfunction syndrome following single wasp sting. *Indian J Pediatr* 2007; **74**: 1111-1112 [PMID: 18174648]

3 **Habermann E**. Bee and wasp venoms. *Science* 1972; **177**: 314-322 [PMID: 4113805]

4 **Sakhuja V**, Bhalla A, Pereira BJ, Kapoor MM, Bhusnurmath SR, Chugh KS. Acute renal failure following multiple hornet stings. *Nephron* 1988; **49**: 319-321 [PMID: 3412546]

5 **Bhatta N**, Singh R, Sharma S, Sinnha A, Raja S. Acute renal failure following multiple wasp stings. *Pediatr Nephrol* 2005; **20**: 1809-1810 [PMID: 16222551]

6 **Ferreira DB**, Costa RS, De Oliveira JA, Muccillo G. An infarct-like myocardial lesion experimentally induced in Wistar rats with Africanized bee venom. *J Pathol* 1995; **177**: 95-102 [PMID: 7472785]

7 **Lamminen AE**, Hekali PE, Tiula E, Suramo I, Korhola OA. Acute rhabdomyolysis: evaluation with magnetic resonance imaging compared with computed tomography and ultrasonography. *Br J Radiol* 1989; **62**: 326-330 [PMID: 2653546]

8 **Restrepo CS**, Lemos DF, Gordillo H, Odero R, Varghese T, Tiemann W, Rivas FF, Moncada R, Gimenez CR. Imaging findings in musculoskeletal complications of AIDS. *Radiographics* 2004; **24**: 1029-1049 [PMID: 15256627]

9 **Zagoria RJ**, Karstaedt N, Koubek TD. MR imaging of rhabdomyolysis. *J Comput Assist Tomogr* 1986; **10**: 268-270 [PMID: 3005381]

10 **Shintani S**, Shiigai T. Repeat MRI in acute rhabdomyolysis: correlation with clinicopathological findings. *J Comput Assist Tomogr* 1993; **17**: 786-791 [PMID: 8370836]

11 **Moratalla MB**, Braun P, Fornas GM. Importance of MRI in the diagnosis and treatment of rhabdomyolysis. *Eur J Radiol* 2008; **65**: 311-315 [PMID: 17482406]

12 **Kakuda W**, Naritomi H, Miyashita K, Kinugawa H. Rhabdomyolysis lesions showing magnetic resonance contrast enhancement. *J Neuroimaging* 1999; **9**: 182-184 [PMID: 10436762]

13 **Kim SH**, Han MC, Kim S, Lee JS. Acute renal failure secondary to rhabdomyolysis. MR imaging of the kidney. *Acta Radiol* 1992; **33**: 573-576 [PMID: 1449883]

14 **Alústiza Echeverría JM**, Castiella A, Emparanza JI. Quantification of iron concentration in the liver by MRI. *Insights Imaging* 2012; **3**: 173-180 [PMID: 22696043 DOI: 10.1007/s13244-011-0132-1]

15 **Siegelman ES**, Mitchell DG, Rubin R, Hann HW, Kaplan KR, Steiner RM, Rao VM, Schuster SJ, Burk DL, Rifkin MD. Parenchymal versus reticuloendothelial iron overload in the liver: distinction with MR imaging. *Radiology* 1991; **179**: 361-366 [PMID: 2014275]

16 **Olimulder MA**, van Es J, Galjee MA. The importance of cardiac MRI as a diagnostic tool in viral myocarditis-induced cardiomyopathy. *Neth Heart J* 2009; **17**: 481-486 [PMID: 20087452]

17 **Friedrich MG,** Sechtem U, Schulz-Menger J, Holmvang G, Alakija P, Cooper LT, White JA, Abdel-Aty H, Gutberlet M, Prasad S, Aletras A, Laissy JP, Paterson I, Filipchuk NG, Kumar A, Pauschinger M, Liu P. International Consensus Group on Cardiovascular Magnetic Resonance in Myocarditis. Cardiovascular Magnetic Resonance in Myocarditis: A JACC White Paper. *JACC* 2009; **53:** 1475-1487 [DOI: 10.1016/i.iacc. 2009.02.007]

18 **Hiramitsu S,** Morimoto S, Kato S, Uemura A, Kubo N, Kimura K, Sugiura A, Itoh T, Hishida H. Transient ventricular wall thickening in acute myocarditis: a serial echocardiographic and histopathologic study. *Jpn Circ J* 2001; **65**: 863-866 [PMID: 11665789 DOI: 10.1253/jcj.65.863]

P- Reviewer: Passadakis PS, Shou ZF **S- Editor**: Song XX
L- Editor: Wang TQ **E- Editor**: Lu YJ

World Journal of Radiology

Submit a Manuscript: http://www.wjgnet.com/esps/
Help Desk: http://www.wjgnet.com/esps/helpdesk.aspx
www.wjgnet.com

World J Radiol 2014 September 28; 6(9): I-V
ISSN 1949-8470 (online)

INSTRUCTIONS TO AUTHORS

GENERAL INFORMATION

World Journal of Radiology (*World J Radiol*, *WJR*, online ISSN 1949-8470, DOI: 10.4329) is a peer-reviewed open access (OA) academic journal that aims to guide clinical practice and improve diagnostic and therapeutic skills of clinicians.

Aim and scope

WJR covers topics concerning diagnostic radiology, radiation oncology, radiologic physics, neuroradiology, nuclear radiology, pediatric radiology, vascular/interventional radiology, medical imaging achieved by various modalities and related methods analysis. The current columns of *WJR* include editorial, frontier, diagnostic advances, therapeutics advances, field of vision, mini-reviews, review, topic highlight, medical ethics, original articles, case report, clinical case conference (clinicopathological conference), and autobiography.

We encourage authors to submit their manuscripts to *WJR*. We will give priority to manuscripts that are supported by major national and international foundations and those that are of great basic and clinical significance.

WJR is edited and published by Baishideng Publishing Group (BPG). BPG has a strong professional editorial team composed of science editors, language editors and electronic editors. BPG currently publishes 43 OA clinical medical journals, including 42 in English, has a total of 15471 editorial board members or peer reviewers, and is a world first-class publisher.

Columns

The columns in the issues of *WJR* will include: (1) Editorial: The editorial board members are invited to make comments on an important topic in their field in terms of its current research status and future directions to lead the development of this discipline; (2) Frontier: The editorial board members are invited to select a highly cited cutting-edge original paper of his/her own to summarize major findings, the problems that have been resolved and remain to be resolved, and future research directions to help readers understand his/her important academic point of view and future research directions in the field; (3) Diagnostic Advances: The editorial board members are invited to write high-quality diagnostic advances in their field to improve the diagnostic skills of readers. The topic covers general clinical diagnosis, differential diagnosis, pathological diagnosis, laboratory diagnosis, imaging diagnosis, endoscopic diagnosis, biotechnological diagnosis, functional diagnosis, and physical diagnosis; (4) Therapeutics Advances: The editorial board members are invited to write high-quality therapeutic advances in their field to help improve the therapeutic skills of readers. The topic covers medication therapy, psychotherapy, physical therapy, replacement therapy, interventional therapy, minimally invasive therapy, endoscopic therapy, transplantation therapy, and surgical therapy; (5) Field of Vision: The editorial board members are invited to write commentaries on classic articles, hot topic articles, or latest articles to keep readers at the forefront of research and increase their levels of clinical research. Classic articles refer to papers that are included in Web of Knowledge and have received a large number of citations (ranking in the top 1%) after being published for more than years, reflecting the quality and impact of papers. Hot topic articles refer to papers that are included in Web of Knowledge and have received a large number of citations after being published for no more than 2 years, reflecting cutting-edge trends in scientific research. Latest articles refer to the latest published high-quality papers that are included in PubMed, reflecting the latest research trends. These commentary articles should focus on the status quo of research, the most important research topics, the problems that have now been resolved and remain to be resolved, and future research directions. Basic information about the article to be commented (including authors, article title, journal name, year, volume, and inclusive page numbers); (6) Minireviews: The editorial board members are invited to write short reviews on recent advances and trends in research of molecular biology, genomics, and related cutting-edge technologies to provide readers with the latest knowledge and help improve their diagnostic and therapeutic skills; (7) Review: To make a systematic review to focus on the status quo of research, the most important research topics, the problems that have now been resolved and remain to be resolved, and future research directions; (8) Topic Highlight: The editorial board members are invited to write a series of articles (7-10 articles) to comment and discuss a hot topic to help improve the diagnostic and therapeutic skills of readers; (9) Medical Ethics: The editorial board members are invited to write articles about medical ethics to increase readers' knowledge of medical ethics. The topic covers international ethics guidelines, animal studies, clinical trials, organ transplantation, *etc.*; (10) Clinical Case Conference or Clinicopathological Conference: The editorial board members are invited to contribute high-quality clinical case conference; (11) Original Articles: To report innovative and original findings in radiology; (12) Research Report: To briefly report the novel and innovative findings in radiology; (13) Meta-Analysis: Covers the systematic review, mixedtreatment comparison, meta-regression, and overview of reviews, in order to summarize a given quantitative effect, *e.g.*, the clinical effectiveness and safety of clinical treatments by combining data from two or more randomized controlled trials, thereby providing more precise and externally valid estimates than those which would stem from each individual dataset if analyzed separately from the others; (15) Letters to the Editor: To discuss and make reply to the contributions published in *WJR*, or to introduce and comment on a controversial issue of general interest; (16) Book Reviews: To introduce and comment on quality monographs of radiology; and (17) Autobiography: The editorial board members are invited to write their autobiography to provide readers with stories of success or failure in their scientific research career. The topic covers their basic personal information and information about when they started doing research work, where and how they did research work, what they have achieved, and their lessons from success or failure.

Name of journal

World Journal of Radiology

ISSN

ISSN 1949-8470 (online)

Launch date

December 31, 2009

Frequency

Monthly

Editor-in-Chief

Kai U Juergens, MD, Associate Professor, MRT und PET/CT, Nuklearmedizin Bremen Mitte, ZEMODI - Zentrum für morpholo-

Editorial office
Jin-Lei Wang, Director
Xiu-Xia Song, Vice Director
World Journal of Radiology
Room 903, Building D, Ocean International Center,
No. 62 Dongsihuan Zhonglu, Chaoyang District,
Beijing 100025, China
Telephone: +86-10-85381891
Fax: +86-10-85381893
E-mail: editorialoffice@wjgnet.com
Help Desk: http://www.wjgnet.com/esps/helpdesk.aspx
http://www.wjgnet.com

Publisher
Baishideng Publishing Group Inc
8226 Regency Drive,
Pleasanton, CA 94588, USA
Telephone: +1-925-223-8242
Fax: +1-925-223-8243
E-mail: bpgoffice@wjgnet.com
Help Desk: http://www.wjgnet.com/esps/helpdesk.aspx
http://www.wjgnet.com

Instructions to authors
Full instructions are available online at http://www.wjgnet.com/1948-5204/g_info_20100312180518.htm.

Indexed and Abstracted in
PubMed Central, PubMed, Digital Object Identifier, and Directory of Open Access Journals.

SPECIAL STATEMENT

All articles published in journals owned by the BPG represent the views and opinions of their authors, and not the views, opinions or policies of the BPG, except where otherwise explicitly indicated.

Biostatistical editing
Statisital review is performed after peer review. We invite an expert in Biomedical Statistics to evaluate the statistical method used in the paper, including *t*-test (group or paired comparisons), chi-squared test, Ridit, probit, logit, regression (linear, curvilinear, or stepwise), correlation, analysis of variance, analysis of covariance, *etc*. The reviewing points include: (1) Statistical methods should be described when they are used to verify the results; (2) Whether the statistical techniques are suitable or correct; (3) Only homogeneous data can be averaged. Standard deviations are preferred to standard errors. Give the number of observations and subjects (*n*). Losses in observations, such as drop-outs from the study should be reported; (4) Values such as ED50, LD50, IC50 should have their 95% confidence limits calculated and compared by weighted probit analysis (Bliss and Finney); and (5) The word 'significantly' should be replaced by its synonyms (if it indicates extent) or the *P* value (if it indicates statistical significance).

Conflict-of-interest statement
In the interests of transparency and to help reviewers assess any potential bias, *WJR* requires authors of all papers to declare any competing commercial, personal, political, intellectual, or religious interests in relation to the submitted work. Referees are also asked to indicate any potential conflict they might have reviewing a particular paper. Before submitting, authors are suggested to read "Uniform Requirements for Manuscripts Submitted to Biomedical Journals: Ethical Considerations in the Conduct and Reporting of Research: Conflicts of Interest" from International Committee of Medical Journal Editors (ICMJE), which is available at: http://www.icmje.org/ethical_4conflicts.html.

Sample wording: [Name of individual] has received fees for serving as a speaker, a consultant and an advisory board member for [names of organizations], and has received research funding from [names of organization]. [Name of individual] is an employee of [name of organization]. [Name of individual] owns stocks and shares in [name of organization]. [Name of individual] owns patent [patent identification and brief description].

Statement of informed consent
Manuscripts should contain a statement to the effect that all human studies have been reviewed by the appropriate ethics committee or it should be stated clearly in the text that all persons gave their informed consent prior to their inclusion in the study. Details that might disclose the identity of the subjects under study should be omitted. Authors should also draw attention to the Code of Ethics of the World Medical Association (Declaration of Helsinki, 1964, as revised in 2004).

Statement of human and animal rights
When reporting the results from experiments, authors should follow the highest standards and the trial should conform to Good Clinical Practice (for example, US Food and Drug Administration Good Clinical Practice in FDA-Regulated Clinical Trials; UK Medicines Research Council Guidelines for Good Clinical Practice in Clinical Trials) and/or the World Medical Association Declaration of Helsinki. Generally, we suggest authors follow the lead investigator's national standard. If doubt exists whether the research was conducted in accordance with the above standards, the authors must explain the rationale for their approach and demonstrate that the institutional review body explicitly approved the doubtful aspects of the study.

Before submitting, authors should make their study approved by the relevant research ethics committee or institutional review board. If human participants were involved, manuscripts must be accompanied by a statement that the experiments were undertaken with the understanding and appropriate informed consent of each. Any personal item or information will not be published without explicit consents from the involved patients. If experimental animals were used, the materials and methods (experimental procedures) section must clearly indicate that appropriate measures were taken to minimize pain or discomfort, and details of animal care should be provided.

SUBMISSION OF MANUSCRIPTS

Manuscripts should be typed in 1.5 line spacing and 12 pt. Book Antiqua with ample margins. Number all pages consecutively, and start each of the following sections on a new page: Title Page, Abstract, Introduction, Materials and Methods, Results, Discussion, Acknowledgements, References, Tables, Figures, and Figure Legends. Neither the editors nor the publisher are responsible for the opinions expressed by contributors. Manuscripts formally accepted for publication become the permanent property of BPG, and may not be reproduced by any means, in whole or in part, without the written permission of both the authors and the publisher. We reserve the right to copy-edit and put onto our website accepted manuscripts. Authors should follow the relevant guidelines for the care and use of laboratory animals of their institution or national animal welfare committee. For the sake of transparency in regard to the performance and reporting of clinical trials, we endorse the policy of the ICMJE to refuse to publish papers on clinical trial results if the trial was not recorded in a publicly-accessible registry at its outset. The only register now available, to our knowledge, is http://www.clinicaltrials.gov sponsored by the United States National Library of Medicine and we encourage all potential contributors to register with it. However, in the case that other registers

become available you will be duly notified. A letter of recommendation from each author's organization should be provided with the contributed article to ensure the privacy and secrecy of research is protected.

Authors should retain one copy of the text, tables, photographs and illustrations because rejected manuscripts will not be returned to the author(s) and the editors will not be responsible for loss or damage to photographs and illustrations sustained during mailing.

Online submissions

Manuscripts should be submitted through the Online Submission System at: http://www.wjgnet.com/esps/. Authors are highly recommended to consult the ONLINE INSTRUCTIONS TO AUTHORS (http://www.wjgnet.com/1948-5204/g_info_20100312180518.htm) before attempting to submit online. For assistance, authors encountering problems with the Online Submission System may send an email describing the problem to bpgoffice@wjgnet.com, or by telephone: +86-10-85381891. If you submit your manuscript online, do not make a postal contribution. Repeated online submission for the same manuscript is strictly prohibited.

MANUSCRIPT PREPARATION

All contributions should be written in English. All articles must be submitted using word-processing software. All submissions must be typed in 1.5 line spacing and 12 pt. Book Antiqua with ample margins. Style should conform to our house format. Required information for each of the manuscript sections is as follows:

Title page

Title: Title should be less than 12 words.

Running title: A short running title of less than 6 words should be provided.

Authorship: Authorship credit should be in accordance with the standard proposed by International Committee of Medical Journal Editors, based on (1) substantial contributions to conception and design, acquisition of data, or analysis and interpretation of data; (2) drafting the article or revising it critically for important intellectual content; and (3) final approval of the version to be published. Authors should meet conditions 1, 2, and 3.

Institution: Author names should be given first, then the complete name of institution, city, province and postcode. For example, Xu-Chen Zhang, Li-Xin Mei, Department of Pathology, Chengde Medical College, Chengde 067000, Hebei Province, China. One author may be represented from two institutions, for example, George Sgourakis, Department of General, Visceral, and Transplantation Surgery, Essen 45122, Germany; George Sgourakis, 2nd Surgical Department, Korgialenio-Benakio Red Cross Hospital, Athens 15451, Greece

Author contributions: The format of this section should be: Author contributions: Wang CL and Liang L contributed equally to this work; Wang CL, Liang L, Fu JF, Zou CC, Hong F and Wu XM designed the research; Wang CL, Zou CC, Hong F and Wu XM performed the research; Xue JZ and Lu JR contributed new reagents/analytic tools; Wang CL, Liang L and Fu JF analyzed the data; and Wang CL, Liang L and Fu JF wrote the paper.

Supportive foundations: The complete name and number of supportive foundations should be provided, e.g. Supported by National Natural Science Foundation of China, No. 30224801

Correspondence to: Only one corresponding address should be provided. Author names should be given first, then author title, affiliation, the complete name of institution, city, postcode, province, country, and email. All the letters in the email should be in lower case. A space interval should be inserted between country name and email address. For example, Montgomery Bissell, MD, Professor of Medicine, Chief, Liver Center, Gastroenterology Division, University of California, Box 0538, San Francisco, CA 94143, United States. montgomery.bissell@ucsf.edu

Telephone and fax: Telephone and fax should consist of +, country number, district number and telephone or fax number, e.g. Telephone: +86-10-85381891 Fax: +86-10-85381893

Peer reviewers: All articles received are subject to peer review. Normally, three experts are invited for each article. Decision on acceptance is made only when at least two experts recommend publication of an article. All peer-reviewers are acknowledged on Express Submission and Peer-review System website.

Abstract

There are unstructured abstracts (no less than 200 words) and structured abstracts. The specific requirements for structured abstracts are as follows:

An informative, structured abstract should accompany each manuscript. Abstracts of original contributions should be structured into the following sections: AIM (no more than 20 words; Only the purpose of the study should be included. Please write the Aim in the form of "To investigate/study/…"), METHODS (no less than 140 words for Original Articles; and no less than 80 words for Brief Articles), RESULTS (no less than 150 words for Original Articles and no less than 120 words for Brief Articles; You should present *P* values where appropriate and must provide relevant data to illustrate how they were obtained, e.g. 6.92 ± 3.86 *vs* 3.61 ± 1.67, $P < 0.001$), and CONCLUSION (no more than 26 words).

Key words

Please list 5-10 key words, selected mainly from *Index Medicus*, which reflect the content of the study.

Core tip

Please write a summary of less than 100 words to outline the most innovative and important arguments and core contents in your paper to attract readers.

Text

For articles of these sections, original articles and brief articles, the main text should be structured into the following sections: INTRODUCTION, MATERIALS AND METHODS, RESULTS and DISCUSSION, and should include appropriate Figures and Tables. Data should be presented in the main text or in Figures and Tables, but not in both. The main text format of these sections, editorial, topic highlight, case report, letters to the editors, can be found at: http://www.wjgnet.com/1948-5204/g_info_list.htm.

Illustrations

Figures should be numbered as 1, 2, 3, *etc*., and mentioned clearly in the main text. Provide a brief title for each figure on a separate page. Detailed legends should not be provided under the figures. This part should be added into the text where the figures are applicable. Keeping all elements compiled is necessary in line-art image. Scale bars should be used rather than magnification factors, with the length of the bar defined in the legend rather than on the bar itself. File names should identify the figure and panel. Avoid layering type directly over shaded or textured areas. Please use uniform legends for the same subjects. For example: Figure 1 Pathological changes in atrophic gastritis after treatment. A: ...; B: ...; C: ...; D: ...; E: ...; F: ...; G: …*etc*. It is our principle to publish high resolution-figures for the E-versions.

Tables

Three-line tables should be numbered 1, 2, 3, *etc*., and mentioned clearly in the main text. Provide a brief title for each table. Detailed legends should not be included under tables, but rather added into the text where applicable. The information should complement, but not duplicate the text. Use one horizontal line under the title, a second under column heads, and a third below the Table, above any footnotes. Vertical and italic lines should be omitted.

Notes in tables and illustrations

Data that are not statistically significant should not be noted. [a]$P < 0.05$, [b]$P < 0.01$ should be noted ($P > 0.05$ should not be noted). If there are other series of P values, [c]$P < 0.05$ and [d]$P < 0.01$ are used. A third series of P values can be expressed as [e]$P < 0.05$ and [f]$P < 0.01$. Other notes in tables or under illustrations should be expressed as [1]F, [2]F, [3]F; or sometimes as other symbols with a superscript (Arabic numerals) in the upper left corner. In a multi-curve illustration, each curve should be labeled with ●, ○, ■, □, ▲, △, *etc*., in a certain sequence.

Acknowledgments

Brief acknowledgments of persons who have made genuine contributions to the manuscript and who endorse the data and conclusions should be included. Authors are responsible for obtaining written permission to use any copyrighted text and/or illustrations.

REFERENCES

Coding system

The author should number the references in Arabic numerals according to the citation order in the text. Put reference numbers in square brackets in superscript at the end of citation content or after the cited author's name. For citation content which is part of the narration, the coding number and square brackets should be typeset normally. For example, "Crohn's disease (CD) is associated with increased intestinal permeability[1,2]". If references are cited directly in the text, they should be put together within the text, for example, "From references[19,22-24], we know that..."

When the authors write the references, please ensure that the order in text is the same as in the references section, and also ensure the spelling accuracy of the first author's name. Do not list the same citation twice.

PMID and DOI

Pleased provide PubMed citation numbers to the reference list, e.g. PMID and DOI, which can be found at http://www.ncbi.nlm.nih.gov/sites/entrez?db=pubmed and http://www.crossref.org/SimpleTextQuery/, respectively. The numbers will be used in E-version of this journal.

Style for journal references

Authors: the name of the first author should be typed in bold-faced letters. The family name of all authors should be typed with the initial letter capitalized, followed by their abbreviated first and middle initials. (For example, Lian-Sheng Ma is abbreviated as Ma LS, Bo-Rong Pan as Pan BR). The title of the cited article and italicized journal title (journal title should be in its abbreviated form as shown in PubMed), publication date, volume number (in black), start page, and end page [PMID: 11819634 DOI: 10.3748/wjg.13.5396].

Style for book references

Authors: the name of the first author should be typed in bold-faced letters. The surname of all authors should be typed with the initial letter capitalized, followed by their abbreviated middle and first initials. (For example, Lian-Sheng Ma is abbreviated as Ma LS, Bo-Rong Pan as Pan BR) Book title. Publication number. Publication place: Publication press, Year: start page and end page.

Format

Journals

English journal article (list all authors and include the PMID where applicable)

1 **Jung EM**, Clevert DA, Schreyer AG, Schmitt S, Rennert J, Kubale R, Feuerbach S, Jung F. Evaluation of quantitative contrast harmonic imaging to assess malignancy of liver tumors: A prospective controlled two-center study. *World J Gastroenterol* 2007; **13**: 6356-6364 [PMID: 18081224 DOI: 10.3748/wjg.13.6356]

Chinese journal article (list all authors and include the PMID where applicable)

2 **Lin GZ**, Wang XZ, Wang P, Lin J, Yang FD. Immunologic effect of Jianpi Yishen decoction in treatment of Pixu-diarrhoea. *Shijie Huaren Xiaohua Zazhi* 1999; **7**: 285-287

In press

3 **Tian D**, Araki H, Stahl E, Bergelson J, Kreitman M. Signature of balancing selection in Arabidopsis. *Proc Natl Acad Sci USA* 2006; In press

Organization as author

4 **Diabetes Prevention Program Research Group**. Hypertension, insulin, and proinsulin in participants with impaired glucose tolerance. *Hypertension* 2002; **40**: 679-686 [PMID: 12411462 DOI:10.1161/01.HYP.0000035706.28494.09]

Both personal authors and an organization as author

5 **Vallancien G**, Emberton M, Harving N, van Moorselaar RJ; Alf-One Study Group. Sexual dysfunction in 1, 274 European men suffering from lower urinary tract symptoms. *J Urol* 2003; **169**: 2257-2261 [PMID: 12771764 DOI:10.1097/01.ju.0000067940.76090.73]

No author given

6 21st century heart solution may have a sting in the tail. *BMJ* 2002; **325**: 184 [PMID: 12142303 DOI:10.1136/bmj.325.7357.184]

Volume with supplement

7 **Geraud G**, Spierings EL, Keywood C. Tolerability and safety of frovatriptan with short- and long-term use for treatment of migraine and in comparison with sumatriptan. *Headache* 2002; **42** Suppl 2: S93-99 [PMID: 12028325 DOI:10.1046/j.1526-4610.42.s2.7.x]

Issue with no volume

8 **Banit DM**, Kaufer H, Hartford JM. Intraoperative frozen section analysis in revision total joint arthroplasty. *Clin Orthop Relat Res* 2002; (**401**): 230-238 [PMID: 12151900 DOI:10.1097/00003086-200208000-00026]

No volume or issue

9 Outreach: Bringing HIV-positive individuals into care. *HRSA Careaction* 2002; 1-6 [PMID: 12154804]

Books

Personal author(s)

10 **Sherlock S**, Dooley J. Diseases of the liver and billiary system. 9th ed. Oxford: Blackwell Sci Pub, 1993: 258-296

Chapter in a book (list all authors)

11 **Lam SK**. Academic investigator's perspectives of medical treatment for peptic ulcer. In: Swabb EA, Azabo S. Ulcer disease: investigation and basis for therapy. New York: Marcel Dekker, 1991: 431-450

Author(s) and editor(s)

12 **Breedlove GK**, Schorfheide AM. Adolescent pregnancy. 2nd ed. Wieczorek RR, editor. White Plains (NY): March of Dimes Education Services, 2001: 20-34

Conference proceedings

13 **Harnden P**, Joffe JK, Jones WG, editors. Germ cell tumours V. Proceedings of the 5th Germ cell tumours Conference; 2001 Sep 13-15; Leeds, UK. New York: Springer, 2002: 30-56

Conference paper

14 **Christensen S**, Oppacher F. An analysis of Koza's computational effort statistic for genetic programming. In: Foster JA, Lutton E, Miller J, Ryan C, Tettamanzi AG, editors. Genetic programming. EuroGP 2002: Proceedings of the 5th European Conference on Genetic Programming; 2002 Apr 3-5; Kinsdale, Ireland. Berlin: Springer, 2002: 182-191

Electronic journal (list all authors)

15 Morse SS. Factors in the emergence of infectious diseases. Emerg Infect Dis serial online, 1995-01-03, cited 1996-06-05; 1(1): 24 screens. Available from: URL: http://www.cdc.gov/ncidod/eid/index.htm

Patent (list all authors)

16 **Pagedas AC**, inventor; Ancel Surgical R&D Inc., assignee. Flexible endoscopic grasping and cutting device and positioning tool assembly. United States patent US 20020103498. 2002 Aug 1

Statistical data
Write as mean ± SD or mean ± SE.

Statistical expression
Express *t* test as *t* (in italics), *F* test as *F* (in italics), chi square test as χ^2 (in Greek), related coefficient as *r* (in italics), degree of freedom as υ (in Greek), sample number as *n* (in italics), and probability as *P* (in italics).

Units
Use SI units. For example: body mass, m (B) = 78 kg; blood pressure, p (B) = 16.2/12.3 kPa; incubation time, t (incubation) = 96 h, blood glucose concentration, c (glucose) 6.4 ± 2.1 mmol/L; blood CEA mass concentration, p (CEA) = 8.6 24.5 μg/L; CO_2 volume fraction, 50 mL/L CO_2, not 5% CO_2; likewise for 40 g/L formaldehyde, not 10% formalin; and mass fraction, 8 ng/g, *etc.* Arabic numerals such as 23, 243, 641 should be read 23243641.

The format for how to accurately write common units and quantums can be found at: http://www.wjgnet.com/1948-5204/g_info_20100312183048.htm.

Abbreviations
Standard abbreviations should be defined in the abstract and on first mention in the text. In general, terms should not be abbreviated unless they are used repeatedly and the abbreviation is helpful to the reader. Permissible abbreviations are listed in Units, Symbols and Abbreviations: A Guide for Biological and Medical Editors and Authors (Ed. Baron DN, 1988) published by The Royal Society of Medicine, London. Certain commonly used abbreviations, such as DNA, RNA, HIV, LD50, PCR, HBV, ECG, WBC, RBC, CT, ESR, CSF, IgG, ELISA, PBS, ATP, EDTA, mAb, can be used directly without further explanation.

Italics
Quantities: *t* time or temperature, *c* concentration, *A* area, *l* length, *m* mass, *V* volume.
Genotypes: *gyrA*, *arg* 1, *c myc*, *c fos*, *etc.*
Restriction enzymes: *Eco*RI, *Hin*dI, *Bam*HI, *Kbo* I, *Kpn* I, *etc.*
Biology: *H. pylori*, *E coli*, *etc.*

Examples for paper writing
All types of articles' writing style and requirement will be found in the link: http://www.wjgnet.com/esps/NavigationInfo.aspx?id=15

SUBMISSION OF THE REVISED MANUSCRIPTS AFTER ACCEPTED

Authors must revise their manuscript carefully according to the revision policies of BPG. The revised version, along with the signed copyright transfer agreement, responses to the reviewers, and English language Grade B certificate (for non-native speakers of English), should be submitted to the online system via the link contained in the e-mail sent by the editor. If you have any questions about the revision, please send e-mail to esps@wjgnet.com.

Language evaluation
The language of a manuscript will be graded before it is sent for revision. (1) Grade A: priority publishing; (2) Grade B: minor language polishing; (3) Grade C: a great deal of language polishing needed; and (4) Grade D: rejected. Revised articles should reach Grade A or B.

Copyright assignment form
Please download a Copyright assignment form from http://www.wjgnet.com/1948-5204/g_info_20100312182928.htm.

Responses to reviewers
Please revise your article according to the comments/suggestions provided by the reviewers. The format for responses to the reviewers' comments can be found at: http://www.wjgnet.com/1948-5204/g_info_20100312182841.htm.

Proof of financial support
For papers supported by a foundation, authors should provide a copy of the approval document and serial number of the foundation.

STATEMENT ABOUT ANONYMOUS PUBLICATION OF THE PEER REVIEWERS' COMMENTS

In order to increase the quality of peer review, push authors to carefully revise their manuscripts based on the peer reviewers' comments, and promote academic interactions among peer reviewers, authors and readers, we decide to anonymously publish the reviewers' comments and author's responses at the same time the manuscript is published online.

PUBLICATION FEE

WJR is an international, peer-reviewed, OA online journal. Articles published by this journal are distributed under the terms of the Creative Commons Attribution Non-commercial License, which permits use, distribution, and reproduction in any medium and format, provided the original work is properly cited. The use is non-commercial and is otherwise in compliance with the license. Authors of accepted articles must pay a publication fee. Publication fee: 698 USD per article. All invited articles are published free of charge.

Published by **Baishideng Publishing Group Inc**
8226 Regency Drive, Pleasanton, CA 94588, USA
Telephone: +1-925-223-8242
Fax: +1-925-223-8243
E-mail: bpgoffice@wjgnet.com
Help Desk: http://www.wjgnet.com/esps/helpdesk.aspx
http://www.wjgnet.com